Title	X-ray surveys of active galactic nuclei in field and cluster environments
Author	Johnson, Olivia
Qualification	PhD
Year	2004

X-ray Surveys of Active Galactic Nuclei in Field and Cluster Environments

---

OLIVIA JOHNSON

Institute for Astronomy
School of Physics

A thesis submitted to the University of Edinburgh
for the degree of Doctor of Philosophy

September 2004

Summary

In recent years, the Chandra and XMM-Newton observatories have provided an unprecedented view of the X-ray sky, with deep surveys resolving the majority of the X-ray flux in the Universe for the first time. This thesis presents three multiwavelength surveys of different environments based on deep X-ray observations, which together aim to develop our understanding of Active Galactic Nuclei (AGN) and their role within the evolution of galaxies and their larger-scale environment.

I present results of the ELAIS Deep X-ray Survey (EDXS), an early Chandra 'blank field' survey designed to characterise the components of the XRB and to study their relation to populations detected in other wavebands. Between 50–64% of the XRB is resolved into sources detected in the two EDXS fields which are optically identified as quasars, bright galaxies, and optically faint sources. The X-ray spectral properties of the sources indicate that those with optically faint and galaxy morphology are likely to house a large population of obscured AGN as predicted by synthesis models of the XRB. These optically resolved sources have fainter X-ray and optical fluxes, harder X-ray spectra, redder optical colours, and more scatter in their X-ray to optical ratios than the quasars in the sample, which is in general consistent with X-ray obscuration of nuclear light in sources in which the host galaxy dominates the optical properties. Detailed comparison of the X-ray and optical/near-IR spectra of selected EDXS sources indicates substantial variety in source morphology and in relative obscuration by gas and dust in the obscured AGN population.

I have conducted an analysis of the AGN content of the $z = 0.83$ galaxy cluster MS1054-03 based on archival Chandra data. I detect 47 X-ray point sources in the MS1054-03 field, of which two are confirmed from pre-existing spectroscopy to be luminous AGN at the redshift of the cluster. At bright fluxes, I find a 2σ excess of point sources compared to the predictions from field surveys, consistent with ~ 6 additional cluster AGN. Combined with the identification of 7 cluster AGN in deep radio observations, these observations suggest significantly enhanced AGN activity in MS1054-03 compared to local galaxy clusters. The excess of X-ray detected AGN is found at radial distances of 1 to 2 Mpc from the cluster centre, suggesting they may be associated with infalling galaxies. The radio AGN are seen within the inner Mpc of the cluster and are largely undetected in the X-ray, suggesting they are either intrinsically less luminous and/or heavily obscured.

I have surveyed the SSA22 protocluster at $z = 3.09$ using both extremely deep XMM-Newton imaging data and narrow-band wide-field Lyα observations of the field. I detect 29 new candidate Lyα emitters and 190 X-ray sources in the region. A Lyman Break Galaxy (LBG) and two Lyα candidates are detected in the X-ray, hosting quasars with estimated bolometric luminosities of $\sim 10^{46}$ erg s^{-1}. The observed AGN fractions of LBGs and Lyα candidates in SSA22 are $\sim 4\%$ and $\sim 1.3\%$, respectively. Stacking analysis of the LBG, Lyα candidate, and submillimetre-selected samples in the field do not result in significant detections, and limit the average hard X-ray luminosity of each type of source to $\sim 5 \times 10^{43}$ erg s^{-1}. There is no evidence of diffuse X-ray emission associated with the protocluster as a whole or with luminous, diffuse regions of Lyα flux in the structure. Soft band X-ray flux on scales of ~ 1 Mpc is limited to $L_{0.5-2\mathrm{keV}} \lesssim 9 \times 10^{43}$ erg s^{-1}, robustly excluding all but the faintest thermal emission seen in local clusters. On smaller scales of ~ 0.6 Mpc which may be more typical of high redshift clusters, the limit is $L_{0.5-2\mathrm{keV}} \lesssim 3 \times 10^{43}$, which just excludes the level of emission seen in clusters at $z \sim 1.3$ The limit on thermal X-ray emission associated with the diffuse Lyα emission, is $L_{0.5-2\mathrm{keV}} \lesssim 1 \times 10^{42}$ erg s^{-1}. Point source limits in these regions exclude AGN with obscuring columns of $N_H \lesssim 10^{23}$ cm^{-2} to $L_{0.5-8\mathrm{keV}} \lesssim 5 \times 10^{43}$ erg s^{-1}, and all but Compton thick sources to $L_{0.5-8\mathrm{keV}} \lesssim 10^{45}$ erg s^{-1}.

Declaration

I hereby declare that this thesis entitled *"X-ray Surveys of Active Galactic Nuclei in Field and Cluster Environments"* is not substantially the same as any that I have submitted for a degree or diploma or other qualification at any other University. I further state that no part of my thesis has already been or is being concurrently submitted for any such degree, diploma or other qualification.

Parts of the work contained in this thesis have been published, or are due to be published, in refereed scientific journals.

> Sections of Chapter 3 are based on my contributions to work published in *"The ELAIS deep X-ray survey - I. Chandra source catalogue and first results"*, J. Manners *et al.*, MNRAS, 343, 293, and in *"Obscured active galactic nuclei in the ELAIS Deep X-ray Survey"*, C. Willott *et al*, MNRAS, 399, 397.
>
> Chapter 4 is based on work presented in the paper *"The content of active galactic nuclei in the* $z = 0.83$ *cluster MS1054-0321,"* O. Johnson, P. N. Best, and O. Almaini, MNRAS, 2003, 343, 924.

This thesis is the outcome of my own work except where specifically indicated in the text.

Olivia Johnson
Edinburgh,
September 2004.

Acknowledgements

First and foremost, thanks to Daniel for living together as if we were married (and occasionally ceding the prime tele watching position) and to Ian for asking what shoes I was wearing. You're my best mates, you are, and I'm enormously grateful for all you've done to see me through my time in Edinburgh.

For the science: A large debt of gratitude is due my supervisors, Omar and Andy, for sharing their knowledge, encouragement, and support. Particular thanks to Omar for that pre-interview cup of tea and to Andy for being 'my old man'. Many thanks to Philip for his unfailingly kind and vastly knowledgeable help over the years. Thanks to James for figures and for writing a bloody great introduction; to Vinay for his views on SRC_SIGNIFICANCE (if not for his views on cricket); to Pete Freeman for gracious provision and modification of the WAVDETECT code; and to Brad, for not minding when I call to talk about statistics. Finally, I am grateful to Peter Brand for accepting me into the programme late in the year, to John Peacock for his efforts to engineer funding for my study and travels, and to the Institute of Astronomy and the School of Physics for financial support.

For the craic: thanks to Louisa, who is hard as nails; to James, who is the gold standard and who also moved quite near to Venice, which is unique; to Mikey Brown, who could still be a rock star; and to Ali, who is alright, for a boy, sometimes, and was invariably and quizzically there when most needed. Many many thanks to the most recent generation of R7 —Michael, Mairi, Ben, and, lately, Miller— for being ludicrously kind and supportive of the cranky old woman in the corner. A special thanks to Michael for understanding about those zebra zebra duckers at XMM HQ.

For miscellaneous good things: thanks to Andy for teaching me to drive stick and climb mountains, and for all the warm, bright time up North; to Tara and Rachel M. for a foghorn, bogs, and girly chat; to Martin for all the drinks (cheers); to Fred and Deb, who turned my father's little girl into a scientist; to Heady, who is still the smarts and the spice; to Brad, for his constant correspondence; to Jeremy, for suggesting the UK in the first place (which I'd "no doubt loathe completely within 6 months anyway "); to Eli, for sunrise over Budapest; to Mairi and Rachel D. for not minding that I left the lights on; Y a Leon para los cabalos para chargar la batteria.

Finally, thanks to Augusta, for giving a fine example of how to go about getting a second degree and for her support over the years, and to my parents, for raising me to think running off to a foreign country to do a costly PhD in an obscure subject was a reasonable thing to do and for consistently providing me with both the reason and the means to keep coming back home. With admiration, gratitude, and love, this is for you.

Contents

List of Figures

List of Tables

CHAPTER 1

Introduction

The Chandra and XMM-Newton X-ray observatories have provided an unprecedented view of the X-ray sky, with deep surveys resolving the majority of the X-ray flux in the Universe for the first time. Most of this flux is thought to be produced by accretion of galactic material onto supermassive black holes in Active Galactic Nuclei (AGN). A growing body of evidence suggests this accretion is not a rare phenomenon found within exceptional galaxies, but rather a key process which is intimately linked to the growth of every galaxy. In this thesis I use X-ray-based, multiwavelength surveys to characterise the newly-resolved AGN population and to investigate the interrelation of AGN, their host galaxies, and their environment on larger scales.

In this introductory chapter, I briefly describe the broad observational characteristics and basic theoretical model of AGN in §1.1, with an emphasis on emission in the X-ray band. In §1.2, I review studies of the cosmic X-ray background (XRB) and their utility in determining AGN demographics. I then discuss evidence of the linked evolution of AGN and their host galaxies (§1.3) and how this process may be affected by the larger-scale environment (§1.4). I conclude with a brief summary of the work presented in this thesis in §1.5.

1.1 Active galactic nuclei

The term Active Galactic Nucleus (AGN) now encompasses a diverse array of historically separate astronomical phenomena. Some of the apparent variety is purely historical, due to biases in the methods by which AGN were first discovered, and much more may be due to the particulars of viewing angle and obscuration along the line of sight. By way of introduction to the nomenclature of the field, I begin by describing the broad observational characteristics of several varieties of AGN encountered in this thesis.

1.1.1 Taxonomy

The first AGN to be recognised were a subset of galaxies distinguished by their compact, luminous nuclei and the strong emission lines of highly ionised species in their optical spectra (Seyfert 1943). Now known to be AGN of relatively low luminosity, **Seyfert galaxies** are generally spiral galaxies in which the extended stellar emission from the galaxy is visible surrounding the unresolved nucleus. Somewhat arbitrary luminosity limits delineate Seyferts from higher luminosity AGN, with Seyferts traditionally having optical nuclear luminosities of $M_B > -21.5 + 5\log h_0$ — where M_B is the Vega absolute B-band magnitude and h_0 is the Hubble constant in units of 100 km s^{-1} Mpc^{-1} — and X-ray luminosities $\lesssim 10^{44}$ erg s^{-1}. Seyferts are subclassified by the particulars of their optical spectra, which typically contain emission lines of the Balmer series of hydrogen, as well as high excitation lines of several cosmically abundant elements. **Type 2** spectra include lines of permitted, semi-forbidden, and forbidden transitions with widths of a few $\times 10^2$ km s^{-1}. In **Type 1** spectra, a broader component is also seen in permitted transition lines, with widths of up to 10^4 km s^{-1}.

Quasars[1] are high luminosity AGN in which the extremely bright central nucleus significantly outshines the host galaxy, leading to a perceived point-like appearance. First identified in the wide-field radio surveys in the late 1950s, quasars had unusually blue unresolved optical counterparts and exhibited broad emission lines, only later recognised as highly redshifted lines of the Lyman series (Schmidt 1963). Quasars have remarkably broad multiwavelength continuum spectra, stretching from radio to γ-ray frequencies. Their emission line spectra are in general similar to Seyfert spectra, except: (i) the bright continuum from the quasar often covers any stellar absorption features; (ii) the flux in the narrow line component relative to the broad line component is often lower in quasars than in Seyferts; and (iii) until recently, there were few examples of radio-quiet Type 2 quasar spectra.

At the low-luminosity end of the range in nuclear activity are **low-luminosity AGN (LLAGN)**, which have bolometric luminosities less than 10^{42} erg s^{-1}and have recently been found to be quite common. **Low-ionisation nuclear emission-line regions (LINERs**; Heckman 1980) are found to populate as many as half of all nearby spirals (Ho et al. 1994). While similar to Seyfert spectra, LINER spectra show particularly strong low-ionisation lines such as [O I] and [N II]. The ratio of [O III]/Hβ commonly used to differentiate between nuclear and stellar emission processes is ambiguous for LINERs, but many LINERs displaying

---

[1] Historically the terms quasar, deriving from Quasi-Stellar Radio Source, and QSO, short for Quasi-Stellar Object, related to the radio-loudness of the source, with QSOs being the radio-quiet variants of quasars. Today they are used interchangeably for 'high luminosity AGN'.

broad lines are found to be powered by LLAGN (e.g., Terashima and Wilson 2003). Whether all LINERs house LLAGN is still an open question.

While quasars were originally identified in the radio, optical surveys seeking to select them on the basis of their unusually blue colour found that only a small fraction ($\sim 10\%$) of them have significant amounts of radio emission. **Radio-loud AGN** emit up to 0.1% of their bolometric luminosity in the radio range, while the radio flux from radio-quiet sources is orders of magnitude lower (see Figure 1.1). Subclassification of radio-loud sources is on the basis of their optical properties: sources with point-like optical counterparts are **radio loud quasars**, while those associated with galaxies are called **radio galaxies**. Radio galaxies are further delineated by the presence of broad lines in their optical spectra, with **broad line radio galaxies (BLRGs)** and **narrow line radio galaxies (NLRG)** the rough equivalent of radio-loud Type 1 and Type 2 AGN. The radio morphology of AGN can be complex, consisting of a compact (< 0.01 pc) flat-spectrum core coincident with the optical AGN, extended double lobes of steep-spectrum emission spanning up to a few Mpc, and well-collimated jets connecting the core to the lobes.

Other classes of AGN which do not feature in this thesis are: (i) **blazars** which exhibit highly polarised emission and extremely rapid variability thought to be due to pole-on viewing of a relativistic jet [2] and (ii) **broad absorption line (BAL) quasars** whose spectra contain strong absorption features associated with an outflow from the central engine.

1.1.2 Common observational characteristics

Regardless of subclassification, all AGN share some common characteristics which have driven AGN surveys and are the basis of our physical understanding of AGN.

- **Compact, luminous nucleus**: All AGN produce an enormous amount of luminosity in an extremely small region. Luminosities of typical AGN range from $\simeq 10^{42}$ erg s^{-1} to $\simeq 10^{48}$ erg s^{-1}, which is 0.01 to 10^4 times the integrated luminosity of a typical non-active galaxy. The vast majority of this emission arises from a region which is unresolved at all wavelengths. An upper limit on the size of the emitting region can be inferred from the short timescale variability of these sources. Since source fluctuations cannot in general take place on shorter timescales than the light-crossing time, the typical variability of AGN on scales of hours to years implies maximum emission region sizes ranging from $\simeq 10^{-4} - 10$ pc.
- **Broad continuum emission**: AGN are known to radiate significantly at all wavelengths at which they have been observed. In most AGN the continuum shape is roughly flat in νF_ν through many orders of magnitude in frequency, from IR wavelengths up through hard X-rays. Normal galaxy spectra, in contrast, are dominated by a super-position of stellar blackbody spectra over a limited temperature range, and emit most of their light over a much narrower range of frequencies — although in some cases thermal re-radiation by dust produces a further significant peak in the far-infrared. AGN therefore usually outshine inactive galaxies by one to several orders of magnitude at

---

[2] Blazars are subclassified as **optically violent variables (OVVs)** if they have typical AGN spectra and **BL Lac objects** if their spectra are line-free.

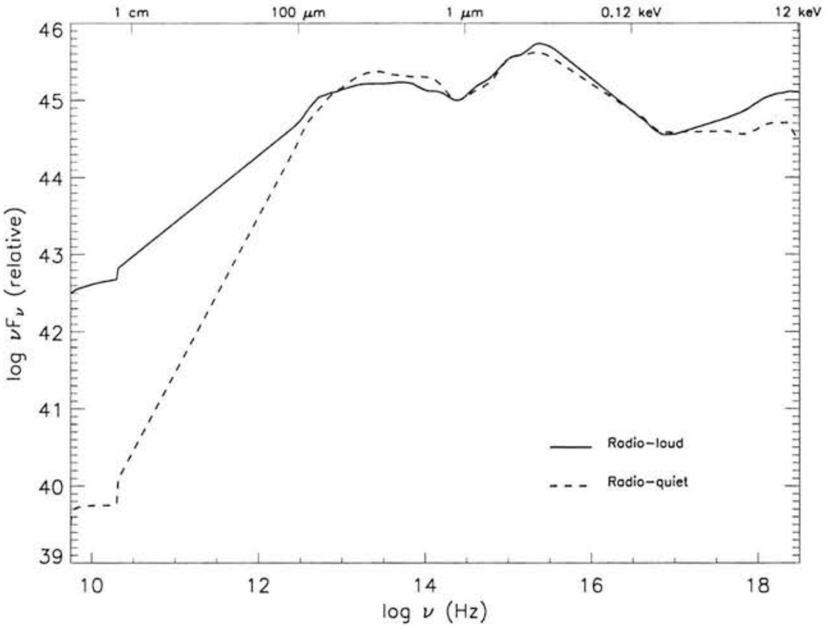

Figure 1.1: *Typical broad-band spectral energy distribution for radio-loud (solid line) and radio-quiet (dashed line) AGN. Data from Elvis et al. (1994).*

radio wavelengths and by as many as four orders of magnitude in X-rays.[3] A schematic diagram of a typical AGN spectral energy distribution is shown in Figure 1.1.

- **Emission lines**: With the exception of the nearly featureless BL Lac objects, prominent emission lines of high excitation transitions are a ubiquitous characteristic of AGN. Common lines in optical/UV spectra include the Lyman and Balmer series and ionised lines of He, C, O, Ne, Mg, Si, and Fe, among others. In the X-ray band, the 6.4 keV Fe line is often observed. Strong line emission, with equivalent widths of up to 100Å, can contribute a significant fraction of the flux in particular broad-band filters dependent on source redshift. In Type 1 spectra both broad and narrow line profiles are seen – with widths of $\simeq 10^4$ km s^{-1} and $\simeq 10^2$ km s^{-1}, respectively – while only narrow lines are present in Type 2 spectra. The broad line component is seen only in permitted transitions, and is consistent with a high density emitting region with electron density, $n_e \simeq 10^9$ cm^{-3}. The narrow component also includes semi-forbidden and forbidden transitions, consistent with lower density material of $n_e \simeq 10^3 - 10^6$ cm^{-3}.

- **Variability**: Multiwavelength variability of both continuum and line emission is observed at some level in most AGN. Non-periodic variability is present over a range of scales from hours to years, with higher amplitude variability observed on longer timescales. A high frequency cutoff in frequency,

---

[3] However, Type 2 Seyfert galaxies often have more narrowly peaked spectra in which the majority of light is emitted in the infrared.

which would limit the size of the emitting region, has yet to be observed. At X-ray wavelengths, significant variability is observed on scales of minutes.

1.1.3 Basic model of AGN

Black hole accretion

In the currently accepted paradigm, AGN are powered by gravitational accretion onto a supermassive black hole via a dissipative accretion disk. Powering AGN through less efficient processes — i.e. nuclear burning in stars — requires massive amounts of fuel and produces enormous amounts of 'ash' which are difficult to reconcile with observed AGN luminosities, lifetimes, and sizes. Gravitational infall of a relatively small amount of material to within a few times the Schwarzchild radius (R_S) of a massive black hole, however, efficiently converts up to a tenth of the rest mass of the accreting material into radiation emitted in a very small volume.

For isotropic accretion onto a black hole, balancing the inward force of gravity with the outward force of radiation pressure links the mass of the central object with the emitted luminosity. The maximum luminosity which can arise from spherically symmetric accretion onto a black hole of mass M is the **Eddington luminosity**:

$$L_E = 1.26 \times 10^{38} (M/M_\odot) \mathrm{erg\ s}^{-1}$$

Likewise, the minimum mass which can produce a given luminosity through isotropic accretion is the Eddington mass:

$$M_E = 8 \times 10^5\ L_{44}\ M_\odot$$

where L_{44} is luminosity measured in units of 10^{44} erg s^{-1} and M_E is in solar masses. For typical Seyfert and quasar luminosities, the Eddington mass is of order $10^6 - 10^8 M_\odot$. More direct measurements of the central mass by virial means typically yield values which are higher by $\sim$ a factor of ten. For a nominal rest mass energy conversion efficiency, $\eta \sim 0.1$, the mass infall rate, $\dot{M}$, necessary to fuel such an AGN radiating at its Eddington luminosity is of order of only a few solar masses per year. While there is clearly ample material in galaxies to fuel AGN at this rate, how orbiting galactic material is disrupted and sheds enough angular momentum to fall onto the black hole is still a major unsolved problem (Shlosman et al. 1989).

AGN emission processes

The broad characteristics of AGN are understood to result from the conversion of gravitational potential energy to thermal radiation in an optically-thick, geometrically-thin accretion disk, and from the subsequent reprocessing of this radiation by various types of circumnuclear material.

- The *UV/optical continuum* is characterised by broad emission from $\sim$ 4000Å through to at least 1000Å (the 'big blue bump'), which is generally attributed to thermal emission from the disk at a distance of order $10^2 R_S$ from the nuclear black hole.

- The *IR continuum* is dominated by a second broad bump rising from an inflection in the broad-band spectrum at $\sim 1\mu$m and falling rapidly in the submillimetre. This component is commonly modelled as thermal emission from hot ($< 2000K$) dust in the nuclear regions.
- The *hard X-ray continuum*, discussed in more detail in §1.1.4, can be modelled to first order by a powerlaw spectrum, $S_\nu \propto \nu^{-\alpha}$ with energy index, α, $\simeq 1$. While the origin of this emission is still subject to debate, many authors invoke inverse-Compton scattering of UV/optical continuum photons by hot electrons in a corona surrounding the disk (e.g., Haardt and Maraschi 1993).
- The slope of the *γ-ray continuum* emission is somewhat softer than that in the X-ray, with $\alpha \sim 1.2$ in the 50–150 keV range and a high energy cutoff at energies of a few hundred keV. This spectrum is successfully fit by saturated pair-production models (Blandford and Levinson 1995).
- The *broad emission lines* result from Doppler-broadened transitions within high-density ($\sim 10^9$ cm^{-3}), photoionised clouds at distances of order $10^3 R_S$ from the central engine, referred to as the Broad Line Region (BLR).
- *Narrow emission lines* are observed from clouds of lower-density ($10^3 - 10^6$ cm^{-3}) material at larger radii ($\sim 10^4 R_S$) — the Narrow Line Region (NLR).
- In radio-loud objects, the *radio emission* is attributed to synchrotron emission from an optically thick medium within the flat-spectrum core and from an optically-thin medium in the extended steep-spectrum lobes. The presence of this emission as well as the complex jet and lobe morphology may relate to rapid rotation of the black hole (Wilson and Colbert 1995).

Unified models

Unified models seek to describe the various classes of AGN discussed in §1.1.1 as intrinsically similar objects, with the observational variety due solely to effects of viewing orientation (e.g., Antonucci 1993, Lawrence 1991). In addition to the accretion disk, warm dust, hot corona, and broad and narrow line regions, models which unify Type 1 and Type 2 objects rely on the presence of thick obscuring material which shields the accretion disk and the nearby broad line region along some lines of sight. While the specific geometry of all of these components is a topic of current debate, it is common to describe this obscuring material as a molecular torus of dust and gas. In this scenario, Type 1 spectra result when the line of sight to the central engine and the broad line region is unobscured; strong non-stellar continuum emission from the accretion disk and both broad and narrow line regions are observed. When these central regions are viewed through the dusty torus, however, the continuum and broad line emission is obscured, resulting in a Type 2 spectrum containing only narrow lines and a weaker non-stellar continuum.

Strong evidence in favour of unification of this sort in Seyferts is obtained by the observation of broad lines and a strong non-stellar continuum in the polarised flux spectrum of several Type 2 Seyferts (e.g., NCG1068; Antonucci and Miller 1985). In these sources, a fraction ($\sim 1\%$) of the light from a hidden Type 1 nucleus is scattered from (and polarised by) 'mirrors' of ionised electrons or of dust which view the central engine free from obscuration. Whether anisotropic emission due to an obscuring torus is a

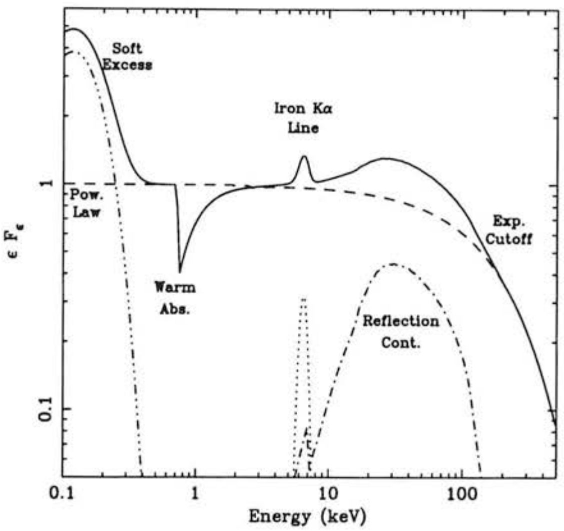

Figure 1.2: *Schematic diagram of the components of a Seyfert 1 X-ray spectrum. Figure from Fabian (1999b).*

ubiquitous feature of AGN is still an open question, however, as surveys for obscured sources, particularly at low luminosities and/or at high redshift, are complicated by the lack of easily observed AGN signatures in the observed-frame optical/UV (i.e., the strong non-stellar continuum and broad permitted-line transitions). The sensitive, high-resolution surveys in the hard X-ray made possible by Chandra and XMM are a powerful method of probing the obscured quasar population, as will be discussed below.

1.1.4 X-ray emission from AGN

This thesis is concerned primarily with detection of AGN at X-ray wavelengths. As noted above, to first order, X-ray spectra of AGN are well-described by a powerlaw model, $S_\nu \propto \nu^{-\alpha}$, where α is the energy index. While the canonical value of α from low-resolution, soft X-ray spectra was $\simeq 0.7$ (Mushotzky et al. 1980), higher-resolution studies have isolated several components in AGN spectra which are not well fit by a single powerlaw. Once these components are accounted for, a value of $\alpha = 0.9$ is more typical of the underlying powerlaw (Nandra and Pounds 1994).

Figure 1.2 illustrates several features which have been noted in the X-ray spectra of AGN. Flux is often seen at very low X-ray energies (< 0.5 keV) which is referred to as the 'soft excess' . This feature has been interpreted both as the high-energy, Compton up-scattered extension of the UV/optical bump (Gondhalekar et al. 1994) and as a blend of X-ray emission lines (Turner et al. 1991). At energies below 2 keV, K- and L-shell absorption edges of several elements have also been observed, which are attributed to a 'warm absorber' along the line of sight (e.g., Reichert et al. 1985). Line emission from the 6.4 keV Fe Kα transition is also detected in some AGN spectra. The line profile is often remarkably broad (of order 10^5 km s^{-1}) and in some cases provides evidence of gravitational redshift (e.g., Tanaka et al. 1995). A

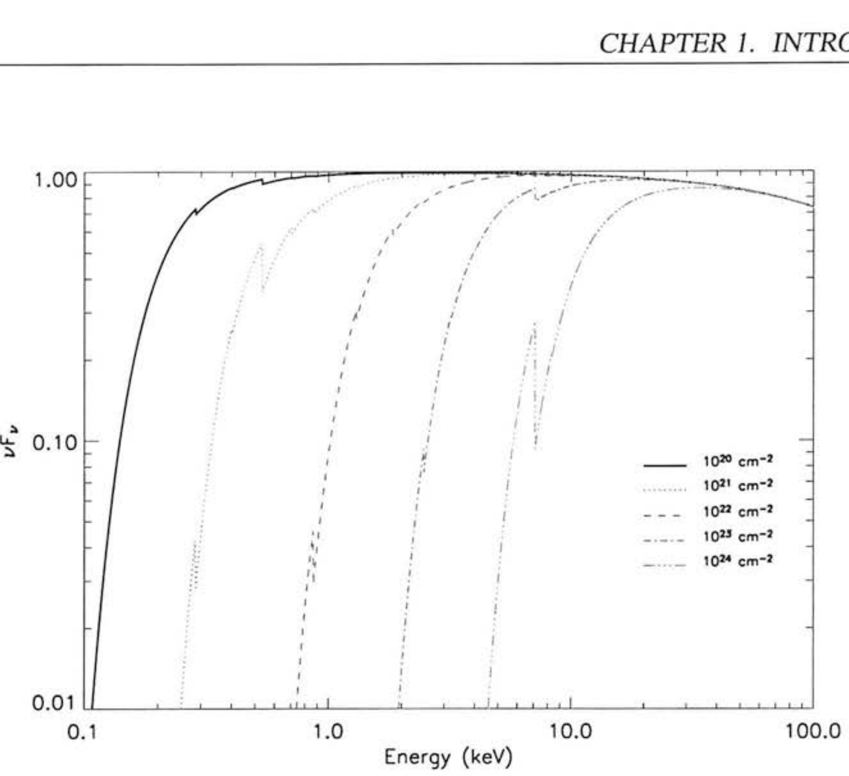

Figure 1.3: *Schematic diagram of the effect of photoelectric absorption for absorbing columns of various depths.*

broad peak observed at roughly 30 keV is consistent with Compton scattering of higher energy photons from a optically-thick gas, and is expected if the X-ray spectrum is reflected off the accretion disk itself (Lightman and White 1988). Finally, as noted above, an exponential cutoff limits emission in the γ-ray range to energies less than a few hundred keV.

Photoelectric absorption

A further significant mechanism which modifies the X-ray spectra of AGN is photoelectric absorption by intervening gas. As discussed above, unified AGN theories describe a circumnuclear molecular torus which blocks emission from the central engine and nearby broad line region along some lines of sight. While the primary effect of this material on optical and UV features is reddening due to dust, the gas in the obscuring torus — or anywhere along the line of sight to the central engine — will affect the X-ray spectrum, producing harder spectra for larger absorbing columns as soft photons are removed through photoelectric absorption.

In photoelectric, or bound-free, absorption, an electron absorbs a photon with energy, E_p, greater than or equal to its binding energy, E_b, and is freed with kinetic energy equal to the difference $E_b - E_p$. The cross-section for photoelectric absorption for a given element contains a series of absorption edges where $E_b = E_p$, and decreases with increasing energy approximately as E^{-3}. The X-ray absorption coefficient, σ_X, also has a strong dependance on atomic number ($\propto Z^5$), so that small amounts of heavy elements contribute significantly to obscuration. The summed cross-section for cosmic material with solar abundances also

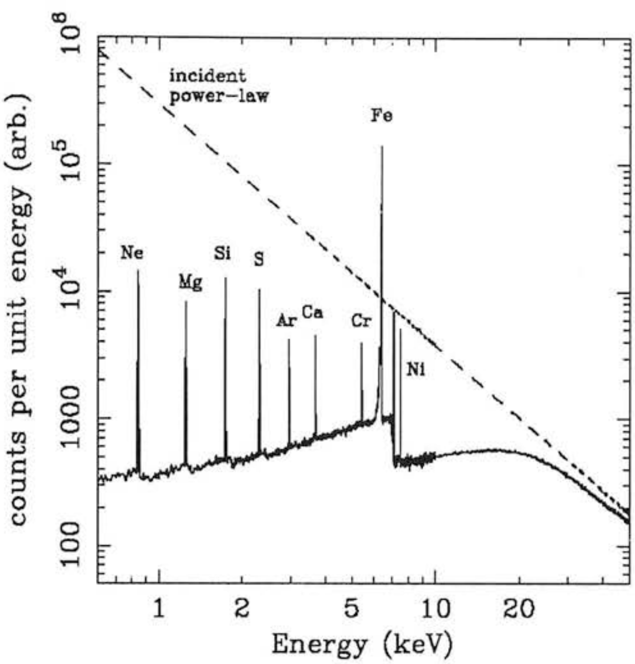

Figure 1.4: *Schematic diagram of the X-ray reflection spectrum observed in Compton-thick objects. Figure from Fabian et al. (2000).*

decreases roughly as $E^{-2.6}$.

The optical depth is given by the integral of the absorption coefficient times the column density along the line of sight: $\tau = \int \sigma_X N_H dl$, where N_H is the number density of hydrogen atoms. For incident powerlaw spectra, such as those of AGN, photoelectric absorption removes soft X-ray photons below a cutoff energy, E_a, which increases as ${N_H}^{\frac{1}{2.6}}$. This effect is illustrated in Figure 1.3, in which simulated powerlaw spectra with a range of absorbing columns are shown. Columns of $\sim 10^{23}$ cm^{-2} are sufficient to hide the majority of the intrinsic flux in the soft X-ray band below 2 keV. For sources at cosmological distances, an increase in redshift mimics a decrease in absorption, with apparent $N_H \propto (z+1)^{2.6}$.

Absorbing columns which are higher than $\simeq 1.5 \times 10^{24}$ cm^{-2} are Compton-thick; the absorption optical depth is greater than 1 for all energies less than ~ 10 keV. The X-ray spectrum is then dominated by the reflection component discussed above. The reflection spectrum depends critically on the particulars of the reflection geometry and of the ionisation state of the reflecting material, and is characterised by strong Fe Kα emission, as shown in Figure 1.4.

Figure 1.3 shows that even heavily obscured AGN will be luminous in the hard X-ray band ($2 - 10$ keV). Detection of Compton-thick sources, on the other hand, requires extremely sensitive observations, preferably allowing resolution of the strong Fe Kα feature. These are the primary reasons the current X-ray satellites — which provide sharp resolution (Chandra) and high throughput (XMM) in the hard band — were expected to detect populations of obscured AGN with unparalleled efficiency, allowing surveys of the AGN population which are far less biased by the effects of obscuration.

1.2 The cosmic X-ray background

Significant populations of obscured AGN are predicted both by unified models of AGN and by synthesis models of the cosmic X-ray background (XRB). The origin of the XRB was a major question in X-ray astrophysics from the advent of the field, when a 1962 experiment designed to measure solar X-rays reflected from the Moon also observed both the first extrasolar X-ray source (Sco X1) and a luminous, diffuse glow of background emission (Giacconi et al. 1962). Though this emission dominates the energy output of the X-ray sky, its cause would remain a hotly contested but largely unanswered question for nearly four decades.

1.2.1 Early surveys

Diffuse or discrete?

The first all sky X-ray surveys carried out in the early 1970s by UHURU and Ariel V showed the XRB to be highly isotropic and therefore extragalactic in nature (Warwick et al. 1980). Two competing theories emerged to explain the emission, one favouring a truly diffuse background of thermal bremsstrahlung from hot intergalactic gas (IGM), the other suggesting a superposition of discrete sources. Measurements taken of the spectrum of the XRB between 3 and 50 keV in the early 1980's by HEAO-1 seemed to favour the diffuse hypothesis. A remarkably good fit to the data was obtained with an isothermal bremsstrahlung model with kT $\sim$ 40 keV (Marshall et al. 1980), as predicted by models (Cowsik and Kobetich 1972). In addition, the spectra of known discrete X-ray emitting objects, like Seyfert galaxies, were found to differ substantially from that of the XRB.

Medium-deep surveys with Einstein conducted through the 1980s were able to resolve about $\sim 25\%$ of the soft (1 - 3 keV) XRB into discrete sources to a sensitivity of 2.6×10^{-14} erg s^{-1} cm^{-2} (Giacconi et al. 1979). While their spectra were not consistent with the observed XRB either, subtracting their contribution left a residual background which was difficult to fit with thermal emission. The hot IGM theory was finally laid to rest definitively by the non-detection of a Compton distortion on the microwave background measured by the Cosmic Background Explorer (COBE; Mather et al. 1990), leaving the source of the majority of the XRB, particularly at the high energies, still unknown.

The spectral mismatch

In the 1990s, ultradeep ROSAT surveys reaching flux limits of $\sim 1 \times 10^{-15}$ erg s^{-1} cm^{-2} resolved up to 70% of the soft background emission into discrete sources (Schmidt et al. 1998). Sources detected with ASCA in the 2.0 – 10.0 keV range to a limiting flux of 5×10^{-14} erg cm^{-2} s^{-1} contributed $\sim 30\%$ of the XRB at these harder energies (Georgantopoulos et al. 1997). Though source confusion was a problem due to large positional inaccuracies, optical identification and spectroscopic followup was possible for a large fraction of sources, which were shown to be predominantly unobscured AGN with a mean redshift of 1.5 (Shanks et al. 1991). The large samples also allowed characterisation of the luminosity function of AGN and its evolution with redshift (Boyle et al. 1993). Extrapolating these relations to faint fluxes and

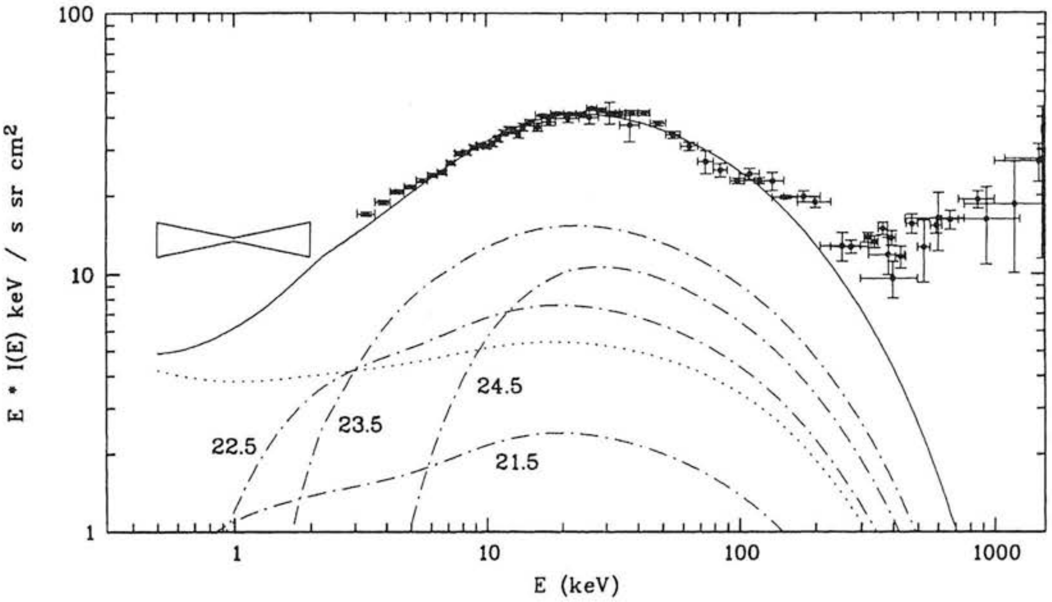

Figure 1.5: *The spectrum of the XRB (data points), with the best-fit synthesis model of Comastri et al. (1995). The dotted line indicates the contribution from unobscured AGN, while the dot-dashed lines show the contribution from various populations of obscured AGN, with* $\log N_H$ *noted. Figure from Comastri et al. (1995).*

integrating over redshift, AGN were predicted to contribute up to 90% of the soft XRB (Shanks et al. 1991, Boyle et al. 1993), and 48 - 80% of the hard XRB (Boyle et al. 1998).

The question of the origin of the majority of the X-ray flux in the Universe remained unanswered, however, as the AGN population resolved by ROSAT below 2 keV could not match the spectrum of the XRB at higher energies. At energies less than a few tens of keV, both the spectrum of a typical unobscured AGN and the XRB spectrum are reasonably approximated by powerlaws. Between 1 and 10 keV, unobscured AGN have indices of $\alpha \sim 1$; the spectrum of the X-ray background is much harder, with $\alpha_{XRB} \simeq 0.4$ (Gendreau et al. 1995). Thus while the AGN observed with ROSAT could account for the XRB at low energies, their summed contribution fell short of the observed XRB background at its 30 keV peak by nearly a factor of 10, as can be seen in Figure 1.5.

1.2.2 Synthesis models

Synthesis models developed through the 1990s to the current day account for the hard spectrum of the XRB emission with populations of variously obscured AGN distributed over a range of redshifts (e.g., Madau et al. 1994, Comastri et al. 1995, Gilli et al. 2001, Wilman et al. 2000, Ueda et al. 2003). While the models have become increasingly complex, they all share the same basic three-step prescription.

- First, X-ray and γ-ray observations of a large sample of AGN are used to define an empirical Type 1 spectrum from a few to few hundred keV. In general, this takes the form of an intrinsic powerlaw (or broken powerlaw) plus a Compton reflection component.

- Type 2 spectra are then modelled, as the unified scheme demands, as Type 1 spectra modified by photoelectric absorption by columns with densities ranging from $10^{21} - 10^{25}$ cm^{-2}. The distribution of absorbing columns is either assumed or, if possible, measured directly from the X-ray data.
- Parameterisations of the X-ray luminosity function (XLF) and its cosmological evolution are derived or adopted from earlier studies. These functions are integrated over ranges in luminosity and redshift to produce an ensemble population of AGN whose summed emission is the model XRB. Finally, the model is tuned to match observed distributions (e.g., sources counts, redshifts, etc.).

Several authors have obtained successful fits to the XRB in this manner. Assuming an XLF derived from the soft-band ROSAT source counts which evolves purely in luminosity (Boyle et al. 1993), Comastri et al. (1995) produced a model which was consistent with all contemporary observational constraints and reproduced the observed background emission to within 6% from 6 to 100 keV [4]. This model confirmed that the XRB flux could be produced almost entirely by populations of AGN, and predicted the majority of the accretion power in the Universe took place in obscured objects with $N_H > 10^{22}$ cm^{-2}. Both the assumed XLF evolution and inferred demographics of the obscured population are subject to substantial uncertainties, however, leaving considerable latitude in the details of the best-fit models.

Miyaji et al. (2000) considered the effects of both luminosity dependent density evolution — in which evolution is slower for low luminosity objects — and of an anti-correlation of luminosity and absorption, as suggested by Lawrence (1991). They note that a model in which the fraction of obscured objects at a given luminosity evolves cosmologically might be needed to fully match observations. Gilli et al. (2001) allowed for differential evolution between obscured and unobscured AGN, and found the observations were best fit by a model in which the Type 2 / Type 1 fraction increases by a factor of ~ 2 from $z = 0$ to $z = 1.3$. Comastri et al. (2001) compared model predictions with 5 - 10 keV source counts and hardness ratios from BeppoSAX, again requiring a large fraction of highly obscured, luminous AGN. However, Wilman et al. (2000) included Compton down-scattering in their models, and found they could not accommodate as high a fraction of obscured objects at high redshift unless supersolar metal abundances are present in the obscuring material.

1.2.3 The obscured AGN population

Confirmation or further constraint of XRB synthesis models prior to the launch of Chandra and XMM was impossible; the obscured AGN predicted by the models were invisible at soft X-ray wavelengths and could not be resolved at higher energies by contemporary instruments. There were, however, indications of an obscured AGN population emerging at faint fluxes in ROSAT and ASCA data. At the limits of deep ROSAT surveys a population of Narrow-Line X-ray Galaxies (NLXG), exhibiting narrow optical lines but relatively

---

[4] At softer energies, there is significant contribution to the XRB flux from non-AGN sources which are not included in synthesis models. (see §1.2.4)

high X-ray luminosity, comprised $\sim$ 10% of source counts (Boyle et al. 1995, Griffiths et al. 2000). NLXGs seemed even more common in the harder ASCA band and in later observations with SAX, but neither of these missions had the positional accuracy necessary to conclusively identify the objects through correlation with observations in other wavebands. Optical spectroscopy revealed AGN signatures in a majority of these objects (Hasinger et al. 1998), and the stacked X-ray spectra of sources with 'galaxy-like' optical counterparts indicated significant absorption (Almaini et al. 1996). Finally, strong signal detected in cross-correlation analyses of $B < 23$ mag galaxies with unidentified faint ROSAT sources and with fluctuations in the remaining unresolved XRB suggested the contribution of galaxy populations to the cosmic X-ray flux might be substantial (Roche et al. 1995, Almaini et al. 1997).

A watershed in XRB studies has taken place over the last five years as deep surveys with Chandra and XMM have resolved the objects comprising the hard XRB for the first time. My work on one of these surveys, the ELAIS Deep X-ray Survey (EDXS) is presented in Chapter 3 of this thesis. Early 'blank field' surveys including the EDXS, the Hawaii Deep Survey of SSA13 (Mushotsky et al. 2000), the XMM survey of the Lockman Hole (Hasinger et al. 2001, Mainieri et al. 2002), the Chandra Deep Field South (CDFS; Rosati et al. 2002), the Chandra Deep Field North (Brandt et al. 2001a, Alexander et al. 2003), and the 13Hr XMM/ROSAT Deep Survey (McHardy et al. 2003) have resolved virtually all of the cosmic background emission in the 0.5-2 and 2-10 keV bands. (For a thorough review of these early surveys, see Brandt 2004.) The composite spectrum of the sources comprising the X-ray background is found to have an energy index of $\alpha = 0.38$, in good agreement with α_{XRB} (Mushotsky et al. 2000). Extrapolating the slope of the source counts in the soft band accounts for the entirety of the XRB at those energies, while the extrapolated hard band counts comprise only $\sim 93\%$ of the 2–10 keV XRB, suggesting there is a faint population still to be resolved at fainter fluxes (Moretti et al. 2003). Rosati et al. (2002) also present the lack of flattening of the source counts in the 5–10 keV band to a flux of 10^{-15} erg s^{-1} cm^{-2} as an indication of an unresolved population which is faint and very hard. Whether the objects seen below 10 keV are responsible for the peak of the background emission at harder energies is still an open question, and the fraction of the total XRB which is resolved is still highly model dependent.

It is now known that the hard X-ray sources comprising the majority of the background flux are indeed obscured AGN, as predicted by synthesis models. The newly-resolved sources are optically identified as quasars ($\sim 20\%$), bright galaxies ($\sim 40\%$), and optically faint objects ($\sim 40\%$), with the quasars dominating the number counts at bright fluxes and the galaxies and optically-faint sources predominating toward fainter fluxes. The populations with galaxy-like and optically-faint morphologies have hard X-ray luminosities consistent with AGN accretion. They also have extended optical morphologies, more varied optical-to-X-ray flux ratios, and redder optical colours than the quasars, as would be expected if the host galaxy light dominates at optical wavelengths. There is also substantial X-ray absorption in these populations, as is evident from their harder X-ray spectra. For example, about 40% of sources in the XMM survey of the Lockman Hole have hard spectra, which X-ray colour-colour diagrams suggest are due to obscuration at soft energies rather than variation of the underlying powerlaw photon index (Mainieri et al. 2002). The constituents of the XRB and the characterisation of the obscured AGN population are discussed more fully in Chapter 3.

Over the past few years, knowledge of the demographics of the obscured AGN populations has been increasing along with the level of spectroscopic completeness of the Chandra and XMM surveys. Accordingly, recent synthesis models (Ueda et al. 2003) include two major revisions: (i) the distribution of obscuring columns is now measured empirically, and is found to be luminosity dependent such that more luminous objects are less likely to be heavily obscured; and (ii) the evolution of the hard XLF, which has been computed correcting for the effects of obscuration, shows a dramatic dependence on luminosity, such that the peak in AGN activity for quasars took place much earlier ($z \sim 2$) than the peak of activity for lower-luminosity AGN ($z \sim 0.5$). Finally, while the prevalence of luminous Type 2 quasars is still not definitively known, there are several spectroscopically confirmed hard-X-ray-selected examples (Stern et al. 2002, Norman et al. 2002, Della Ceca et al. 2003, Gandhi et al. 2004).

1.2.4 Non-AGN contributors

While the majority of the XRB originates in active galaxies, a small fraction of the emission may arise from other sources. Quantifying or constraining the flux from these non-AGN contributors is a further goal of current XRB studies.

Diffuse gas

Cosmological hydrodynamical simulations predict filamentary structures of diffuse gas between clusters of galaxies, known as the warm/hot intergalactic medium (WHIM), which is shock heated to temperatures of 10^5 - 10^7 K. Phillips et al. (2001) simulate the expected contribution of bremsstrahlung and line emission from this material and find that it could contribute $\sim 5\%$ of the extragalactic background in the soft X-ray band (0.5 - 2.0 keV), consistent with the currently unresolved component. Deeper X-ray surveys will provide stronger constraint of the diffuse contribution, which is of considerable cosmological interest. While measurements of baryon density at high redshift are in good agreement with predictions from big bang nucleosynthesis models, baryon density at low redshift is a factor of 2-4 too low. The WHIM could contain up to 40% of local baryons. The first conclusive WHIM detection was made by Fang et al. (2002), who perform X-ray spectroscopy of diffuse material within a poor group of galaxies with Chandra's dispersive gratings and find O VIII Lyα absorption accounting for $\sim$ 10% of the 'missing' baryons, and 30-40% of the expected WHIM.

Clusters

Gas in clusters of galaxies with temperatures of $10^6 - 10^8$ K emits soft X-rays via thermal processes which contribute to the extragalactic background. The percentage of the XRB attributable to clusters is constrained by the luminosity function for clusters and its evolution with redshift, which are well known, and cannot be greater than $\simeq 10\%$ in the soft band and a few percent at higher energies (e.g., McHardy et al. 1998).

Stellar processes

The deepest Chandra surveys are beginning to probe the contribution from star-forming galaxies. About 2% of the soft XRB flux originates in sources with $S \leq 10^{-15}$ erg s^{-1} cm^{-2} and $-2 \leq \log \frac{f_X}{f_I}, \leq -1$ which are identified with rapidly star-forming, dust-enshrouded, emission line galaxies at $z \simeq 1$ and are luminous in the infrared (Alexander et al. 2002, Bauer et al. 2002). The emission in these objects reflects the summed contribution of massive X-ray binaries and supernovae, and may also include contributions from Compton scattering of infrared photons, synchrotron-dominated pluerions, and starburst-driven superwinds (Natarajan and Almaini 2000). At fluxes of order 10^{-16}–10^{-17} erg s^{-1} cm^{-2}, large numbers of 'normal' galaxies appear which may contribute as much as 5–10% of the soft XRB. At the bright end of this range are objects with luminosities of $L_{0.5-8\,\mathrm{keV}} \leq 10^{41}$ erg s^{-1} cm^{-2} and $\log \frac{f_X}{f_I} \leq -2$ in which the X-ray emission likely arises in low luminosity AGN, Ultra-luminous X-ray Sources (ULXs; Matsumoto et al. 2001), and vigourous star formation Hornschemeier et al. (2003a). At lower z and faint fluxes, this population overlaps with the typical inactive galaxies which exhibit $\log \frac{f_{0.5-2\,\mathrm{keV}}}{f_I} \leq -3$ and are expected to dominate the source counts at fluxes of a few times 10^{-18} erg s^{-1} cm^{-2}(Hornschemeier et al. 2003b).

1.3 The coevolution of AGN and their hosts

One important application of the multiwavelength survey data which has resolved and characterised the XRB is in probing the role of AGN in the evolution of their host galaxies. Over the past five years it has become clear that (i) virtually all galaxies contain a massive nuclear black hole and (ii) the mass of this central object is tightly correlated with the mass of the galaxy's spheroidal component. These results strongly suggest that accretion onto a central black hole in luminous AGN is not a rare phenomenon found within exceptional galaxies, but rather a key process which is intimately linked to the growth of every galaxy.

1.3.1 Evidence for coevolution

The ubiquity of nuclear black holes

While the observed characteristic properties of AGN described in §1.1.2 quickly led to speculation they were powered by black hole accretion (e.g., Salpeter 1964), it was not until several decades later that conclusive observational proof of the existence of supermassive nuclear black holes was obtained.

The first and most direct way to detect nuclear black holes is with high-quality dynamical measurements of the nuclear regions of nearby galaxies, which can resolve motions of stars and gas within the sphere of influence of the black hole.[5] Sharp radial increases in rotational velocity consistent with Keplerian motion around dark objects of $> 10^6 M\odot$ have now been observed in several dozen galaxies (see Merritt and Ferrarese 2001b and references therein), and are notably evident in stellar motions in our own Galactic

---

[5] $r_h = GM_\bullet/\sigma^2$, where σ is the velocity dispersion of the galaxy bulge (Merritt and Ferrarese 2001b).

Centre (Genzel et al. 2000) and in the velocities of circumnuclear water masers in the Seyfert 2 galaxy NGC 4258 (Miyoshi et al. 1995).

A second method to measure black hole masses in active galaxies, in which emission in the central regions is dominated by the AGN, is the reverberation mapping technique. This technique relies on dynamical modelling of the broad line region, where the velocity of the BLR clouds is inferred from the widths of the lines and the distance from the black hole is given by the time delay between continuum and spectral variability. Black hole masses for several dozen Seyfert 1 galaxies and quasars have been obtained in this way (Wandel et al. 1999, Kaspi et al. 2000, Peterson et al. 2004).

In conjunction, these survey techniques have shown that nearly every local galaxy harbours a supermassive black hole. Moreover, there is evidence that the black holes observed locally were formed in periods of luminous AGN accretion. Estimates of accretion energy integrated over cosmic time can be obtained either from the optical luminosity function of AGN or from the X-ray background and combined with an assumed radiative efficiency ($\eta \sim 10\%$) to derive the total mass density expected within black holes. This value, $\rho_\bullet$, is estimated at $\sim 2 \times 10^5 M_\odot$ Mpc^{-3} from the optical LF (Chokshi and Turner 1992) and $\sim 3 \times 10^5 M_\odot$ Mpc^{-3} from the XRB (Fabian and Iwasawa 1999). The value measured locally, though stellar- or gas-dynamics or reverberation mapping techniques is $\rho_\bullet \sim 5 \times 10^5 M_\odot$ Mpc^{-3} (Merritt and Ferrarese 2001a). This consistency is strong evidence that every galaxy must go through a luminous AGN phase.

The $\sigma - M_\bullet$ relation

As black hole mass measurements were accumulated, surprisingly strong correlations were found between the mass of the central object and indicators of the mass of the bulge component of the host galaxy (e.g., Magorrian et al. 1998, Ferrarese and Merritt 2000, Gebhardt et al. 2000). The tightest of these relationships — between the black hole mass, $M_\bullet$, and the velocity dispersion of the host galaxy bulge, σ, — is illustrated in Figure 1.6, and holds over four orders of magnitude in black hole mass. The ratio of black hole to galaxy spheroid mass implied by this relation is roughly 10^{-3}, and is largely consistent between active and quiescent galaxies ($\langle M_\bullet / M_{bulge} \rangle = 0.09\%$ for quasars, 0.12% for Seyferts, and 0.13% for inactive galaxies; Merritt and Ferrarese 2001b).

1.3.2 Coevolution theories

The remarkably tight $\sigma - M_\bullet$ relationship strongly suggests a fundamental link between the evolution of nuclear black holes and their host galaxies, and introduces a theoretical challenge: how can accretion onto a nuclear black hole on scales of $\ll 0.1$ pc be linked to the development of galactic bulges on kiloparsec scales? As noted by Merritt and Ferrarese (2001b), even given some intrinsic link between galactic bulges and nuclear black holes in the early universe, it is challenging to imagine scenarios by which this relation could remain so exact throughout the galaxy mergers which are a fundamental component of hierarchical cosmologies. Over the past five years, interest in this problem has spawned a great many models of the coevolution of AGN and their host galaxies. While a full review of these theories is outside the scope of this introduction, I will review in very basic terms two popular genres of model which successfully

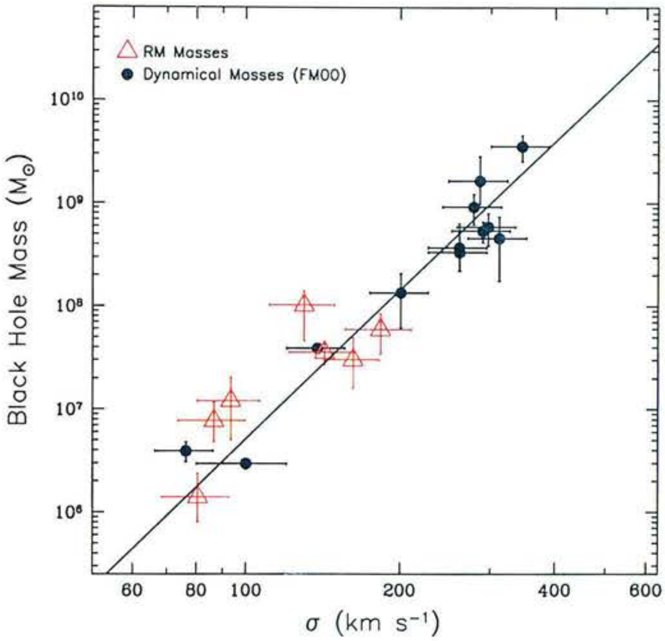

Figure 1.6: *Black hole mass versus velocity dispersion for samples of active and quiescent galaxies. The circles indicate quiescent galaxies in which $M_\bullet$ has been measured from dynamics of stars and gas in the nuclear region (Ferrarese and Merritt 2000), while the triangles indicate AGN in which $M_\bullet$ is estimated with reverberation-mapping techniques. Figure from Merritt and Ferrarese (2001b).*

reproduce the $\sigma - M_\bullet$ relation.

'Hidden quasar' models

The first of these predates the discovery of the $\sigma - M_\bullet$ relation, and was first suggested by Silk and Rees (1998) and subsequently developed by many authors (e.g., Fabian 1999a, King 2003, Granato et al. 2004). In these models, the collapse of a supermassive black hole with $M_\bullet \sim 10^6 M_\odot$ precedes the initiation of stellar processes in the galactic bulge. During the period in which the stellar mass of the bulge is built up, the nuclear black hole is 'hidden' within the dusty environment of rapid star formation. It accretes material, however, and radiates as an AGN, driving an outflow which is proportional to its accretion rate and thus proportional to its mass. When the velocity of this outflow exceeds the escape velocity of the bulge, it ejects the interstellar material which is the fuel for both AGN accretion and star formation. The tight $\sigma - M_\bullet$ relation is thus a result of AGN feedback simultaneously ending the period of active accretion and terminating star formation in the bulge.

One can illustrate the potential significance of AGN feedback with a classic energetic argument: assuming an accretion efficiency $\eta \sim 0.1$ and adopting $\langle M_\bullet / M_{bulge} \rangle = 10^{-3}$, the energy generated by an AGN during its luminous phase is $\sim 10^{-4} M_{bulge} c^2$; assuming a typical bulge velocity dispersion of 300 km s^{-1}, the binding energy of the bulge is $10^{-6} M_{bulge} c^2$, or just 1% of the energy generated by the AGN.

While there is observational evidence of strong outflows from AGN — notably in radio-loud objects, in BAL quasars, and in the observed effect of AGN on the intracluster medium of nearby galaxy clusters (see §1.4) — the fraction of the accretion energy typically channelled into outflows rather than radiated is not known. This issue is currently of wide-spread interest, as AGN feedback may provide a mechanism to limit cooling at the cores of galaxies and galaxy clusters and to halt star formation within the most massive objects at high-redshift. Such a mechanism is needed to reconcile several observational failings of semi-analytic galaxy formation models which have grown out of the otherwise well-supported Λ-CDM hierarchical cosmology (e.g., Almaini 2004 and references within).

'Growing quasar' models

In the second variety of AGN-host galaxy coevolution model, the link between black hole and bulge mass results results not from a feedback mechanism, but simply from the reliance of both black hole accretion and star formation upon the same reservoir of fuel. In one such model proposed by Archibald et al. (2002) for the coevolution of massive ellipticals, small black holes of $10 - 1000 M_\odot$ form by gravitational collapse at the same time a rapid burst of star formation occurs in the galaxy bulge. While the stellar mass is built up quickly, black hole growth occurs gradually, curbed first by the Eddington limit and then because gas dynamics and star formation within the bulge restrict the amount of fuel which reaches the central region of the galaxy. In combination, these effects produce the observed proportionality between the black hole and bulge masses within the galaxy. Other models of simultaneous galaxy and black hole growth through mergers also rely on stellar processes to exhaust the gas supply or to keep it from cooling to the galactic centre (Burkert and Silk 2001, Kauffmann and Haehnelt 2000).

These two types of models lead to different predictions about the prevalence and characteristics of AGN within high-redshift populations. The first describes a black hole capable of powering a luminous AGN which is obscured within a dust-enshrouded star-forming galaxy. When the AGN is able to blow out the obscuring dust and gas, it simultaneously halts rapid star formation and shines through as an unobscured quasar, leading to an observed delay between the peak of star-formation and AGN activity. A similar delay is expected from the second model, but in this case because the nuclear black hole is too small throughout the majority of the star-forming period to power a luminous quasar. Star-forming galaxies in this model should contain only moderately luminous AGN, which may not be heavily obscured by the time they are visible.

1.3.3 High redshift populations

By a happy coincidence, the ability to probe the obscured AGN population with current X-ray instruments is complemented by the relatively recent development of several techniques to identify high-redshift galaxies. One important use of deep X-ray observations, therefore, is to directly observe black hole accretion within forming and evolving galaxy populations, and thus constrain coevolution models. Characterising the X-ray properties of high-redshift populations is a major goal of the surveys I present in Chapter 5 of this thesis. Here I conclude this section with a summary of these populations.

Submillimetre galaxies

The bulk of the far-infrared and submillimetre background emission arises from a population of extremely luminous star-forming galaxies first resolved with early surveys (e.g., Smail et al. 1997, Barger et al. 1998, Hughes et al. 1998) made with the Submillimetre Common User Bolometer Array (SCUBA) camera on the James Clerk Maxwell Telescope (Holland et al. 1999). The emission in these sources is a signature of star formation, resulting from the absorption by dust of optical/UV flux from hot, young stars and subsequent thermal re-radiation at infrared and submillimetre wavelengths. The discovery of the SCUBA population was widely interpreted as the first probe of the epoch of formation of massive elliptical galaxies at high redshift (e.g., Dunlop 2001). However, it proved extremely difficult to conclusively identify the sources in other wavebands, and thus to confirm their redshifts. This is due to two effects: (i) the positional accuracy of the submillimetre detections is limited by the low SCUBA resolution ($\sim 10 - 15''$) and (ii) the sources are extremely faint at optical/UV wavelengths due to dust obscuration, leading to a high surface density of possible counterparts within these large error circles.

Counterparts can be found for the majority of SCUBA sources in the radio, however, because young, massive stellar populations produce supernovae and associated synchrotron emission. Exploiting the positional accuracy possible in the radio band, Chapman et al. (2003a) obtained spectroscopic identifications of a sample of submillimetre sources with 1.4 GHz counterparts. These observations confirm that all but a few percent of the SCUBA-detected galaxies have redshifts $2 < z < 4$; the median redshift is $z = 2.4$. The submillimetre fluxes then correspond to luminosities consistent with star-formation rates of $\sim 1000 M_{\odot}$ yr^{-1}. Locally, similarly prodigious star formation is seen within Ultra-Luminous Infrared Galaxies (ULIRGs; e.g., Genzel et al. 2000). However, the submillimetre galaxies at $z = 2.4$ have roughly 1000 times the sky density of the relatively rare ULIRGs, and dominate the Universal star-formation activity at that epoch. HST imaging of SCUBA counterparts has revealed a high fraction of merging systems, and supports the interpretation of these sources as proto-ellipticals (Chapman et al. 2003b).

EROs

Another population considered likely progenitors of massive ellipticals is that of 'extremely red objects' (EROs), which have colours ($R - K > 5$ or $I - K > 4$) and properties suggestive of old and/or dusty galaxies at $z \simeq 1 - 2$ (e.g., Roche et al. 2003). Spectroscopic studies identify signatures of two types of $z > 1$ galaxy within the ERO population: (i) old, passively evolving ellipticals and (ii) star-forming or post-starburst galaxies which are heavily reddened by dust. The ERO population as a whole is very highly clustered — with a clustering strength that exceeds that of local ellipticals — suggesting EROs, too, are massive systems (Daddi et al. 2000, McCarthy et al. 2001). One evolutionary scenario posits that the older populations of EROs are the evolutionary descendants of the submillimetre population described above, which evolve passively once the major period of star formation has ended and the central AGN has stripped

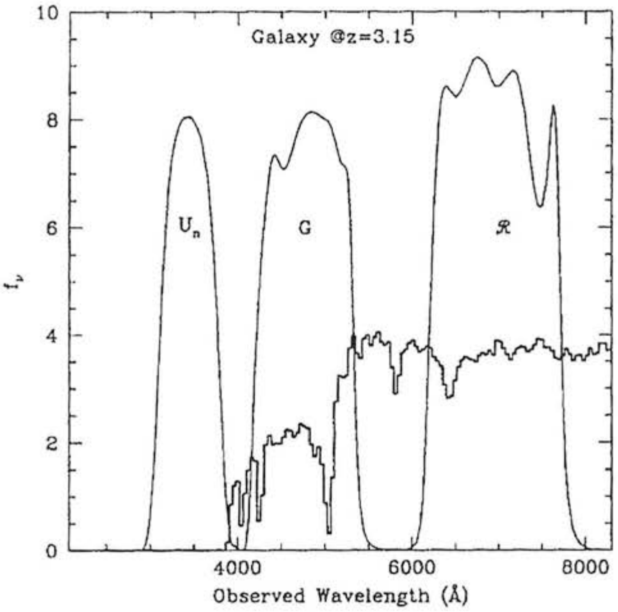

Figure 1.7: *Illustration of the Lyman break selection technique. The histogram is the UV spectral energy distribution of a $z = 3.15$ star-forming galaxy, with intensity given in an arbitrary scale. The curves show the transmittance of broad-band filters used to isolate the 912Å continuum break: the U_n filter in the absorbed region blue-ward of the break, and the G and R filters sampling the continuum red-ward of the break. Figure from Giavalisco (1998).*

the gas and dust from the system. There is also some evidence that the old passively evolving EROs are more highly clustered that the dusty starburst EROs, as would be expected were they massive galaxies which formed first in high density environments (Daddi et al. 2002). ERO number counts are too low to fit models in which the local elliptical population evolve passively, but can be matched by models that include both passive evolution and galaxy merging (Roche et al. 2002, 2003).

Lyman break galaxies

Somewhat lower-mass star-forming galaxies at high redshift have been effectively selected on the basis of the sharp continuum discontinuity at 912Å which is a common feature of galaxy spectra resulting from photoionisation of hydrogen within the galaxy. The 'Lyman break' technique, illustrated in Figure 1.7, consists of comparing deep integrations taken through broad-band filters selected to straddle this feature, and has been most widely applied to select objects with $z \sim 3$, in which the break and other identifying spectral features are conveniently located in the optical band. Large samples of Lyman Break Galaxies (LBGs) have been obtained in this way (e.g., Steidel et al. 2003) and have been used in conjunction with measurements of Lyα-forest flux decrements to trace the large scale distributions of matter at $z \sim 3$ (Adelberger et al. 2003). Follow-up spectroscopy of these samples in their rest-frame UV yields spectra which are very similar to local starbursts (Giavalisco and Dickinson 2001), and near-IR spectroscopy of the rest-frame optical can usefully constrain star-formation histories and dust content (Shapley et al. 2001). Fitting to stellar-population synthesis models indicates that more luminous LBGs are younger, dustier, and have higher star formation rates (Shapley et al. 2001). There is also evidence of large-scale outflows of gas — likely winds driven by stellar processes — which drive away nearby intergalactic gas (Adelberger et al. 2003). These results suggest an evolutionary sequence in which LBGs undergo a short (50-100 Myr) period of rapid (of order $10^2 M_\odot$ yr^{-1}) star-formation followed by a longer ($>$ 200 Myr) period of more moderate (of order $10 M_\odot$ yr^{-1}) activity (Shapley et al. 2001). The implied stellar masses of LBGs are $\sim 10^{10-11} M_\odot$ (Shapley et al. 2001, Giavalisco and Dickinson 2001). High-resolution HST images reveal that brighter LBGs have compact morphologies typical of collapsed systems, while the fainter sources show more irregular and fragmented morphology (Giavalisco and Dickinson 2001). The clustering properties of the Lyman break population are consistent with residence in large dark matter haloes ($M \lesssim 10^{12} M_\odot$) which are a very biased tracer of mass. Overdensities of LBGs implying assemblies of mass consistent with present day massive galaxy clusters ($M \sim 10^{15} M_\odot$) have also been observed (Steidel et al. 1998; see Chapter 5).

Lyα emitters

Another survey technique by which star-forming galaxies at high redshift are identified relies on detection of strong 1216Å Lyα line emission through tuned narrow-band imaging. Because Lyα is a resonance line and very easily absorbed, copious Lyα emission is expected only from young stellar populations in the absence of dust. Selection by high equivalent width Lyα emission was therefore proposed to isolate galaxies at the very earliest stages of star-formation (Charlot and Fall 1993). While there have been several successful searches for Lyα emitters around known high-redshift objects (Hu and McMahon 1996, Moller and Warren 1998, Venemans et al. 2003), the technique proved less useful for 'blank field' surveys, as the strength of the Lyα line, and even whether it is seen in emission or absorption, varies among galaxies. However, Lyα surveys can probe much fainter populations than those relying on detection of the Lyman break, as they do not depend on high signal to noise detection of continuum flux. In deep narrow-band imaging of a field previously surveyed with the Lyman-break technique, Steidel et al. (2000) find that roughly 80% of the Lyα candidates are too faint to have been detected based on a continuum break and estimate that only 20%–25% of Lyman break sources show significant Lyα emission, regardless of galaxy magnitude.

1.4 The large-scale environment of AGN

Star-forming activity within galaxies is known to depend critically on upon the density of the local environment. Determining the effect of environment on AGN activity may therefore be a fruitful way to investigate the related evolution of AGN and their host galaxies. Studying the AGN content of dense galaxy cluster and protocluster environments is another important application of modern X-ray survey data, which for the first time has resolution sufficient to resolve faint point sources from the luminous, diffuse emission from intracluster gas. This thesis presents two such surveys, one of a massive, X-ray-bright cluster at $z = 0.83$ (Chapter 4) and one of a complex protocluster region at $z \sim 3$ (Chapter 5). Here I give a brief description of galaxy clusters, discuss the known effect of environment on star-forming activity, and introduce the study of AGN within dense environments.

1.4.1 Galaxy clusters

Clusters of galaxies are the largest gravitationally bound structures in the Universe, containing tens to thousands of galaxies and a hot intracluster medium (ICM) within a common potential well. Classification of cluster 'richness', following the scheme of Abell (1958), is based on the number of cluster galaxies found within $1.5h^{-1}$ Mpc of the cluster centre which have magnitudes within two magnitudes of the third brightest cluster galaxy. All rich 'Abell clusters' contain > 30 galaxies in this core region, with Abell class 0 containing < 50 and Abell class 5 containing > 300. Poorer clusters are referred to with Abell class < 0, and smaller gravitationally bound systems of 3 to $\sim 10^2$ galaxies without a common ICM are called galaxy groups.

The space density of rich Abell clusters is $\sim 10^{-5}$ Mpc^{-3}, roughly three orders of magnitude lower than that of bright galaxies (Bahcall 1999). These systems are largely viralised, with typical galaxy velocity dispersions, $\sigma \sim 750$ km s^{-1}, implying dynamical masses of order $10^{14} - 10^{15}h^{-1}M_\odot$ (Bahcall 1999). In the context of hierarchical structure formation, massive clusters evolved from rare peaks in the primordial density fluctuations and thus are home to the oldest and most massive galaxies in the Universe. Overall, 55% of galaxies reside within poorer clusters and groups, while only 5% are found within rich clusters. Cluster members can be found up to several Mpc from the cluster centre, but the majority are found in a core region — ranging in size from ~ 0.1 Mpc in small groups to ~ 2 Mpc for the most massive clusters — outside of which the galaxy overdensity drops to $\sim 1\%$ of its peak value (Bahcall 1999). Substructure is seen in some clusters which are not yet fully dynamically relaxed or are merging with another group or cluster.

The intracluster gas, which comprises the majority of the baryonic mass of the cluster, is in approximate hydrostatic equilibrium within the potential well and is heavily concentrated in the central few kpc. The gas is heated through adiabatic collapse and shock heating to temperatures of T$\sim 10^7 - 10^8$ K (kT$\sim 2-14$ keV) and produces luminous, diffuse X-ray emission via thermal bremsstrahlung. In poorer clusters with lower virial temperatures, line transitions also contribute significantly to the X-ray flux. Clusters emit mainly in the soft X-ray band, with typical luminosities of $\sim 10^{44}$ erg s^{-1}. Spectral fits to thermal bremsstrahlung models imply electron densities of $n_e \sim 10^{-3}$ cm^{-3} and metallicities of ~ 0.3 solar. The large observed gas masses ($\sim 10^{13} - 10^{14}h^{-2.5}M_\odot$) require that much of the gas is of cosmological origin. ICM metallicity, however, is seen to correlate closely with the luminosity of cluster members with early-type morphology, indicating significant enrichment from gas stripped or ejected from these galaxies (David et al. 1991).

Cluster surveys

Clusters are currently identified either through optical/IR searches for galaxy overdensities or through X-ray detection of the intracluster gas. X-ray observations are of prime importance because they allow both efficient identification of clusters over well-defined survey areas and direct measurement of the properties of the ICM. While the most distant X-ray-luminous clusters identified with Einstein and ROSAT are at $z \simeq 0.8$ (e.g., Gioia et al. 1990, Rosati et al. 1998), Chandra and XMM observations of cluster candidates selected at the limit of ROSAT's sensitivity have confirmed clusters up to $z \simeq 1.3$ (Rosati et al. 2004, Hashimoto et al. 2002). Both large-area and serendipitous surveys currently underway with Chandra and XMM will begin to systematically explore the population of clusters at $z > 1$ (Romer et al. 2001, Pierre 2003, Green et al. 2004). The X-ray identification of similarly dense regions at higher redshifts is a significant observational challenge, as virialised clusters with a luminous ICM will be both much rarer at high redshift and much fainter due to the $\frac{1}{1+z^4}$ dependence of surface brightness.

Planned surveys of the Sunyaev-Zel'dovich (S-Z) signature on the cosmic background microwave (CMB) radiation should aid in identification of intracluster gas at higher redshifts. The S-Z effect, arising from the inverse-Compton scattering of microwave photons from hot electrons in the ICM, is observed as a decrement in background flux at frequencies below the peak of the CMB and an increment at higher frequencies. The magnitude of the signal depends upon properties intrinsic to the cluster (i.e. electron density, temperature, and size) but is only weakly dependent on distance due to the increased CMB flux toward higher redshift. S-Z surveys will therefore be nearly equally efficient at any redshift > 0.5 (Birkinshaw 2004). Instruments capable of sensitive S-Z observations on arcminute scales over large fields of view are currently being developed (Runyan et al. 2003, Kneissl et al. 2001).

There has recently been considerable progress in identifying dense protocluster environments without a dense ICM through targeted survey techniques. These methods, which are discussed more fully in Chapter 5, rely on luminous high-redshift radio galaxies as signposts of dense environments, tuning observations to detect galaxy populations at the redshift of the radio galaxy (Venemans et al. 2002, Pascarelle et al. 1998, Kurk et al. 2003). In addition, as noted above and discussed at length in Chapter 5, the blank-field surveys for Lyman break galaxies have identified several significant galaxy overdensities at $z \sim 3$ (Steidel et al. 1998).

1.4.2 Galaxy evolution in dense environments

The galaxy populations within clusters differ dramatically from those in the field, illustrating the substantial effect of environment on both star-forming activity and morphological evolution. Locally, rich clusters are populated predominantly by massive, red, elliptical and S0 galaxies which — in sharp contrast to the field galaxy population — fall on a well defined locus of colour and luminosity (e.g., Bower et al. 1992). Population synthesis models indicate that this red sequence is consistent with an early epoch of formation ($z_f > 2$) and subsequent passive evolution of the galaxies comprising it. Red sequences consistent with passive evolution are observed in clusters to at least $z \sim 1.3$ (van Dokkum and Stanford 2003). Spiral galaxies within cluster cores are also, in general, redder than in the field population. Locally only 1 of 4 cluster spirals exhibits colours which are ≥ 0.2 magnitudes bluer than the cluster sequence, compared to 3 of 4 field spirals (Butcher and Oemler 1984). In addition to these passively-evolving galaxies, a population of bluer, late-type galaxies is observed in some clusters which appears to have evolved significantly on timescales of order 10^6 yr (Ellingson 2003). These blue galaxies tend to populate the less dense regions of clusters (the 'morphology-density relationship'); in dynamically relaxed clusters this leads to a radial dependence of the typical morphological type, with passively evolving early-type galaxies toward the core and blue spirals toward the edges. The fraction of blue galaxies, f_b, is also a function of cluster redshift (the Butcher-Oemler effect; Butcher and Oemler 1984), and there is tentative evidence that f_b is higher in poor clusters (Margoniner et al. 2001) and in less dynamically relaxed clusters (e.g., Metevier et al. 2000, Smail et al. 1998).

Both the morphology-density relationship and the Butcher-Oemler effect are thought to reflect an evolutionary sequence in which populations of massive ellipticals form coevally in cluster cores at high redshift and are supplemented by infall of field galaxies throughout cosmic time. Some mechanism within the dense cluster environment then halts star-formation in these newcomers, so that they, too, evolve passively onto the cluster red sequence.

Quenching star formation in clusters

Several mechanisms may play a role in the quenching of star formation within the cluster environment, all of which result in the removal of the cool interstellar material required to form stars. Abadi et al. (1999) show that 80% of a galaxy's gas can be removed through ram-pressure stripping in the dense cluster environment, but also that this process is only efficient in galaxies which pass directly through the dense cluster core. Similarly, evaporative stripping of cool gas by the hot intracluster medium is effective only in the richest environments. In lower density regions such as galaxy groups, removal of gas through tidal interactions and 'galaxy harassment' (frequent high-speed encounters) may be more efficient, and may act to suppress star-formation on relatively short timescales of a few Gyr (e.g., Moore et al. 1996, Fujita 1998). Finally, galactic mergers or near misses and/or compression in the dense cluster medium might first trigger starburst activity in new cluster members, which can expel interstellar gas through supernovae and strong stellar winds (Martin 1999).

Ellingson (2003) uses the evolution of morphological gradients in clusters to constrain the relative timescales of the infall of field galaxies and their transformation to the cluster red sequence, and finds (i) a decrease in galaxy infall rate of a factor of $\sim$ 3 from $z \sim 0.45$ to $z \sim 0.2$ and (ii) a timescale for transformation to passive evolution of $\sim$ 2 Gyr. As the time required to evolve a blue stellar population to a passively evolving one after the cessation of star-formation is roughly 1–2 Gyr, this result suggests an extremely rapid quenching of star-forming activity, and may require that star-forming activity begins to be suppressed in galaxies prior to their joining the cluster. This conclusion is supported by recent studies with large-scale redshift surveys such as the 2-degree Field Galaxy Redshift Survey (2dFGRS; Colless et al. 2001) and the Sloan Digital Sky Survey (SDSS; Stoughton et al. 2002), which find that the star-formation activity is correlated with environment density even at surface densities lower than those expected in galaxy groups (e.g., Lewis et al. 2002, Gómez et al. 2003, Mateus and Sodré 2004).

Triggering star formation in clusters

There is also some evidence that the dense cluster environment may initially enhance star-forming activity in galaxies just joining the cluster. Populations of 'E+A' or 'k+A' galaxies have been observed in moderate redshift clusters ($z \sim 0.3$) whose spectra are consistent with recent, vigourous star-formation which has been halted in the last 1–1.5 Gyr (Dressler and Gunn 1983, Couch and Sharples 1987, Poggianti 2003). Populations of emission-line galaxies with significant radio emission and high dust extinction which may represent the dusty starburst progenitors of these systems have been found in roughly 10% of both field and cluster galaxies (Poggianti et al. 1999, Smail et al. 1999). Whether the post-starburst populations are more common in clusters than in the field is still a debated question, with some studies finding a significant excess (Dressler et al. 1999, Poggianti et al. 1999) and others finding none (Balogh et al. 1999). It is therefore still unknown if clusters act first to trigger star-forming activity, or simply quench activity already present in infalling field galaxies. If triggered star-formation does occur within clusters, this might argue that galaxy-galaxy mergers play a substantial role in regulating star-forming activity in clusters, as starburst systems are often associated with strong mergers. Indeed, merging morphologies are observed in many of the cluster k+A galaxies (Ellingson 2003). Others, however, show no indication of strong merging, suggesting another mechanism must be at work.

1.4.3 AGN in dense environments

Given the apparent evolutionary link between galaxies and their central black holes, the study of the environmental dependence of AGN activity is extremely well motivated as a means to understanding both the physical trigger of black hole accretion and the link with star-forming activity. As noted by Best (2004), if AGN activity is related mainly to the availability of the cold gas which also fuels star-formation activity, the environmental dependence of star formation activity which is clear in cluster galaxy populations should also be apparent in the prevalence of cluster AGN. On the contrary, if black hole growth is independent of local environment, the fraction of cluster AGN could be equivalent to the field fraction, with the mass function of black holes simply following the mass function of galactic bulges within the cluster galaxy population. Finally, if accretion onto a central black hole is triggered by galactic mergers as suggested by some models (e.g., Heckman et al. 1986), AGN demographics might be expected to follow neither those of the star-forming nor of the cluster populations, but rather to trace out the environments in which merging is most common.

Several optical studies have sought to quantify the AGN fraction within clusters. Dressler et al. (1985) concluded that AGN activity was suppressed in clusters, stating that only 1% of cluster galaxies hosted luminous AGN, while 5% of field galaxies did. However, as pointed out by Edge (1992), this survey was magnitude and not volume limited, and thus included bright field AGN over a very large redshift range. Later studies concluded there was no evidence for an environmental dependence, with roughly 1–2% of all galaxies containing luminous AGN regardless of cluster membership (e.g., Dressler et al. 1999, Carter et al. 2001). The large-scale galaxy redshift surveys have allowed a more detailed investigation of the relation between AGN activity and local galaxy density. Kauffmann et al. (2004) selected high luminosity AGN within the SDSS on the basis of their optical emission lines and found them less likely to populate high-density environments. However, when Miller and Owen (2003) selected primarily lower luminosity AGN from the same survey, they found no evidence for environmental dependence. In order to reduce biases due to obscuration, Best (2004) selected only radio-loud AGN in the 2dFGRS by cross-correlating with the NRAO VLA Sky Survey at 1.4 GHz. This author found no strong dependence of AGN activity on local density — with the exception of a decrease in activity seen in very rarified regions — but did find dependencies on the larger-scale environment, with radio-loud AGN most prevalent in groups and poor clusters and avoiding field regions and cluster cores. He also reports that nearly all AGN found in rich environments lack optical emission lines, suggesting optical surveys relying on line emission will be strongly biased. The radio luminosity of these line-free AGN is a strong function of the local galaxy density, suggesting that the radio emission is significantly boosted in dense environments (see Barthel and Arnaud 1996).

X-ray surveys of dense environments offer a method of assessing the AGN content which relies neither on optical emission lines nor on radio-loudness. Until recently, however, X-ray surveys of clusters were hindered by the difficulty of separating AGN emission from the bright, diffuse ICM emission in low-resolution images. The high resolution of Chandra in conjunction with sensitive multi-scale wavelet detection algorithms have made sensitive X-ray surveys of AGN within luminous clusters possible for the first time. A series of Chandra surveys of clusters, which are detailed in §4.1, have amassed evidence that AGN are prevalent within dense clusters and that they both affect and are affected by their environment (e.g., Cappi et al. 2001, McNamara et al. 2001). AGN have been detected in most clusters, with more luminous sources seen toward higher redshift. However, not all moderate- to high-redshift clusters contain powerful AGN, suggesting that other variables, such as cluster dynamical state or environment richness, determine the prevalence of luminous AGN within a cluster (Molnar et al. 2002). In at least two clusters — MS1054-03 at $z = 0.83$ (see Chapter 4) and A2104 at $z = 0.15$ (Martini et al. 2002) — there is tentative but intriguing evidence that the galaxies hosting the luminous AGN may be recent arrivals to the cluster environment in which activity has been triggered. Studies of large sample of objects are currently underway to assess the prevalence of cluster AGN and its dependence on factors such as redshift, environment richness, and dynamical state (Dowsett et al. 2004).

1.4.4 AGN and the development of the ICM

While a full review of these applications is outside the scope of this introduction, it is worth noting that observations of the intracluster gas provide important constraints on large-scale structure formation models. (Indeed, nearly all of the surveys for AGN within clusters have been done with archival data obtained primarily to study the intracluster gas.) The evolution of the cluster mass function with redshift is among the key testable predictions of hierarchical cosmologies and comparisons of the baryon density measured within clusters with that predicted by big-bang nucleosynthesis models provide evidence of a low density Universe with $\Omega_m \simeq 0.2$ (Bahcall 1999). The evolution of the scaling relations (e.g., between X-ray luminosity and temperature) reflects the formation history of the cluster gas. In turn, the detailed physics of this gas governs the assembly of baryonic matter in forming structures. Developing an understanding of the heating and cooling of this material is an important current aim of cluster studies which will extend well-developed theories of the growth of large-scale structure into the far messier business of galaxy formation.

It is becoming clear from current X-ray surveys that AGN exert a far-reaching effect on the structure and energetics of the cluster environment. Bubble-like cavities observed in the hot ICM of low and intermediate redshift clusters result from energy injection from AGN hosted by brightest cluster galaxies (McNamara et al. 2001). In high-redshift protocluster environments without a luminous ICM, radio galaxy jets may provide an important feedback mechanism, both through injection of mechanical energy in relativistic electrons and through photoionisation by CMB photons Inverse-Compton scattered off them (Fabian et al. 2003, Scharf et al. 2003, Carilli et al. 2002), curbing cooling at the cluster core. AGN, therefore, may be critically linked not only the development of their host galaxies, but of their larger-scale environment as well.

1.5 This thesis

This thesis presents surveys of AGN in three different environments which aim to explore the characteristics of the AGN population as a whole — in particular the newly-resolved obscured AGN — and to explore the links between AGN, their host galaxies, and their environment at larger scales.

- In Chapter 3, I discuss my work in support of the ELAIS Deep X-ray Survey, an early 'blank field' Chandra survey designed to characterise the components of the XRB and their relation to populations at other wavelengths.
- In Chapter 4, I examine the AGN content of a massive, X-ray bright galaxy cluster at $z = 0.83$, using an archival Chandra image of the field.
- In Chapter 5, I present a survey of the SSA22 protocluster region at $z = 3.09$ which is based on an extremely deep XMM exposure.

While all these surveys benefit from complementary data at many wavelengths, they are based primarily on the X-ray data and are possible only due to the increased sensitivity and resolution available with Chandra and XMM. Because of this, I begin in Chapter 2 with an introduction to X-ray observations and the capabilities of the new instruments.

CHAPTER 2

X-ray observations

Most of the work presented in this thesis would have been impossible 5 years ago, prior to the launch of the Chandra and XMM-Newton observatories. Several fundamental challenges in observing cosmic X-rays delayed the advent of extra-solar X-ray observations until the 1960s, and hindered the growth of X-ray astronomy through much of the next four decades. However, as technological advance has produced increasingly more capable X-ray instruments, the science has rapidly matured. Chandra and XMM-Newton, both launched in 1999, provide images and spectra of X-ray sources with resolution, positional accuracy, and sensitivity for the first time rivalling those of optical observations. The revolutionary effect this has had on the field would be difficult to overestimate, as long-standing theories about the X-ray Universe can now be directly tested with observations.

In this chapter I discuss the capabilities of these new instruments in the context of the traditional limitations of X-ray astronomy (§2.1), the characteristics of modern X-ray CCD data (§2.2), and data reduction requirements specific to Chandra (§2.3) and to XMM-Newton (§2.4).

2.1 X-ray telescopes

2.1.1 Requirements

The most basic challenge in detecting cosmic X-rays is that all observations must be made above the majority of the Earth's atmosphere. As discussed in §1.1.4, X-rays are readily destroyed through photoelectric absorption, with a cross-section for interaction decreasing as roughly E^{-3}. X-rays at the hard (high energy) end of the 0.5 - 10 keV range can penetrate less than a thousandth of Earth's atmosphere prior to absorption, while those at the soft (low energy) end are stopped by less than a millionth. Because of this, all but extremely hard ($>$ 30 keV) X-ray sources must be observed with instruments aboard a rocket or a satellite.

Another major difficulty in X-ray observing is the extremely low count rates of most X-ray sources, compared both to their emission in other wavebands and to the background flux detected at X-ray energies due to unresolved background sources, cosmic rays, and charged particle flux. X-ray telescopes must have reasonably large active areas in order to be sensitive to the low count rates coming from the source, while still minimising the recorded background signal.

A final substantial problem in designing an X-ray instrument is that, due to their high energies, X-rays scatter rather than reflect from traditional optical elements at all but the smallest incidence angles. One consequence is that they are therefore very difficult to focus. While a focusing telescope is not necessary to detect cosmic X-ray sources, it is clearly desired in order to easily achieve good positional accuracy, to maximise the ratio of signal to noise, and to image X-ray sources. To achieve this, X-ray mirrors must have grazing incidence design, as well as exceptionally smooth surfaces. Similarly, traditional optical systems which provide dispersive spectroscopy at lower wavelengths must be substantially modified to allow true X-ray spectroscopy.

2.1.2 X-ray detectors

Non-imaging detectors

The first cosmic X-ray detectors were simple laboratory *Geiger counters* flown aboard rockets. Geiger counters consist of a container encasing a volume of gas and a charged anode, which is fronted by a thin window which is transparent to X-rays. X-rays are detected when they enter the chamber and ionise atoms in the gas. The released electrons are accelerated toward the anode, releasing more electrons via collisions along the way. The pulse of electrons received at the anode is then detected as an electronic charge. In *proportional counters*, the final amount of charge collected at the anode is proportional to the energy of the incoming X-ray. Photoelectric absorption takes place in the inner shells of a heavy atom, releasing a single high energy electron plus Auger electrons produced when electrons from higher shells de-excite to the lower level. Secondary electrons are then released through collisions with nearby atoms, with the final number of free electrons, N, equal to the energy of the photon, E, divided by the mean energy required to release secondary electrons, w. The energy resolution is governed by the variance in the number of electrons produced in the initial impact, $\sigma_N^2 = FN$, where the Fano factor, F, is an attribute of the detecting gas. As the cross-section for absorption decreases with energy, proportional counters become increasingly inefficient toward higher energies. An early detector effective at very high energies ($>$ 20 keV) is the *scintillation counter*, which uses a solid crystal rather than a gas chamber to absorb the X-rays, and registers the light produced by this interaction, rather than an electrical current.

Rocket experiments of the 50s observed only the Sun, which was then thought to be the only cosmic source bright enough in the X-ray to be detected. In 1962, the first extra-solar X-ray sources were detected serendipitously in an experiment officially designed to measure reflected Solar X-rays from the surface of the Moon (Giacconi et al. 1962). Throughout the 60s, much of the X-ray sky was explored with rocket missions, and refining the positional accuracy of the observations in order to identify optical counterparts became a major goal. Some early designs placed a simple honeycomb collimator in front of the detection window, limiting the areas in the sky from which X-rays could be observed, and achieved a positional accuracy of a few square degrees. The modulation collimator was a combination of two grids placed over a moving X-ray detector and an aspect camera which tracked the movement of this detector optically, and reduced error circles to about an arcminute.

Position sensitive detectors

The first focusing instruments were launched aboard satellites in the 1970s. Focusing telescopes required development of position sensitive X-ray detectors, and several designs have been used:

- The *imaging proportional counter (IPC)* functions similarly to the proportional counters described in the previous section but, rather than a single anode wire, the anode is a plane of resistive material which can detect an event at a specific x,y position. Spatial resolution in IPCs is set by the amount that the initial electron cloud diffuses before it contacts the anode plane. Energy resolution is dominated by the properties of the gas, specifically the Fano factor described above. The quantum efficiency, and thus energy range of operation, is limited on the low energy end by absorption by the gas chamber window material, and on the high energy end by the decreasing cross-section for interaction.
- *Microchannel plates* are composed of typically millions of lead glass channels with diameters on the order of 10 μm, maintained in a strong electric field. Incoming X-rays collide with the slanted wall of the channel, ionising atoms in the glass. Liberated electrons are accelerated rapidly downwards, prompting further collisions and generating an electron cascade which is then read out by electronics below. Since X-rays with energies less than $\sim$ 5 keV cannot readily cross into neighbouring channels, the positional accuracy of a single-plate MCP is set primarily by the width of the channels. In practice, multi-layer instruments contain two or more plates separated by small gaps which allow some lateral diffusion. MCPs provide virtually no energy information, as most electrons liberated from the channel edge are rapidly recaptured and, in general, only one free electron results from the absorption of the X-ray. MCPs are not spectacularly efficient, and, again, the operational energy range is set on the low end by absorption in protective filters and and at the high end by the decreasing likelihood of photoelectric interaction.
- The current generation of X-ray observatories make use of solid state *charge coupled detectors*

(CCDs), adapted for use in the X-ray regime. In most ways, the X-ray CCDs on Chandra and XMM are analogous to familiar optical CCDs. Incident photons release charge in a semiconducting detector through photoelectric absorption. A matrix of potential wells is maintained by a gate structure, which keeps the charge localised throughout the integration. A total charge which is proportional to the photon flux is then moved to a read-out node by clocking the voltages on the gates in sequence. The current produced within in each gated region, or pixel, during the integration is then amplified and recorded. CCD spatial resolution is limited primarily by pixel size. Energy resolution is again dependent on the Fano factor of the detecting material, but can be degraded significantly by photon pile-up and by charge transfer inefficiency (CTI), discussed below (see §2.2.2). The overall efficiency of the CCD is set by the quantum efficiency of the detector, as well as the transmission properties of any filters used, e.g., to avoid contamination by UV light.

Background rejection

There are three major types of background flux of concern to the X-ray astronomer: that emitted by cosmic X-ray sources, that from cosmic rays, and that due to charged particles associated with solar activity and/or trapped in the Earth's atmosphere. The cosmic X-ray background, as discussed in §1.2, is comprised primarily of truly diffuse Galactic interstellar medium emission at low energies and the superposed flux of AGN at higher energies. Galactic emission rates vary depending on galactic latitude and longitude. The extragalactic background contributed a uniform flux in low resolution detectors, but is largely resolved by modern instruments.

Depending on position, X-ray instruments are exposed to high-energy protons and electrons trapped in the Earth's magnetic field, a steady flux of ions in the solar wind, and episodic bursts of large amounts of charged particles from solar flares and Coronal Mass Ejections (CMEs). Satellite orbits are chosen carefully with these radiation environments in mind as, in addition to adding observational noise, radiation flux can overload telemetry and damage detectors. An early surprise with Chandra, which is flown in a high Earth orbit, was the extent of soft proton radiation which could be focused onto the detectors by the mirrors, which lead to significant degradation of the energy resolution of some of the CCD chips (see §2.2.2). To protect instruments, they are stowed or shut down during periods of known high particle flux (for example, when passing through the radiation belts in the Earth's magnetosphere, or during CMEs). Data which is taken during flare periods is largely useless, as the background flux far outshines any source flux; a first step in X-ray data reduction is the temporal filtering of these bad periods.

Cosmic ray flux is not focused by mirrors in focusing systems, and permeates all types of instruments, creating the majority of the false events measured by X-ray detectors. There are three main methods of rejecting these spurious events:

- In the *anti-coincidence method*, the detecting surface is surrounded by a material which is insensitive to X-rays but which can detect cosmic ray hits. Events which are detected simultaneously by the primary detector and this 'guard' protector are then identified as cosmic rays and can be excluded from analysis.

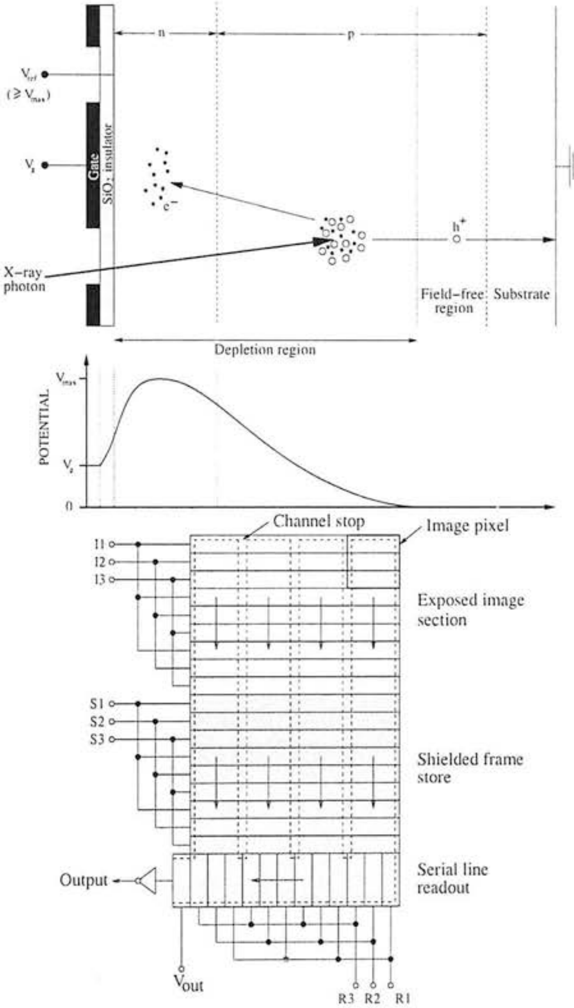

Figure 2.1: *X-ray detection in a CCD. Left) Charge liberated by an X-ray photon is collected under the gate region by the voltage structure of the device. Right) In frame store CCDs, such as those aboard Chandra, charge collected in pixels in the exposure region is moved very rapidly (for ACIS, 41μs) along the columns into the frame store by varying the voltages I. Charge in the shielded region is then shifted vertically and horizontally (by clocking voltages S and R, respectively) to the read-out node ($V_{\rm out}$). For ACIS, the nominal time to empty the full frame store, and therefore the standard integration time, is 3.2 s. (Figures courtesy of J. Manners.)*

- *Pulse rise-time discrimination* relies on the temporal profile of the detected charge: real X-rays are stopped by the detector and thus give rise to a short pulse of charge while cosmic rays proceed through the detector, leaving a trail of ionised atoms and a correspondingly longer pulse of emission.

- Modern X-ray CCDs record not only the position and energy of the detected event but also an indication of the distribution of charge over the detecting pixels. Certain distributions, referred to as 'grades', are far more likely for spurious events than for X-rays, and calibration of this allows development of highly effective *grade-based filtering schemes.*

2.1.3 X-ray mirrors

From the 1970s, larger X-ray telescopes began to be launched aboard Earth-orbiting satellites, allowing much longer integration times as well as larger scientific payloads including far more sophisticated instruments and focusing optics. As mentioned above, the primary restriction on X-ray mirror design is that at most incidence angles X-rays will pass through or be absorbed by most materials. At very small angles of incidence, however, X-rays can be reflected. The largest allowed angle for which reflection rather than scattering is achieved, or critical angle, α_c, is set by the the density of the material comprising the reflecting surface, ρ, and the energy of the incoming photon. Critical angle in general increases with the atomic number of the reflecting material, so heavier elements such as gold or iridium are more efficient reflectors of X-rays and are commonly used in X-ray optics. Higher energy photons have smaller critical angles, which decreases the efficiency of grazing incidence systems in harder energy bands. For heavy elements, Aschenbach (1985) gives $\alpha_c = 69.4\ \sqrt{\rho}/E$, with units of arcminutes, g cm^{-3}, and keV, leading to critical angles for gold mirrors of roughly 5 degrees at 1 keV and just 0.5 degrees at 10 keV. For this reason, many X-ray focusing telescopes operated only in the soft X-ray (< 2 keV), and it was not until the current generation of X-ray observatories that increased sensitivity and collecting area allowed focused images of hard X-ray sources. The large reflecting areas required present an enormous technical challenge, as the surfaces must be machined to an extremely high level of smoothness and kept meticulously clean.

In the Wolter Type I design, which has been used almost exclusively in major X-ray observatories, incident rays at grazing angles are focused through reflections off the elements of coaxial, confocal, hyperbolic / parabolic mirror pairs, as illustrated in Figure 2.2. To increase collecting area, these mirror pairs are nested. The total available reflective surface of these shells, comprising a series of thin rings, is the aperture of the telescope. This area convolved with the efficiency of the reflecting material with wavelength is the effective area (EA). Figures 2.3a and 2.3b illustrate the complex relationship between effective area, energy, and distance from the optical axis. The resolution afforded by such a mirror design is also complexly dependent on both energy and off-axis angle, such that the point spread function (PSF) degrades toward higher energies and off-axis angles. 'Ghost rays', which reflect from only one of the hyperbolic/parabolic mirror surfaces are also possible in severely off-axis sources.

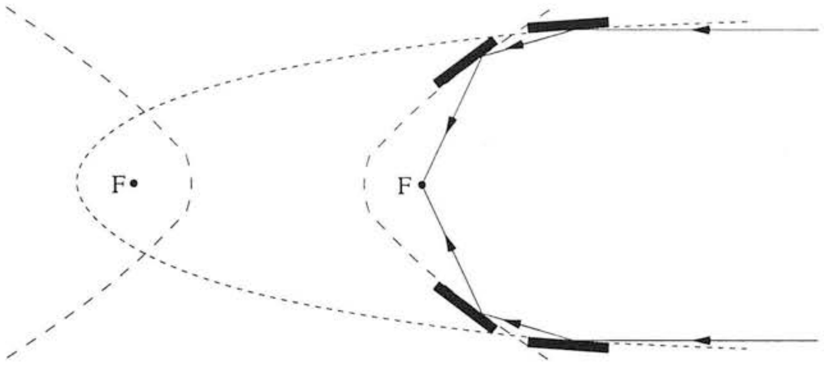

Figure 2.2: *Wolter Type I X-ray Mirrors. X-rays incident at grazing incidence are focused by reflection of both components of coaxial, confocal parabolic/hyperbolic mirror pairs. Increased reflecting area is achieved by nesting shells.*

2.1.4 X-ray spectroscopy

As noted above, the low count rates from X-ray sources and the proportional response of many types of X-ray detector allow moderate spectroscopic resolution. The *imaging spectroscopy* allowed by modern X-ray CCDs forms a major part of this thesis, and is described fully in §2.2.2. In addition to the imaging detectors described above, several devices have been developed expressly for X-ray spectroscopy.

- A precursor to the CCD, the *solid state spectrometer (SSS)* functioned through photoelectric absorption of X-rays resulting in ionisation of atoms in the detecting material, in this case a solid state semiconductor. Operating at extremely cold temperatures, this charge could be read out directly, rather than used to initiate an electron cascade. The lower ionisation threshold of the SSS material offered a substantial increase in energy resolution over IPCs, but provided no spatial resolution.
- *Crystal spectrometers* function via Bragg reflection, in which X-rays of wavelength, λ, incident at angle , θ, on a crystal with lattice spacing, d, are reflected only when $n\lambda = 2d\sin\theta$, where n is an integer. For a given crystal with fixed lattice spacing, different wavelength ranges can be sampled by varying the angle of incidence. The resolution of such a device is high ($\lambda/\Delta\lambda \sim 300$), but the efficiency of the system is extremely low (i.e. $\leq 0.1\%$) and so only very bright sources can be successfully observed.
- *X-ray calorimeters* have not yet been used aboard a major X-ray mission, but form an important part of the Astro-E2 mission (originally the spectroscopic mission associated with Chandra), which is due for launch in 2005. Calorimeters function through conversion of absorbed X-ray energy to heat in an extremely cold absorber. The small variance in temperature resulting from X-ray absorption

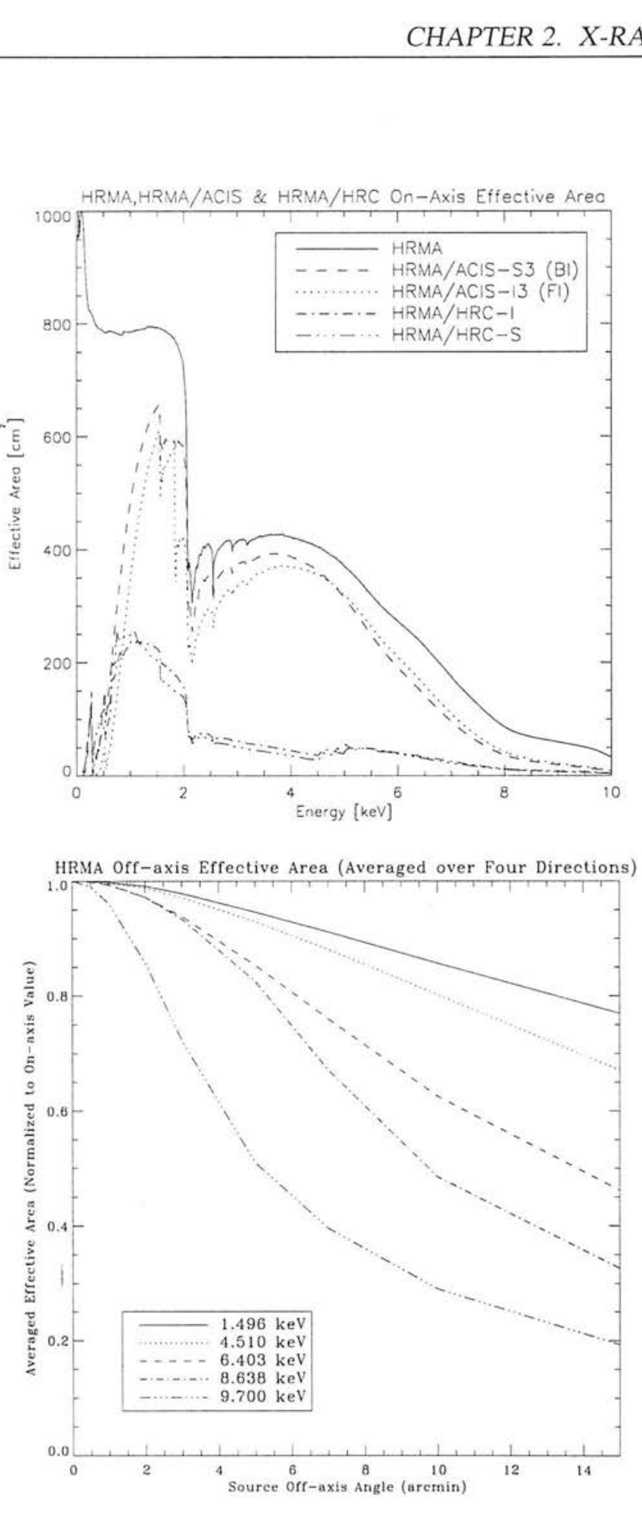

Figure 2.3: *Energy and off-axis angle dependencies of Chandra's mirror EA. Top) EA of Chandra's High Resolution Mirror Assembly (HRMA) and detectors vs. energy. The structure seen near 2 keV is due to X-ray absorption into the Ir K edge in these Ir-coated mirrors. Bottom) HRMA EA vs. off axis angle for selected energies, normalised to the on-axis EA. Due to the smaller critical angles at high energy, the 9.7 keV EA decreases most rapidly for off-axis sources. Figures from the Chandra Proposer's Observatory Guide.*

is converted to measurable signal through a silicon thermistor with electrical resistance which is a strong function of temperature. Calorimeters promise high efficiency as well as the highest spectral resolution afforded by any non-dispersive spectrometer.

Dispersive spectroscopy is also possible at X-ray wavelengths using high period transmission and reflection gratings. Chandra has two sets of gratings - the High Energy Transmission Gratings (HETG; energy range $\sim 0.4 - 10$ keV) and the Low Energy Transmission Gratings (LETG; energy range $\sim 0.07 - 7$ keV) - which are inserted behind the mirrors during gratings mode observations and produce spectra with $E/\Delta E \simeq 60 - 1000$. The two sets of gratings are contained in two circular aluminium plates which can be swung into the light-path behind the X-ray mirrors. Each plate contains hundreds of circular grating facets, each of which is comprised of finely spaced gold-plated grating bars off which the X-rays are dispersed. The support plates are machined so that the centres of the grating facets lie along one surface of the Rowland torus, illustrated in Figure 2.4. The grating spacing, height, and width are tuned to enhance efficiency in odd orders, and minimise even orders. When inserted behind the mirrors, the gratings diffract X-rays in a dispersed spectrum according to the grating diffraction relation $m\lambda = p\sin\theta$, where m is the integer order number, λ the photon wavelength, p the spatial period of the grating lines, and θ the dispersion angle. The dispersed spectrum will be focused along a second surface of the Rowland torus, which determines the positioning of the spectroscopy mode detectors. The Rowland geometry maintains the telescope focal properties in the dispersion direction for a large range of diffraction angles. Grating efficiency in the first order is $\sim 10\%$.

XMM's Reflection Grating Spectrometers (RGS) function simultaneously with the imaging CCDs by sharing the incident light beam, and provides spectra with $E/\Delta E \simeq 200 - 800$ between 0.35 and 2.5 keV. Behind two of the three XMM mirrors, arrays of roughly 180 reflection grating segments are mounted at grazing incidence to the converging beam which intersect $\sim 50\%$ of the light. They gratings are oriented along one side of a Rowland torus. Light is reflected to a dispersed focus along the opposite side of this torus, with dispersion given by $m\lambda = d(\cos\beta - \cos\alpha)$, where d is the spacing between grating grooves, α is the angle between the grating plane and the reflected ray, and β is the angle between the grating plane and the incident ray. The peak effective area of the RGS pair is ~ 150 cm^2, or roughly 5 times that of the Chandra transmission spectrographs.

2.2 X-ray data

In this section I describe the general properties of X-ray data, and how these data are processed to obtain scientifically useful information. Though the discussion is of modern-day CCD data, the general techniques presented are valid and have been used for many types of X-ray detector. The high energy and low count rates of cosmic X-radiation allow most X-ray detectors to function as photon-counting devices, preserving not only the position but the energy of each X-ray event. In contrast to optical data, X-ray data consists not of an integrated image, but of an event list in which various attributes of individual photons are tabulated. Much of X-ray analysis is comprised of filtering and binning the event list in different ways. For example,

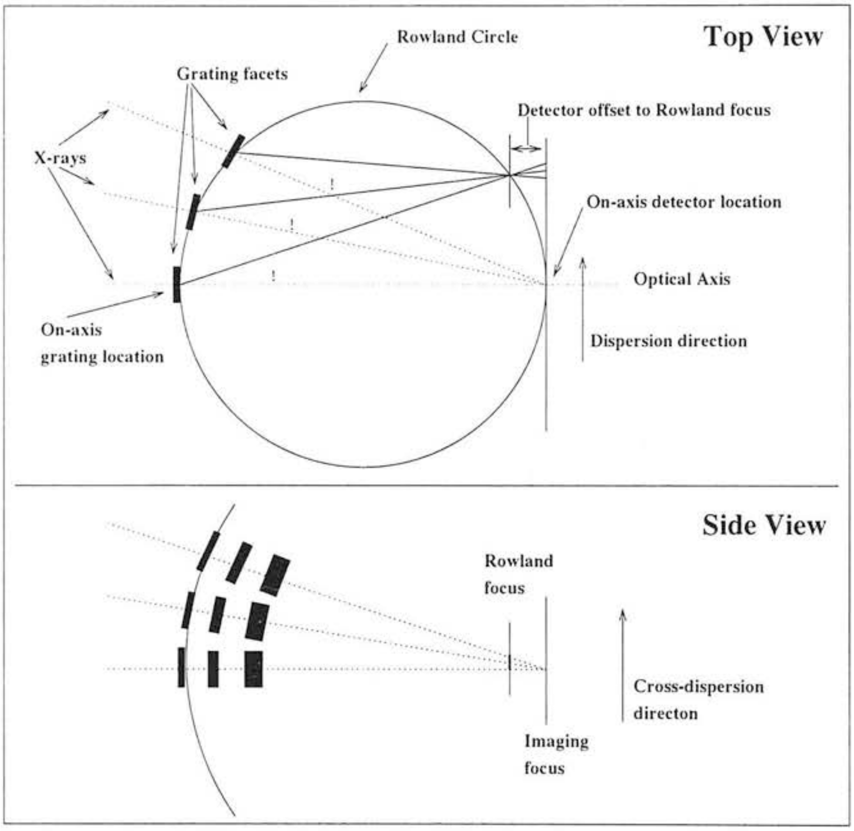

Figure 2.4: *Diagram of Rowland geometry. The circle whose diameter is the distance from the grating plane to the focal plane along the optical axis is the Rowland circle. Rotating this circle around the z axis describes the Rowland torus. To minimise grating induced optical aberration, both grating facets and spectroscopic detectors follow the Rowland geometry. Figure from the Chandra Proposer's Observatory Guide.*

binning on sky position will produce X-ray images, binning on time creates light-curves, and binning on energy yields spectra.

2.2.1 X-ray imaging

X-ray images are formed through spatial binning of calibrated event-lists. Energy filtering prior to image binning allows images in several wavelength bands to be extracted from the same event-list, and multicolour images to be produced. Also, broad spectral information is often obtained through source photometry in multiple bands. A commonly quoted property of X-ray sources is their hardness ratio, HR, usually defined as the ratio of the difference of fluxes in two bands over their sum: $HR = \frac{H-S}{H+S}$, where S and H are, e.g., 0.5 – 2 keV flux and 2 – 10 keV flux.

Exposure maps

Mirror effective area, filter transmission, and detector quantum efficiency are all position and energy dependent, and must be corrected to produce a physically meaningful image. This is commonly done by constructing an exposure map which determines the relative sensitivity of different parts of the detector. Dividing the raw data by this map then corrects for instrumental variation across the chip, analogous to the 'flat-fielding' of optical data. Specifically, the raw image counts C during exposure time $\tau_{\rm eff}$ at position $\hat{\mathbf{p}}$ within pulse height range Δh are related to source photon flux S at a given energy λ by

$$C(\Delta h, \hat{\mathbf{p}}) = \tau_{\rm eff} \int_{\lambda \in \Delta\lambda} d\lambda E(\Delta h, \lambda, \hat{\mathbf{p}}) S(\lambda, \hat{\mathbf{p}}) \tag{2.1}$$

where the integral in wavelength extends over all wavelengths which contribute to pulse heights in Δh. The quantity $E(\Delta h, \lambda)$ is the exposure map, in units of cm^2 counts photon^{-1}. Choosing a wavelength range over which this quantity is reasonably constant allows its extraction from the integral, and creation of a 'fluxed' image by division of the raw image by the exposure map and the exposure time:

$$\int_{\lambda \in \Delta\lambda} d\lambda S(\lambda, \hat{\mathbf{p}}) = \frac{C(\Delta h, \hat{\mathbf{p}})}{\tau_{\rm eff} E(\Delta h, \lambda, \hat{\mathbf{p}})} \tag{2.2}$$

In practice, construction of an exposure map is a three step process. First, the motion of the source on the detector due to spacecraft dither must be specified. Then, an instrument map, which is essentially the product of the mirror effective area and the filter/detector quantum efficiency is produced. Finally, the aspect information is combined with the instrument map to determine the accumulated exposure at any point on the sky.

Effective area and quantum efficiency both vary significantly with energy. Therefore the calculation of the instrument map requires assumption of a source spectrum. Since Equation 2.2 is valid only so far as $E(\Delta h, \lambda)$ is constant over $\Delta\lambda$, creation of an exposure map suitable for broad bands is best done piece-wise over locally constant bins. These bins are then weighted according to the assumed source spectrum. For many observations, a single spectrum will not be suitable for all objects within a field, or for all areas of an

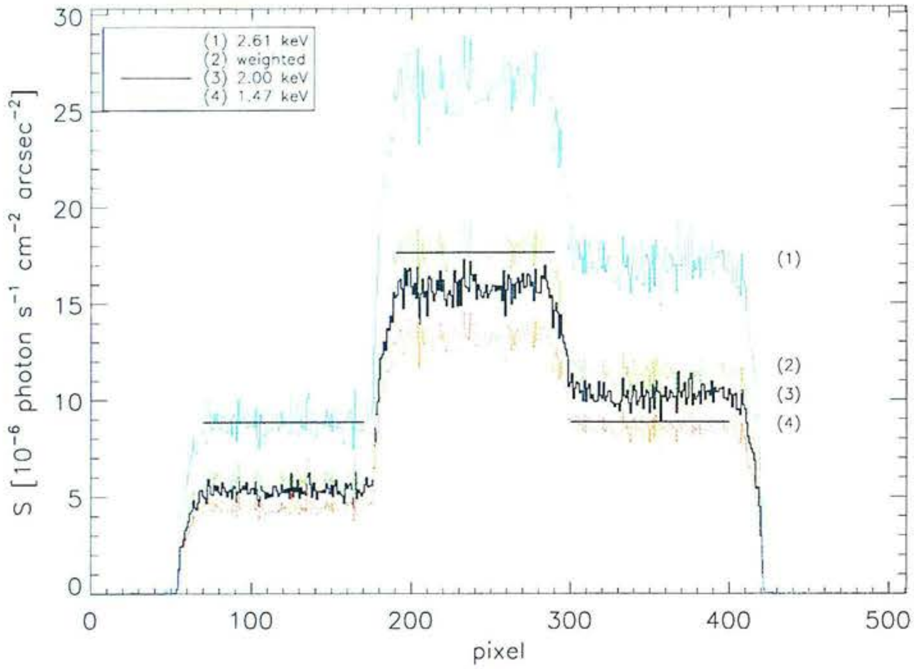

Figure 2.5: *This figure, taken from John Houck's memo An Introduction to Exposure Maps, illustrates the flux errors which can result from assumption of a single spectrum in creating an exposure map for a field with various spectral regions. The simulated data shown consists of two partially overlapping disks of uniform and equal surface brightness, one emitting at 1.47 keV and the other at 2.61 keV. The overlapping region therefore has twice the flux comprised of photons of both energies. The horizontal black lines indicate the input flux, while the coloured histograms indicate the recovered flux using four different exposure maps - three monochromatic maps at 1.46 keV, 2.61 keV, and 2.0 keV, and one map which weights equally 1.46 keV and 2.61 keV. Flux errors of up to 40% are evident, illustrating that even for a known input spectrum it is impossible to correct the entire image with a single map.*

extended object. An indication of the magnitude of the errors in the inferred flux resulting from the use of an inappropriate exposure map can be seen in Figure 2.5.

2.2.2 Pulse height spectra

Energies are generally listed in two ways in X-ray event-lists. The *pulse height*, or PHA , is the signal recorded by the detector, which is proportional to the true incident photon energy. The energy, or *PI*, is then derived from this value via knowledge of the proportionality of the system. This second value is what is used to filter images by energy, as described above. However, due to the finite energy resolution of the CCD, a range of energies will produce the same pulse height. PI values listed in X-ray event-lists are therefore only approximate. Pulse height spectra are created by filtering events spatially to isolate source and background regions, then binning the resulting lists on PHA. These spectra are then interpreted through comparison with models of source emission which are convolved with models of instrument response.

Response matrices

Two calibration files must be constructed to facilitate spectral fitting. Spectral 'blurring' due to the finite resolution of the detector is expressed in the X-ray spectral redistribution matrix (RMF), while instrumental effects due to mirror effective area, filter transmission, and detector quantum efficiency are specified in the ancillary response file (ARF).

As discussed above, due to the limited intrinsic energy resolution of X-ray CCDs, photons of a range of energies ΔE are detected at pulse height h. Mapping from energy to pulse height then requires a spreading of the observed counts, which is conveniently expressed as a matrix multiplication. The RMF contains the ensemble of probabilities, $R(E, h)$, of detecting photons of energy E at pulse heights h. For high-resolution systems (i.e. dispersive gratings), the response is very nearly diagonal, while for low-resolution detectors such as proportional counters it is much less so. X-ray CCDs are intermediate cases. While the response is largely diagonal there is some off-axis structure, indicating significant non-linearities due to escape peaks and low-energy tails.

RMFs are relatively static and are distributed as standard instrumental calibration products. Their construction for a given dataset requires only correct specification of the detector conditions and source position to select the appropriate RMF from a pre-defined library. In contrast, the ARF, which contains the mirror, filter, and detector efficiencies as a function of energy, must be calculated for each observation. Like exposure maps, ARFs are based on an aspect histogram which details the position of the source on the chip throughout the exposure. This information is then used to average instrumental effects over exposure time to deduce the combined system response versus energy.

The RMF and ARF are combined to produce a total response with which to convolve candidate source models for comparison with the real data. The source model multiplied by the ARF alone would produce the spectrum observed by a 'perfect' detector with infinite energy resolution; folding this spectrum through the RMF then mimics the resolution of the actual data. Since the RMF is probabilistic, it is possible only to say how likely the observed counts distribution is to have arisen from a given source spectrum. This is done by minimising a fit statistic, such as χ^2 or Cash, through variation of the source model parameters. For spectra with very few counts, which are quite common in X-ray observations, a statistically acceptable fit is often obtained for a variety of models.

Pile-up, trailing, and CTI

As noted above the energy resolution of X-ray CCDs is degraded by two effects. Pile-up occurs when charge from more than one photon is accumulated in a pixel within an integration. This charge is then transferred to the readout and recorded as if it were a single event, giving an energy which is artificially high and a count rate which is artificially low. Though the primary effect is hardening of the spectrum, imaging data can also suffer due to inappropriate rejection of piled-up events. Events will be rejected if the combined energy is higher than the system threshold, or if they have suffered 'grade migration' - a change in shape of events which are piled up - and are no longer in the standard set. Since X-ray integrations are quite short (of order seconds) and count rates are generally quite low in comparison, pile-up is only a problem for the brightest sources. For the very brightest sources, trailing of flux along a readout row, or accumulation of 'out of time events', is also a problem, as flux detected in a pixel during readout will be combined with the shifting flux from a pixel farther from the node. These problems can be mitigated by following an observing strategy to minimise pile-up (e.g., using shorter exposure times and/or a subarray with a shorter readout) or by a variety of post-processing techniques (e.g. estimate the extent of pile-up by using only grades which are rarely populated by piled-up events).

Charge transfer inefficiency (CTI) refers to imperfect transfer of charge through the pixels to the readout node. As charge is transferred, some can become trapped in the imperfections in the lattice of the CCD, thus altering the apparent energy and grade distribution of the detected event. The degree to which events are effected are related to their position relative to the readout node, with events falling in pixels far from the readout node effected more than those nearby. CTI is in general a static quality of the CCD chip at its operating temperature, and an understood component of the finite energy resolution of the detector. CTI can be significantly increased by damage to the chip, resulting in more charge traps being created. The effects observed for a source badly effected by CTI are (i) lower pulse heights for a given energy, (ii) degradation of spectral resolution, (iii) grade migration for events smeared along the readout node and an associated decrease in detection efficiency if the new grades are not of the standard set. The only remedy for data badly affected by CTI is post-processing based on detailed calibration of the effected CCD chips.

2.3 Chandra data

2.3.1 Instrument description

Chandra consists of: the High Resolution Mirror Assembly (HRMA); two Advanced CCD Imaging Spectrometers, one square array for imaging (ACIS-I) and one rectangular array for spectroscopy (ACIS-S); two High Resolution Cameras, again one for imaging (HRC-I) and one for spectroscopy (HRC-S); and two sets of transmission gratings, the Low Energy Transmission Grating (LETG) and the High Energy Transmission Grating (HETG). The four detectors are on a translation stage such than any can be moved into the focus of the HRMA, and either grating can be inserted into the light path between the HRMA and the focal plane, giving eight possible telescope configurations.

The HRMA comprises 4 mirror shells of the Wolter type I design, coated in Iridium and with an effective area ranging from ~ 800 cm^2 at 0.25 keV to ~ 100 cm^2 at 8 keV (see Figure 2.3). The FWHM of the PSF of the HRMA in conjunction with a detector is roughly 0.5 arcseconds on axis, degrading with off axis angle and with energy.

The ACIS contains a total of 10 silicon X-ray CCDs, any 6 of which can be operated simultaneously, and all having 1024×1024 24μm pixels. The four chips comprising the ACIS-I array are arranged to provide a square FOV 16.9 arcminutes on a side, while the six chips of the ACIS-S array (designed for use with the HETG) are arranged lengthwise giving a FOV of 8.3 by 50.6 arcminutes. Two of the chips on the

S array are back-illuminated (BI) - the gate structure of alternating voltages defining the pixel regions is facing away from the incident X-rays - which provides increased low energy response.

ACIS has an operational range from 0.2 - 10 keV, and an energy-dependent efficiency of 30-90%. Energy resolution at launch ranged from $E/\Delta E \sim 14 - 50$; CTI induced by radiation damage by focused soft protons sustained soon after Chandra's launch has degraded resolution in the FI chips by factors of up to 2. These effects have been carefully calibrated and corrections applied during standard data processing ameliorate much of the CTI degradation. Nominal exposure integration time for the full ACIS frame is 3.2 sec, but resolution of 3 msec is possible for single rows.

The HRCs are CsI-coated multichannel plate pairs, with a readout pixel size of ~ 0.13 arcseconds. They have an operational range from 0.08 - 10 keV, though they are only 30% efficient at 1.0 keV and just 10% efficient at 8.0 keV. The I array is a single plate with a field of view of 30 by 30 arcminutes, while the S array, designed for use with the LETG, is comprised of 3 plates with a total FOV of 6 by 99 arcmin which roughly follow the Rowland geometry. HRC time resolution is 16 μsec.

Each set of gratings contains approximately 540 grating facets supported by an aluminium frame machined to follow the Rowland torus. Each grating facet contains grating bars with periods of roughly 1μm, supported by larger period support bars or a substrate. Operating over a combined energy range of 0.07 - 10 keV, they form a dispersed spectrum focused along the opposite side of the Rowland torus, with resolution $E/\Delta E \simeq 60 - 1000$.

In the following discussion I focus solely on ACIS imaging data, which is used in the analyses presented in Chapter 3 and Chapter 4.

2.3.2 Pipeline processing

Chandra standard processing is applied to all ACIS data prior to dissemination to the observers, and proceeds through though a number of levels:

- *Level 0* processing involves transfer of the spacecraft telemetry to FITS files, and separation into discrete observations. Level 0 products in general are of no use to the end user.
- In *Level 1* processing the aspect solution, which determines the pointing of the telescope with time, is applied. If calibration improves after the pipeline has been run, it may beneficial to reprocess data from the Level 1 products stage.
- *Level 2* products are the usual starting point for science analysis. Level 2 processing includes temporal filtering on Good Time Intervals (GTI) in which the aspect solution is stable and instruments are functioning properly, cosmic ray rejection, and derivation of sky positions (i.e. RA and Dec) of events.
- *Verification and Validation* is then performed by scientists at the Chandra X-ray Center to ensure the successful processing of the dataset before the data are delivered to the observer.

Processing of level 2 eventlists into science products is carried out with the CIAO (Chandra Interactive Analysis of Observations) software. Detailed descriptions of the processing steps required to carry out all common analysis tasks with ACIS data are given in the CIAO Threads webpages at `http://cxc.harvard.edu/ciao/guides/acis_data.html`.

2.3.3 Data preparation

The first step in preparing ACIS data is to use the scripts provided to set the observation-specific bad pixel file which is used by many of the subsequent tasks. It is then necessary to check if calibration data has improved since the level 2 pipeline processing was completed and, if so, if reprocessing from the level 1 stage will improve the data quality. Possible reasons to do so include calibration updates to telescope geometry, CTI correction, and detector gain. In addition choices can be made about the randomisation of pixel and PHA values to avoid aliasing problems, removal of residual charge from cosmic ray detections, and removal of streaks resulting from readout flaws affecting some chips. Improvement of observation astrometry may also be gained at this stage if there is any known flaw in the aspect solution, or if extremely precise positions (~ 0.2 arcsec) are known for any sources in the field. Finally, eventlists should be filtered temporally to exclude periods of background flaring, and can optionally be filtered by energy to exclude ranges where the EA is low to increase the overall signal-to-noise.

2.3.4 Imaging analysis

The construction of images and exposure maps as detailed in §2.2.1 is fairly straightforward with Chandra ACIS data, and is accomplished with the CIAO tasks `dmcopy` and `mkexpmap`. `mkexpmap` relies on an aspect histogram, produced with `asphist`, and an instrument map, produced with `mkinstmap`. The instrument map may be calculated for a single energy or, more accurately, may take as input a spectrum by which to weight the instrument response.

Merging of eventlists from different observations is facilitated by the `dmmerge` tool, with the caveat that the resulting eventlist not be used for spectral analysis due to the loss of information necessary for the creation of accurate RMFs. The off-axis PSF is a complex function of energy and off-axis position; detailed models are can be constructed with the `ChaRT` tool to aid in analysis. The mean astrometric accuracy of the ACIS images is 0.6 arcsec.

Wavelet detection with `WAVDETECT`

Among the CIAO tools is the wavelet detection tool `WAVDETECT`, which can identify and characterise both point and diffuse sources to very low fluxes. Wavelets are oscillatory and scaleable functions which deviate from unity over a localised region and normalise to unity. Any function which is normalised to one and satisfies the condition

$$W_{\sigma,a}(x) = \frac{1}{\sigma}W(\frac{x-a}{\sigma}) \tag{2.3}$$

where a is a translation parameter and σ is a scaling parameter, is suitable. For source detection in images, `WAVDETECT` uses the Marr, or 'Mexican Hat', wavelet, derived from a two dimensional Gaussian:

$$W(\sigma_x, \sigma_y, x, y) = \frac{1}{2\pi\sigma_x\sigma_y}[2 - \frac{x^2}{\sigma_x^2} - \frac{y^2}{\sigma_y^2}]\, e^{-\frac{x^2}{2\sigma_x^2} - \frac{y^2}{2\sigma_y^2}} \tag{2.4}$$

Wavelet detection works through convolution of the wavelet function with the image, D, to produce a correlation image given by

$$C(\sigma_x, \sigma_y, x, y) = \int\int dx'\, dy'\, W(\sigma_x, \sigma_y, x - x', y - y')\, D(x', y') \equiv < W * D > \tag{2.5}$$

Since $\int W(\sigma_x, \sigma_y, x, y) = 0$, the correlation image will be zero provided the image is uniform at the scale of the wavelet., as can be seen by writing the correlation function in terms of the positive and negative areas of the wavelet, PW and NW:

$$C =< PW * D > + < NW * D > \tag{2.6}$$

However, if there is flux in excess of the local background at a given position, the first term will dominate and the correlation value will be positive.

The significance of the correlation, $S_{i,j}$, is determined through comparison with the probability of obtaining the correlation, $C_{i,j}$, given the number of background counts in the wavelet region, $n_{B_{i,j}}$:

$$S_{i,j} = \int_{C_{i,j}}^{\infty} dC\, p(C|n_{B_{i,j}}) \tag{2.7}$$

where $p(C|nB_{i,j})$ is the probability sampling distribution for $C_{i,j}$ given $n_{B_{i,j}}$. The sampling distribution does not have an analytic form given the background values likely to be observed with Chandra, and so has been determined through simulations and summarised in analytic fits where possible and a look-up table where it is not. An important user input to the `WAVDETECT` algorithm is the threshold significance, S_o, below which a correlation is judged a detection. The common choice for this value is the inverse of the number of pixels in the image, e.g. $\sim 10^{-6}$ for a 1024×1024 pixel field, which will lead, on average, to one false detection per field.

If $n_{B_{i,j}}$ is determined from the raw data, source counts will be spuriously included and artificially increase $S_{i,j}$ (i.e. *decrease* the significance of the detection). To avoid this, an iterative cleansing procedure is used to create a source-free background which is then used in the creation of final correlation images. Spatial variation of exposure over the chip will also lead to false detections wherever features in the exposure map occur at scales less than or equal to that of the wavelet (e.g. near detector edges or bad columns). Assuming the exposure variation causes a deficit in counts, ΔD, in the negative region of the wavelet, the effect can be written:

$$C =< PW * D > + < NW * (D - \Delta D) >= - < NW * \Delta D > \tag{2.8}$$

The correlation value is thus positive, and a false source detection may occur. A correction for this is made by calculating the value of the correlation which would be measured if the exposure was uniform over the wavelet scale, $C_{i,j_{corr}}$. Separating the correlation value into terms due to source (S) and background (B)

counts, it can be written

$$C_{i,j} =< W * S >_{i,j} + < W * (E\ B_{norm}) >_{i,j} \tag{2.9}$$

where E is the exposure and B_{norm} is the 'flat-fielded' background equal to $E_{i,j}B_{i,j}$. $C_{i,j_{corr}}$ is then given by

$$C_{i,j_{corr}} = C_{i,j} - < W * (E\ B_{norm}) >_{i,j} + E_{i,j} < W * B_{norm} >_{i,j} \tag{2.10}$$

`WAVDETECT` takes a series of wavelet scales, an image, an exposure map, and a calibration of the PSF across the field as input, as well as parameters, such as the significance threshold, which control the detection process. In the first phase, the `wtransform` task performs iterative cleaning to produce a background map and produces a final correlation map for each σ_x, σ_y scale pair. This detection phase is entirely independent of PSF properties. In the second phase, the `wrecon` task determines source properties. For each scale pair a smoothed flux image, F, is calculated such that

$$F_{i,j,} = \max\left(\frac{< PW * D >_{i,j}}{< PW * E >_{i,j}} - B_{i,j_{norm}}, 0\right) \tag{2.11}$$

For each source, the flux image for the scale pair most closely matching the PSF at i, j is used to determine a local maximum and the pixels for which this is a maximum. These pixels define the source cell. The list of cells is then examined in order of increasing scale size, and sources are added to a sourcelist only if no other source has been identified at smaller scales within the source cell. Each source in the resulting sourcelist is then characterised through measurements (e.g. of position, net counts, etc.) within the source cell using the original data, the smoothed background, and the input exposure map.

2.3.5 Spectral analysis

PHA source and background spectra and the RMF and ARF calibration files are created in CIAO with the tools `dmextract`, `mkrmf`, and `mkarf`. Specification of calibration files with which to construct the RMF - called FEFs (FITS Embedded Functions) - is based both on the position of the source and the condition of the detector at the time of observation, and is aided by the CIAO tool `acis_fef_lookup`.

There are two complications to basic spectral analysis as described in §2.2.2 when processing ACIS data. The first is that contamination of the detectors and/or associated filters has made the low energy QE a function of time, as added absorption occurs in the contaminating material. While the exact composition of the material is not yet known, models of its effects have been developed from calibration data which can be used to ameliorate most of the problem. Corrections for the excess absorption can be made either through inclusion in an ARF or as an extra model component during spectral fitting.

The second complication arises in spectral analysis of extended sources, which may extend over a region corresponding to multiple FEFs and significantly variable detector response. The ARF and RMF for such a region therefore must be a composite the calibration files appropriate to subregions within the region boundaries, weighted by the flux incident on each subregion. Tools for constructing these files are provided in `mkwrmf` and `mkwarf`.

2.4 XMM data

2.4.1 Instrument description

XMM-Newton comprises three sets of nested mirror shells each containing 58 thin mirrors, yielding the highest effective area of any X-ray telescope: ~ 4650 cm^2 in total at 1.5 keV. Angular resolution for XMM data is dominated by the mirror PSF, which has an on-axis FWHM of ~ 6" and a 50% encircled energy radius of ~ 15".

Each of XMM's three X-ray mirrors is equipped with an European Photon Imaging Camera (EPIC) CCD: there are two Metal Oxide Semi-conductor cameras (MOS1 and MOS2) and a p-n camera. The MOS cameras contain 7 front-illuminated chips, arranged to overlap and roughly follow the focal surface. The p-n camera is a single Silicon wafer, with 12 back-illuminated CCDs embedded. The field of view of both types of detector is roughly circular, with a diameter of ~ 30 arcmin. While both types of detector are sensitive over an energy band of 0.2 - 12 keV, the p-n camera has significantly higher quantum efficiency at all wavelengths, most markedly so at the soft and hard ends of the energy range. The final effective areas of the detectors are also dependent on filter selection. MOS and p-n pixel sizes are 1.1" and 4.1", respectively, but all EPIC data are resampled into 0.05" pixels by the pipeline processing. Both cameras allow imaging spectroscopy with energy resolution of E/ΔE $\sim 20 - 50$. The front-illuminated MOS camera is undergoing appreciable CTI degradation on-orbit, while this effect is negligible for the back-illuminated p-n chip. The p-n can also be read out extremely quickly, making it particularly useful for timing experiments.

XMM datasets contain data from all six science instruments on board: three EPIC CCDs, two (Reflection Grating Spectrometer (RGS) spectrometers, and the optical monitor (OM). Below I discuss only EPIC data, which was used in the analysis presented in Chapter 5 of this thesis.

2.4.2 Pipeline processing

XMM pipeline processing is extensive, and includes the reduction of the raw telemetered data into calibrated event lists as well as the processing of these lists into scientific data products such as images and source lists.

In the first stage, the raw data are examined, telescope attitude throughout the observation recorded in an orbit file, and Good Time Intervals (GTIs) identified in which the attitude is stable. For each CCD, additional GTIs specify when data have been successfully accumulated, and the positions of bad pixels are noted. The appropriate calibration data for the observation time and mode are selected, and the current electronic gain is calculated. The raw data are then processed: detector positions are converted to sky co-ordinates, detected charge pulse height (PHA) is converted to photon energy (PI), and events from separate CCDs are merged into a single eventlist. A final calibrated event list is produced for each instrument for each contiguous observation period, which lists for each detected event: time, position (in chip, detector, and sky coordinates), energy (in PHA and PI), pattern number, and event quality flag. p-n eventlists contain two further pattern related fields: pattern ID and pattern sequence. The pattern data are indicative of the shape of the event, equivalent to Chandra grades; the quality flag encodes various other event attributes, such as proximity to the edge of the FOV (see §2.4.3).

If no significant updates to the calibration are made after the completion of the pipeline processing there is no need to reproduce the calibrated event lists. The XMM Science Analysis System (SAS) task `cifbuild` determines the optimum set of calibration data based on the date of observation and the date of analysis and compares it with that included in the pipeline processing. Calibrated event lists form the foundation for further stages of pipeline processing, which generate images, exposure maps, and sourcelists for each observation. Though, in principle, these science products can also be used directly if the calibration has not changed, they are commonly and beneficially recreated by the user.

2.4.3 Data preparation

Several steps of processing are necessary to ready the calibrated event list for science analysis. If the observation contains more than one exposure, the exposure event lists must be merged prior to any further reductions. Using the `merge` task, datasets should be combined in chronological order, and corresponding orbit files must be also be joined. Data from different instruments (e.g. MOS 1 & MOS 2) cannot be usefully combined until after the creation of exposure maps, as exposure maps calculated for multi-instrument images will not be correct.

Several types of events should be filtered out of the calibrated event lists to improve data quality. In SAS, filtering is done with the `evselect` command, which takes as input an event list and a string of filtering expressions, and outputs a filtered event list. Filtering can be done destructively, so that the events not meeting the filter criteria are removed from the eventlist, or non-destructively, so that unwanted events are merely flagged as unusable. It is often desirable to destructively filter out certain types of events as a first step in data reduction, as this substantially reduces the file size and speeds further processing. The necessary levels of filtering are:

- *Energy filtering.* Much of the contamination of XMM images is in very low energy events. Filtering the data by the event energy (`PI` column) to exclude low energy events is common, and significantly reduces eventlist size and improves signal to noise. The p-n calibration team recommend a low energy cutoff value of 150 eV, and apply this to all p-n data in the pipeline. For imaging work, MOS counts above 300 eV should be valid. Filtering all eventlists to contain only events with energies between 200 eV and 15 keV (expression `(PI in 200:15000)`) reduces the number of counts in the pipeline processed lists by $\sim 10 - 20\%$. Further raising the lower limit to 300 eV when making images visibly improves the signal to noise.

- *Filtering by* `FLAG`. Each event is assigned an event quality flag, listed in the `FLAG` column. Highest quality events have a flag of zero, while non-zero values may indicate, e.g., coincidence with a bad pixel or identification as a cosmic ray. Sets of acceptable flag values have been produced by the XMM calibration team, and data should be filtered to include only these events (expressions `#XMMEA_EP` for p-n and `#XMMEA_EM` for MOS). More conservative filtering can include only FLAG=0 events (expression `(FLAG==0)`). The pipeline lists have already had the `#XMMEA_EP` filter applied. Application of the `#XMMEA_EM` filter reduces the number of pipeline processed MOS counts by $\sim 40\%$.

- *Filtering by* `PATTERN`. Equivalent to CCD grade, the event pattern can be used to discriminate valid X-ray events from invalid ones. Pattern values of 0 – 12 indicate charge spread over one to four pixels in ways typical of real X-ray events; higher values are more likely to indicate corrupted or spurious detections. For imaging, all events with pattern values higher than 12 should be removed from the data (expression `(PATTERN<=12)`). Only a few percent of MOS pipeline processed counts are removed by this filter, and $\sim 10\%$ of p-n counts. For imaging spectroscopy, good calibration of the p-n instrument is available only for events detected in one or two pixels, corresponding to pattern numbers 0 – 4, and so further filtering is needed (expression `(PATTERN<=4)`). Finally, p-n images in the ultrasoft XMM standard band (0.2 -0.5 keV) are constructed from only single events, as this excludes a good deal of detector noise.

- *Filtering periods of high background.* XMM EPIC data contain two types of background event - a flaring external background and a fairly stable internal background. The latter, due to high energy particles interacting with the detectors and detector housings, has a relatively low and constant 2 – 7 keV rate of a few $\times 10^{-3}$ counts cm^{-2} s^{-1} keV^{-1}. The former, due to 'soft' protons (i.e. $E_{proton} <$ a few × 100 keV) channelled by the mirrors onto the detectors, seriously degrades data quality during flaring periods, which must be filtered out. The recommended procedure for identifying periods of high background is the construction of a rate curve in the 10 – 15 keV band, where proton flaring is most evident. The quiescent rate can then be determined by eye, and a GTI file generated which excludes times at which the rate exceeds this level. Ideally, any hard X-ray sources which might vary should be removed prior to construction of this curve.

2.4.4 Imaging analysis

Images are created from the filtered event lists with the SAS `evselect` command, which bins events into pixels based on their spatial coordinates. Filtering expressions are used to restrict the energy band of the resulting image. Standard XMM bands are 0.2–0.5, 0.5–2, 2–4.5, 4.5–7.5, 7.5–12, and 0.2–12 keV.

Exposure maps are created with the SAS `eexpmap` task. Unlike CIAO, SAS has no utility to create maps valid for polychromatic source spectra; `eexpmap` performs the exposure calculations for a single energy halfway between specified lower and upper energies. As cosmic sources are generally not monochromatic, this can lead to significant errors in derived broadband fluxes (see Figure 2.5). To avoid this one should ideally create a number of exposure maps in narrower bands over which the response is roughly uniform and perform an appropriately weighted sum by hand.

The output of `eexpmap` is a map in seconds; dividing an image by an exposure map gives a 'flattened' image in units of count rate. To obtain meaningful fluxes, a further conversion from counts s^{-1} to erg s^{-1} cm^{-2} is needed. In SAS this conversion is done with Energy Conversion Factors (ECFs), which are provided for standard bands by the XMM Survey Science Centre (SSC-LUX-TN-0059, Issue 3.0). For non-standard bands, ECFs must be calculated using the X-ray spectral analysis package `XSPEC`, which computes the expected count rate and flux from a given spectral model, RMF, and ARF. Standard RMFs for each detector are available from the XMM-SCC, while observation specific ARFs must be extracted from images constructed from the dataset in use. To maintain consistency with the standard ECFs, p-n images should include only patterns 0–4 and MOS images only patterns 0–12. The assumed spectral model for the calculations is a powerlaw with photon index, $\gamma = 1.7$, and photoelectric absorption by a Galactic column of 3×10^{20} atoms cm^{-2}. The `XSPEC fakeit` task will convolve the model with the instrument response, and the `flux` and `countrate` commands will return the flux and countrate in given bands, which are divided to give an ECF in units of 10^{11} erg cm^{-2} counts^{-1}.

Source detection with the XMM-SAS `edetect` chain

The standard XMM pipeline source detection is multi-phase, using a sliding-box technique to identify sources and maximum likelihood fitting to characterise them. The algorithms are run on multiple images simultaneously, and so combine information in different bands.

For each detector, a mask is constructed with the SAS task `emask` to exclude areas where the exposure is below or spatial variation is above given thresholds. A sliding box algorithm (SAS `eboxdetect`) is then used to search the regions within the mask, identifying significant departures from the local background. These 'sources' are then removed and the resulting image smoothed with a spline-fitting method (SAS `esplinefit`) to produce a background map. Deviations from this background map are identified in a second, more sensitive, sliding box detection. The task `emldetect` (Cruddace et al. 1988) is then used to run simultaneous maximum likelihood PSF fits to the source counts in each input image, and provide measures of source properties for sources above a given likelihood threshold. Detection likelihoods are defined as equivalent likelihoods, L_2, which are related to the probability, p, of the source resulting from random Poissionian fluctuation, by $L_2 = -\ln p$. Finally, the source lists from each instrument are merged on the basis of positional coincidence, using `srcmatch`.

As noted by Watson et al. (2003), several factors can cause this detection chain to return unreliable results:

- Errors in the PSF model can cause detection of spurious sources around bright or extended sources.
- Uncalibrated brightening at the edges of the EPIC chips can lead to spurious source detection.
- Poor determination of the background level by `splinefit` can lead to large numbers of spurious sources.

In Chapter 5, I describe the use of `WAVDETECT` with XMM data to avoid these problems in a deep survey field.

2.4.5 Spectral analysis

PHA spectra are extracted with the `evselect` task, which takes as input an eventlist and spatial (and other) filtering expressions, and outputs a spectrum properly formatted for use in `XSPEC` or other X-ray fitting programs. As noted above (see §2.4.3), due to the current state of EPIC spectral calibrations, p-n spectra should be constructed only of FLAG = 0 and PATTERN ≤ 4 events, while all 'good' MOS events with PATTERN ≤ 12 can be included. Background spectra are also extracted with `evselect`, and should be taken from source-free regions of the detector most similar to the source region. For MOS images annular background regions are suggested, while p-n attributes are most similar along readout rows. Given source and background regions, the `eregionanalyse` task optimises the source extraction radius by using the EPIC PSF model to estimate source and background counts in the aperture and maximising signal to noise. Response matrices are generated with the `arfgen` and `rmfgen` tasks.

CHAPTER 3

The ELAIS Deep X-ray Survey

The resolution of the cosmic X-ray background was one of the earliest and most significant achievements of the current generation of X-ray telescopes. In this chapter I describe work done in collaboration on the ELAIS Deep X-ray Survey (EDXS), which was designed to identify the constituents of the XRB and to study their relation to populations detected in other wavebands. I introduce the major questions facing early Chandra and XMM surveys in §3.1 and describe the data comprising the EDXS and its basic reduction in §3.2. In §3.3, I discuss results from the full sample of EDXS sources, with an emphasis on the characterisation of the components of the XRB. I present detailed analysis of individual EXDS sources in §3.4, and conclude with a review of EDXS results in §3.5 and a summary of open questions in §3.6.

The work presented here is collaborative. My primary roles within the EDXS collaboration were leading the X-ray spectral analysis and assisting with follow-up spectroscopy of EDXS sources. As noted in the text, James Manners completed the the basic X-ray reductions presented in §3.2.1 and the source count calculations at the start of §3.3.1 (Manners 2002, Manners et al. 2003). The identification of optical counterparts described at the beginning of §3.2.3 was done by Eduardo Gonzalez-Solares (Gonzalez-Solares 2003, Gonzalez-Solares et al. 2004). Chris Willott acquired, reduced, and analysed the optical and IR spectra described in §3.4.1 (Willott et al. 2003, 2004). All other work described in this Chapter is my own.

3.1 Introduction

As discussed in §1.2, the origin of the bright, diffuse, cosmic X-ray background was a major open question in high energy astrophysics from the advent of the field. By the late 1990's, the existence of a significant cosmological hot gas component had been ruled out by the lack of a Compton distortion in the cosmic microwave background spectrum (Mather et al. 1990). However, the discrete sources — mostly luminous quasars — known to comprise the majority of the XRB below 2 keV were too soft to account for the background emission at higher energies. At its 30 keV peak, the spectrum of the XRB was observed to be a full order of magnitude above the estimated quasar contribution. XRB synthesis models successfully reproduced this peak with the superposed emission of a large population of obscured AGN, which are largely invisible in the soft X-ray band due to photoelectric absorption (e.g. Comastri et al. 1995, Gilli et al. 2001).

Chandra and XMM were designed to provide sharp resolution, good positional accuracy, and high sensitivity up to 10 keV, and were expected to resolve the XRB and allow investigation of the obscured AGN population. The survey presented in this Chapter was one of several deep 'blank field' surveys awarded substantial observing time early in the Chandra and XMM missions to address a number of basic questions about the X-ray emitting objects in the Universe.

How much of the background emission is resolved? The deepest surveys with instruments prior to Chandra and XMM resolved a substantial fraction of the XRB and characterised the AGN population that comprised it well enough to extrapolate its contribution at fainter fluxes. The deepest ROSAT surveys detected roughly 1,000 X-ray emitting objects per square degree to a limiting flux of $S_{(0.5-2\ \mathrm{keV})} \simeq 10^{-16}$ erg s^{-1} cm^{-2}, directly resolving 70-80% of the soft XRB (Hasinger et al. 1998). Less sensitive surveys in the 2-10 keV band with ASCA and BeppoSAX suffered from source confusion but were able to resolve $\sim$ 30% of the background at these energies (Georgantopoulos et al. 1997). Models of the luminosity function and its evolution based on these data predicted that active galaxies could contribute 30–90% and 48–80% of the soft and hard X-ray backgrounds, respectively (Shanks et al. 1991, Boyle et al. 1993, 1998). Determining the source counts of X-ray objects at faint fluxes and their contribution to the XRB was the most basic aim of the early deep surveys with Chandra and XMM.

What are the components of the XRB? Though most of the sources in the ROSAT and ASCA surveys were optically identified as unobscured quasars which could not contribute the majority of the XRB flux, these surveys did provide evidence of another type of source which might dominate the hard XRB. A small fraction of X-ray sources were optically identified as galaxies, and this fraction was seen to increase toward faint X-ray fluxes (Georgantopoulos et al. 1997) and in hard X-ray surveys (Griffiths et al. 2000). Both the positive correlation of the $B < 23$ galaxy population with the unresolved XRB (Roche et al. 1995, Almaini et al. 1997) and the indication of a harder X-ray spectrum in sources with galactic morphology (Almaini et al. 1996) further suggested that the galaxy population might contribute significantly to the XRB flux. The large positional errors of ASCA sources and of faint ROSAT sources ($\lesssim 25''$) hindered the direct study of source counterparts toward faint X-ray and optical fluxes. Unambiguous identification of the optical counterparts of X-ray sources was a second major goal of early Chandra surveys, which could achieve positional accuracy of $0.5 - 2.5''$ across the ACIS-I field of view.

Is there a large population of obscured AGN? Successful XRB synthesis models which account for the XRB with populations of variously obscured AGN were consistent with the results of deep surveys with ROSAT, ASCA, Einstein, and GINGA (Comastri et al. 1995, Gilli et al. 2001). Because sensitive, high-resolution surveys were unavailable in the hard band, however, the demographics of the obscured population were poorly constrained. While the emergence of hard X-ray sources with galactic morphology toward faint fluxes provided possible evidence for a sizable obscured AGN population (Almaini et al. 1997, McHardy et al. 1998), the X-ray emission mechanism in these sources was unknown and could have been powered by stellar processes in starburst galaxies instead of or as well as by accretion onto an active nucleus (Boyle et al. 1995). Directly testing the synthesis models was another major motivation behind early surveys with Chandra and XMM. The moderate resolution pulse height spectroscopy these surveys provide for large samples of objects can effectively discriminate between X-ray emission processes and estimate obscuring columns in Type II AGN.

3.2 The ELAIS Deep X-ray Survey

The ELAIS Deep X-ray Survey (EDXS) consists of Chandra exposures of two 'blank field' regions and was designed to investigate the components of the XRB and their relation to populations in other wavebands. The two fields comprising the survey were originally selected as part of the European Large Area ISO Survey (ELAIS), which covered a total of 12 square degrees at 15 and 90 μm and smaller areas at 6.7 and 175 μm (Oliver et al. 2000). The mainly extragalactic scientific goals of the IR survey required that the regions be at high Ecliptic latitude, contain minimal galactic cirrus and include no bright IRAS sources. The low galactic column made these fields ideal for X-ray survey work as well. The N1 region centred at 16:10:01 +54:30:36 and the N2 field at 16:36:58 +41:15:43 were adopted for the EDXS.

The EDXS was planned to be among the deepest of the early surveys, with 75 ks Chandra exposures of each field and an additional 150 ks XMM exposure of N2. Unfortunately, the actual XMM orbit was found to differ from pre-launch predictions such that the maximum possible contiguous observation of the N2 field is only ~ 10 ks. As the operational overhead involved in accumulating the originally planned integration in 15 separate pointings would have been excessive, another field was targeted instead (see Chapter 5). The EDXS is therefore of only moderate depth, compared with some contemporary surveys (e.g. Alexander et al. 2003, Rosati et al. 2002).

The survey's major strength is its uniquely deep multiwavelength coverage: in addition to multiband data at IR, radio, and optical wavelengths in both fields, N2 has been mapped with SCUBA to 8 mJy at 850μm. Table 3.1 lists the deep broad-band imaging accumulated in each region. In addition, the analysis of two fields helps to mitigate the effects of cosmic variance, which is observed to alter source counts by up to 30% at bright fluxes, and up to 5% for fainter sources (Tozzi et al. 2001). Finally, the depth of the EDXS is sufficient to probe sources with fluxes of $\sim 10^{-15} - 10^{-14}$ erg s^{-1} cm^{-2} which are near to the break in

Instrument	Band	N1	N2
Chandra	0.5 – 10 keV	√	√
WFC	U (3580Å)	√	√
	g' (4850Å)	√	√
	r' (6240Å)	√	√
	i' (7740Å)	√	√
	Z (8760Å)	√	√
WHT/PFC	R (6370Å)		√
	I (8100Å)		√
CIRSI	J (1.2 μm)	√	√
	H (1.6 μm)	√	√
INGRID	K (2.2 μm)	√	√
UKIRT UFTI/UIST	J (1.2 μm)		√
	H (1.6 μm)		√
	K (2.2 μm)		√
ISO	6.7μm		√
	15μm	√	√
	90μm	√	√
	175μm	√	√
SCUBA	850μm		√

Table 3.1: *Data available in the ELAIS N1 and N2 survey fields.*

the number counts distribution and therefore comprise the bulk of the XRB.

3.2.1 X-ray source detection

The Chandra data were taken with the ACIS imaging array, which, as noted in §2.3 is comprised of a grid of 4 front-illuminated CCDs and has a field of view of $16.9' \times 16.9'$ on a side. Though two chips in the neighbouring spectroscopic array were also active during the observations, the point spread function is significantly degraded at such large off-axis angles and the data from these chips have been disregarded. Initial reduction of the observations was done by James Manners, whose Edinburgh thesis is partly based on these data (Manners 2002).

The raw ACIS event lists were filtered to exclude periods of high background as identified from lightcurves of the background regions. The final usable exposures of N1 and N2 were 71.5 ks and 73.4 ks, respectively. Soft, hard, and full band images were constructed from the background-filtered lists by further filtering by pulse height energy into 0.5 – 2, 2 – 8, and 0.5 – 8 keV bands and then binning into $0.984''$ pixels. Exposure maps were computed which account for the spatially varying quantum efficiency of the chips, mirror vignetting, and the dither of the field of view throughout the observations. We have assumed a power-law spectrum with a photon index γ = 1.7, which is typical of unobscured AGN. Fully reduced 0.5 – 8 keV images of N1 and N2 are shown in Figure 3.1.

Sources were detected using the CIAO WAVDETECT software (Freeman et al. 2002), a multi-scale wavelet detection algorithm which is discussed fully in §2.3.4. 'Mexican Hat' wavelets of scale i =

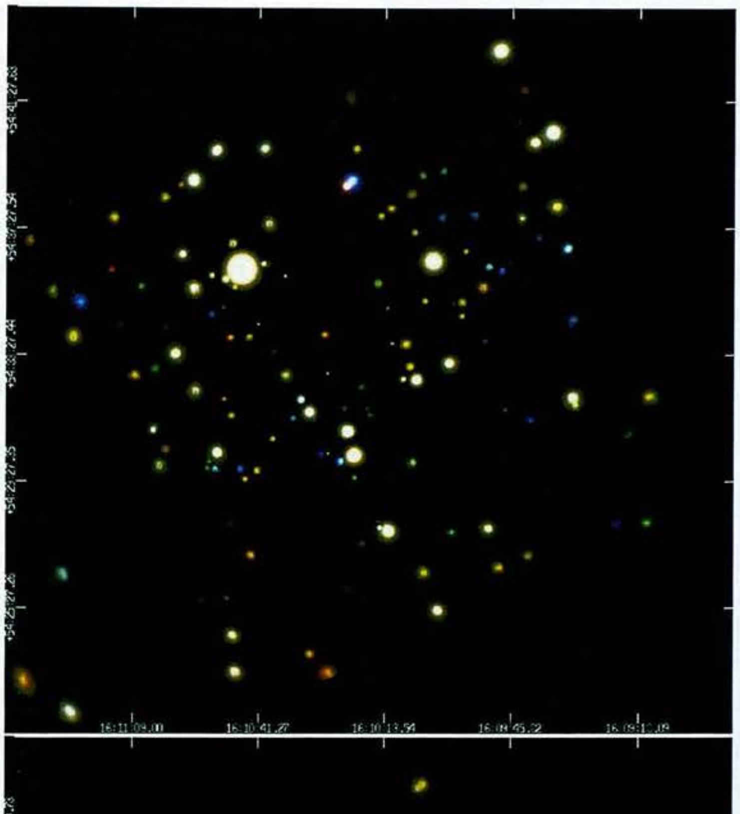

Figure 3.1: *Adaptively smoothed 'true-colour' images of the N1 (top) and N2 (bottom) fields, constructed from the soft-band (red), full-band (green), and hard-band (blue) X-ray data. Figure courtesy of J. Manners.*

$\sqrt{2}, 2, 4, 4\sqrt{2}, 8, 8\sqrt{2}, 16, 16\sqrt{2}$, and 32 pixels were used; $\sqrt{2}i$ is the zero-crossing point. The minimum scale is chosen to enclose roughly 90% of the on-axis PSF and larger scales are well matched to off-axis and/or extended sources. With the source detection threshold set at the inverse of the number of pixels — 9.5×10^{-7} for the EDXS images — we expect a single false detection per field. Simulations suggest that 98.5%-99.5% of sources above our flux limit are successfully detected (Manners et al. 2003).

In the full (0.5 – 8.0 keV), soft (0.5 – 2.0 keV), and hard (2.0 – 8.0 keV) bands, limiting sensitivities were 1.1×10^{-15}, 4.6×10^{-16}, and 2.2×10^{-15} erg s^{-1} cm^{-2}, respectively. 225 sources were detected at the 3σ level in the full band, 127 in the N1 region and 98 in the N2 region. 2 sources in N1 and 3 sources in N2 were detected only in the soft band, while 1 source in N1 and 2 sources in N2 were detected only in the hard band. In total, then, there are 233 distinct point sources in the EDXS fields. In addition, two faint, soft X-ray clusters were detected in N2. The survey catalogue is presented in (Manners et al. 2003).

3.2.2 X-ray spectral analysis

Hardness ratios

I calculated broad band X-ray hardness ratios for each source, defined as $HR = \frac{(H-S)}{(H+S)}$, where H and S are the background-subtracted source counts in the hard (2.0 – 8.0 keV) and soft (0.5 – 2.0 keV) bands, respectively. Net source counts were extracted from the exposure corrected hard and soft band images within circular regions centred on the WAVDETECT positions. The apertures were scaled to mimic the degradation of the Chandra PSF with off-axis angle in each band and had minimum radii of 10 pixels. Background counts were extracted from source-free regions in annuli around each source and subtracted. The net, source, and background counts thus obtained were consistent within the errors with those reported by WAVDETECT. Background subtraction and exposure correction have increasingly significant effects on the calculated HR toward faint fluxes, as shown in Figure 3.2. If background subtraction is not performed, the intrinsically hard background creates a bias toward harder values which is greater for fainter sources. Conversely, hardness ratios calculated without exposure correction are biased toward softer values, as the ACIS effective area is higher in the soft band. These corrections are not included in the analysis of some contemporary surveys (e.g., Rosati et al. 2002), leading to a steeper observed trend toward harder values with decreasing flux.

Pulse height spectra

Imaging spectroscopy is possible for the brighter sources in our field; I have analysed the spectra of 39 sources with more than 100 counts. Pulse height spectra were extracted from within the WAVDETECT position ellipse for each source, and response matrices and auxiliary response files were constructed for each position. Where sources were split between chip nodes, the response matrix is that for the node containing the majority of the flux. As the sources were small and bright, the background contribution was expected to be minimal and no background spectra were extracted. Spectra were binned to at least 15 counts per channel, and fit to an absorbed powerlaw at zero redshift. As absorbing column, N_H, and energy index, α, could not be simultaneously constrained for most sources, a best fit N_H was found for an index fixed at

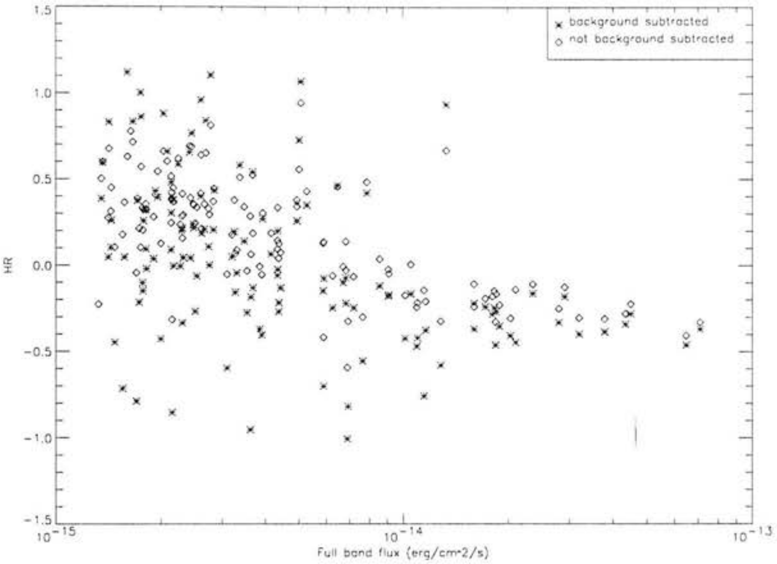

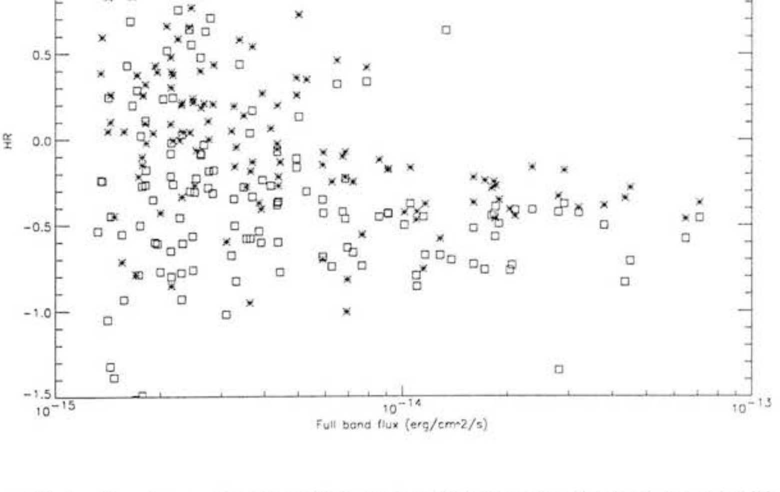

Figure 3.2: *The effect of background subtraction and exposure correction on computed hardness ratios. top) Full band (0.5 – 8.0 keV) X-ray flux vs. HR calculated with and without background subtraction, for sources in N1. bottom) Full band X-ray flux vs. HR calculated with and without exposure correction, for sources in N1.*

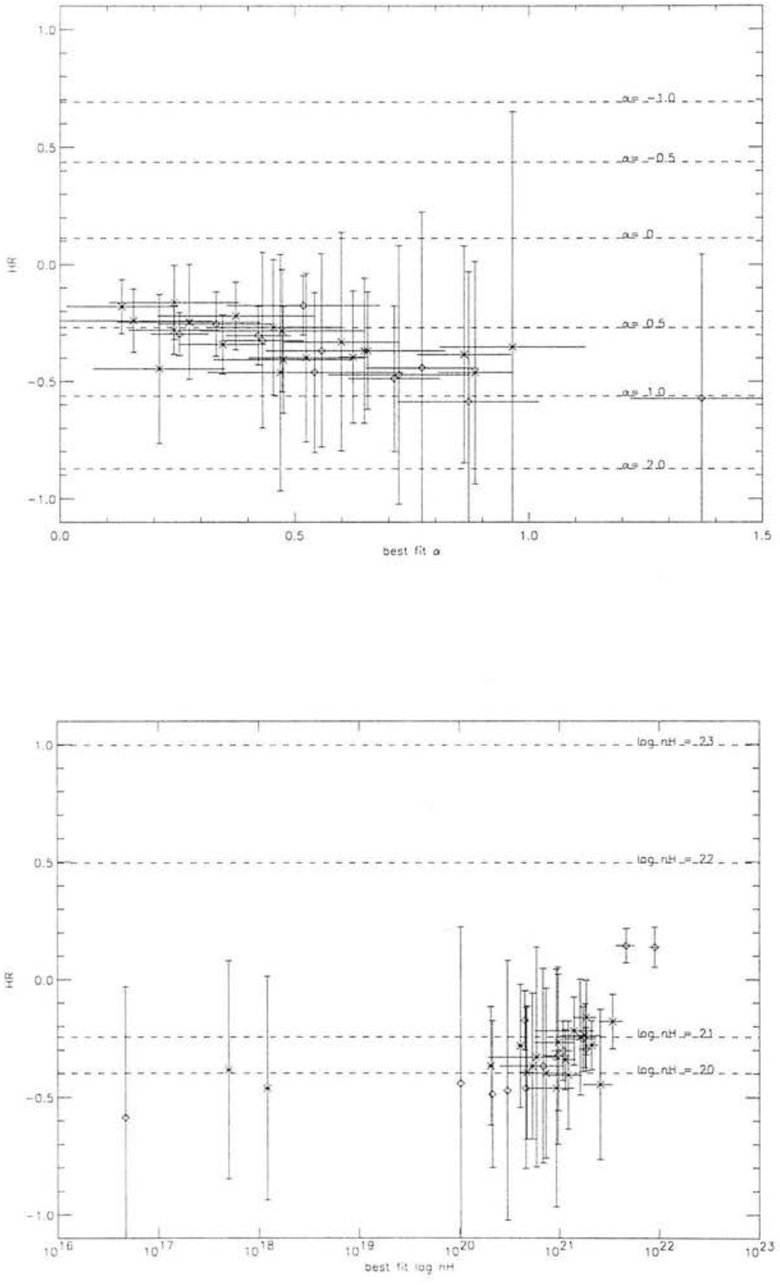

Figure 3.3: *The consistency of X-ray spectral analysis via broad-band hardness ratio and more detailed imaging spectroscopy. top) Energy index, α, obtained from fits to pulse height spectra of 39 bright EDXS sources versus hardness ratio, with the expected hardness values for various α overlaid in dashed lines. The model for fitting and for generating the dashed lines was an absorbed powerlaw at zero redshift with galactic absorption. bottom) As above, absorbing column from spectral fitting versus hardness ratio, with expected values for various columns overlaid in dashed lines. The model is an absorbed powerlaw at zero redshift with $\alpha = 0.7$.*

$\alpha = 0.7$, and a best fit energy index was found for absorption fixed at the Galactic value ($N_H = 1.07 \times 10^{23}$ cm^{-2}). The values found are, in general, consistent with the hardness ratio analysis, as shown in Figure 3.3.

3.2.3 Optical identification

The observation and identification of optical counterparts of the EDXS sources comprise Chapters 8 and 10, respectively, of a PhD thesis by Eduardo Gonzales-Solares (IAC; Gonzalez-Solares 2003). Optical counterparts to the EDXS sources were identified primarily in r'-band images with a limiting magnitudes of ~ 25. Optical sources were detected using the SExtractor algorithm (Bertin and Arnouts 1996) and then matched to the X-ray sourcelist. The matching procedure accounted for positional uncertainties ranging from 0.5 - 2.5$''$ over the field due to the growth of the Chandra PSF with off-axis angle. Of the 225 X-ray sources, 17 ($\sim$ 8%) fall outside the field of view of the r'-band images or are coincident with chip gaps or other image defects. An additional 50 sources ($\sim$ 22%) are below the photometric limit of 25.2. The remaining $\sim$70% of the X-ray sources have identified r'-band counterparts, examples of which are shown in Figure 3.4. A maximum of 5% chance associations is expected. A full description of the identification process is given in Gonzalez-Solares et al. (2004).

Source optical morphologies are classified according to agreement with a stellar point spread function, as quantified in the SExtractor 'stellarity' parameter, CLASS STAR. The output of a neural network classifier, the value of this parameter ranges from 0.0 for significantly extended sources to 1.0 for those with perfectly stellar PSFs. For the EDXS sample, we have divided sources with quasar-like and galaxy-like counterparts at CLASS STAR $= 0.7$. In practice, as seen in Figure 3.5, morphological classification is increasingly ambiguous for fainter sources with lower signal to noise and cannot be considered reliable near to the image limiting magnitude. Gonzalez-Solares (2003) has performed a detailed analysis of the reliability of the CLASS STAR parameter with flux, which indicates reasonable reliability to a r'-band magnitude limit of 24. I therefore treat sources with $r' > 24$ as morphologically unknown.

3.2.4 Optical spectroscopic identification

I obtained optical spectra of a subset of EDXS sources with the multi-object spectrograph on the Calar Alto 3.5m telescope in Almeria, Spain. Four slit masks were machined to allow observation of 57 sources in N1 and 53 sources in N2 in two series of exposures in each field. The slits were positioned on the optical counterparts of the Chandra sources; for sources with no optical counterpart, the X-ray position was used. The total integration time on each source was $\sim$ 130 minutes.

Initial reductions required manual identification of the source and background extraction regions for each slit, and the range in the dispersion direction for which they were valid. Using the IRAF task `apall`, I defined apertures at a given dispersion position. The position of the spectrum along the dispersion axis was then traced and fit interactively over the appropriate range. Finally, a sky spectrum and sky-subtracted object spectrum were extracted for each source. Wavelength calibration was done with the tasks `identify` and `dispcorr` which allowed determination of the dispersion solution for each slit from comparison lamp

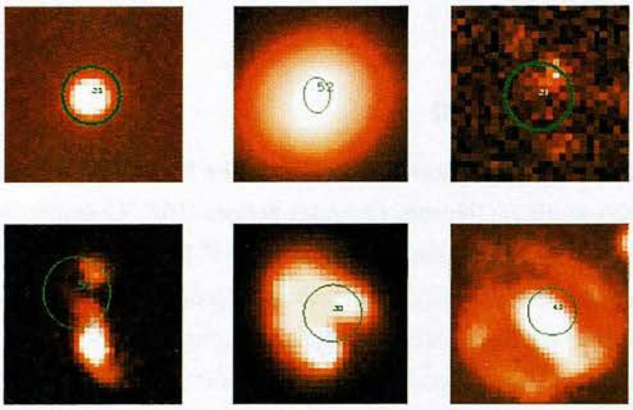

Figure 3.4: *Optical counterparts to EDXS sources. Top row, from left: r'- band postage stamps of a bright quasar, a bright early-type galaxy, and an optically faint source. As discussed in §3.3.1, these three basic source types comprise the majority of the 2 – 8 keV XRB. Bottom row: r'- band postage stamps of sources with merging or disturbed morphologies, which are fairly common among EDXS counterparts.*

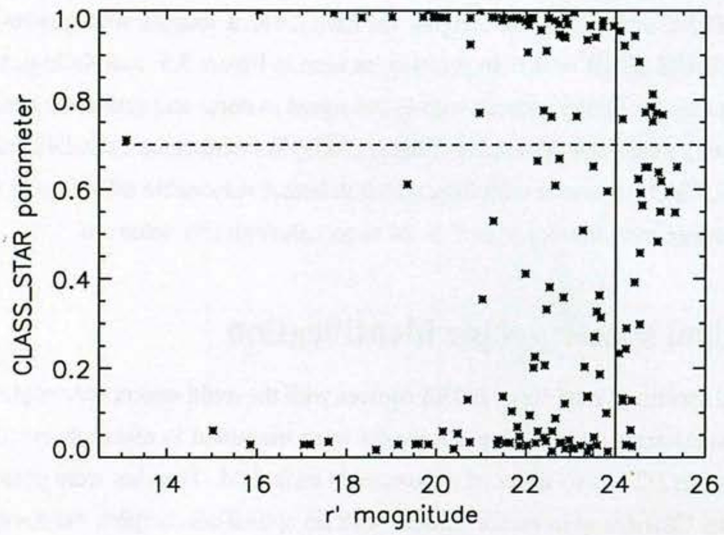

Figure 3.5: *The diminishing reliability of the SExtractor CLASS STAR parameter with object magnitude. The CLASS STAR parameter, ranging from 0 for extended sources to 1 for unresolved sources, versus r'-band magnitude for EDXS counterparts identified in an r'- band image with a limiting magnitude of ~ 25. I adopt a limit for classification of $r' < 24$ (solid line), and choose 0.7 (dashed line) as the division between point-like and galaxy-like morphologies.*

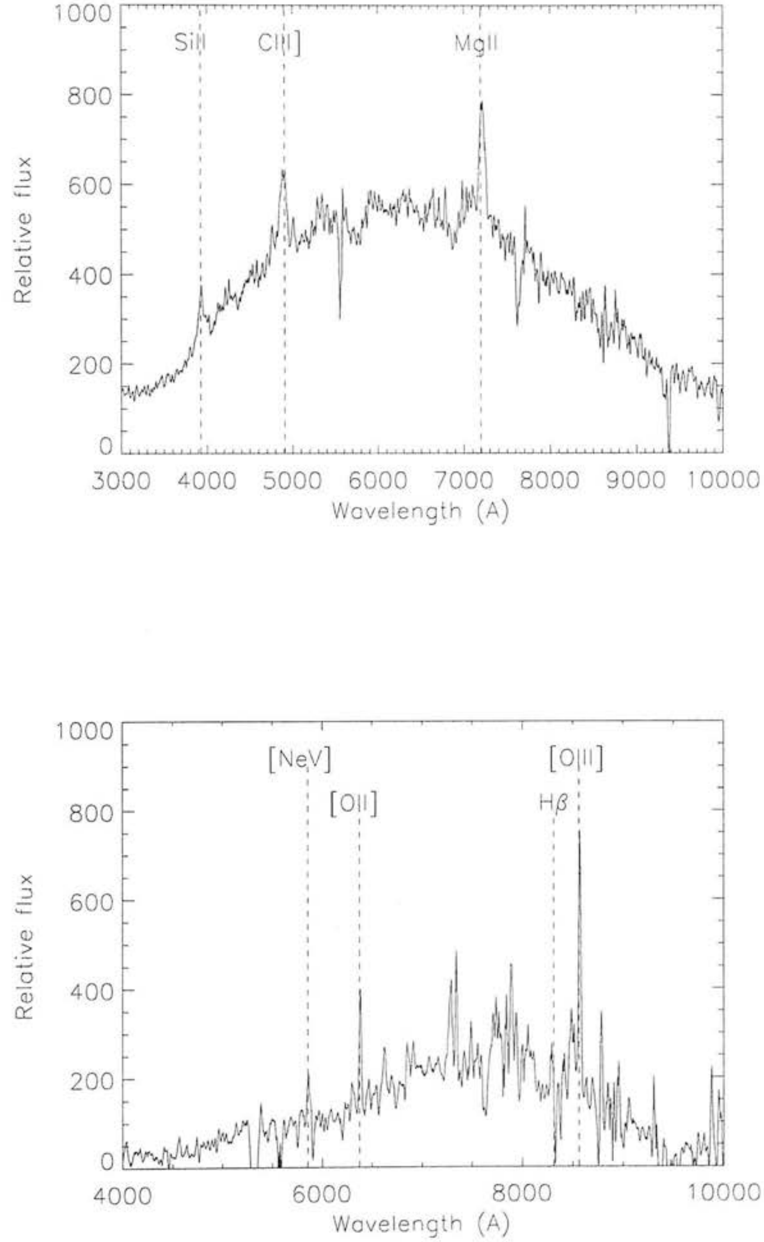

Figure 3.6: *Top) Optical spectrum of N1:75, a broad-line QSO at* $z = 1.57$ *observed with MOSCA. Bottom) Optical spectrum of N2:79, a narrow-line AGN at* $z = 0.71$ *observed with MOSCA.*

Source	z	r'	HR	Instrument
N1:04	1.06	21.54	-0.24	MOSCA
N1:19	2.70	21.51	-0.25	MOSCA
N1:48	1.92	19.98	-0.38	MOSCA
N1:67	0.89	21.99	-0.33	MOSCA
N1:69	0.27	18.75	-0.37	MOSCA
N1:75	1.57	20.79	-0.35	MOSCA
N1:81	2.02	22.16	-0.82	MOSCA
N2:04	1.62	22.66	+0.04	MOSCA
N2:06	2.04	< 25.2	-0.51	MOSCA
N2:07	2.40	22.22	-0.17	MOSCA
N2:15	1.56	24.82	-0.18	Subaru
N2:21	1.57	25.19	-0.51	Subaru
N2:25	2.61	23.07	0.20	ISIS
N2:28	~ 1.1	25.81	-0.14	Subaru
N2:32	1.00	22.59	0.96	ISIS
N2:34	2.09	< 25.2	-0.26	ISIS
N2:35	2.74	24.72	0.16	GMOS
N2:41	1.93	21.83	-0.59	MOSCA
N2:47	0.88	23.43	-0.45	Subaru
N2:54	1.45	20.93	-0.30	MOSCA
N2:56	2.11	21.30	-0.47	MOSCA
N2:60	1.50	23.82	-0.58	Subaru
N2:61	1.39	24.08	-0.39	Subaru
N2:68	2.22	24.02	-0.56	ISIS
N2:79	0.71	22.16	+0.72	MOSCA
N2:87	2.67	22.07	-0.10	MOSCA

Table 3.2: *Spectroscopically identified EDXS sources.*

exposures, and application of the solution to the object data.

Reduction of the data was complicated by uncharacterised distortions in both spatial and spectral coordinates from slit to slit, and by overlap of adjacent spectra. Application of aperture traces determined from bright objects to fainter objects was therefore not possible, and only spectra of sources with clearly detected continua — of which there were 56 ranging in r' magnitude down to ~ 22.5 — were extracted and examined. Of these sources, 14 had spectra of sufficient quality to provide redshift information. These sources are listed in Table 3.2.

Also listed in Table 3.2 are redshifts we have obtained of selected objects with other optical and near-IR instruments. Spectroscopy of small samples of optically red sources and optically faint quasars within the EDXS survey is presented in (Willott et al. 2003) and (Willott et al. 2004), respectively. Including 4 objects identified as stars, then, there are spectroscopic identifications of only 29 out of 233 ($\sim 12\%$) of the EDXS sources.

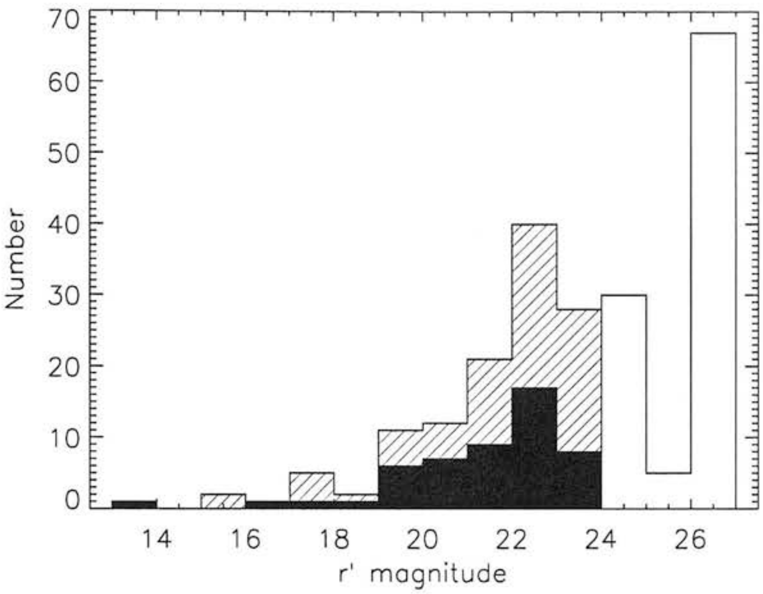

Figure 3.7: *Distribution of optical counterparts of EDXS sources. Source histograms with r'- band magnitude are shown for 51 point-like sources (black), 72 extended sources (lined), and 102 sources with unknown morphology (white). In the latter category are 35 optically faint ($r' > 24$) sources with possibly extended morphology and 50 sources not detected in the r'- band.*

3.3 The EDXS sample

3.3.1 The components of the XRB

As reported in Manners et al. (2003), at least half of the 2 – 8 keV background is resolved in EDXS sources at fluxes $S_{2-8\ \mathrm{keV}} < 10^{-13}$ erg s^{-1} cm^{-2} and greater than the 2.2×10^{-15} erg s^{-1} cm^{-2} flux limit. The resolved flux is 50% of the background measured with Beppo-Sax by (Vecchi et al. 1999) and 64% of the background measured with ASCA by (Ueda et al. 1999). Combining the contribution from the EDXS sources with that from sources at $S_{2-8\ \mathrm{keV}} > 10^{-13}$ detected with ASCA (della Ceca et al. 1999) and that from sources with 6×10^{-16} erg s^{-1} cm^{-2} $< S_{2-8\ \mathrm{keV}} < 2.2 \times 10^{-15}$ erg s^{-1} cm^{-2} detected in the Chandra Deep Field North 1 Ms survey (Brandt et al. 2001a), the resolved fractions are 66% and 84%, respectively. As illustrated in Figure 3.4, we find the sources comprising the XRB to be identified optically as unobscured quasars, bright galaxies, and optically faint objects. Histograms of the number of sources with unresolved, extended, and morphologically ambiguous optical counterparts as determined from the CLASS STAR parameter are plotted in Figure 3.7 versus r'-band magnitude. Of the 225 full-band EDXS sources, 51 (23%) are optically unresolved, 72 (32%) are resolved, 35 (15%) are ambiguously resolved with $r' > 24$, and 67 (30%) are unidentified in the r'-band images. Sources with point-like optical counterparts dominate at bright optical fluxes. The majority of these sources are unobscured Type I quasars which would have been selected in optical and soft X-ray surveys. Toward fainter r'-band magnitudes, the galactic and

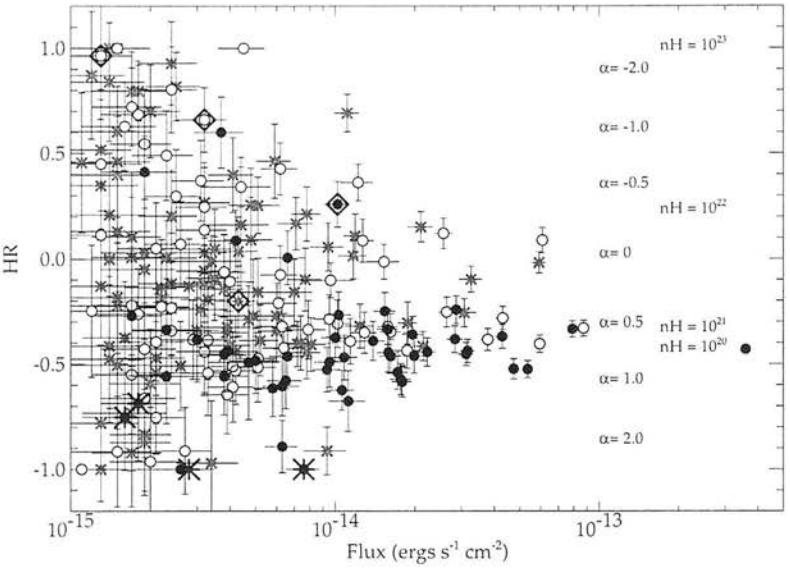

Figure 3.8: *Full band X-ray flux versus hardness ratio for EDXS sources. Symbols indicate source morphology for point-like sources (filled circles) extended sources (open circles), and sources of unknown morphology (crosses). The hardness value expected from from absorbed power-law spectra with various values of energy index, α, and absorbing column, N_H, are shown at right. The values of α are for a $z = 0$ AGN with Galactic absorption, while the values of N_H are for a $z = 0$ AGN with $\alpha = 0.7$. The four soft objects indicated with large crosses are spectroscopically confirmed stars. The four objects denoted with large diamonds are spectroscopically confirmed Type II AGN. A binned version of this figure is shown in 3.9.*

optically faint populations become far more prevalent, suggesting the emergence of a large new population of X-ray source.

3.3.2 The obscured AGN population

The X-ray spectral properties of the sources indicate that these optically faint sources are likely to comprise the large population of obscured AGN predicted by XRB synthesis models. Hardness ratios are plotted against full band X-ray flux in Figures 3.8 and 3.9. As noted by contemporary surveys (Mushotsky et al. 2000, Giacconi et al. 2001, Hasinger et al. 2001, Hornschemeier et al. 2000), harder sources are seen at fainter X-ray fluxes, signalling the emergence of the harder population comprising the majority of the XRB. In typical AGN powerlaw spectra, hard counts can be boosted over soft counts by either (i) a decrease in the underlying powerlaw index or (ii) an increase the absorbing column. Evidence from XMM surveys suggest that the spectral variation observed is due to the latter (Rosati et al. 2002). Assuming an $\alpha = 0.7$ power-law spectra typical of AGN, the range of hardnesses observed in the EDXS sample suggests absorbing columns of up to $N_H \sim 10^{23}$ atoms cm^{-2} at zero redshift. As the apparent absorption column in the X-ray band scales as $(1+z)^{2.6}$, actual columns in higher redshift sources will be significantly higher.

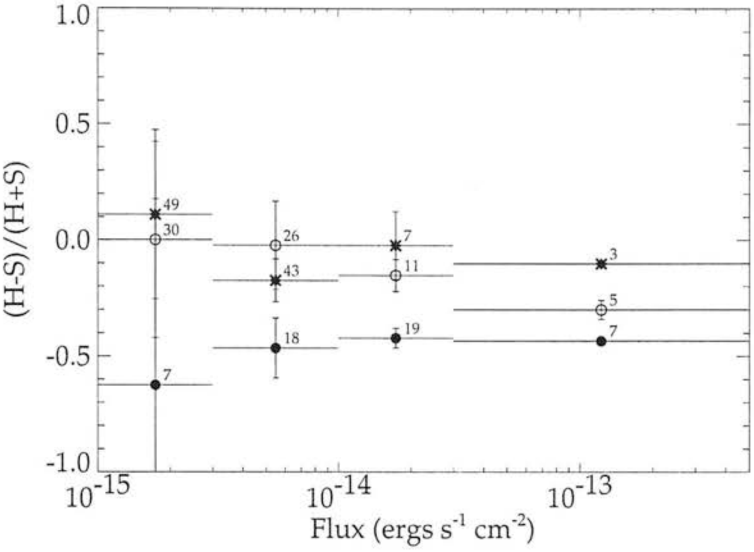

Figure 3.9: *Error-weighted average hardness ratio for EDXS sources sorted by morphology and binned by flux. As in Figure 3.8, filled circles indicate point-like sources, open circles indicate galactic morphology, and crosses indicate faint sources of unknown morphology. The number of sources in each bin are indicated to the right of the data point, and the error bars indicate the variance within the bin.*

The symbols in Figure 3.8 indicate the CLASS STAR morphological classification. Point-like sources generally cluster around a HR of -0.5 at all fluxes, which is consistent with a power law of $\alpha \simeq 0.7$ modified only by Galactic absorption and is typical of Type I quasars. Sources with galactic and ambiguous morphology are seen in this region, but also populate increasingly hard regions of the diagram toward fainter fluxes. This is seen more clearly in Fig. 3.9, which shows error-weighted average hardness ratios for sources of different morphologies binned by flux. The trend toward harder X-ray spectra at fainter X-ray flux is seen only in sources with galactic and unknown morphology, as would be expected if the AGN within these objects were obscured at both optical and X-ray wavelengths. The optically faint / unidentified population which dominate the source counts at the faintest X-ray fluxes have X-ray spectral properties similar to the resolved galaxy population, suggesting they may be similar objects at higher redshift.

Comparison of the broad band optical and X-ray properties support this interpretation. r$'$-band magnitude is plotted versus full band X-ray flux in Figure 3.10 for sources in the EDXS, with symbols again indicating source morphology. Overplotted are lines of constant X-ray to optical ratio, appropriate for the Sloan Gunn r' filter:

$$\log(\frac{f_X}{f_{r'}}) = \log f_X + 5.69 + \frac{r'}{2.5}$$

Among point-like sources optical luminosity is seen to scale with X-ray luminosity as is expected in quasars where both the X-ray and optical flux is dominated by the AGN; nearly all exhibit X-ray to optical ratios $0 \leq \log(\frac{f_X}{f_{r'}}) \leq 1$. In contrast, sources with galaxy-like morphology show no tight relation between X-ray

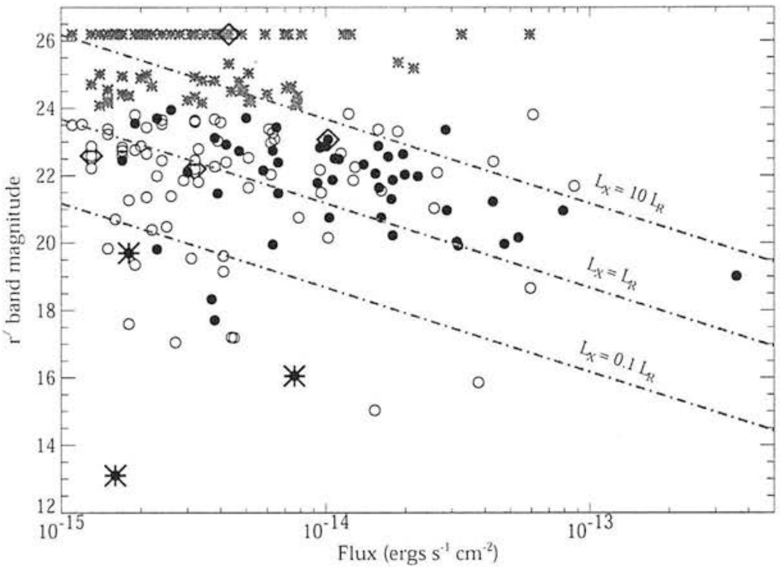

Figure 3.10: *r'-band magnitude versus full band X-ray flux for EDXS sources. Filled circles indicate point-like sources, open circles indicate galaxy morphology, and crosses indicate faint sources of ambiguous morphology. Dotted lines indicate constant X-ray to optical luminosity ratio, $\frac{L_X}{L_R}$, as noted. The three objects marked with large crosses with $\frac{L_X}{L_R} < 0.1$ are spectroscopically confirmed stars. The four objects indicated with large diamonds are spectroscopically confirmed Type II AGN.*

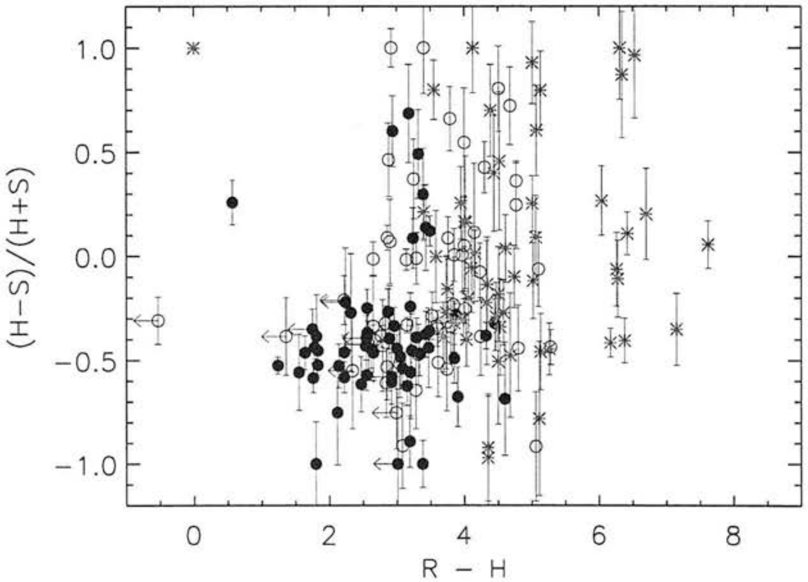

Figure 3.11: *X-ray hardness versus $r' - H$ colour for EXDS sources. Filled circles indicate point-like sources, open circles indicate galactic morphology, and crosses indicate faint sources of ambiguous morphology. Upper and lower limits for sources detected in a single band are indicated with arrows.*

and optical fluxes, suggesting that the host galaxies and not the central AGN dominate the optical emission.

The ratio of optical to X-ray flux has been found to be a valuable diagnostic of source type in surveys with high levels of spectroscopic completeness. In the CDFN survey, unobscured quasars are seen at bright fluxes with $0 \leq \log(\frac{f_X}{f_{opt}}) \leq 1$, while fainter sources with $-1 \leq \log \frac{f_X}{f_{opt}}, \leq 1$ are often spectroscopically identified as luminous Type II AGN (Hornschemeier et al. 2000). However, of four spectroscopically confirmed Type II AGN within the EDXS marked in Fig. 3.10, only one has a notably outlying value of $\frac{f_X}{f_{r'}}$, suggesting a more complex relation between absorption of optical light by dust and of X-ray emission by gas in these objects.

Figure 3.11 plots X-ray hardness versus optical $r' - H$ colour, with source morphologies indicated as before. The unobscured quasars clustering around a hardness value of -0.5 are also fairly blue, while the galaxies and optically faint sources are increasingly hard and red, consistent with obscuration of the central engine at both X-ray and optical wavelengths. Several optically faint, X-ray-emitting sources are also Extremely Red Objects ($r' - H > 5$).

3.4 Individual EDXS sources

3.4.1 Obscured AGN

The EDXS and contemporary surveys have resolved the majority of the 2 – 8 keV XRB flux into a population of sources which are optically and X-ray faint and appear to be obscured at both wavelengths. These sources may comprise the vast population of obscured AGN called for by synthesis models of the XRB. However, due to their optical faintness, this most interesting subsample of the EXDS sources is also the hardest to study. The MOSCA multi-object spectroscopy of a large sample of sources described in §3.2.4 was effectively limited to sources with continua brighter than $r' < 22.5$. Of 15 objects successfully identified at these flux levels, most were ordinary unobscured quasars and only two had hard X-ray spectra. Understanding the characteristics of the obscured AGN population which likely emits the majority of the X-ray flux in the Universe will require challengingly sensitive multiwavelength studies of hard X-ray selected objects.

In Willott et al. (2003), we present a multiwavelength study including a comparison of near-infrared and X-ray spectroscopy of three hard X-ray selected, optically faint ($R > 25$) EDXS sources with extremely red colours ($R - K > 6$). Here, I discuss these each in turn.

N2:25

N2:25 is an optically unresolved source with an R-band magnitude of 23.07, a hardness ratio of 0.20, and an $R - K$ colour of ~ 4. In comparison, unobscured high-redshift quasars typically have $R - K \sim 2$. We have obtained optical and K-band spectra of this source which are shown in Figure 3.12 and Figure 3.13, respectively. The redshift is determined by these data to be 2.61. Permitted lines of Hα, Lyα, NV, and CIV are seen with widths of 1900-2400 km s^{-1} and most likely arise in the broad line region of this AGN.

Consideration of both the optical continuum and these BLR lines suggests an optical absorption of $A_V \sim 1$.

In contrast, the hard X-ray spectrum suggests much more substantial absorption. The X-ray pulse height spectrum of N2:25, shown in Figure 3.14, and appropriate calibration data were extracted and reduced as described in §3.2.2 and fit to an absorbed powerlaw model using XSPEC. As the source contains only 85 counts, it was not possible to simultaneously constrain both the energy index, α, and the absorbing column. Fixing the index at $\alpha = 0.7$, a best fit column density of $N_H = (2.9 \pm 0.7) \times 10^{23}$ cm^{-2} was obtained. Varying α from 0.5 to 2 resulted in densities of $N_H = (3.8 \pm 0.8) \times 10^{23}$ cm^{-2} and $(2.4 \pm 0.6) \times 10^{23}$ atoms cm^{-2}, respectively. Assuming $N_H \simeq 3 \times 10^{23}$ cm^{-2} and a galactic gas-to-dust ratio, the X-ray absorption implies optical extinction of $A_V \simeq 150$.

The discrepancy between the small absorption seen in the optical with the heavy column detected in the X-ray suggests that either (i) the gas-to-dust ratio in the nucleus of N2:25 varies significantly from the Galactic value or (ii) the geometry of the nuclear region is such that the optical light does not pass through the material obscuring the X-ray emission. Accounting for obscuration, the intrinsic X-ray luminosity of N2:25 is $L_{(2-10)} = 4.7 \times 10^{44}$ erg s^{-1}, which is broad agreement with that expected from unobscured quasars given the optical and broad emission line fluxes observed in N2:25. This argues against a geometry in which the optical light is scattered into our line of sight. Similar sources are reported in the literature (Simpson 1998, Akiyama et al. 2000, Risaliti et al. 2001, Maiolino et al. 2001b, Comastri et al. 2001), and may be explained by unusually high gas-to-dust ratios or peculiar dust composition in the regions near to some AGN (Maiolino et al. 2001b,a).

In Willott et al. (2004) we explore the absorption properties of the gas and dust in obscured quasars identified in the EDXS. Near-IR and/or optical spectra were obtained for a subset of nine quasars with $R > 23$ which were detected with Chandra at higher than the 5σ level. Emission lines in the spectra allowed redshift determination for eight of these. Fits to the broad band photometry and near-IR spectroscopy of these sources to a quasar template constrained the amount of reddening by dust toward these sources. The broad-band X-ray hardness ratios of these sources were converted into estimates of the gas absorbing column by assuming underlying obscured powerlaw spectra with an energy index of α. The dust extinction is plotted versus the absorption by gas for these sources and for a sample of Seyfert galaxies surveyed by Maiolino et al. (2001b) in Figure 3.15. The majority of sources show gas-to-dust absorption ratios which are up to ten times higher than those expected from the Galactic gas-to-dust ratio. However, only one other source — N2:35 — shows the extreme disparity between gas and dust absorption seen in N2:25.

N2:21

The optical counterpart of N2:21 is a faint ($R = 25.02$), red ($R - K = 6.4$) galaxy, which is also coincident with a strong radio source ($S_{1.4\mathrm{GHz}} = 119$ mJy). Figure 3.16 presents the IR spectrum of N2:21 which shows the Hα line and faint lines of Hβ and [OIII] and sets the redshift at 1.575. These lines are narrow (unresolved to 80Å = 1500 km s^{-1}), and typical of those seen in high redshift radio galaxies. A high resolution radio image at 8.4 GHz, shown in Figure 3.16, reveals the standard core / jet morphology and confirms this identification. The optical spectrum showed no continuum or line emission, as expected for a faint source in this redshift range.

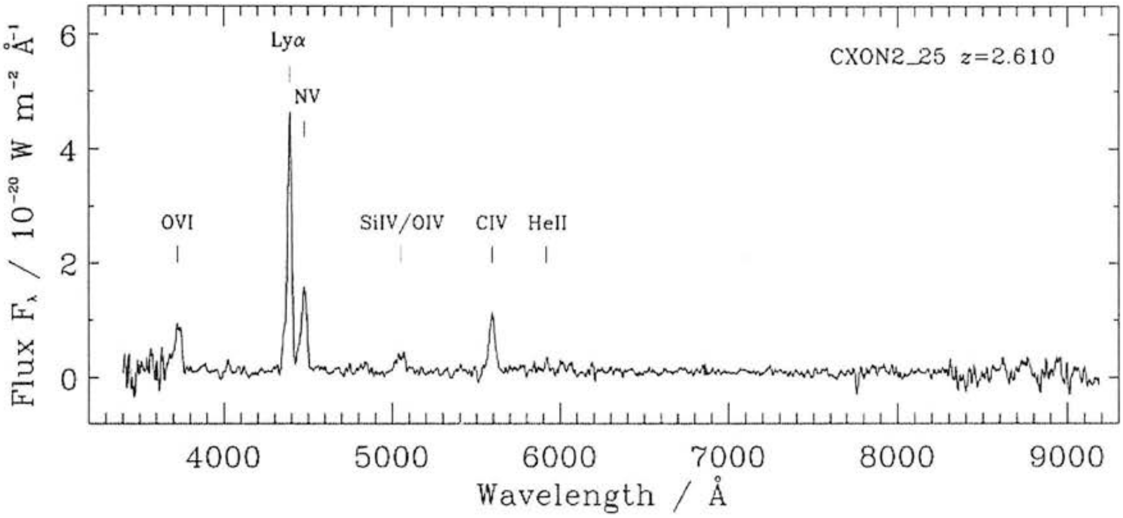

Figure 3.12: *Optical spectrum of N2:25 obtained with the ISIS spectrograph on the William Hershel Telescope. This spectrum has been smoothed with a boxcar filter of 15 Å. Figure from Willott et al. (2003).*

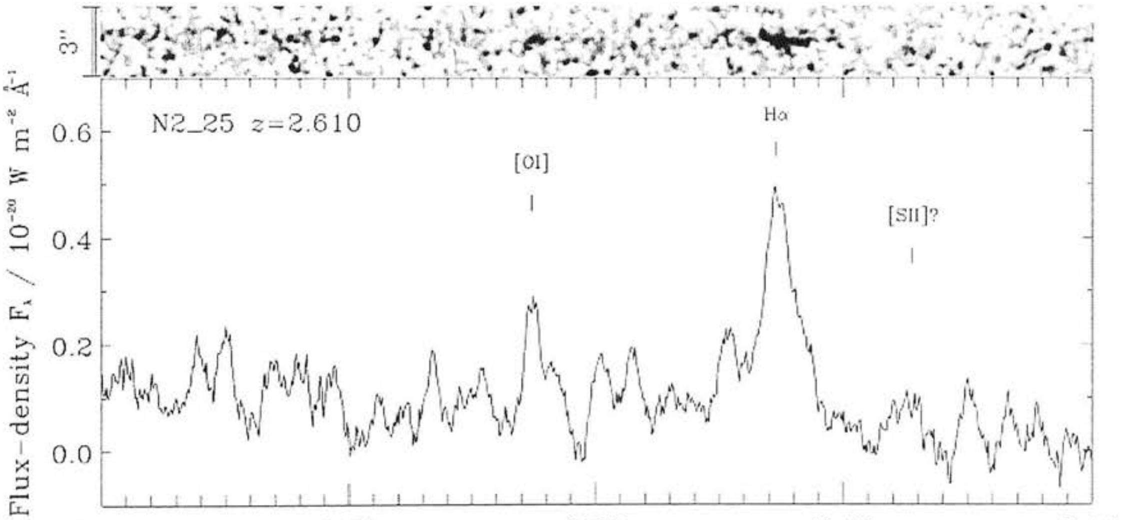

Figure 3.13: *K-band spectrum of N2:25 obtained with the IRCS spectrograph on Subaru. A grayscale of the two-dimensional spectrum with a width of 3'' is shown above. [OI] and Hα are clearly visible in both the one and two dimensional spectra, while the flux responsible for the [SII] detection is offset in the cross-dispersion direction by 0.4'' from the other lines. Figure from Willott et al. (2003).*

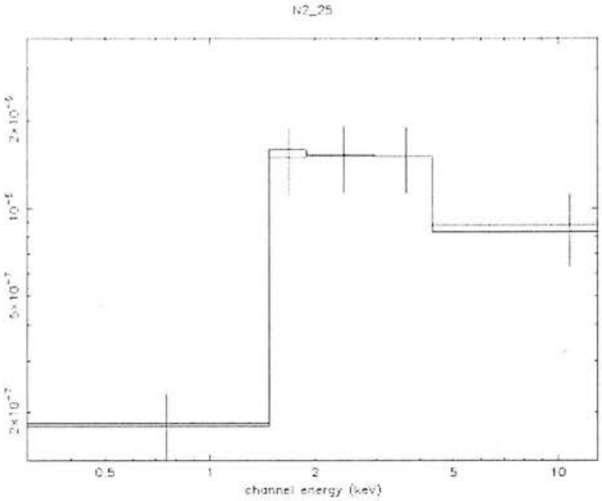

Figure 3.14: *X-ray pulse height spectrum of N2:25, overlaid with an obscured powerlaw model with fixed energy index $\alpha = 0.7$. The best fit indicates an obscuring column of $\sim 3 \times 10^{23}$ cm^{-2}.*

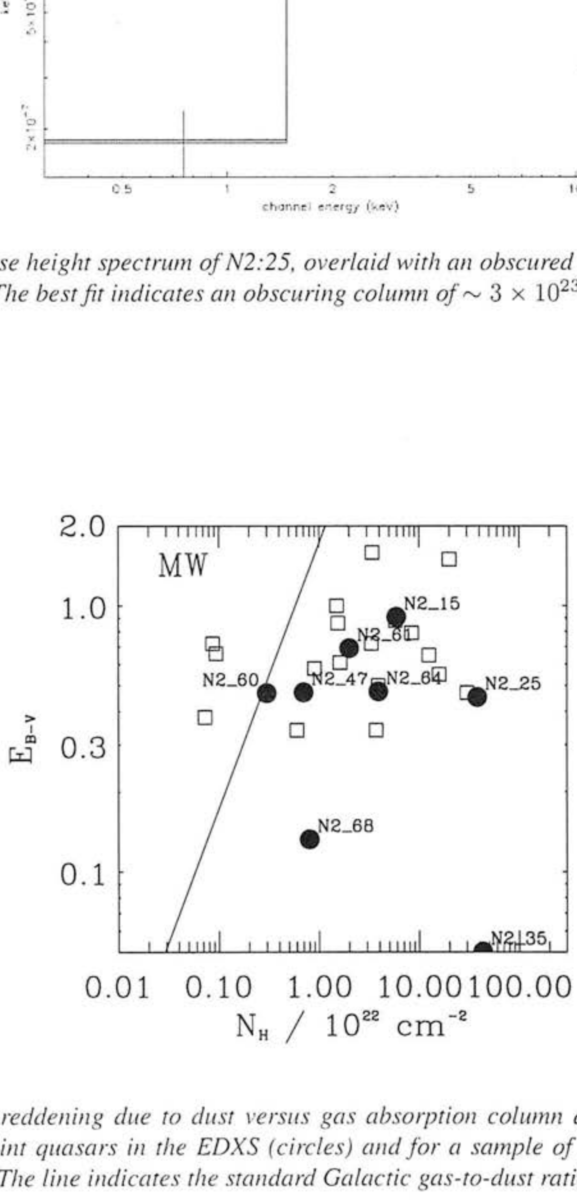

Figure 3.15: *Optical reddening due to dust versus gas absorption column density derived from X-ray spectra for optically-faint quasars in the EDXS (circles) and for a sample of Seyfert galaxies (Maiolino et al. 2001b; squares). The line indicates the standard Galactic gas-to-dust ratio. Figure from Willott et al. (2004).*

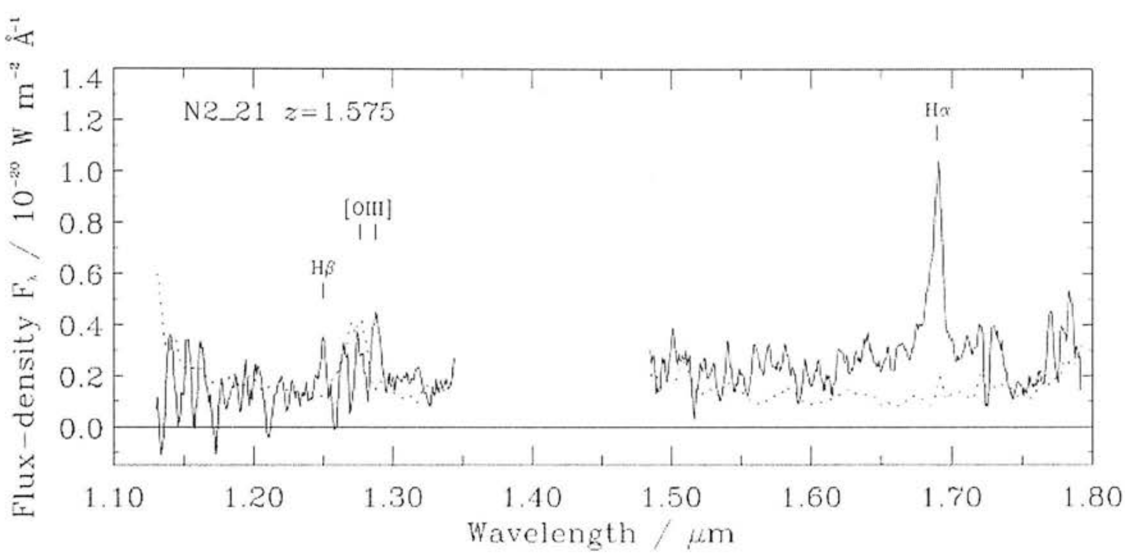

Figure 3.16: *K-band spectrum of N2:21 obtained with the OHS spectrograph on Subaru. RMS noise is shown with the dotted line.*

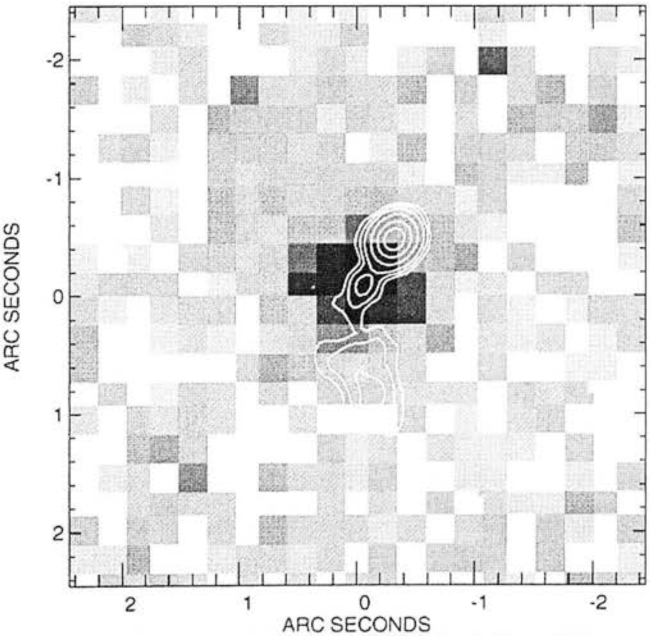

Figure 3.17: *8.4 GHz VLA contours of N2:21 overlaid on a K-band image. The contours are at levels of* $3, 6, 12, 36, 96, 192 \times 60\mu Jy$.

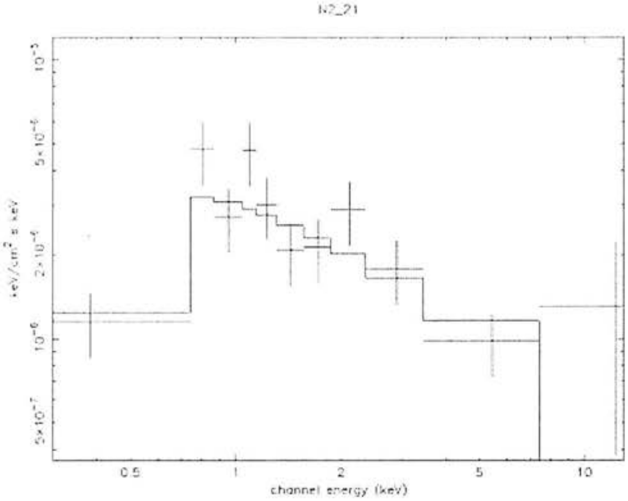

Figure 3.18: *X-ray pulse height spectrum of N2:21, overlaid with an obscured powerlaw model. The best fit indicates an energy index* $\alpha = 0.8$ *and an obscuring column of* $\sim 7 \times 10^{21}$ cm^{-2}.

The X-ray spectrum of N2:21 was constructed from 125 source counts, and is shown in Figure 3.18. The best-fit absorbed powerlaw model gives $N_H = (7.0 \pm 5.1) \times 10^{21}$ cm^{-2} and $\alpha = 0.8 \pm 0.22$. Fitting the energy index at 0.7 yields an absorbing column of just $(5.4 \pm 3.1) \times 10^{21}$ cm^{-2}. That the gas absorption is so low in this object — it is formally consistent with Galactic values — is surprising in a radio galaxy in which only narrow lines are observed. The non-detection of a broad component gives a lower limit on the absorption to the broad line region of $A_V > 5$, based on the typical ratio of broad-line to narrow-line flux $\simeq 40$ in unobscured, radio-loud quasars (Jackson and Eracleous 1995). Comparison of the ratio of Hα to Hβ to the value expected in case B recombination suggests another 3 magnitudes of extinction to the narrow line region. The total dust extinction then is $A_V > 8$, suggesting an X-ray column of $N_H > 1.5 \times 10^{22}$ cm^{-2}, similar to those typically seen in high redshift radio galaxies, and significantly greater than that measured in N2:21.

Possible explanations for this discrepancy are discussed fully in Willott et al. (2003). Several scenarios by which the X-ray emission arises outside the nucleus are ruled out on the basis of the X-ray properties of the source.

- The compactness of the X-ray source as well as its X-ray spectrum argue against thermal emission from a cluster of galaxies. Viable fits to thermal emission were obtained only for temperatures $T > 10$ keV, which is much hotter than is typical of hot intracluster gas.
- The X-ray spectral index is too flat to be consistent with an extrapolation of synchrotron emission in this source.
- Were the soft X-ray photons nuclear emission Thompson scattered into our line of sight with a typical scattering fraction of $\sim 1\%$, the hard X-ray luminosity would be expected to be $> 10^{46}$ erg s^{-1}, while the measured value is much lower ($L_{2-10\ \mathrm{keV}} = 2 \times 10^{44}$ erg s^{-1}) and consistent with

that expected from the empirical relation of [OIII] line to intrinsic hard X-ray flux.

- Finally, inverse-Compton scattering of synchrotron-generated IR photons from the quasar off relativistic photons in the lobes is not viable as the observed X-ray luminosity implies a magnetic field energy density which is too low for a compact radio galaxy.

We conclude that the X-ray emission mechanism of N2:21 remains unclear. Several examples of extended soft X-ray emission which is coincident with the lobes of high redshift radio galaxies have been detected with Chandra (Fabian et al. 2001, Carilli et al. 2002, Fabian et al. 2003). In one of these (PKS 1138-262, Carilli et al. 2002), the authors suggest the X-ray emission is heated by shocks caused by expansion of the radio source into the surrounding medium. Though a very high density medium would be required, this mechanism cannot be ruled out for N2:21. Similarly, it is possible that the soft X-ray emission does originate from the obscured nucleus, and that the gas-to-dust ratio of the obscuring material is simply much lower than usual.

N2:28

N2:28 is optically identified as a faint ($R = 25.8$), extremely red ($R - K = 6.1$) galaxy, which is located in a group of ten very red objects described by Roche et al. (2002). The infrared spectrum of N2:28 shows a faint continuum, but no emission lines. Redshift constraints obtained using the HYPERZ photometric redshift package as described in Willott et al. (2003) yield a redshift of ~ 1.1, with 90% confidence that $0.80 < z < 1.20$. The hardness ratio of this source is somewhat harder than that of unobscured quasars at -0.14 ± 0.18. Fitting the pulse height spectrum constructed from 32 source counts to an obscured powerlaw with a fixed index $\alpha = 0.7$ at $z = 1.1$ gives a best-fit absorbing column of $N_H = (4.5 \pm 2.6) \times 10^{22}$ cm^{-2}. Assuming $z = 1.1$, the hard X-ray luminosity of N2:28 is $L_{2-10 \text{ keV}} = 1.6 \times 10^{43}$ erg s^{-1}, which rises to $L_{2-10 \text{ keV}} = 2.2 \times 10^{43}$ erg s^{-1} if corrected for intrinsic absorption by the absorbing column estimated above. The X-ray absorption and luminosity suggest an obscured AGN similar to local Seyfert galaxies, which is consistent with the observation of a resolved host with no central point source in both the optical and IR bands.

The detailed study of individual hard X-ray selected sources reveals considerable variety in the objects comprising the hard XRB, with N2:25, N2:21, and N2:28 identified as a reddened quasar, a high redshift radio galaxy, and a Seyfert-type galaxy at a redshift of ~ 1, respectively. This sample, and the sample of reddened quasars studied in Willott et al. (2004), indicates there is also substantial variation in the absorption properties of gas and dust in these objects. While the gas-to-dust absorption ratio in these objects is typically up to ten times that expected from the Galactic ratio, similar to local Seyferts, objects like N2:25 and N2:35 are seen with one hundred times more obscuration from gas. In N2:21 either the soft X-ray properties are governed by the radio source rather than the AGN or the gas absorption is conspicuously low compared to the optical extinction. That the classification of a given AGN as obscured may be dependent on the wavelength at which it is observed complicates both the unified model of AGN and synthesis models of the

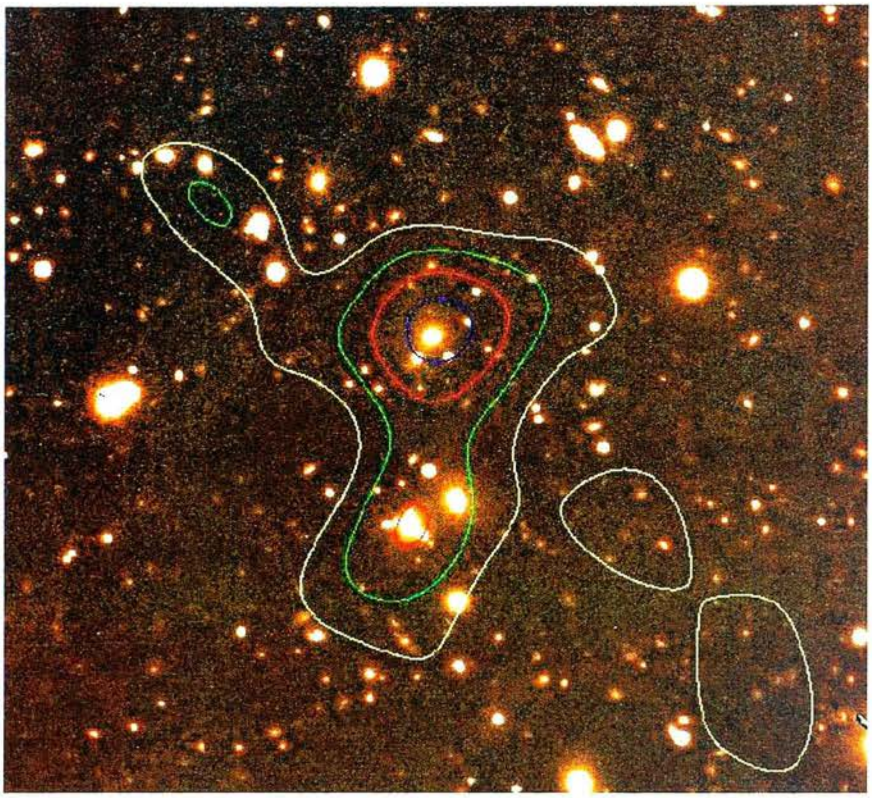

Figure 3.19: *r' image of the galaxy cluster CXOEN2 J163637.3+410804. The overlaid contours are of the soft X-ray image smoothed by a Gaussian with a FWHM of $10''$.*

XRB. Further follow-up of the hard X-ray sources identified in surveys such as the EDXS will be necessary to address these issues.

3.4.2 Diffuse emission

In addition to point sources, faint, soft diffuse emission is detected from two galaxy clusters within the EDXS fields. These sources were characterised by running WAVDETECT with scales much larger than the PSF, i.e., $i = 16, 16\sqrt{2}, 32, 32\sqrt{2}$, and 64. No extended sources were found in the N1 region, while two were found within N2. The most significant is easily seen by eye, and consists of 205 counts in a region ~ 17 times larger than the expected Chandra PSF centred on a bright peak at 16:36:37.38, +41:08:04.9. By IAU convention, this source is named CXOEN2 J163637.3+410804. The soft band flux in this region, including the contribution from a faint point source $52''$ from the core (N2:101), is $L_{0.5-2\ \mathrm{keV}} = 1.46 \pm 0.15 \times 10^{-14}$ erg s^{-1} cm^{-2}.

Optical r' imaging reveals a bright elliptical galaxy at the position of the peak cluster emission, and an overdensity of similar galaxies in the region (see Figure 3.19). Spectra of three of these galaxies confirm they are cluster members at a redshift of 0.42, making the soft band luminosity $L_{0.5-2\ \mathrm{keV}} \simeq 1 \times 10^{43}$

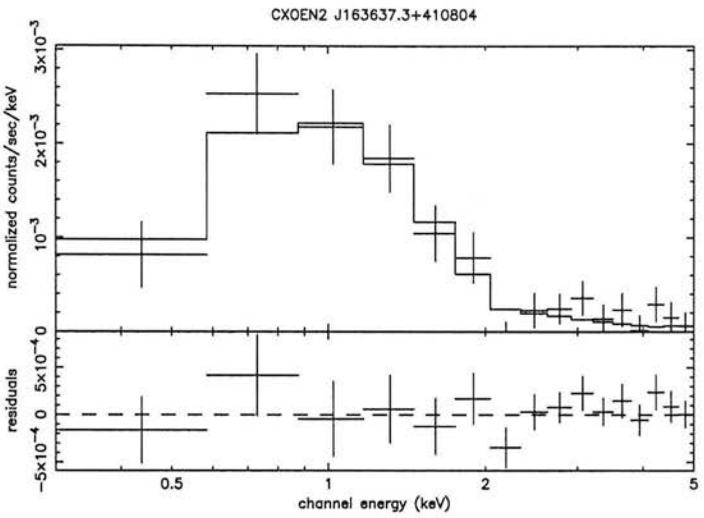

Figure 3.20: *Pulse height spectrum of the cluster CXOEN2 J163637.3+410804. The spectrum was fit to a Raymond-Smith thermal plasma, with residuals shown below, yielding an abundance of 0.3 solar and a temperature of* ~ 2.7 *keV.*

erg s^{-1}. The X-ray spectrum of the diffuse emission was extracted as discussed in §3.2.2 and fit to the Raymond-Smith model for a thermal plasma using XSPEC. The best fit and residuals are shown in Figure 3.20, and correspond to an abundance of 0.3 solar and a plasma temperature of 2.73 ± 0.81 keV.

The second significant extended source in N2 is detected at the edge of the field of view at 16:37:28.5, +41:00:13 and may be centered outside of the image area. No further analysis of this source was attempted.

3.5 Summary of EDXS results

In this chapter, I emphasize the results of the EDXS to which I made a significant and direct contribution. To summarize the results of the survey as a whole, I here briefly describe all the EDXS-related papers.

- **Manners et al. (2003)** describe reduction of the X-ray data and present the catalogue of EDXS sources, along with analysis of the source counts, hardness ratios, and optical classifications. This work is described more fully in §3.2.1, §3.2.2, §3.3.1, and §3.3.2.
- **Gonzalez-Solares et al. (2004)** present deep U, g', r', i', and H observations of the EDXS field, and report on the optical and near-IR properties of the X-ray sources. Counterparts are found for 80% of the full-band sources, and photometric redshifts have been computed for this sub-sample. Two peaks are seen in the redshift distribution, one at $z \sim 0.5$ comprised mainly of sources with galaxy morphologies and another at $z \sim 2$ comprised mainly of point-like sources. The optical identification program is briefly described in §3.2.3

- **Willott et al. (2003)** discuss detailed multiwavelength observations of three EXDS sources selected to be typical of the obscured AGN comprising the majority of the hard XRB. These sources — a reddened quasar, a radio galaxy, and a Type 2 AGN — illustrate the diversity of the hard X-ray selected AGN population and the variation in obscuration by gas and by dust in these systems. These results are discussed in §3.4.1.
- **Willott et al. (2004)** study the obscuration by dust and by gas in a sample of optically-faint, reddened quasars in the EDXS sample. Near-infrared data is used to constrain the amount of dust reddening of the restframe UV/optical light, and X-ray spectra are used to estimate the gas absorption column. The resulting gas-to-dust ratios are found to be much higher than the Galactic value, and are more similar to values found for local Seyfert galaxies. These results are discussed in §3.4.1.
- **Almaini et al. (2003)** report on the relationship between the X-ray- and submillimetre-detected sources in the EDXS field. Only 1 of 17 sources detected by SCUBA at 850 μm in the EDXS field is also detected with Chandra. The upper limits set by the non-detections exclude all but Compton-thick AGN in these sources. Despite the low direct overlap rate, there is strong evidence for angular clustering between the two populations, implying that the X-ray- and submillimetre-bright populations may trace the same large scale structure and may form an evolutionary sequence.
- **Manners et al. (2004)** present a cross-correlation of 15μm sources in the European Large Area ISO Survey catalogue with the EDXS detections. The AGN fraction of sources with $0.8 < S_{15\mu\mathrm{m}} < 6$ is found to be $\sim 19\%$. Stacking the hard X-ray counts at the locations of the individually undetected ISO sources results in a low significance detection which is consistent with X-ray emission from star formation. In the absence of a large undetected population of Compton thick sources, these results indicate that the cosmic star-formation history can be effectively constrained by mid-infrared surveys.

3.6 Conclusions

In this Chapter, I have presented work done in collaboration on the ELAIS Deep X-ray Survey which covers ~ 0.16 square degrees to a limiting flux of $S_{0.5-8\ keV} = 1.1 \times 10^{-15}$ erg s^{-1} cm^{-2}and detects 235 X-ray sources. Roughly 70% of these sources have counterparts in r'-band images to $r' = 25.2$ and $\sim 12\%$ of the EDXS sample has been spectroscopically identified to date. I have characterised the X-ray spectra of the EDXS sources in broad-band hardness ratios and, where possible, through moderate resolution imaging spectroscopy, and I have confirmed the values of α and N_H implied by the hardness ratio analysis are consistent with values obtained through spectral fitting for the brightest sources. Combining the X-ray spectral information with data at optical and near-IR wavelengths, I have drawn conclusions about the make-up of the EDXS sample as a whole and about the relative obscuration by gas and dust in individual objects.

Returning to the questions with which I began this Chapter, it is clear that substantial progress has been made in understanding the origin of the hard XRB. As noted in §3.3.1, over half of the hard XRB is resolved at the flux limit of the EDXS. While the resolved fraction varies between survey fields — likely due to clustering in structures larger than the fields of view — the deepest contemporary surveys resolve all but 5%-15% of the hard XRB with the greatest uncertainty now being the magnitude of the background emission itself. A recent compilation of surveys by Moretti et al. (2003) finds that $94.3^{+7.0}_{-6.7}\%$ and $88.8^{+7.8}_{-6.6}\%$ of the soft and hard XRB emission can be ascribed to discrete sources with 2.4×10^{-17} erg $\mathrm{s}^{-1}\ \mathrm{cm}^{-2} < S_{0.5-2\ \mathrm{keV}} < 10^{-11}$ erg $\mathrm{s}^{-1}\ \mathrm{cm}^{-2}$ and 2.1×10^{-16} erg $\mathrm{s}^{-1}\ \mathrm{cm}^{-2} < S_{2-10\ \mathrm{keV}} < 8 \times 10^{-12}$ erg $\mathrm{s}^{-1}\ \mathrm{cm}^{-2}$, respectively. The fraction of the total XRB resolved is still model dependent.

The major components of the XRB have also been conclusively identified. The objects comprising the EDXS sample are optically identified as quasars (23%), galaxies (32%), and optically faint objects (15%), and the relative sizes of these populations seem roughly consistent among deep survey fields (e.g., Mushotsky et al. 2000, Tozzi et al. 2001). I find that EDXS sources at fainter X-ray fluxes have harder X-ray spectra, as required to match the XRB, and that sources with galactic optical morphology, which are increasingly prevalent towards fainter X-ray fluxes, appear to dominate this trend. The average X-ray spectral properties of the optically faint counterparts, which comprise the majority of sources at the faintest fluxes, are consistent with those of the resolved galaxy population, suggesting they are similar objects at higher redshift.

Finally, there is good evidence that the sources comprising the majority of the XRB flux are indeed obscured AGN, as predicted by synthesis models. At the fluxes probed by our survey, virtually every unresolved extragalactic X-ray source must be powered by an AGN. The galaxies and optically-faint objects which dominate the number counts toward faint fluxes show greater variation in the X-ray-to-optical flux ratios than the quasar population, as would be expected if the host galaxy rather than the central X-ray source dominated the optical light. These sources also have redder $r' - H$ colours typical of early-type host galaxies and/or dust obscured active galactic nuclei. Surveys with higher levels of spectroscopic completeness (e.g., Barger et al. 2003) confirm the sources dominating the XRB flux are indeed Type 2 AGN.

While the exploratory phase of Chandra and XMM deep field surveys such as the EDXS is now largely completed, work remains to be done to characterise and understand the source populations they have revealed. The basic assumption of XRB synthesis models — that the background flux is the superposed emission from a large population of variously obscured AGN — has been borne out by the field surveys, but the demographics of the obscured population are far from understood. Surveys with high levels of spectroscopic completeness find a far higher fraction of moderately-obscured, low-redshift ($z < 1$) sources than predicted by the synthesis models, as well as strong evidence for luminosity-dependent evolution (Cowie et al. 2003, Steffen et al. 2003). Conversely, luminous, heavily-obscured Type 2 QSOs have been found in smaller numbers than expected, though tight limits on the number of Compton-thick objects are not yet available. A further complication, seen clearly in §3.4, is that obscuration by gas in the X-ray band does not always imply obscuration by dust in the optical, and vice versa, so that classification of a given object as Type 1 or Type 2 may be wavelength dependent.

As is amply illustrated by the low number of EDXS redshifts obtained in the multi-object spectroscopy campaign described in §3.2.4, obtaining spectroscopic redshifts is the major bottleneck to interpretation of the deep survey data. This is largely due to the extreme optical faintness of the sample; $> 40\%$ of the EDXS sample is at $R > 24$. As the obscured AGN population dominates at these faint optical magnitudes, spectroscopic observations of many of the most interesting, and most typical, XRB constituents will be challenging even with 8m class instruments. One way forward is to select interesting subsets of the X-ray sources for intensive observing campaigns to study the physics of individual objects in detail. A complementary route is to revisit the XRB synthesis models with the benefit of multiband observations of the deep Chandra and XMM survey fields, which will more tightly constrain the characteristics of the AGN population as a whole.

CHAPTER 4

The AGN content of MS1054-03

Efficient surveys of AGN within luminous galaxy clusters at X-ray wavelengths have only recently become possible, thanks to the ability of Chandra to resolve faint point-sources within regions of luminous, diffuse emission from intracluster gas. The study presented in this chapter surveys the AGN content of a massive, dynamically young, X-ray bright cluster at $z = 0.83$ which is already known to contain at least six radio-loud AGN.

I give a brief introduction to the study of AGN within clusters in §4.1. §4.2 describes the compilation of the X-ray sourcelist and the identification of optical counterparts. In §4.3, the X-ray number counts in the MS1054-03 field are derived and the excess over the expected counts in a 'blank field' is identified. Possible reasons for the excess are discussed in §4.4, along with its relation to the radio source excess observed by Best et al. (2002). Finally, I summarize my conclusions in §4.5. A slightly modified version of this chapter is published in Johnson et al. (2003).

4.1 Introduction

Optical studies suggest that active nuclei are relatively rare in cluster environments. Surveying low redshift ($\bar{z} \sim 0.04$) cluster fields, Dressler et al. (1985) found only 1% of cluster members showed evidence for AGN activity in their optical spectra. A subsequent study of several distant clusters revealed no increase in the cluster AGN fraction to $z \sim 0.5$ (Dressler et al. 1999). Recently, however, surveys of cluster fields at other wavelengths are uncovering surprisingly large numbers of cluster AGN.

Joint radio / far infrared surveys of galaxies within nearby ($z \leq 0.25$) rich Abell clusters conducted by Reddy and Yun (2004) and Morrison and Owen (2003) indicate populations of radio-loud AGN hosted by red ellipticals in the cluster core. In these sources, the radio emission appears to be boosted via ram pressure and/or thermal compression of the radio lobes in the dense cluster environment. As discussed in Chapter 1, Best (2004) finds similar evidence of environmental boosting in radio-loud AGN identified in the 2dFGRS, and that the fraction of cluster galaxies hosting a radio-loud AGN decreases within cluster cores. Miller and Owen (2003) report in increase in the frequency of radio galaxies in Abell 2255, a merging cluster system at $z = 0.08$, and suggest the activity has been triggered by the merger. With the exception of the study of MS1054 discussed fully below, no radio studies of AGN within high redshift clusters have been undertaken.

X-ray surveys of point sources within cluster fields have been hindered by the high levels of soft X-ray flux from the hot intracluster medium and by the traditionally poor angular resolution of X-ray telescopes. The current generation of X-ray observatories, however, offers unprecedented resolution and positional accuracy, as well as high sensitivity over the full X-ray band. Furthermore, multi-scale wavelet detection techniques (e.g., Freeman et al. 2002) can now reliably separate small-scale point source emission from surrounding larger-scale diffuse cluster emission. Consequently, several studies of point sources serendipitously observed in pointed cluster observations have recently been published, nearly all of which report an excess of point sources in these fields compared to source counts in cluster-free fields.

At low redshift, the excess of X-ray sources seems to be largely due to low luminosity AGN (LLAGN) associated with the cluster. Lazzati et al. (1998), using a wavelet detection algorithm on ROSAT PSPC data, examined the fields of A194 ($z = 0.018$) and A1367 ($z = 0.022$) and found 26 and 28 sources, respectively, where only 9 were expected. Sun and Murray (2002) re-observed A1367 with Chandra and resolved 59 point-like sources, 8 of which are confirmed cluster members. The identified sources, with typical X-ray luminosities of a few $\times 10^{41}$ erg s^{-1}, have spectra consistent with radiation from central nuclei, thermal halos, and stellar components. In addition to these identified objects, a 2.5 σ excess in source counts at bright fluxes is found in both hard and soft bands. If these unidentified sources are also associated with the cluster, they have X-ray luminosities consistent with LLAGN and unusually low optical luminosities. A similar, though slightly more X-ray luminous population was reported in A2256 ($z = 0.06$) by Henry and Briel (1991), who found twice as many sources in a ROSAT PSPC observation than were expected for a blank field. Among these sources, they noted two cluster member AGN with $L_{(0.1-2.4 \text{ keV})} \sim 10^{42}$ erg s^{-1}, as well as a number of optically 'dark' objects with comparable X-ray fluxes.

At higher redshifts, more luminous AGN are found in several clusters. In the field of A2104 ($z = 0.154$), Martini et al. (2002) find that all X-ray sources with optical counterparts brighter than $R = 20$ and

$B - R$ colours consistent with the cluster sequence are indeed AGN in the cluster, with $L_{2-10\ \mathrm{keV}}$ ranging from $10^{41} - 10^{45}$ erg s^{-1}. Only one of the six has spectral characteristics which would have led to it being optically identified as an AGN. The AGN hosts in A2104 are photometrically and spectroscopically similar to old, red galaxies, but have a higher velocity dispersion than non-AGN cluster members, suggesting some may be falling into the cluster for the first time. Cappi et al. (2001) identify X-ray source excesses in 3C295 ($z = 0.46$) and RXJ0030 ($z = 0.5$) at fluxes consistent with luminosities at the cluster redshift of $10^{42} - 10^{43}$ erg s^{-1}, and both are found to contain spectroscopically confirmed cluster AGN. Finally, Pentericci et al. (2002) report the association of 2, and possible association of as many as 6, AGN with L$\sim 10^{42} - 10^{45}$ erg s^{-1} in a protocluster around the $z = 2.16$ radio galaxy MRC 1138-262.

Not all moderate to high redshift clusters contain luminous AGN, however. Molnar et al. (2002) found an excess of sources around A1995 ($z = 0.32$) at fluxes consistent with starburst luminosities at the cluster redshift. They also surveyed MS0451 ($z = 0.55$) and found no evidence for an excess of sources. This is not inconsistent with MS0451 housing a population similar to that seen in A1995, which would be too faint to observe in the more distant cluster, but it does rule out a population of more luminous sources such as those seen in 3C295 and RXJ003. They conclude that not all clusters exhibit source excesses at these flux levels, and suggest that different types of sources appear to dominate in different clusters.

This chapter presents X-ray observations of one of the most distant known galaxy clusters, MS1054-0321, and is the first X-ray study in an ongoing programme to investigate the prevalence of AGN activity in galaxies as a function of redshift and dynamical state (Dowsett et al. 2004). At $z = 0.83$, MS1054-03 is a well studied, rich (Abell class 3) cluster with a bolometric luminosity of $L_X = 1.2 \times 10^{45} h^{-2}$ erg s^{-1}. It was the most distant cluster in the Einstein Medium Sensitivity Survey X-ray selected cluster sample (Gioia et al. 1990) and has been the subject of an extensive observing campaign yielding a Hubble Space Telescope (HST) mosaic (van Dokkum et al. 2000), deep ground-based infrared and optical imaging (Franx *et al.*, in preparation), and Keck spectroscopy (van Dokkum et al. 2000). Substantial substructure in the distribution of galaxies is matched by the diffuse soft X-ray emission, and weak-lensing analysis indicates that the cluster is young, massive, and still relaxing (Hoekstra et al. 2000). Though the Butcher-Oemler fraction, $f_B = 0.22 \pm 0.05$, is fairly low for this redshift, the fraction of early-type galaxies in the central regions of the cluster (44%) is quite low and the fraction of merging systems (17%) is quite high (van Dokkum et al. 2000). Extremely deep radio observations at 5 GHz have revealed 6, and possibly 7, radio-loud AGN associated with the cluster (Best et al. 2002). I have analysed a 91 ksec Chandra exposure of the field to probe the AGN content in the X-rays.

Throughout this chapter, I assume an $\Omega_0 = 0.3$, $\Lambda_0 = 0.7$, and H$_0$ = 70 km s^{-1} Mpc^{-1} cosmology.

4.2 X-ray source list

My analysis uses an archival 91 ksec exposure of MS1054-03 taken with the back-illuminated Chandra ACIS-S3 detector on 2000 April 21-22, and first published in Jeltema et al. (2001). I reduced the data with standard CIAO tools, using the calibration database files in CALDB version 2.1, which include an improved ACIS-S3 gain map. There were three periods of significant background flaring during the integration which

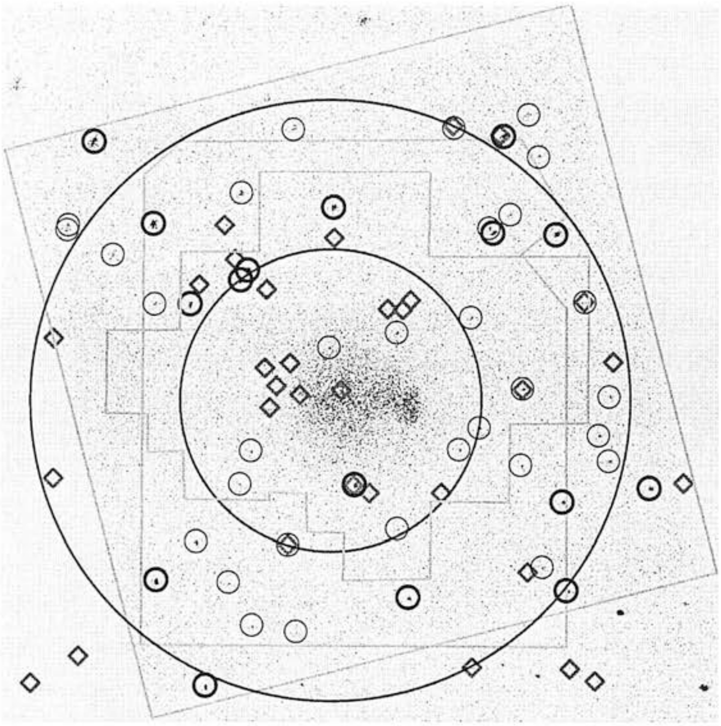

Figure 4.1: *X-ray point sources in the MS1054-03 field. The grayscale is binned full band ACIS-S data, displayed so that North is up and East is to the left. The 47 detected X-ray point sources within the ACIS-S3 chip are circled, with the darker circles indicating 0.5 – 8 keV flux greater than* $\sim 5 \times 10^{-15}$ *erg cm*$^{-2}$ *s*$^{-1}$ *(see §4.3.2). The radio sources of Best et al. (2002) are marked with diamonds. The large circles are radii of 1 and 2 Mpc from the cluster centre at 10 57 00.2, -3 37 36.0 (J2000). The outer grey box delineates the edges of the S3 chip which is 8.3′ on a side. The irregular central contour is the FOV of HST imaging in this field. The roughly rectangular contour aligned North-South is the FOV over which KECK spectroscopy is available for selected objects.*

I excluded, leaving a useable exposure of 74 ksec. The data were filtered by pulse height energy into soft (0.5 – 2 keV), hard (2 – 8 keV), and full (0.5 – 8 keV) bands. Exposure maps were made in each band to estimate variation in effective exposure across the sky due to instrumental effects and source dither. These maps are energy dependent, and were made assuming a power-law spectrum with a photon index γ = 1.7, typical of unobscured AGN at our flux limit ($\sim 10^{-15}$ erg s^{-1} cm^{-2}; see Figure 3 of Tozzi et al. 2001). The WAVDETECT source detection algorithm (Freeman et al. 2002) was used to construct independent point source lists in each band. A significance threshold of 6.1×10^{-7} was used, corresponding to an average detection of less than one false source over the area of a single, full-resolution ACIS chip. I further limited my source lists by rejecting sources with a WAVDETECT source significance parameter of less than 3.0. Though this cut-off is arbitrary — the few sources with lower values may be real — visual inspection suggests it is a reasonable, conservative limit and its definition in terms of this parameter is computationally convenient. I find 47 sources in the full band, 33 in the soft band, and 24 in the hard band. Excepting a soft band only detection of a peak in the cluster emission, there are no soft or hard band detections which are not also full band detections. I will use only the full band source list in the rest of this analysis, and fluxes and luminosities are quoted for the observed 0.5 - 8 keV band.

I used the Starlink ASTROM package to astrometrically correct the X-ray source positions. AGN with accurately known coordinates in the optical and/or radio were aligned with their Chandra counterparts in a 6-parameter fit. Eleven sources were used in total, and achieved a good coverage of the chip. The RMS fit residuals were all $< 1.2''$, with a mean of $0.48''$. The positional errors include the error in RA and Dec from WAVDETECT, of order $0.25''$ for a typical source, with a $0.5''$ astrometric error added in quadrature.

Hardness ratios for each source are defined as $\frac{H-S}{H+S}$, where H and S are the counts in the 2 – 8 keV and 0.5 – 2 keV bands, respectively. Background subtracted hard and soft band counts were obtained through aperture photometry in the WAVDETECT source regions. The detected sources are listed in Appendix A, and shown in Fig. 4.1.

4.2.1 Optical counterparts

As illustrated in Figure 4.1, there is a wealth of optical observations of MS1054-03, none of which completely match the ACIS-S3 $8.3' \times 8.3'$ field of view (FOV). Deep HST mosaics were made from 6500 s Wide-field Planetary Camera 2 (WFPC2) exposures in the F606W and F814W filters, and cover a central area of $\sim 5' \times 5'$, corresponding to a radius of $\sim$ 1 Mpc from the cluster centre at the cluster redshift (van Dokkum et al. 2000). Spectroscopy of selected objects has been obtained with the Keck Low Resolution Imaging Spectrometer over an area of $\sim 6.8' \times 6.8'$. Targets were selected from a photometric catalogue created from a 900 s Keck I-band image; highest priority was given to objects which were within the area of the HST mosaic with magnitudes between +0.2 and -2.0 mag of the magnitude of the brightest cluster galaxy (20.2). Five multi-object spectroscopic masks were observed, 4 for exposure times of 2400 s and the last for 1200 s. The campaign yielded redshifts for over 200 objects in the field, 130 of which are confirmed cluster members (van Dokkum et al. 2000).

Where coverage allowed, optical counterparts for X-ray sources were identified from the Keck data and the HST mosaic. Each identification was examined by eye, and the largest observed offset was 1.35

arcsec. All 15 X-ray sources in the HST FOV were identified. 19 out of 31 sources in the Keck FOV were identified, of which 7 were in the HST FOV. In all, optical counterparts were found for 27 of the 47 X-ray sources. Restframe U - B colours are available for only 11 sources within the HST FOV (cf. van Dokkum et al. 2000); none of these lie within 0.2 mag of the cluster sequence. However, as the HST data cover only the inner regions of the cluster, available optical colour data can give no indication of the likely cluster membership of sources further from the cluster centre (see §4.3.2, §4.4.4).

Spectroscopic redshifts were available for just 7 of the X-ray sources, of which two were found to be at the cluster redshift. CXOU105702.7-033943 (source 19) is a visually confirmed match to KECK ID 564. It has extended morphology, is on the cluster sequence, and is also detected in the radio (see §4.4.3). It has a rest frame $L_{(0.9-14.6\mathrm{keV})} = 5 \times 10^{42}$ erg s^{-1}, and a hardness ratio of 0.08 which corresponds to an obscuring column of a few times 10^{22} cm^{-2} for a typical powerlaw spectrum with energy index, α, of 0.7 to 1. CXOU105710.6-033500 (source 7) is consistent with being a match to KECK ID 2152, which is brighter and bluer than the cluster sequence. It has a rest frame $L_{(0.9-14.6\mathrm{keV})} = 2.6 \times 10^{43}$ erg s^{-1}, and a hardness ratio of -0.79, suggesting a somewhat softer spectrum with $\alpha \sim 1.6$ for an unobscured powerlaw.

4.3 Source counts

I am interested in how many more of the detected X-ray sources in the MS 1054 field may be associated with the cluster. In the absence of complete spectroscopic identifications, I begin by looking for an excess over the source counts expected in a cluster-free field.

4.3.1 Determining the source counts

Determination of the survey area available to this observation at a given flux is complicated by variation of the effective exposure over the field due to instrumental effects, and by the diffuse emission from the hot cluster gas. I account for these effects by calculating a flux limit map, which indicates the flux of the faintest source which would have been included in our source list at each position on the chip. The sky area available at a given flux limit is then the summed value of all pixels with lower values.

I have chosen to limit my catalogue in terms of the WAVDETECT source significance parameter, σ_{src}, defined as

$$\sigma_{src} = \frac{C_{src}}{1 + \sqrt{0.75 + C_{bkg}}} \qquad (4.1)$$

where C_{src} are the net source counts and C_{bkg} are the background counts within the source region (Chandra X-ray Center 2002).

The detected source counts are related to the incident source flux, S (erg cm^{-2} s^{-1}), the effective exposure area, EA (cm^2), and the exposure time, τ (s), by

$$C = S \times EA \times \tau \times K \qquad (4.2)$$

where K is a conversion factor from ergs to counts assuming a $\gamma = 1.7$ powerlaw spectrum.

The background counts in the source region depend on the local background level, B, as well as the size of the source, D, which for point sources mainly reflects the off-axis degradation of the Chandra PSF. I treat the diffuse cluster emission as local background.

Therefore the flux limit, S_{lim}, for inclusion in my $\sigma_{src} > 3$ source list is

$$S_{lim} = 3 \times \frac{1 + \sqrt{0.75 + (B \times D)}}{EA \times \tau \times K} \tag{4.3}$$

In practice, maps of the same size and resolution as the data were made for quantities B, D, and EA, allowing calculation of S_{lim} for each pixel. The derivation of the exposure map is discussed in the previous section.

To produce a map of the true background plus the diffuse cluster emission, I first subtracted all identified point sources using the CIAO tool `dmcalc`. I filled the resulting 'holes' with pixel values sampled from the Poisson distribution whose mean and standard deviation equalled that of the surrounding background pixels with `dmfilth`. This source-free image was then smoothed with a 30″ Gaussian kernel using `csmooth`. I compared my background estimate to the output background image from WAVDETECT to ensure no significant error was introduced by the inclusion of low significance 'sources' in my map which are excluded during the wavelet detection process. The WAVDETECT background image was not used directly due to minor artefacts left from the iterative subtraction of bright sources.

In theory, the size of a detected point source should equal the size of the Chandra PSF, which depends largely on source angular distance from the optical axis, and also to some extent on source energy. The Chandra PSF library contains radially averaged encircled energy curves for several off-axis angles at a number of calibration energies, and these data were interpolated to create a map of PSF size over the extent of the S3 chip. I used the calibration data at 1.49 keV, as this was the value chosen for the WAVDETECT input parameter `eenergy` which specifies the PSF curves used in the detection algorithm. Comparing the source sizes reported by WAVDETECT for detected sources with those predicted by my source size map, I noted the WAVDETECT values were significantly higher at low off-axis angles. This appears to be due to a trend toward higher values of the WAVDETECT source extent parameter, PSFRATIO, near the optical axis, and not to an inconsistency in the expected PSF size (WAVDETECT PSF_SIZE parameter). Since our estimation of the limiting flux hinges on whether the source would have been detected by the wavelet detection algorithm, I have empirically fit the dependence of WAVDETECT source size on off-axis angle and included this in my source size map.

4.3.2 The source excess

Figure 4.2 shows the resulting number counts for the MS 1054 field. I have overplotted the best fit to number counts from the ELAIS Deep X-ray Survey (EDXS) presented in Manners et al. (2003). I choose the EXDS number counts computed in the 0.5 - 8 keV band for ease of comparison. Comparisons of the EDXS counts in soft and hard bands show them to be fully consistent with counts derived from other Chandra deep surveys, notably that of Mushotsky et al. (2000) obtained with the S3 chip. An excess of

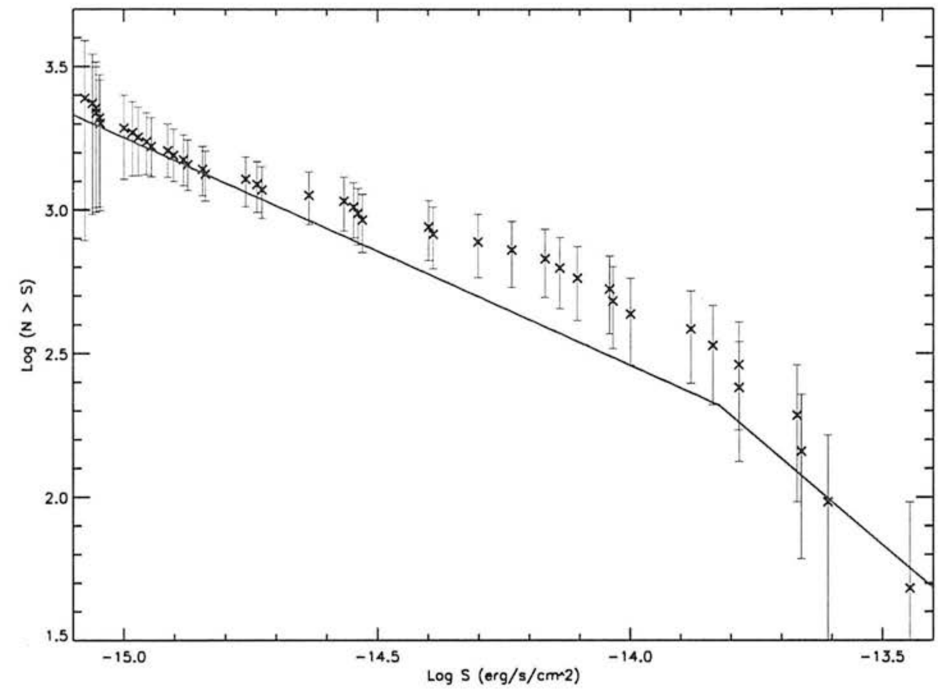

Figure 4.2: *Log N - Log S for MS1054-03 field. Points are number counts for the cluster field, while the solid line represents the counts expected from a blank field. At fluxes brighter than* 1.5×10^{-14} *erg* s^{-1} cm^{-2}, *the blank-field slope is Euclidean; the slope at fainter fluxes is the best fit to the EDXS counts from Manners et al. (2003).*

sources is seen at moderate fluxes in the MS1054-03 field, reaching $\sim 50\%$ at 5×10^{-15} erg cm^{-2} s^{-1}, which corresponds to a source luminosity of $\sim 10^{43}$ erg s^{-1} at the redshift of the cluster. Sources with fluxes in the range contributing to this excess are highlighted in Figure 4.1, where they are seen to avoid the cluster centre.

I have repeated the analysis with sources detected independently in the soft and hard bands. Consistent with earlier papers (Cappi et al. 2001, Pentericci et al. 2002), I detect an excess of comparable significance in the soft band sources but no significant excess of hard sources.

To investigate where in the field these excess sources are, I compare radial source histograms for the data and a simulated field with the same spatially-dependent sensitivity. The latter was made by converting the flux limit map described above to an 'expected source' map, using the EXDS number counts to obtain the fractional expected source count per pixel at each limiting flux. Cumulative radial source counts for my data and for the cluster-free field are compared in Figure 4.3 from a distance of 400″ to the cluster centre. I show both the sources detected to the survey limit (upper, dark line), and those contributing to the excess at fluxes above 5×10^{-15} erg s^{-1} cm^{-2} (lower, light line). The 47 sources detected at all fluxes compare

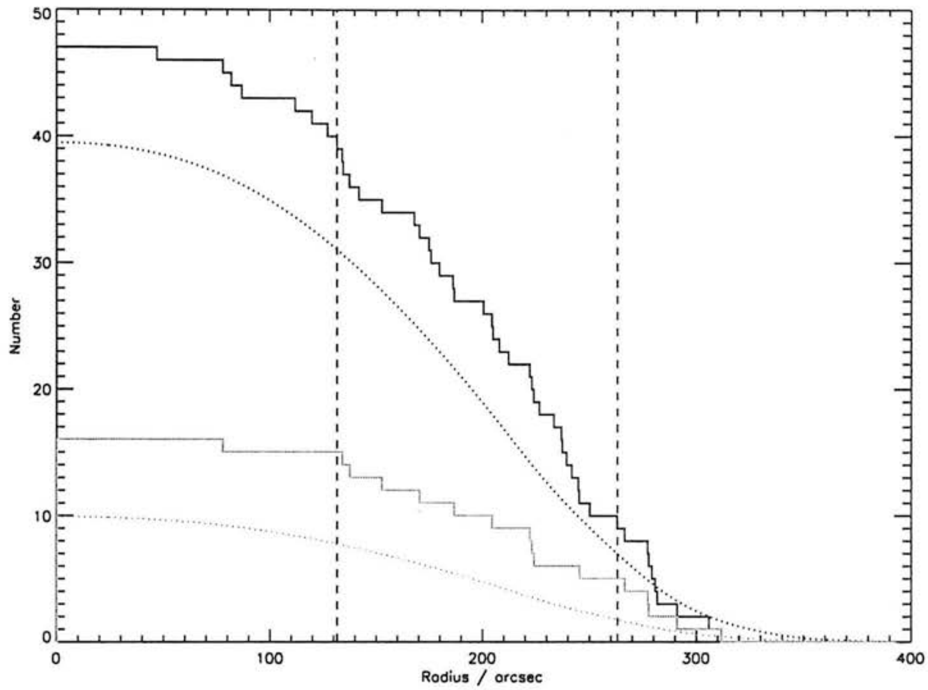

Figure 4.3: *Cumulative radial histogram of sources in MS1054-03 field, moving in from a distance of 400″ to the cluster centre at 10 57 00.2, -3 37 36.0 (J2000). The detected sources (solid histogram) are compared with sources expected from a cluster-free field (dotted curve; see text). The upper, dark curves are for the full X-ray sample, and the lower, light curves are for sources with $S > 5 \times 10^{-15}$ erg s^{-1} cm^{-2}. The vertical lines indicate radii of 1 and 2 Mpc at the cluster redshift. The decrease toward larger radii is due to decreased sensitivity toward higher off-axis angles and, at the largest radii, to extension beyond the edge of the active area of the ACIS-S3 chip.*

with 40 sources expected over the same area for a cluster-free observation. As sources 105715.7-033502 and 105715.7-033506 may constitute a single object (see footnote to Table A), I reliably detect 6 sources more than we would expect in a blank field. This is only a 1σ excess overall, and is fully consistent with observed levels of cosmic variance in Chandra deep survey fields (Manners et al. 2003). At fluxes higher than 5×10^{-15} erg s^{-1} cm^{-2}, however, we expect only 10 sources, and detect 16, which corresponds to an excess of $\sim 2\sigma$. It is clear from Figure 4.3 that this excess arises in the outer regions of the cluster between 1 and 2 Mpc. The two confirmed X-ray detected cluster AGN, one brighter and one fainter than the 5×10^{-15} erg s^{-1} limit, are found 134″ and 222″ from the cluster centre, corresponding to distances of $\sim$ 1.0 and 1.7 Mpc.

4.4 Discussion

4.4.1 Cosmic variance

While the probability of randomly observing as many excess sources as are seen in this field over the entire flux range is 0.19, the result at brighter fluxes has a probability of only 0.05. As noted by Cappi et al. (2001), the magnitude of the excess – $\sim$ 50% at 5×10^{-15} erg s^{-1} cm^{-2} – is higher than the 20%-30% variation seen in deep field surveys due to cosmic variance. Furthermore, the fact that this magnitude of excess sources has been detected in all but one of the seven Chandra pointed observations of clusters argues strongly against explanation by cosmic variance.

4.4.2 Gravitational lensing

As noted in Cappi et al. (2001), gravitational lensing of background sources by the cluster is also not a viable explanation for the observed effect. An intervening lens produces two effects which alter the apparent source counts in opposite senses. The apparent luminosity of sources is boosted by the lens, but the sky area in the lensed regions is decreased. Whether an increase or a deficit of sources is observed depends critically on the slope of the number counts being lensed. If the unlensed integral source counts are described as a powerlaw

$$N(> S_\nu) \propto S_\nu^{-\alpha} \tag{4.4}$$

then the counts boosted by a factor $\mu(\theta)$ will be

$$N'(> S_\nu) = \frac{1}{\mu(\theta)} N(> \frac{S_\nu}{\mu(\theta)}) = \mu^{\alpha-1} N(> S_\nu) \tag{4.5}$$

where θ is the angular distance from the lens centre. For source populations with an integral slope $\alpha < 1$ the apparent source counts will be depleted, while those with steeper slopes will be enhanced.

The effect of lensing by clusters of galaxies on the resolved and unresolved components of the X-ray background (XRB) is discussed at length in Refregier and Loeb (1997), who predict an overall depletion of resolved sources due to the shallow slope of the XRB number counts at fluxes fainter than $\sim 10^{-14}$ erg s^{-1}. The measured slope of the full band EXDS number counts over the flux range (1.1 - 15)$\times 10^{-15}$ erg $s^{-1} cm^{-2}$ is $\alpha \sim 0.8$, steepening to a Euclidean slope at brighter fluxes (Manners et al. 2003). Lensing in the MS1054-03 field should lead to a deficit rather than an excess of in the number counts at all fluxes fainter than the break.

To investigate whether this effect might be significant enough to significantly deplete the source counts in the inner regions of the cluster, I model the cluster as a single isothermal sphere (SIS) with a central density profile $\rho(r) \propto r^{-2}$. While clearly a gross approximation to the complex mass structure observed in MS1054-03, the SIS profile provides a simple estimate of the magnitude of the lensing effect. For a SIS lensing potential, the lensing factor, $\mu(\theta)$, can be expressed as

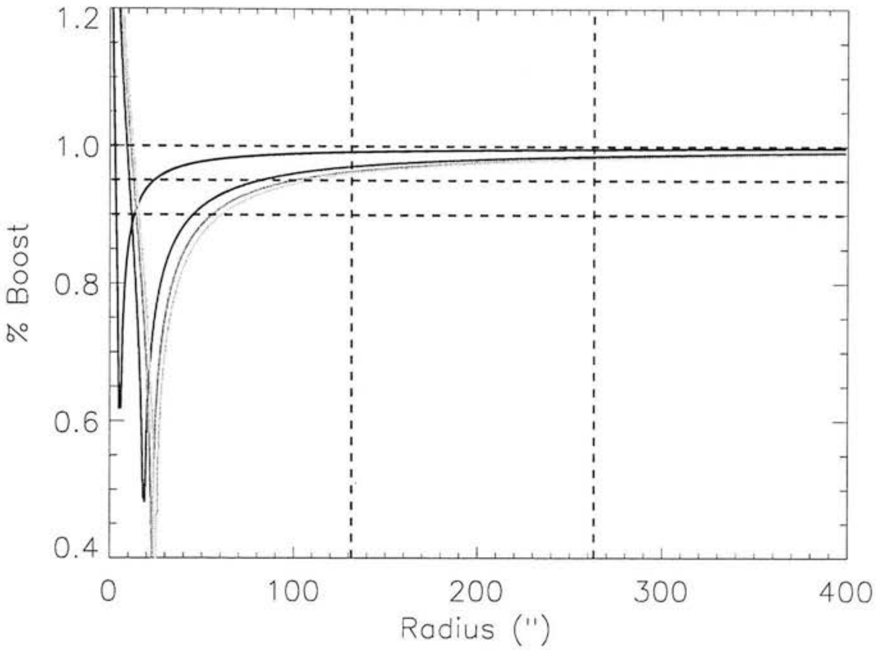

Figure 4.4: *Fractional boost of integral number counts due to gravitational lensing of background populations by MS1054-03, as a function of radius. The curves show lensing boost from background sources at a redshift of, from top,* $z = 1$*, 2, 3, and 4, while the vertical dotted lines mark 1 and 2 Mpc at* $z = 0.83$ *and the horizontal lines mark source count deficits of 10%, 5%, and 0%.*

$$\mu(\theta) = \left|1 - \frac{\theta_E}{\theta}\right|^{-1} \tag{4.6}$$

where $\theta_{(E)}$ is the Einstein radius. Following Blandford and Narayan (1992), $\theta_{(E)}$ is given in terms of the angular diameter distances between the source and the lens, D_{LS}, and between the source and the observer, D_{OS}:

$$\theta_E = \frac{4\pi\sigma^2}{c^2}\frac{D_{LS}}{D_{OS}} = 2.6''\sigma_{300}^2\frac{D_{LS}}{D_{OS}} \tag{4.7}$$

where σ_{300} is the velocity dispersion of the lens, in units of 300 km s^{-1}.

The velocity dispersion of MS1054-03 has been measured dynamically (Tran et al. 1999; $\sigma \sim 1170 \pm 150$ km s^{-1}) and estimated through weak lensing analysis (Hoekstra et al. 2000; $\sigma = 1215^{+63}_{-67}$ km s^{-1}). I adopt a value of 1200 km s^{-1}.

Figure 4.4 shows the expected fractional boost of source counts as a function of radius for background populations at $z = 1$ through $z = 4$. The effect of lensing on the measured source counts is less than 5% beyond $\sim$ 1 Mpc and less than 10% beyond $\sim$ 0.5 Mpc. As we expect detection of only a few sources interior to 0.5 Mpc in a blank field (see Figure 4.3), the lensing deficit is effectively negligible at all radii.

4.4.3 Radio overlap

Best et al. (2002) conducted extremely deep radio observations of MS1054-03 at 5 GHz with a full-width-half-power primary antenna beam diameter of $9'$. They detected 34 sources to a 6σ level of 32 μJy, compared with 25 expected from a blank field. The excess radio source counts are all found within 1 Mpc of the cluster centre, and 8 sources are spectroscopically confirmed cluster members. Of the cluster radio sources, seven appear to be powered by AGN. On the basis of radio flux density to optical emission line flux ratio, Best et al. (2002) report six cluster AGN and one ambiguous source with a ratio between that expected for AGN and that expected for star-forming galaxies. The ambiguous source is detected in the X-ray image with a $L_{(0.5-8\ \mathrm{keV})} \sim 10^{43}$ erg s^{-1}, however, which confirms it is an AGN. Four of these host galaxies are in merging systems, suggesting the activity may be induced by interactions.

Six sources are detected in both radio and X-ray, only one of which is at the cluster redshift. The single cluster AGN detected in both the X-ray and the radio is CXOU105702.7-033943 (source 19; Best et al. source 14). As stated earlier, the optical counterpart has galactic morphology and colours on the cluster sequence and the X-ray hardness ratio is consistent with a typical AGN powerlaw spectrum with moderate ($\sim 10^{22}$ cm^{-2}) intrinsic absorption. The radio and X-ray luminosities are in good agreement with the Elvis et al. mean SED for radio-loud AGN (see below, and Figure 4.5).

The fraction of X-ray sources detected in the radio – 6 out of 47 – is consistent with the observation that $\sim$ 10% of all AGN are radio-loud (e.g., Sramek and Weedman 1980). If this fraction holds within the cluster, we would expect no more than one of the two confirmed or six suspected X-ray AGN to be radio-loud. Referencing the mean SED of Elvis et al. (1994), the expected radio flux for a radio-quiet QSO with $L_{(0.5-8\ \mathrm{keV})} \sim 10^{43}$ erg s^{-1} cm^{-2} is an order of magnitude lower than the radio detection limit. The detection of just one of the X-ray AGN in MS1054-03 at radio wavelengths is therefore consistent with expectation.

The small fraction of radio sources detected in the X-ray – 6 out of 34 – is perhaps more surprising. While many of the field radio sources are likely to be starburst galaxies which we would not expect to detect in X-ray observations at this depth, at least 7 of the sources are radio-loud cluster AGN which should emit strongly in the X-ray. However, since the radio to X-ray flux ratio in AGN is seen to vary by several orders of magnitude (Brinkmann et al. 2000, Bauer et al. 2002), it is difficult to estimate the expected X-ray luminosity of the radio AGN. In figure 4.5 I plot the radio flux of the seven cluster radio AGN versus the expected X-ray flux calculated from the Elvis et al. (1994) mean radio-loud QSO SED. Following the Elvis *et al.* SED, all seven sources could have been detected in our X-ray observation. Though scatter around the mean might account for the non-detection of the fainter radio sources, the brightest sources have predicted X-ray fluxes which are 1 to 2.5 orders of magnitude brighter than the flux limit.

Dense absorbing columns could provide a possible explanation. Obscuration of 12 – 70% of the 0.5 - 8 keV X-ray flux expected from the faintest four radio detections would be sufficient to put them below the

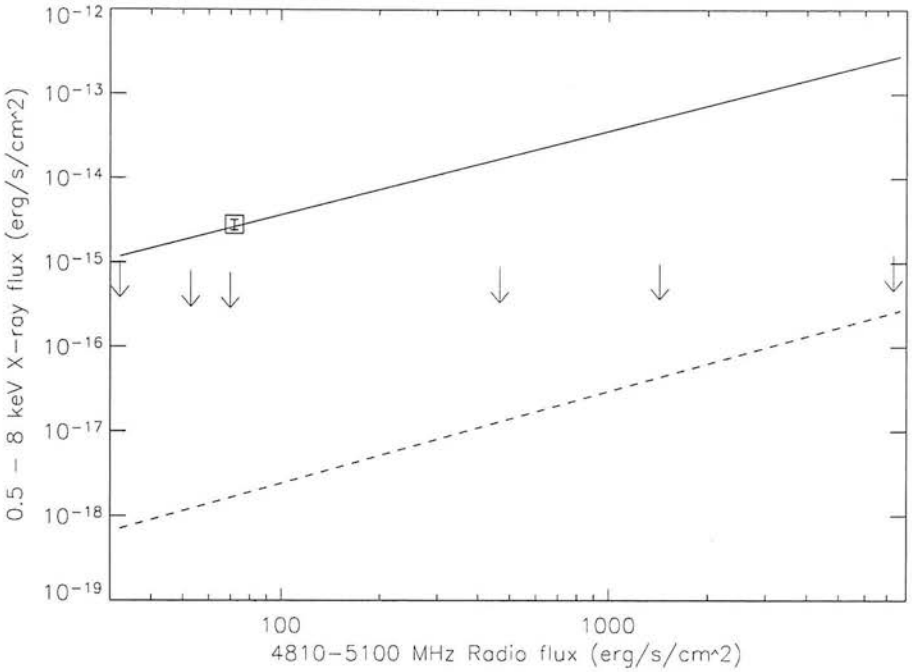

Figure 4.5: *Radio flux versus expected X-ray flux for the 7 confirmed radio sources in MS1054-03. The upper, solid line makes the X-ray flux predicted for the measured radio flux by the Elvis et al. (1994) mean radio-loud QSO SED; the lower, dotted line marks the flux predicted by the Sambruna et al. (1999) relation for radio-loud AGN. (See text for details.) The upper limits indicate the limiting flux of the X-ray image at the location of the radio sources, and the square shows the measured X-ray flux of CXOU105702.7-033943.*

X-ray detection limit. This level of absorption would result from relatively modest columns of $\sim 5 \times 10^{21}$ cm^{-2} up to a few times 10^{23} cm^{-2}. For the brightest three radio sources, 95% to 99% of the expected X-ray flux would need to be absorbed to push them below the detection limit. Absorbing columns of 10^{24-25} cm^{-2}, as are found to be relatively common in Seyfert 2s (e.g., Maiolino et al. 1998), would be needed for these three objects.

It is possible the Elvis *et al.* mean SED, derived from a sample of 18 luminous X-ray selected radio-loud QSOs, is not representative of the weaker radio AGN populating MS1054-03. Sambruna et al. (1999) include weaker radio galaxies in their X-ray survey which, in the unified model, contain substantial absorption along the line of sight and may more closely resemble the sources in our cluster. The dotted line in Figure 4.5 shows their empirical relation of lobe 5 GHz luminosity to hard X-ray flux, assuming that lobe emission dominates the radio flux, and extrapolating hand band X-ray flux to full band flux using an unobscured powerlaw spectrum with an energy index, $\alpha = 0.7$. The resulting expected X-ray fluxes are likely too high, as non-negligible radio flux may arise from the compact core and obscuring material having little effect on the hard band flux may significantly absorb flux at lower energies. However, even these optimistically high fluxes suggest that all seven radio AGN in MS1054-03 may be too faint to be observed in the X-ray.

A third possibility is that the radio luminosities may be contaminated by a stellar component. The low optical emission line flux to radio flux density values, as well as the red optical colours of the radio sources which are consistent with the cluster sequence, argue against a post-starburst origin. However, we cannot entirely rule out some amount of the radio emission arising from stellar activity rather than AGN activity, and this could help to explain the X-ray non-detections.

If the stellar contamination to the radio fluxes is low, and if the usual radio-loud to radio-quiet ratio holds throughout the cluster, the radio-detected AGN may trace a larger AGN population nearer to the the cluster core. For the 7 detected radio-loud AGN, one would expect ~ 70 radio-quiet counterparts. Like the radio-loud but X-ray quiet sources, these would need to be either heavily obscured or simply much less luminous than the detected X-ray sources to avoid detection in the current data. While a vast increase in the fraction of heavily obscured objects in the inner regions of the cluster seems improbable, a population of less luminous AGN, such as those observed in clusters at low redshift, cannot be ruled out. Alternatively, the radio-loud to radio quiet fraction within the core of MS1054 may be elevated due to a dependence on AGN luminosity and/or environment, perhaps due to boosting of the radio flux, as discussed by Best (2004).

4.4.4 Radial distributions

The X-ray detected AGN seem not to be distributed randomly within the cluster but rather to populate the outer 1–2 Mpc, suggesting they may just be falling into the cluster. Similarly, Martini et al. (2002) note that while the galaxies hosting the cluster AGN in A2104 have colours on the cluster sequence, their velocity dispersion is larger than the mean cluster dispersion, perhaps suggesting recent infall. If galaxies hosting luminous cluster AGN are found to be recent arrivals to the dense cluster environment, it may indicate the AGN activity is induced by infall. As discussed in §1.4.2, it is an open debate whether introduction into a cluster environment serves purely to quench star formation activity in infalling field galaxies, or results in an initial enhancement in activity before quenching begins (cf. Poggianti 2002, and references therein). The post-starburst 'k+a' galaxies seen in abundance in distant clusters (Dressler et al. 1999) may be evidence of the latter scenario, if it is found that starburst activity in the field is not sufficient to account for them. If the conditions prompting starbursts in infalling members also serve to fuel AGN, the detection of an excess of AGN at the edges of dynamically active clusters may be expected, and could be a discriminator between the two scenarios described above.

Finally, it is worth emphasizing in this context that the AGN identified by radio observations are found somewhat nearer to the cluster centre (< 1 Mpc). If they are the radio-loud members of a population of weaker AGN which are below the X-ray flux limit, they may indicate a decrease of AGN activity in host galaxies which have been longer resident in the dense cluster environment.

4.5 Conclusions

I have detected an excess of point sources in the field of the rich cluster MS1054-03 at $z = 0.83$. The excess is most significant at fluxes brighter than $S_{(0.5-8\ \mathrm{keV})} = 5 \times 10^{-15}$ erg s^{-1} cm^{-2} (corresponding to a rest frame $L_{(0.9-14.6\ \mathrm{keV})} \simeq 10^{43}$ erg s^{-1} for cluster members) and arises in the outer parts of the cluster field, at angular separations consistent with radial distances of 1 - 2 Mpc from the cluster centre. The observed source counts cannot be accounted for by cosmic variance, and gravitational lensing of background counts by the cluster is expected to be negligible across the field. I conclude the most likely explanation of the excess counts is a population of luminous (L $\sim 10^{43}$ erg s^{-1}) AGN associated with the cluster. The X-ray excess arises between 1 and 2 Mpc from the cluster centre, exterior to the excess of radio sources identified by Best et al. (2002). Follow-up observations will be necessary to completely identify the X-ray detections in this field, but the association of two luminous AGN with the cluster is already confirmed from existing observations. CXOU105710.6-033500 (source 7) is 1.7 Mpc from the cluster centre with a luminosity of 2.6×10^{43} erg s^{-1}, and CXOU105702.7-033943 (source 19) is 1.0 Mpc from the cluster centre with a luminosity of 5.0×10^{42} erg s^{-1}. Including the further 6 radio AGN detected at 5 GHz by Best et al. (2002), there are at least 8 luminous active nuclei associated with MS1054-03.

This study augments earlier results, confirming that luminous AGN can and do reside in rich cluster environments. The luminosities of $\sim 10^{43}$ erg s^{-1} we observe at $z = 0.83$ suggest this population is similar to that seen in 3C295 and RXJ0030 at $z \sim 0.5$ (Cappi et al. 2001). Fainter populations such as the LLAGN seen in nearby clusters and the starburst population seen in A1995 at $z = 0.32$ may also be present in higher redshift clusters such as MS1054-03. The radio AGN detected by Best et al. (2002) but not detected in the X-ray may be evidence of just such a weaker population in MS1054-03. However, there is no low redshift equivalent to the population of luminous sources which are apparently common in high redshift clusters like MS1054-03. As not all clusters exhibit a population of point sources, the extent and strength of AGN activity within a cluster is likely dependent on both redshift and dynamical state. Further study will be directed to examining these relations. Finally, the fact that the luminous X-ray sources in MS1054-03 are observed only at the edges of the cluster is suggestive of infall induced activity, the quenching of which may give rise to fainter AGN at smaller cluster-centric radii. Exploring this possibility is another motivation for further complete surveys of AGN in distant clusters.

CHAPTER 5

SSA22

The SSA22 region is thought to contain an overdensity of ~ 150 galaxies at $z \simeq 3.09$ within a region of 10 by 14 comoving Mpc and is almost certainly the precursor to a bright X-ray cluster. Populations of Lyman Break Galaxies, Lyα emitters, and submillimetre-bright galaxies comprise the protocluster, which also contains luminous, diffuse, Lyα emission on scales of up to 100 kpc. In this chapter, I first supplement the known catalog of objects associated with the protocluster with wide-field narrow-band Lyα observations of the field. I then present an extremely deep (150 ks) XMM-Newton survey of the region.

In §5.1, I discuss the motivation for X-ray studies of protoclusters at high redshift, and introduce the SSA22 region. I describe the reduction and analysis of the narrow-band data in §5.2 and the basic reduction of the X-ray data in §5.3. I then present the results of the X-ray survey: the direct X-ray detections of protocluster members in §5.4; a stacking analysis of the high redshift populations in §5.5; and limits on diffuse X-ray emission in §5.6. I summarize my work on the SSA22 protocluster in §5.7.

5.1 Introduction

The characteristics of massive clusters and of the galaxy populations which comprise them provide important tests of structure formation and galaxy evolution models. Extending the study of clusters through the formation epoch of the hot intracluster medium and the peaks in star-formation and AGN activity will allow integrated study of the coevolution of AGN, their host galaxies, and the environment on larger scales. In recent years, Chandra and XMM observations have confirmed cluster candidates selected at the limit of ROSAT's sensitivity with redshifts of up to ~ 1.3, and large-area and serendipitous surveys are currently underway to explore the cluster population at $z > 1$. However, as noted in §1.4, X-ray detection of galaxy overdensities at $z > 1.5$ is a significant observational challenge, as virialized clusters with a luminous ICM will be both much rarer and much fainter at high redshift.

Considerable progress has been made in identifying dense environments at higher redshift through targeted survey techniques. Surveys of the fields of powerful radio galaxies at $2 < z < 4$ — which are extremely massive and thus expected to preferentially inhabit the densest regions of the Universe — have revealed significant excesses of high redshift populations of Lyα emitters, luminous submillimetre galaxies, and extremely red objects (e.g., Venemans et al. 2002, Pascarelle et al. 1998, Kurk et al. 2003). Spectroscopic follow-up has confirmed these excesses are at the redshift of the radio galaxies, which emerge as effective signposts of protocluster environments. Large scale surveys based on the detection of the redshifted 912 Å Lyman continuum break have also identified significant overdensities of galaxies at $z \sim 3$, of which the topic of this chapter is the most striking example.

An overdensity of $z \simeq 3.09$ galaxies in the SSA22 field was first noted by Steidel et al. (1998), who reported a highly significant spike in the distribution of redshifts obtained during spectroscopic follow-up of a Lyman-break survey designed to identify the Lyman break in objects with $2.7 < z < 3.4$ (Steidel et al. 2003). In the final spectroscopic catalog, 22 galaxies and one faint QSO are identified with $3.074 < z < 3.108$ out of a total of 65 confirmed high redshift Lyman Break Galaxies (LBGs) in the region. The density of LBGs at $z \simeq 3.09$ is roughly 6 times the average value. From the magnitude of this overdensity, Steidel et al. (1998) argue that LBGs are massive systems of roughly $10^{12} M_{\odot}$ which are highly biased tracers of mass and the progenitors of modern day galaxies with $L > L^{*}$. Accounting for the estimated inefficiency of the spectroscopic identification, the structure at $z \simeq 3.09$ is likely to be a precursor to a massive X-ray bright cluster containing 30-60 such galaxies.

Multiwavelength observations have identified a complex variety of sources associated with the forming cluster. A follow-up narrow-band imaging survey designed to isolate the Lyα line at $3.054 < z < 3.120$ identified 120 additional protocluster candidates, and confirmed a galaxy overdensity of $\simeq 6$ with respect to the field population (Steidel et al. 2000). In addition, two luminous Lyα nebulae were detected with luminosities of $\sim 10^{44}$ erg s^{-1}and physical sizes of ~ 100 kpc. A subsequent deeper Lyα survey conducted by Matsuda et al. (2004) identified 35 extended nebulae, of which the two Steidel et al. (2000) sources — 'Blob 1' (B1), and 'Blob 2' (B2) — are the largest and most luminous. Submillimetre observations of the field reveal a luminous submillimetre counterpart ($S_{850\mu m} = 20$ mJy) at the location of B1, a marginal detection of B2, as well as an excess of submillimetre sources in the field, 3 of which are confirmed to

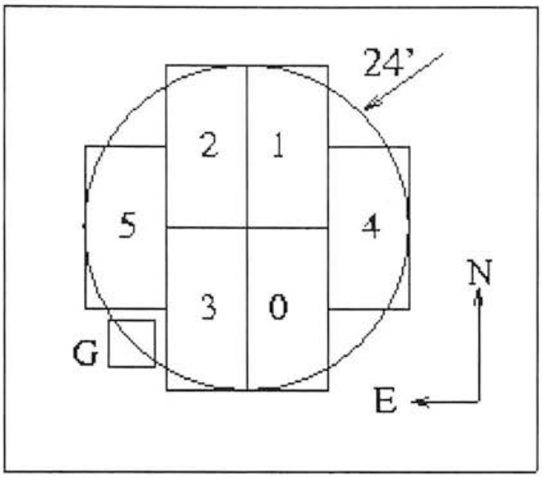

Figure 5.1: *Schematic of the focal plane of the Palomar Large Format Camera. Figure from http://www.astro.caltech.edu/~ras/lfc/lfc.html.*

be associated with the protocluster (Chapman et al. 2001, Chapman and Baugh 2004). Several additional studies have attempted to constrain the heating mechanism of the diffuse Lyα emission (see §5.6; Taniguchi et al. 2001, Ohyama et al. 2003, Chapman et al. 2004, Bower et al. 2004). Finally, a 75 ks Chandra observation of the field was obtained, though never published, and is available in the public archive.

The goals of the X-ray study presented in this chapter are to determine the X-ray properties of the high redshift populations comprising SSA22 and of the diffuse material associated with the protocluster. Throughout the chapter, I adopt a flat ΛCDM cosmology with $\Omega_\Lambda = 0.7$ and $H_0 = 70$ km s^{-1} Mpc^{-1}. In this model, $1''$ corresponds to 7.7 kpc at $z = 3.09$.

5.2 Narrow-band imaging

The Steidel et al. (2000) deep narrow-band (NB) Lyα survey was conducted in a $9.7' \times 9.7'$ region in the protocluster field. To search for likely protocluster members over a wider field of view, I have conducted a similar — though shallower — survey over a substantially larger region using the Palomar Large Format Camera (LFC). The LFC is a mosaic of six 2048×4096 pixel CCDs mounted at the prime focus of the 200-inch Hale Telescope at the Palomar Observatory. At the focal plane, the 15μm pixels correspond to $\sim 0.18''$ on the sky and the total field of view is a $25' \times 25'$ cross (see Figure 5.1).

The NB data were obtained on 3, 5, and 6 August 2002 by S. Chapman, who also provided a fully reduced 3 hr integration in the g' filter obtained on 4 August 2002. The NB interference filter is identical to that described in Steidel et al. (2000), with a bandwidth of FWHM = 80 Å centred at 4970 Å, and is sensitive to Lyα line emission at $3.054 < z < 3.120$.

5.2.1 Mosaic reductions

Reduction of the data were done with the `mscred` package (v4.7) within the NOAO Image Reduction Analysis Facility (IRAF: v2.12). The raw LFC data were assembled into `mscred`-compatible multi-extension FITS (MEF) files using the `lfcassemble` script [1] and then processed following the reduction sequence developed for the NOAO Deep Wide-Field Survey (Jannuzi et al. 2002).

The processing of the initial calibration frames was done with MEF-compliant versions of the standard IRAF `ccdproc` and associated tasks. Gain and readnoise values were measured with `mscfindgain` and the combined bias was generated with `zerocombine`. The `mscred` version of `ccdproc` also produces bad-pixel masks during this stage of reduction on which saturated pixels, bleed trails, and known chip defects are flagged. No dark frames were obtained, and bias frames were obtained only for the final observing night. There is substantial structure in LFC chip 0 in some bias exposures which is possibly due to residual charge not cleared from the CCD prior to observation and leads to a low-level artefact in the reduced images. Useful flats were obtained on only the first and last nights of observing, so data taken on 5 August has been processed with the dome flat from the final night.

Sky flats were constructed for each night from the dithered source exposures. It was necessary to exclude several exposures from further analysis due to a severe light leak affecting LFC chip 4. Object masks were created for the remaining exposures with the `objmask` task, which combines the pre-existing bad-pixel masks with a mask of objects detected in each image. These masks were then input to the `sflatcombine` task, which produces a blank-sky image by averaging the unmasked regions of the dithered images. There were no pupil-ghost or fringing effects visible in the blank sky flats, which were applied to the individual object frames with `ccdproc`.

The default LFC World Coordinate System (WCS) for the g'-band was set with the `mscsetwcs` task, and improved by alignment of objects in the images to catalogued stars. Unsaturated bright stars were selected from the USNO-A2 catalogue with `mscgetcat`. As large offsets from the default astrometry were present, initial rough alignment was done with `msczero`, which overlays the catalogue positions on the data and facilitates user input of the necessary shift. The astrometric correction was then refined by interactively fitting the x and y positions of objects to the catalog positions with `msccmatch`. Several dozen stars were used in the final fits, and the residuals in x and y were of order $0.4''$.

The positions of cosmic rays were added to the bad pixel masks (`craverage`, `crplusbpmask`) and the bad pixels were replaced with values interpolated from surrounding pixels (`fixpix`). The individual MEF frames were then resampled into a uniform pixel scale and projected relative to a common position — chosen to match the scale and projected position of the g'-band image — with the `mscimage` task. Large scale variation in the sky background was removed with `mscskysub`. The relative scaling of the images was determined by measuring the intensity in a number of object regions in each exposure and interactively fitting to intensities measured in a reference exposure (`mscimatch`). Finally, the exposures from all three nights were combined using `mscstack`.

The resulting NB image, which is shown in Figure 5.2 with the locations of confirmed or likely pro-

---

[1] Provided at http://wopr.caltech.edu/~mph/lfcred.

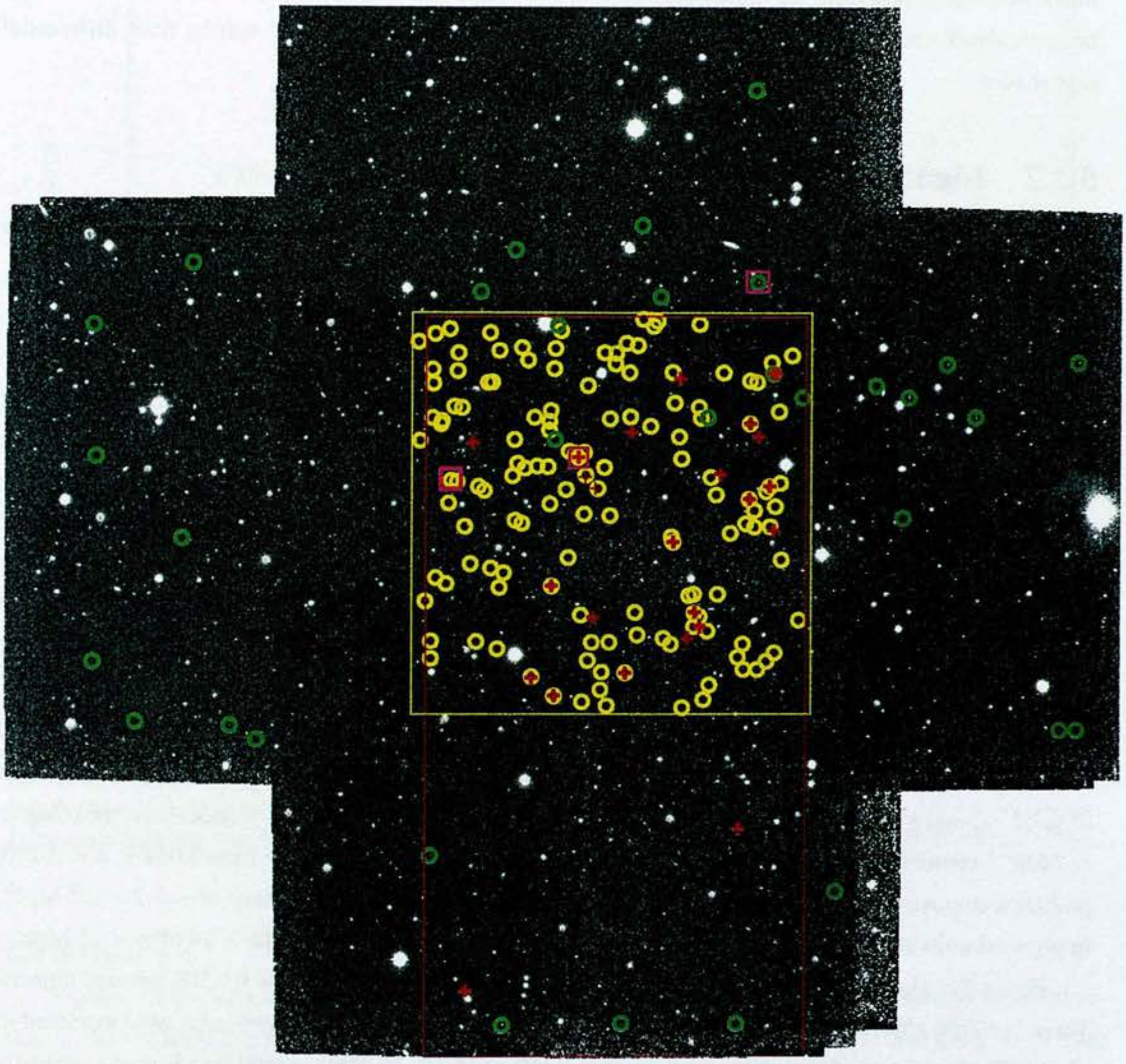

Figure 5.2: *Reduced narrow-band mosaic of the SSA22 field. The yellow square and red rectangle indicate the approximate FOV of the deep narrow-band (Steidel et al. 2000) and Ly-break (Steidel et al. 1998) surveys discussed in 5.1. Red crosses mark the locations of spectroscopically confirmed protocluster members, and the yellow and green circles indicate candidate members identified in deep (Steidel et al. 2000) and wide-field (§5.2) narrow-band Lyα imaging, respectively. The positions of three protocluster candidates directly detected in the X-ray are indicated with magenta squares and discussed further in §5.4.*

tocluster members overlaid, consists of 7.12 hr of integration, and has seeing of $1.1''$ FWHM. The 1σ magnitude limit within an aperture the size of the seeing disk is NB = 24.46 mag. The 3 hr g-band integration also has seeing of $1.1''$ FWHM, and reaches a magnitude limit of $g' \simeq 26.5$ mag.

As no spectrophotometric standard stars were observed, zero-points for both the NB and the g'-band image were estimated from the Guide Star Catalog B_J magnitudes. Absolute calibration is not necessary because identification of Lyα excess objects, as discussed in the next section, will be from differential magnitudes.

5.2.2 Identification of candidate protocluster members

As the FWHM of the NB filter is 80 Å, a Lyα emission line with an equivalent width ≥ 80 Å would at least double the counts in the NB image, resulting in a colour shift of $\Delta M_{g'-NB} \sim 0.75$. Following Steidel et al. (2000), I aim to select candidate Lyα excess sources with $\Delta M_{g'-NB} \geq 0.7$ — corresponding to an excess of narrow band flux of a factor of 1.9 — and begin by constructing a catalogue of NB-selected objects.

Object detection and photometry were done with the SExtractor algorithm (Bertin and Arnouts 1996) running in 'double-image' mode, which allows the apertures determined from one image (the 'detection image') to be used to measure magnitudes in a second (the 'measurement image'). The detection image was convolved with a Gaussian filter with a FWHM of 5 pixels ($0.9''$), chosen to approximate the PSF of the images. Thresholds were set such that objects with $1.5\times$ the unfiltered sky noise in an area of at least 5 connected pixels were detected. Isophotal apertures determined from the detection image were used to measure the magnitudes in both images from which colours were computed. A larger ellipsoidal aperture was used to obtain the total magnitudes in the detection band (`MAG_AUTO`; see Bertin and Arnouts 1996).

Large numbers of spurious sources were detected at the edges of the field due to the higher background noise level where fewer dithered frames had been coadded. A mask was therefore used to isolate regions of good exposure on the chip. The total useful survey area was ~ 430 square arcmin, corresponding to $\sim 740h^{-1}$ comoving Mpc^2 at $z = 3.09$. The NB filter is sensitive to the Lyα line from $3.054 < z < 3.120$, probing a comoving radial distance of 43 h^{-1} Mpc, and giving a total survey volume of $\sim 3.2 \times 10^5$ Mpc^3. In physical units at the distance of the protocluster, this volume is roughly 14 Mpc × 14 Mpc × 15 Mpc.

Figure 5.3 plots the $g' - NB$ colour plotted versus the total NB magnitude for NB-selected objects. There are 2756 objects in the NB-selected catalog for which valid isophotal magnitudes were extracted in g' and NB; the faintest of these has a total NB magnitude of 25.17. Though the catalogue is photometrically complete only to $NB \sim 24.5$, my object is to identify as many $z = 3.09$ sources as possible and so I consider all NB detections.

The locus of points in the $g' - NB$ versus NB magnitude plane is marked with a solid line in Figure 5.3 and lies roughly 0.2 mag above zero. This is due to the difference in throughput between the B_J band used to zero the images and the g' and NB filters, and reflects the average source colour. A small trend with NB magnitude is seen — the average colour shift decreases slightly from sources at the brightest magnitudes, which are mainly stars, to sources at fainter magnitudes, which are dominated by galaxies — but this variation is minimal and a single value of 0.21 is adopted as the $g' - NB$ zeropoint. Narrow-band excess sources are selected which have $g' - NB \geq 0.7$ mag above this zeropoint, as marked by the dashed

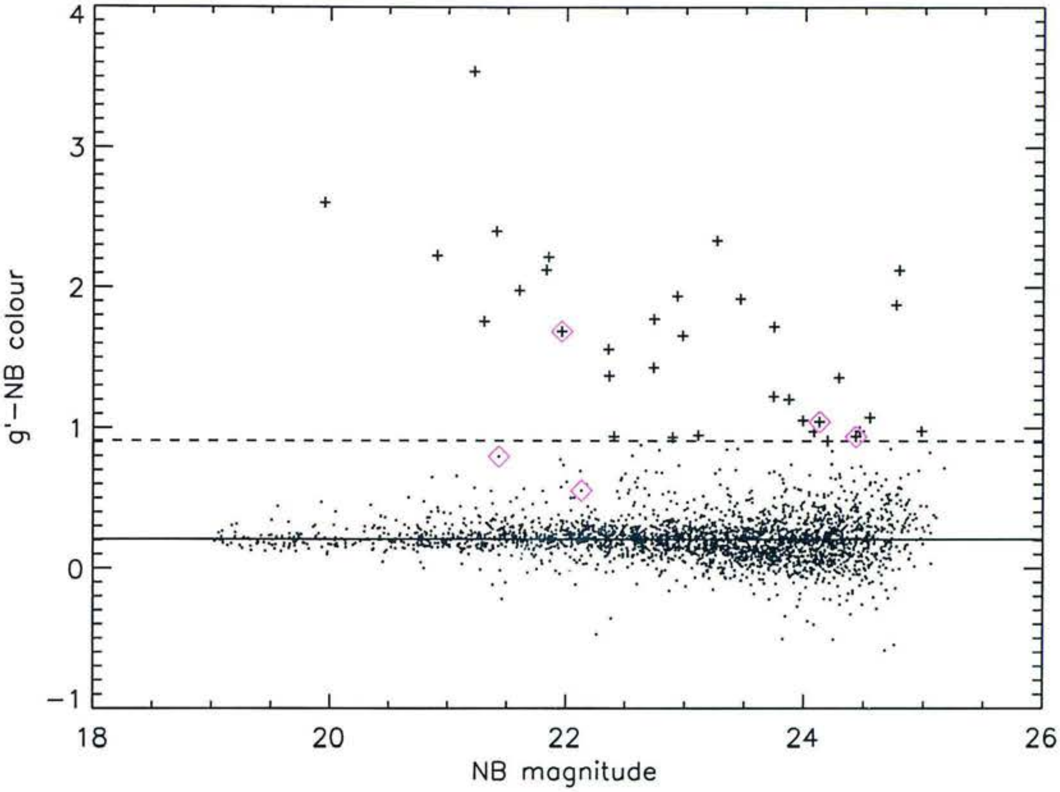

Figure 5.3: *Total NB magnitude vs.* $g' - NB$ *colour for NB-selected sources in the SSA22 field. The solid line marks the locus of points at 0.21 mag; the dotted line indicates the colour shift of* ≥ 0.7 *mag above this locus which defines NB excess objects. Crosses indicate sources selected as Ly*α *excess candidates. Diamonds indicate sources selected as Ly*α *excess candidates in the deep Ly*α *survey of Steidel et al. (2000).*

line in Figure 5.3.

Significant scatter about the locus is seen which increases towards fainter magnitudes and is an indication of the variation in continuum colour of sources between the NB filter at 4970 Å and the g'-band filter with a central wavelength of 4660 Å. Excluding the clear excess points, the standard deviation in $g' - NB$ for the NB-selected objects is 0.15 mag. In the absence of deep imaging in a nearby band with which to determine the source colour, an uncertainty of 0.1 – 0.2 mag exists on each object and decreases the sensitivity of the narrow-band selection. That two of the sources identified as $z \simeq 3.09$ candidates in the Steidel et al. (2000) deep survey (diamonds in Figure 5.3) fail to be selected by the current survey is likely due to this effect.

The 34 sources meeting the criteria for narrow-band excess selection are marked with crosses in Figure 5.3. Each candidate source was examined by eye in both the NB and g' filters. Two sources are likely associated with artefacts in the NB image. The remaining 32 sources comprise my Lyα excess candidates, which are listed in Appendix B.

As noted by Steidel et al. (2000) and discussed by Cowie and Hu (1998), the narrow bandpass is sensitive not only to the Lyα line emitted at $3.054 < z < 3.120$ but also to the [O II] $\lambda3727$ line at $0.323 < z < 0.344$ and to [OIII] $\lambda4959/\lambda5007$ at zero redshift. In the absence of complementary data, none of my Lyα candidates can be individually confirmed as a protocluster member. However, it is likely that the majority of the excess objects are at the target redshift. The volume probed at $z \sim 3$ is roughly 20 times larger than that at $z \sim 0.3$ and the volume probed at $z = 0$ is negligibly small (Steidel et al. 2000). Furthermore, the magnitude of the excess emission detected argues for a high redshift origin. The mean observed equivalent width of > 200 Å implies rest frame equivalent widths which would be unusually large for [O II] emission at $z \sim 0.3$. More extensive studies also provide evidence of a low contamination rate. Using broad-band photometry, Steidel et al. (2000) confirm that 5 of 77 (6%) narrow-band excess sources in their deep SSA22 survey are lower redshift sources. Similarly, in a sample of 56 narrow-band excess sources identified by Fynbo et al. (2003), follow-up spectroscopy showed that 4 (7%) were foreground objects, 11 (20%) had no emission line detected to a 3σ limit, and the remaining 41 (73%) were Lyα emitters at the target redshift.

The spatial distribution of these sources with respect to other confirmed or candidate protocluster members can be seen in Figure 5.2. That several candidates are identified at the edges of the useful FOV suggests varying data quality between the NB and g' images may be influencing the selection of candidates and that inferences about the morphology of the protocluster based on these data should be made only cautiously. Steidel et al. (1998) note an apparent Southern edge to the spectroscopically confirmed $z \sim 3$ overdensity in their Ly-break survey field (red rectangle in Figure 5.2). The majority of new candidates extend to the North and East of the confirmed Ly-break overdensity, and do not seem to extend to the edge of the FOV. The lack of new Lyα detections in the Southern half of the protocluster region may be due to added noise in this region due to the bias artefacts in chip 0.

5.3 X-ray data

XMM observations of the SSA22 field were obtained in two segments: observation 0094310101 on 18 Oct 2002 (revolution 0539) with a scheduled length of $\sim$ 69 ks, and observation 0094310201 on 15–16 Dec 2002 (revolution 0553) with a scheduled length of $\sim$ 81 ks. Observation 0094310101 was further split into Scheduled ($\sim$ 7.5) ks and Unscheduled ($\sim$ 57) ks exposures due to technical problems during data acquisition. All observations are centred at 22:17:34.2, +00:15:1.00 and are taken in Full Window mode through the Thin1 filter.

5.3.1 Basic reduction

Initial reductions of the data were done following the standard procedures and using XMM SAS tools, as described in 2.4. The `cifbuild` task was used to compile a list of the best calibration available for the observation dates as of March 2004. As some of the calibration components differed significantly from those available for pipeline processing, the raw MOS and pn data were reprocessed into event lists using

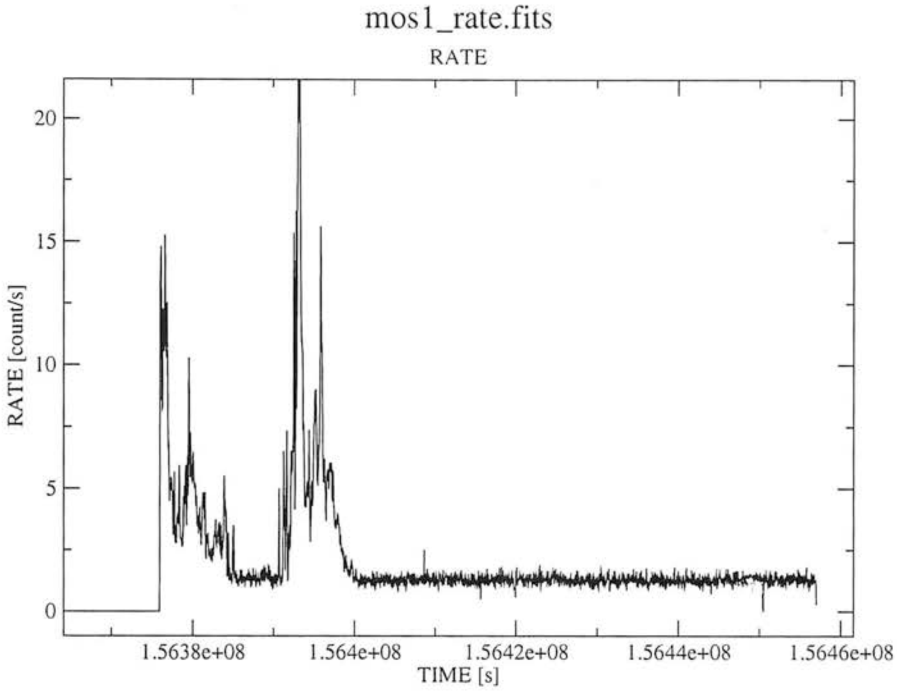

Figure 5.4: *10 – 15 keV light curve for the MOS exposure 00943010201 illustrating significant flaring in the background rate.*

the `emchain` and `epchain` tasks, respectively.

The lists were then filtered by energy, `FLAG`, and `PATTERN`, as discussed in 2.4.3. For imaging, event lists were constructed with energies between 0.2 and 15 keV, with `PATTERN` values of 12 or lower, and the usual `#XMMEA_EM` and `#XMMEA_EP` quality flags. These 'standard filter' event lists contain ~ 55% and ~ 67% of the pipeline-processed counts for the MOS and pn cameras, respectively. For spectroscopy, more conservatively filtered lists were produced, for which only single and double pn events (`PATTERN` $\geq$ 4) of the highest quality (`FLAG = 0`) are included. These lists contain ~ 54% and ~ 49% of the pipeline processed MOS and pn counts. Examination of images made with both filters suggested using the conservative filter for all pn analysis, as many artefacts remain in the standard filter pn image, particularly at soft energies.

Rate curves for each instrument were produced by binning all events with energies greater than 10 keV into 50 s bins to test for background flaring. While data from the first orbit was unaffected by flares, significant flaring can be seen at the beginning of the second orbit exposure, as shown in Figure 5.4. Quiescent count rates were chosen at 2 counts s^{-1} for the MOS chips and 9 counts s^{-1} for the pn detector. Non-flaring intervals were defined using the `tabtigen` task, and applied to the data using `evselect`. As each detector may record flares slightly differently, this was done for MOS1, MOS2, and pn separately. Approximately 20 ks of data were affected by the background flaring, and ~ 30 – 35% of counts remaining

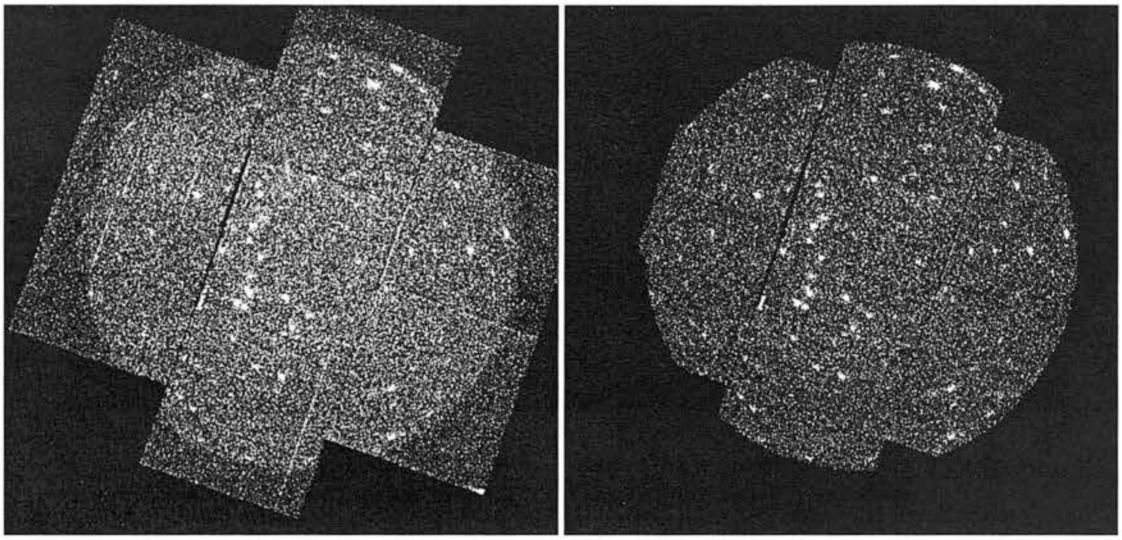

Figure 5.5: *Left) 0.3 – 4.5 keV unfiltered MOS 1 image of SSA22 from pipeline processed data. Right) The same data with standard* `FLAG` *and* `PATTERN` *filters and background flaring removed.*

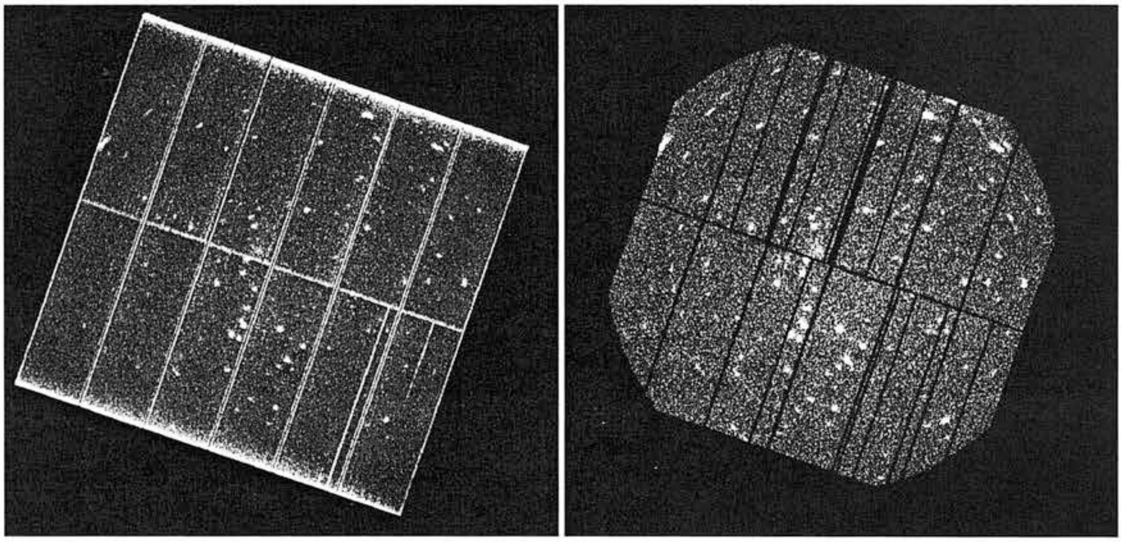

Figure 5.6: *Left) 0.3 – 4.5 keV unfiltered pn image of SSA22 from pipeline processed data. Right) The same data with conservative* `FLAG` *and* `PATTERN` *filters and background flaring removed.*

after energy, `FLAG`, and `PATTERN` filtering were associated with these times.

Figures 5.5 and 5.6 illustrate the effect of `FLAG`, `PATTERN`, and background flare filtering for MOS1 and pn data, respectively. An image of the SSA22 field produced from the pipeline-processed 0.3 – 4.5 keV event list is shown for both pn and MOS alongside the significantly cleaner image constructed from the filtered event lists.

Images and exposure maps were produced with the standard SAS tools, `evselect` and `eexpmap`. As the FWHM of the on-axis PSF is $\sim 6''$, the events in the full (0. 5 – 8 keV), soft (0.5 – 2 keV), and

Band (keV)	MOS 1 ECF	MOS 2 ECF	pn ECF
0.5–8.0	1.067	1.071	3.396
0.5–2.0	1.980	1.977	6.596
2.0–8.0	0.510	0.518	1.457

Table 5.1: *XMM energy conversion factors for the full, soft, and hard bands, in units of* 10^{11} *counts* cm^2 erg^{-1}.

hard (2 – 8 keV) bands were binned into 4.35″ pixels and the resulting images trimmed to 512×512 pixels. `eexpmap` does not permit the input of an assumed spectrum, and instead calculates exposure for a monochromatic source with an energy at the mid-point of the energy bands. As discussed in §2.2.1, this can lead to significant errors in the derived fluxes for broad energy bands, but will not significantly alter the source detection process. The resultant maps are in units of seconds, and count rate maps are created by dividing the image by the exposure map. Energy conversion factors (ECFs) giving the ratio between count rate and flux for a given detector and band were derived as discussed in §2.4.4 and are listed in Table 5.1. These values include a detector-specific cm^2 term which accounts for the energy dependent effective area of the mirror-filter-detector system multiplied by a band-specific counts erg^{-1} term appropriate for an $\alpha = 0.7$ powerlaw absorbed by a column of 3×10^{20} cm^{-2}.

Finally, full EPIC images and exposure maps were created from the individual instrument images in each band. The images were summed directly, after setting all pixels with zero exposure to zero counts. The standard SAS routine for merging with exposure map correction, `emosaic`, makes no attempt to account for the varying effective area of the detectors. This is a significant effect, as the pn is about twice as sensitive as the MOS cameras, with the actual factor strongly dependent on energy. To account for this, I multiplied the exposure maps by effective area — found by dividing the ECF by the counts per erg conversion for the appropriate band — before summing. The combined EPIC image will reach fainter fluxes than those from individual instruments, and the combined exposure map is sufficient to 'flat-field' the counts image for the purposes of source detection. However, the fluxes inferred from this image are very uncertain due to both the assumption of monochromatic mid-band source spectra for the single instrument exposure maps and the necessarily rough effective area correction in the merged map, and are not used to derive source properties.

5.3.2 Source detection

As discussed fully in §2.4.4, the standard SAS detection chain, `edetect_chain`, takes as input images in several bands and executes the full series of SAS tasks needed to produce a final source list. The detection process has two stages. In the source detection phase, two increasingly sensitive iterations of a sliding-box algorithm are run on images in each energy band. Some sensitivity to extended emission is obtained by increasing the box size in several subsequent passes through the data. The detection likelihoods in each band are transformed to equivalent single-band detection likelihoods, and sources with values above a given threshold are considered detections. In the source characterisation phase, maximum-likelihood PSF fits are performed in each of the bands simultaneously to determine a final likelihood value and the source characteristics. Because the PSF varies between pn and MOS, this method is not suitable for use on the combined EPIC images, and is ideally used on data from the three detectors separately. Detector specific source lists are then merged into an all EPIC source list based only on positional coincidence.

The detection chain was run on the SSA22 data in the $0.5-2$ and $2-8$ keV bands. A sliding box of 3×3 pixels ($13.05''\times13.05''$) was used to roughly match the half energy width of the on-axis PSF. Likelihood thresholds of 6 and 10 were used for the `eboxdetect` detection and `emldetect` characterisation phases, respectively, giving a final source-list limited roughly to $\sim 4\sigma$ detections. 194 sources were detected, the positions of which are overlaid on the merged EPIC image in Figure 5.7.

Careful examination shows that while most sources which are obvious to the eye in the merged EPIC image have been detected, several spurious sources have also been marked. As noted in §2.4.4, the SAS chain is known to produce spurious sources at chip edges, in the PSF wings of bright sources, and in regions where the background is poorly reproduced by the spline fit (Watson et al. 2003). Indeed, in Figure 5.7, evidence of all these effects is seen. Most markedly, clusters of false sources are detected in crowded regions and in a regions of increased local background. In the first case, it is likely that the smoothed background map is a poor representation of the actual background because masking of flux in apertures around many near-by sources will leave a larger-scale deficit. In the second, it is likely that the scales probed by the sliding-box simply are not sensitive to significantly extended flux variations, which are then split into multiple spurious detections. The failure rate of the box-detect method has been quantified by Valtchanov et al. (2001), who compared various detection methods on simulated XMM data. Running the standard XMM chain with an `emldetect` likelihood threshold of 10 on an image with 36 input sources of various count-rates and separations, they find that 32 are successfully detected but 13 spurious detections are produced. For a test image containing point source / extended source pairs with varying count-rates and separations, `emldetect` recovered 22 of 24 input sources, but produced 89 false detections.

The WAVDETECT algorithm, discussed in §2.3.4, should provide several advantages over the box-detect method. As the detection phase of WAVDETECT is entirely independent of an assumed PSF, it is possible to run it accurately on the merged EPIC image, which should probe fainter fluxes. Furthermore, as discussed in Chapter 4, multi-scale wavelet detection techniques are able to reliably separate small-scale point source emission from surrounding larger-scale background variation. This facility should also alleviate the independent detection of PSF wings in bright sources. The WAVDETECT background maps — a weighted sum of the background maps produced after iterative source cleansing at each wavelet scale — are far smoother than the spline-fit maps and effectively disregard flux from sources at many scales while retaining the overall background level. Finally, corrections for exposure variation are made at each scale during the source detection phase, limiting false detections due to chip gaps and edges.

In Figure 5.8 I show the merged EPIC image overlaid with the locations of 190 sources identified using a variant of the WAVDETECT algorithm which has been developed for use with XMM (P. Freeman, private communication). As in the standard CIAO WAVDETECT, a PSF-independent detection phase (`wtransform`) is used to identify significant sources at each wavelet scale, i. The source characterisation phase (`wrecon`) is also largely PSF independent, as the source properties are derived from source cells identified from the distribution of flux. However, the characteristic size of the XMM PSF at the location

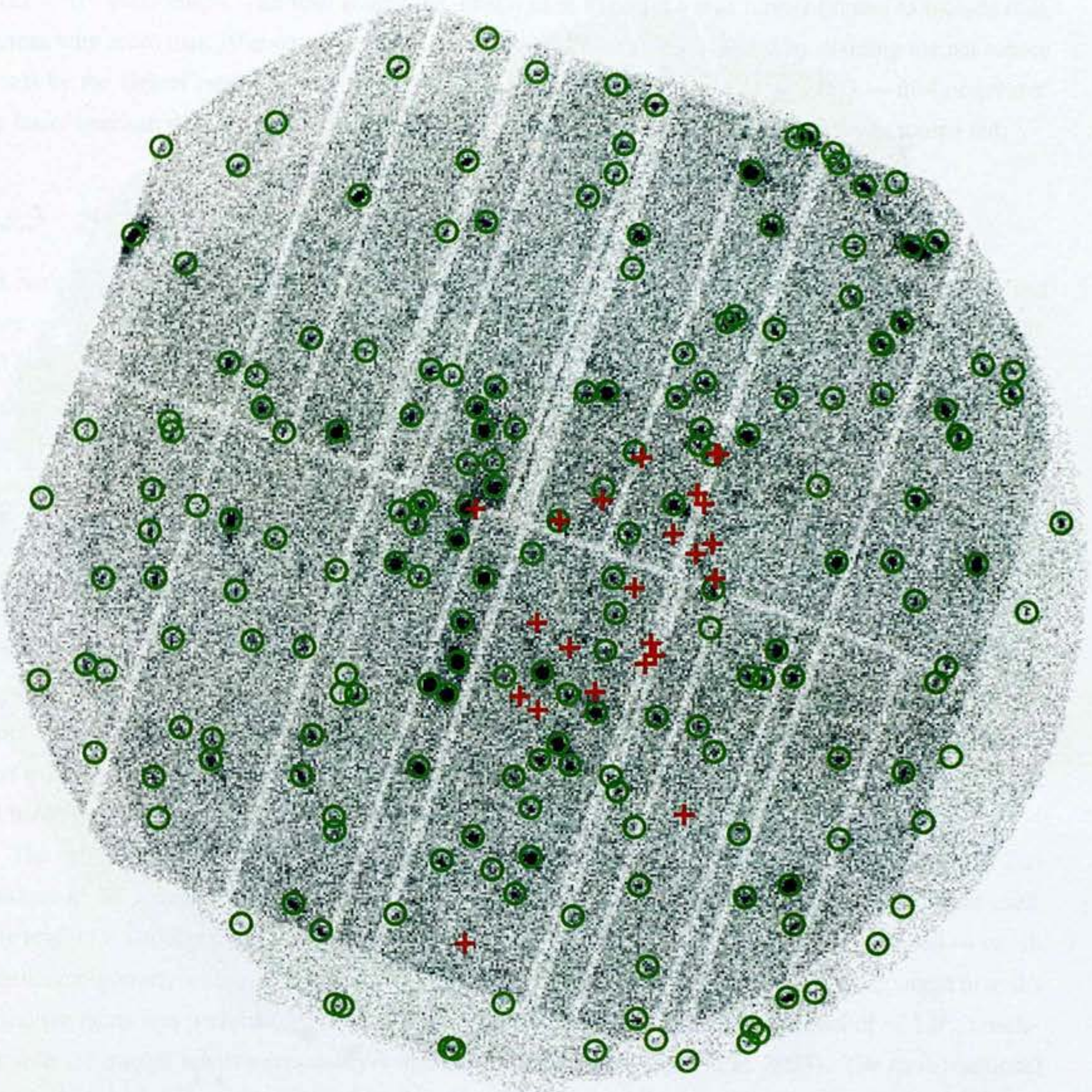

Figure 5.7: *Full band merged EPIC image overlaid with the positions of 194 sources identified by the SAS detection chain (green circles) and the locations of the spectroscopically confirmed protocluster members (red crosses). The FOV of any one EPIC camera is a circle with a diameter of roughly 30 arcmin; the image above is roughly 31 arcmin on a side with North toward the top of the page and East to the left. Several spurious detections are obvious near the edges of the field and in regions of high local background.*

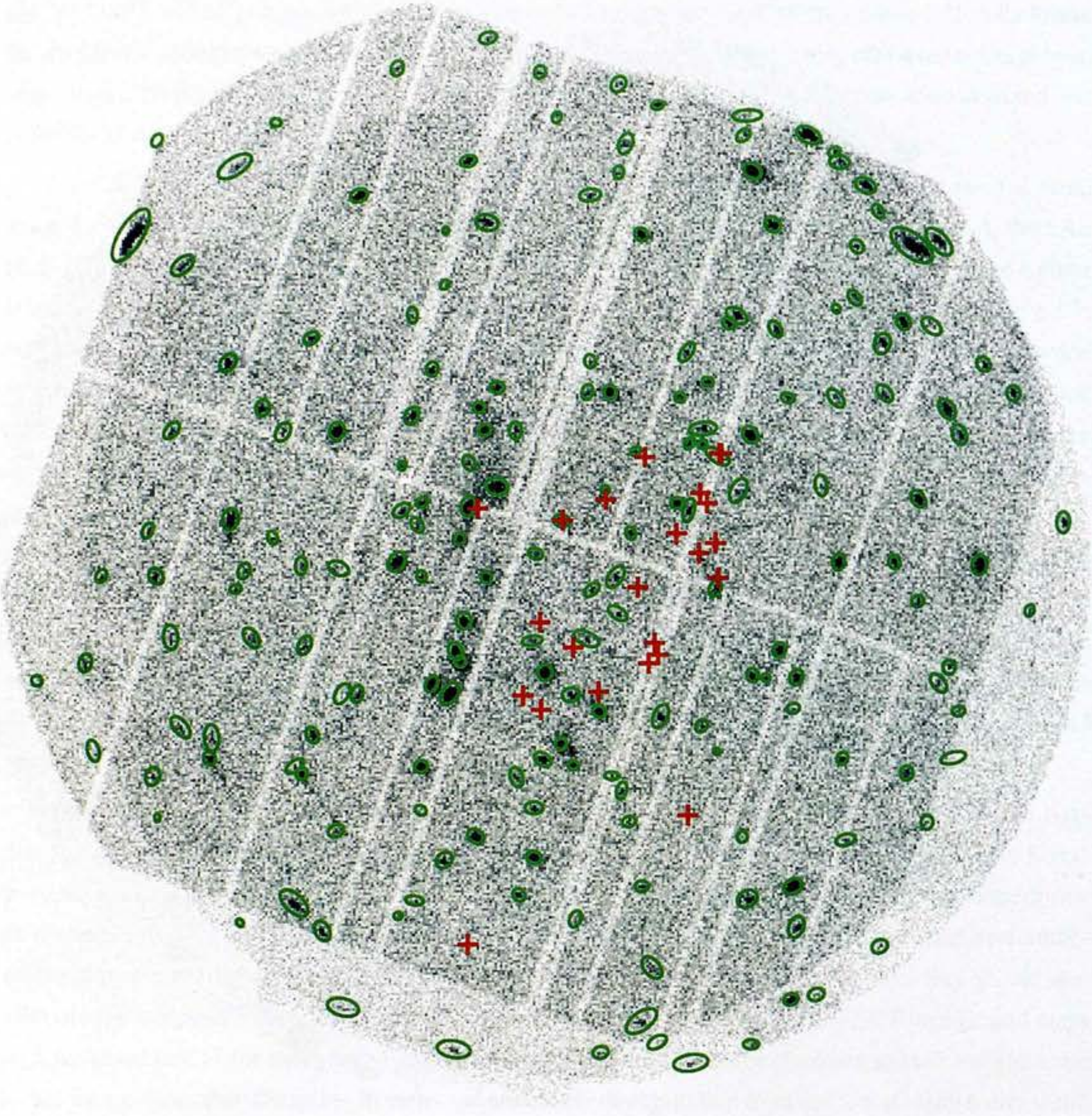

Figure 5.8: *Full band, merged EPIC image overlaid with the 190 source regions identified with a variant of the CIAO WAVDETECT algorithm (green ellipses) and the locations of the spectroscopically confirmed protocluster members (red crosses). As in Figure 5.7, the image is roughly 31 arcmin on a side with North toward the top of the page and East to the left.*

of a detected source is used to select the smoothing function used. The sourcelist shown in Figure 5.8 was produced running `wtransform` and `wrecon` on the full band, merged EPIC image with wavelet scales of $i = \sqrt{2}$, 2, $\sqrt{4}$, 4, $\sqrt{8}$, 8, $\sqrt{16}$, and 16. The significance threshold was set conservatively at 10^{-7}; one false event is expected to be identified in 10^7 pixels, and less than one false source should be detected in a 512×512 pixel image. The final source-list displayed in Figure 5.8 was further limited to include only sources with more than 10 counts and with source significance values — found by dividing the net source counts by the Gehrel's error on the background counts ($\sigma_G = 1 + \sqrt{(BKG + 0.75)}$) — of 4 or greater. Far fewer spurious detections are evident in this catalogue, which I adopt as the final X-ray source list. [2]

5.3.3 Source characterisation

For each source position identified in the full band EPIC image, source counts, background counts, and mean exposure values were determined within apertures with $8.7''$ radii for each detector in the full, soft, and hard bands. Source and exposure values were obtained from the image and exposure map, respectively. Background counts were obtained from the output WAVDETECT background image, which is a weighted sum of the backgrounds determined at scales larger than the typical PSF size. Net counts within the aperture were found by subtracting the background counts from the source counts, and were converted to total net counts by dividing by the fractional encircled energy within the aperture. The fraction of source energy within a $8.7''$ radius was found as a function of off-axis angle using the Extended Accuracy Model of the XMM PSF provided by the SAS team. Fluxes were then derived by dividing the total counts by the mean exposure within the aperture and by the appropriate ECF. Figures 5.9, 5.10, and 5.11 illustrate that the fluxes obtained through aperture photometry are consistent with those obtained from the SAS tools to within their errors. Slightly more scatter is seen in the full band fluxes in 5.11 because the SAS tools obtain the full band fluxes incorrectly by adding the soft and hard band values, while I derive full band fluxes using the full band images and corresponding ECFs.

The source positions were astrometrically aligned with the deep g'-band image described in §5.2. The positions of 27 optical counterparts of X-ray sources with $g' < 23$ and compact morphology were used. Only bright (> 100 counts) X-ray sources — for which the X-ray position should be well defined — which were unambiguously associated with a single g'-band counterpart were selected. A six-component fit to the optical positions was performed with the ASTROM package, yielding a mean residual of $\sim 1.5''$, consistent with the quoted relative astrometry within the EPIC cameras (Ehle et al. 2003). The total positional errors include both the error in the individual source positions computed by WAVDETECT and this average astrometric error.

Appendix C summarizes the properties of the X-ray detections in the SSA22 field. The positions, positional errors, and source significance values are taken directly from the WAVDETECT source list obtained for the full-band EPIC image. The net counts are the sum of background-subtracted, exposure-

---

[2] The use of WAVDETECT with XMM data was also tested by Valtchanov et al. (2001), who rejected it due to significant numbers of missed and spurious detections in the point source and diffuse + point source simulated images. However, these authors misinterpret the threshold significance parameter and set it so that a few dozen false detections are expected for each field.

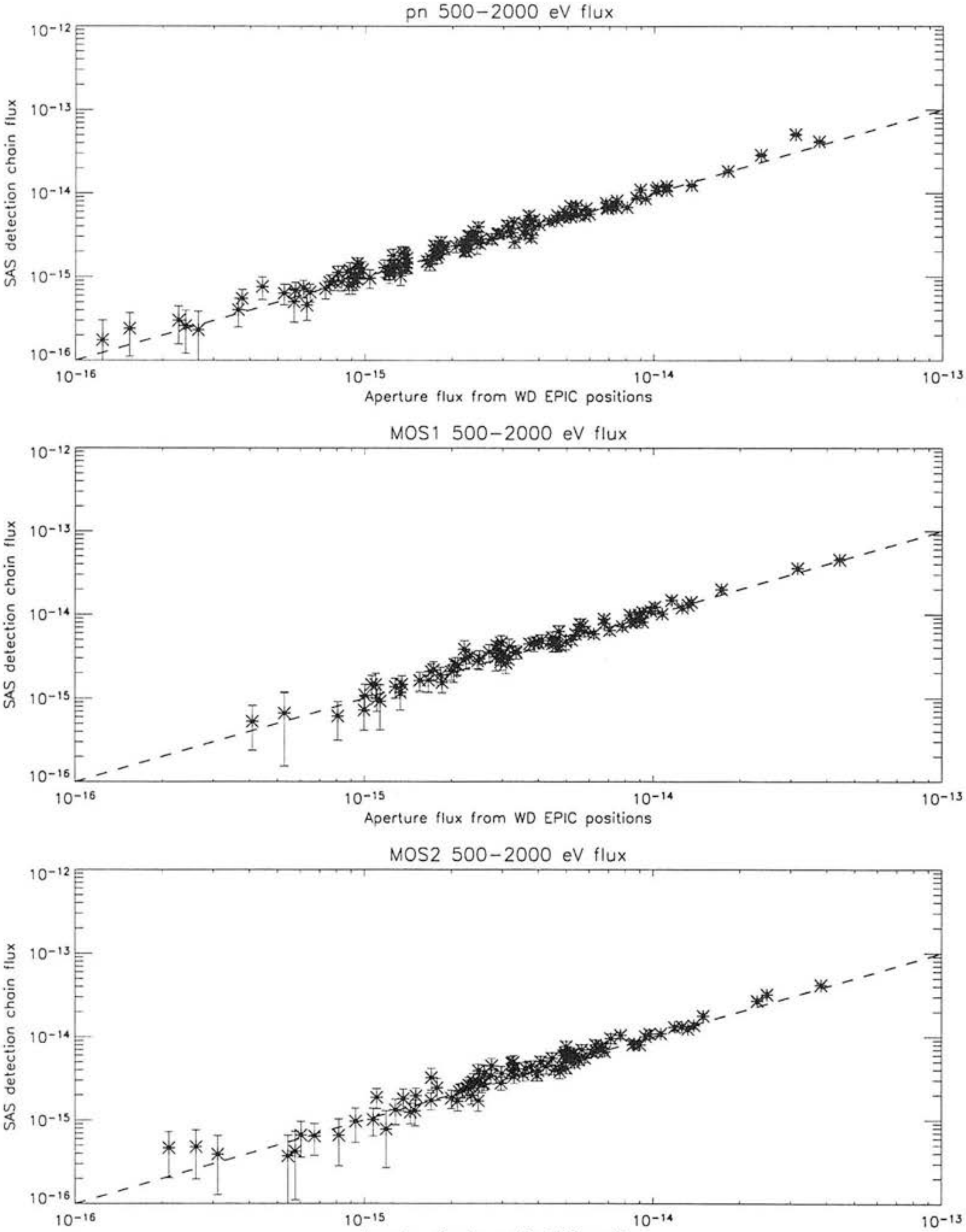

Figure 5.9: *Comparison of soft band fluxes obtained with the SAS detect tools and aperture photometry at the WAVDETECT positions.*

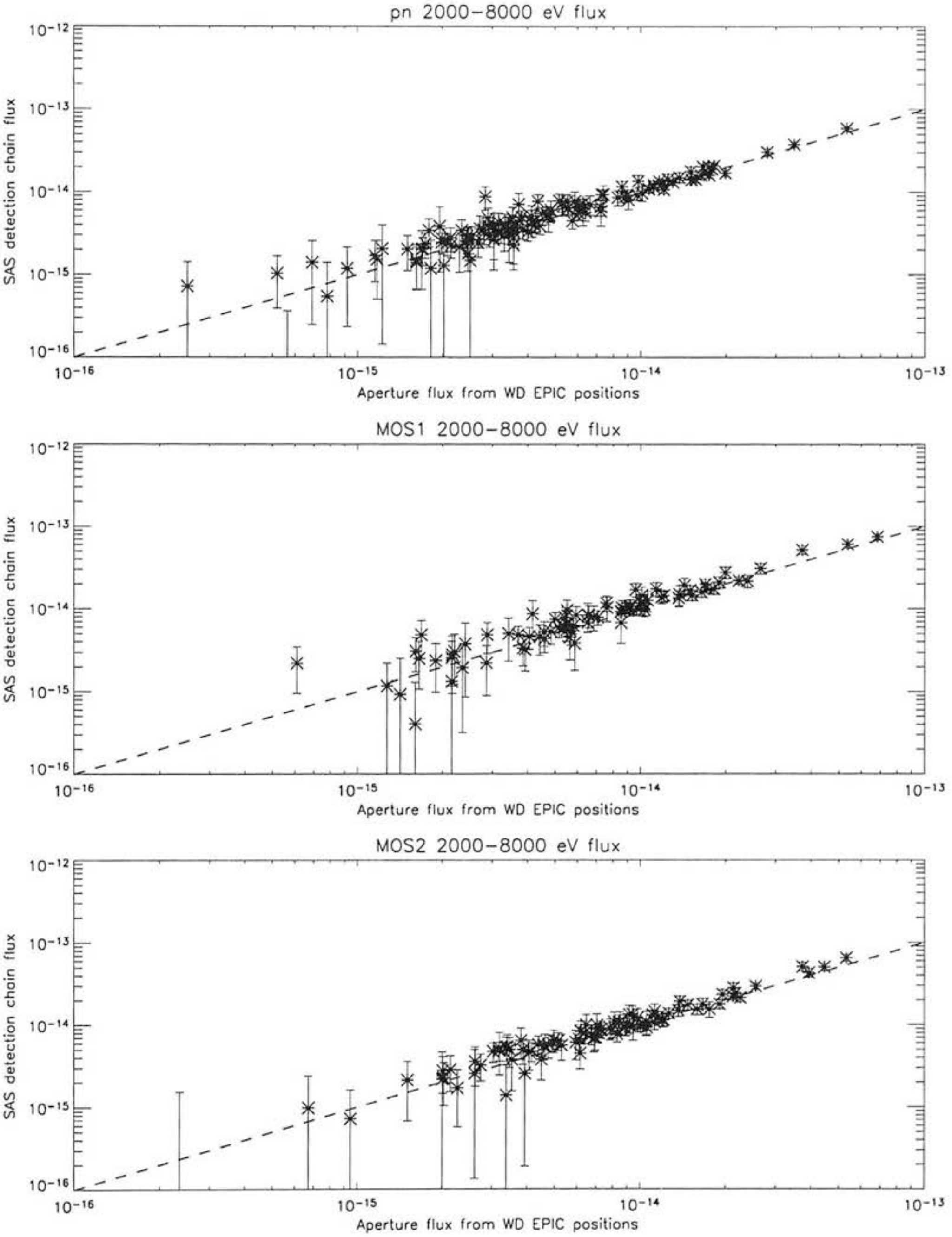

Figure 5.10: *Comparison of hard band fluxes obtained with the SAS detect tools and aperture photometry at the WAVDETECT positions.*

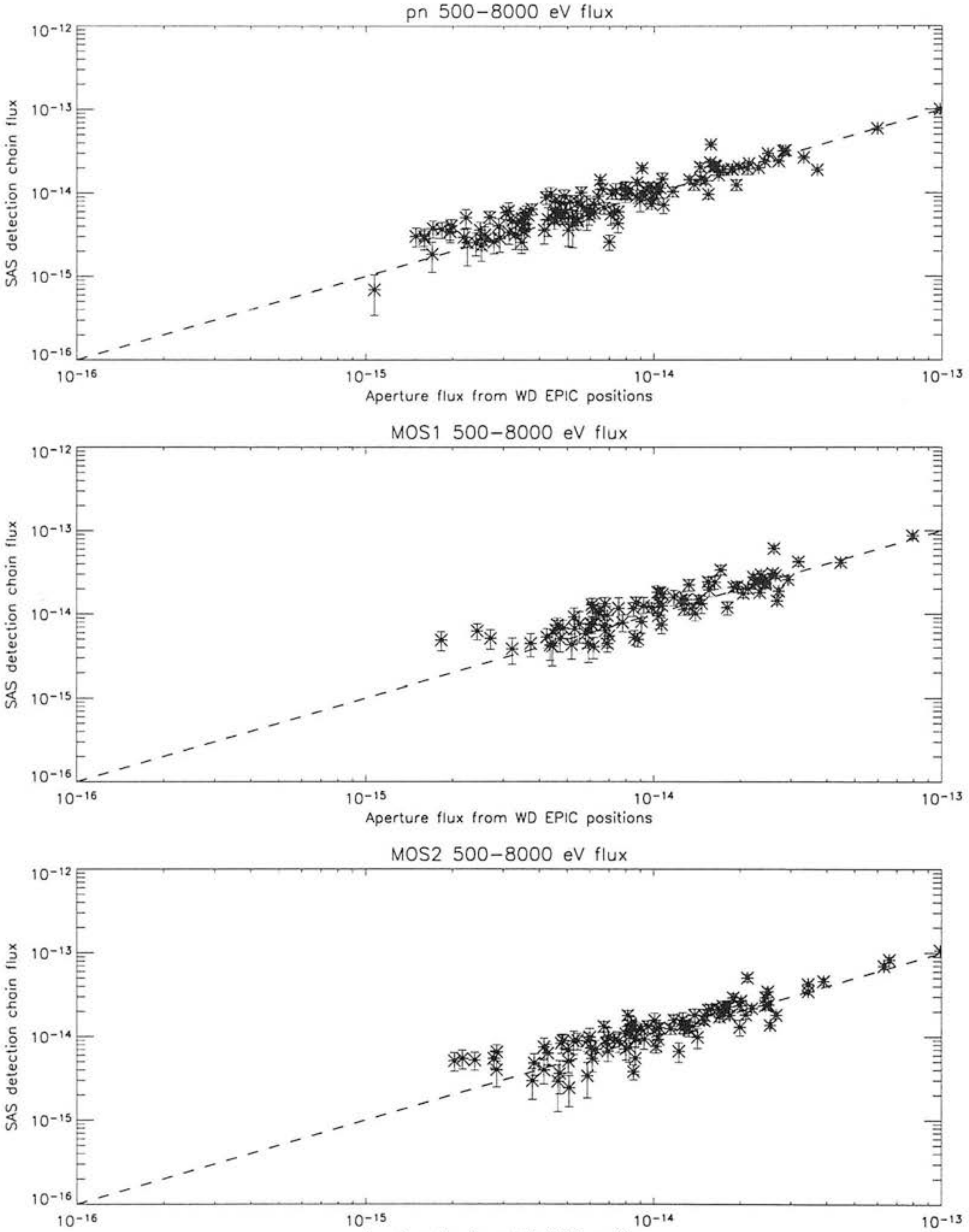

Figure 5.11: *Comparison of full band fluxes obtained with the SAS detect tools and aperture photometry at the WAVDETECT positions.*

corrected total counts detected by the individual EPIC images. The fluxes are an error-weighted sum of the fluxes found by each instrument. The hardness ratios are defined as $\frac{H-S}{H+S}$, where H and S are the 0.5 – 2 keV and 2 – 8 keV band error-weighted average count rates given by each instrument, incorporating background subtraction and exposure correction. In cases where sources fell partially outside of the FOV or on chip gaps for a given instrument, information from this instrument was excluded from the sum or average.

5.4 Direct detections

As a first examination of the X-ray properties of the high redshift populations in the SSA22 field, the X-ray catalogue presented in Appendix C was cross-correlated with catalogues of known or candidate protocluster members. In total, there are 176 galaxies definitely or possibly associated with the $z = 3.09$ structure:

- Among 78 $2 < z < 4$ galaxies identified through the Lyman break technique, there are 23 spectroscopically identified LBGs with $z = 3.09 \pm 0.03$ (Steidel et al. 2003, Tables 19 & 20).
- 70 objects in the deep survey of Steidel et al. (2000) show narrowband excesses or deficits which are most likely associated with Lyα in the range $3.05 < z < 3.12$. 14 of these are previously confirmed LBGs within the protocluster, 56 are new protocluster candidates. In addition, 64 Lyα excess objects are identified at fluxes fainter than the conservative $NB \leq 25.0$ limit imposed on the primary catalogue, and may also be associated with the protocluster.
- The analysis described in §5.2 identified 32 possible Lyα emitters in the shallower wide-field narrowband imaging. Only three of these had been previously identified, yielding 29 new Lyα candidates.
- There is an overdensity of SCUBA sources in this field — 18 in total — and radio identification has confirmed that 3 of these sources are luminous starforming galaxies associated with the protocluster (Chapman and Baugh 2004).

Catalogues of Lyα, submillimetre-detected, and spectroscopically confirmed high redshift LBGs were compared with the astrometrically corrected X-ray positions. Three sigma search radii were determined using an assumed 0.5″ error on the optical and radio positions as well as the total error on the X-ray position. This latter error includes the centroiding error of the source — ranging from $\sim 0.2''$ to $\sim 7.5''$ — and the 1.5″ astrometric error. Six distinct X-ray sources were consistent with the positions of protocluster candidates to within the 3σ radii. However, inspection of the g'-band image reveals that in three cases the X-ray centroid is better matched to other optical sources within the error circle. Narrow-band and g'-band images of the remaining three directly detected sources are shown in Figures 5.12, 5.14, and 5.16, X-ray pulse height spectra are shown in Figures 5.13, 5.15, and 5.17, and source properties are summarized in Table 5.2.

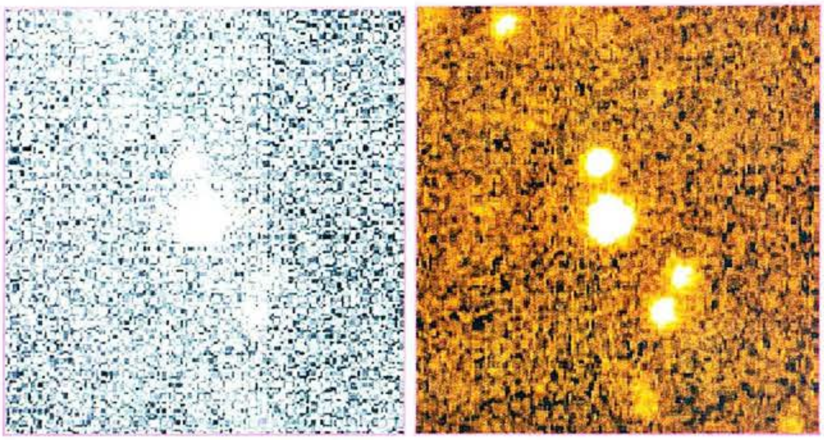

Figure 5.12: *Narrow-band (left) and* g'*-band images of X-ray source 102, an AGN in the SSA22 protocluster also identified in the LBG survey of (Steidel et al. 1998, 2000). Images are 20 arcsec on a side, with North to the top of the page and East to the left.*

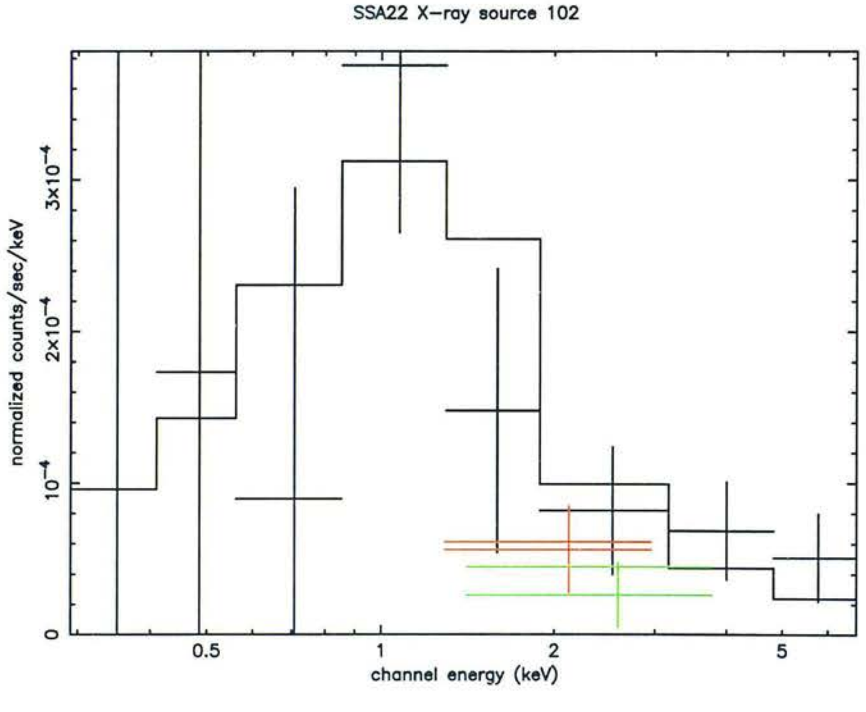

Figure 5.13: *Pulse height spectra of X-ray source 102. The data are from the pn (black), MOS1 (red), and MOS2 (green) cameras and the histograms are of a simultaneously fit obscured powerlaw model convolved with the instrument response for each camera. The best fit parameters, with a reduced* χ^2 *of 0.78, indicate an energy index* $\alpha = 0.7 \pm 0.5$ *and an obscuring column of* $0 \pm 0.1 \times 10^{22}$ cm^{-2}.

Source	z	$S_{0.5-2\text{ keV}}$ (erg s^{-1} cm^{-2})	$L_{2-8\text{ keV}\,abs}$ (erg s^{-1})	HR	N_H (atoms cm^{-3})	L_{bol} (erg s^{-1})
102 (SSA 22a-D12)	3.083	0.6×10^{-15}	5.0×10^{43}	0.03	3×10^{23}	1.3×10^{46}
127 (NB1866)	3.048	6.0×10^{-15}	4.8×10^{44}	-0.36	4×10^{22}	3.8×10^{46}
62 (LFC_NB28)	-	1.6×10^{-15}	1.3×10^{44}	-0.46	2×10^{21}	0.7×10^{46}

Table 5.2: *Direct X-ray detections of protocluster members and candidates in the SSA22 field. Properties listed are observed 0.5 – 2.0 keV flux, rest-frame 2.0 – 8.0 keV luminosity, X-ray hardness ratio, implied absorbing column assuming a powerlaw spectrum with a energy index of 0.9, and estimated bolometric luminosity derived from the absorption-corrected X-ray luminosity.*

5.4.1 X-ray detection of a Lyman Break Galaxy

X-ray source 102 is identified with Steidel et al. (2003) SSA 22a-D12, a QSO identified in the original Lyman-break survey of the field. The R-band magnitude of this source is 21.61, yielding X-ray to optical ratios — $\log \frac{f_X}{f_R}$ = -1.1 and -0.46 for the soft and hard X-ray bands, respectively — typical of AGN (Hornschemeier et al. 2001). The observed soft band flux corresponds to a 2 – 8 keV rest frame luminosity of 5.0×10^{43} erg s^{-1}. The X-ray hardness ratio, $HR = 0.03$, indicates a fairly hard spectrum, implying an intrinsic absorption of $\sim 10^{23}$ cm^{-2} for a powerlaw with energy index, α, of 0.9. The rest frame 0.5 – 2 keV and 2 – 8 keV luminosities, corrected for this absorption, are then 3.8 and 4.3×10^{44} erg s^{-1}, respectively, giving an estimated bolometric luminosity of 1.3×10^{46} erg s^{-1} (Elvis et al. 1994). Steidel et al. (1998) note that it is found at one of the three local peaks in the surface density of LBGs and Lyα emitters, which is a factor of two denser than the factor of 6 enhancement of the protocluster as a whole.

The 'special' location of SSA 22a-D12 may indicate it is more massive than the average LBG. Indeed, its X-ray luminosity is higher than would be expected based on simple assumptions about the LBG population. Assuming i) the stellar mass of an $L^\star$ LBG of $1 - 2 \times 10^{10} M_\odot$ (Shapley et al. 2001), ii) that this mass will comprise the galactic bulge, and iii) that the local black-hole mass / spheroid mass relation (Merritt and Ferrarese 2001b) holds in this population, the LBGs in SSA22 are expected to contain black holes of order $10^7 M_\odot$ with bolometric Eddington luminosities of $\sim 10^{45}$ erg s^{-1}. For an unobscured quasar, this implies observed 0.5 – 2 and 2 – 8 keV (rest-frame 2 – 8 keV and 8 – 32 keV) fluxes of $\sim 4 \times 10^{-16}$, just at the soft band point source sensitivity of the full EPIC image, and below the hard band limit. Less massive black holes, those radiating at sub-Eddington levels, and those with intrinsic absorbing columns of a few $\times 10^{22}$ cm^{-2} will therefore be too faint to be detected in either band in the current survey.

While the census of AGN in the protocluster LBGs is thus limited by sensitivity, the X-ray detection of a single AGN among the LBG population — corresponding to a 4% detected AGN fraction — is consistent with the estimated levels of nuclear activity in LBGs in the field. Steidel et al. (2002) find an AGN fraction of $\simeq 3\%$ in a sample of ~ 1000 $z \simeq 3$ LBGs based on examination of their optical/UV spectra, and Brandt et al. (2001a) and Nandra et al. (2002) both find an equivalent fraction of AGN among LBGs within the Chandra Deep Field North based on the 1Ms Chandra exposure. The hard band flux limit of the Nandra et al. (2002) study excludes luminous obscured AGN (i.e., with unobscured rest frame luminosities of $> 10^{44}$ erg s^{-1}) within their LBG sample at $z \sim 3$ unless they are Compton thick, but cannot exclude a larger population of low-luminosity AGN. However, a stacking analysis of the individually undetected sources in their sample, discussed more fully below, suggests that star formation and not LLAGN provide the X-ray luminosity of this class of object at fainter flux levels.

The current data cannot provide a full census of accreting black holes in star-forming galaxies within SSA22 protocluster. In addition to the X-ray sensitivity issues described above, the identification of LBG candidates on the basis of a rest-frame UV continuum break biases against heavily obscured galaxies which might be too red and/or faint to meet the selection criteria, as noted by Nandra et al. (2002). However, estimates by Barger et al. (2001) suggest $\sim 4\%$ of galaxies are undergoing luminous accretion onto a central black hole at any time. That a similar fraction of AGN is seen both within the LBG population as a whole and within the SSA22 sample suggests that neither field nor cluster star-forming galaxies at $z \sim 3$ are going through a period of enhanced nuclear activity.

5.4.2 X-ray detection of Lyα emitters

X-ray sources 127 and 62 are coincident with protocluster candidates selected in the Steidel et al. (2000) deep Lyα survey (NB1866) and the wide-field Lyα survey described in §5.2 (LFC_NB28), respectively. Both sources have properties consistent with Type I AGN: unresolved morphology on the g' and NB images, relatively soft X-ray spectra, and — assuming an $\alpha = 0.7$ powerlaw with a Galactic absorption of 3×10^{20} cm^{-2} — hard X-ray luminosities of $L_{(2-8\ \mathrm{keV})} \simeq 10^{44}$ erg s^{-1} implying bolometric luminosities of $> 10^{46}$ erg s^{-1}. NB1866 is spectroscopically identified (S. Chapman, private communication) as a luminous AGN, with lines of NV, CIV, and broad Lyα in emission at $z = 3.048$ and in absorption at $z = 3.029$. This source is slightly outside the target range of the filter, and lies 27.5 h^{-1} comoving Mpc (or 9.62 Mpc in physical units at $z = 3.09$) nearer to us than the SSA22 redshift peak. No redshift is available for LFC_NB28.

Previous searches for X-ray emission from Lyα emitters were published by Malhotra et al. (2004) and Wang et al. (2004) based on the the Large Area Lyman Alpha (LALA) survey, which targeted sources at redshifts of 4.5 and 5.7. None of 101 Lyα candidates selected at $z \sim 4.5$ are detected in ~ 175 ks Chandra observations to an on-axis limiting flux of $\sim 3 \times 10^{-16}$ erg s^{-1} cm^{-2} in the observed 0.5 – 10 keV band. This flux limit is sufficient to exclude luminous quasars with rest-frame full-band luminosities of $> 10^{44}$ erg s^{-1}, unless they are Compton thick. In tandem with the lack of optical signatures of AGN in any of the 47 spectroscopically confirmed objects, Malhotra et al. (2004) conclude that there is no evidence for quasar activity in their sample.

Luminous Lyα emission from galaxies at high redshift is thought to be an effective signpost to the formation of early generations of stars, as production of high Lyα equivalent widths (> 240 Å) via stellar processes requires a young massive star population with a very low metallicity (Charlot & Fall 1993). As Lyα emission will also be produced by accretion onto a central black hole, however, the selection technique may also identify galaxies which host an AGN. The Wang et al. (2004) results suggest contamination of the Lyα sample by quasars is very low at $z \sim 4.5$, while 2 of 150 Lyα candidates (1.3%) in the SSA22 field are identified with quasars. This reflect a very mild increase in the AGN fraction of Lyα-selected objects — which could be due either to the lower redshift or to the association with a dense environment — but it is not statistically significant. If the AGN fraction is constant between the two surveys, only a single AGN

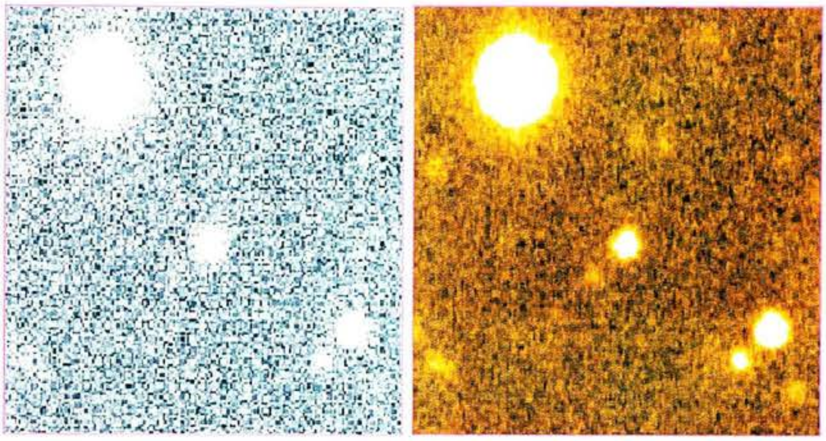

Figure 5.14: *Narrow-band (left) and g'-band images of X-ray source 127, an AGN in the SSA22 protocluster also detected in the deep Lyα survey of Steidel et al. (2000). Images are 20 arcsec on a side, with North to the top of the page and East to the left.*

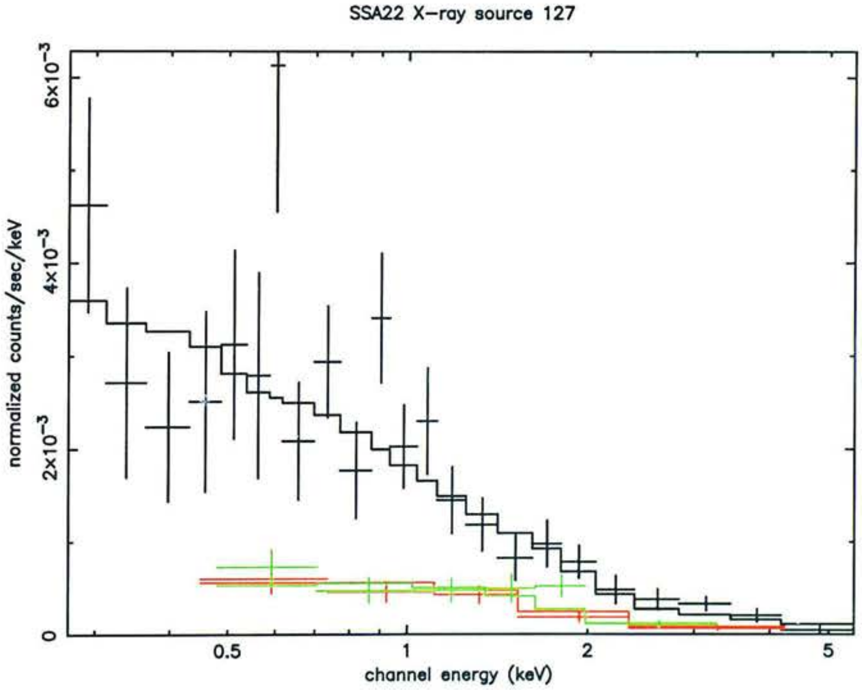

Figure 5.15: *Pulse height spectra of X-ray source 127. The data are from the pn (black), MOS1 (red), and MOS2 (green) cameras and the histograms are of a simultaneously fit obscured powerlaw model convolved with the instrument response for each camera. The best fit parameters, with a reduced χ^2 of 1.08, indicate an energy index $\alpha = 0.6 \pm 0.2$ and an obscuring column of $0 \pm 0.2 \times 10^{22}$ cm^{-2}..*

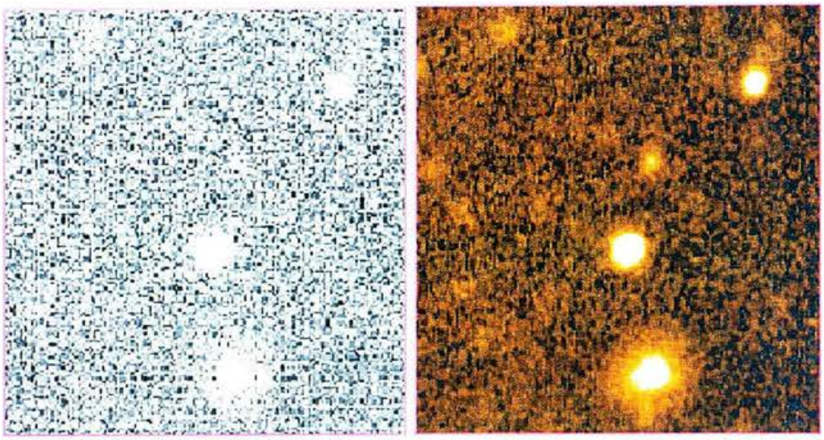

Figure 5.16: *Narrow-band (left) and g'-band images of X-ray source 62, an X-ray detected Lyα emitter. Images are 20 arcsec on a side, with North to the top of the page and East to the left.*

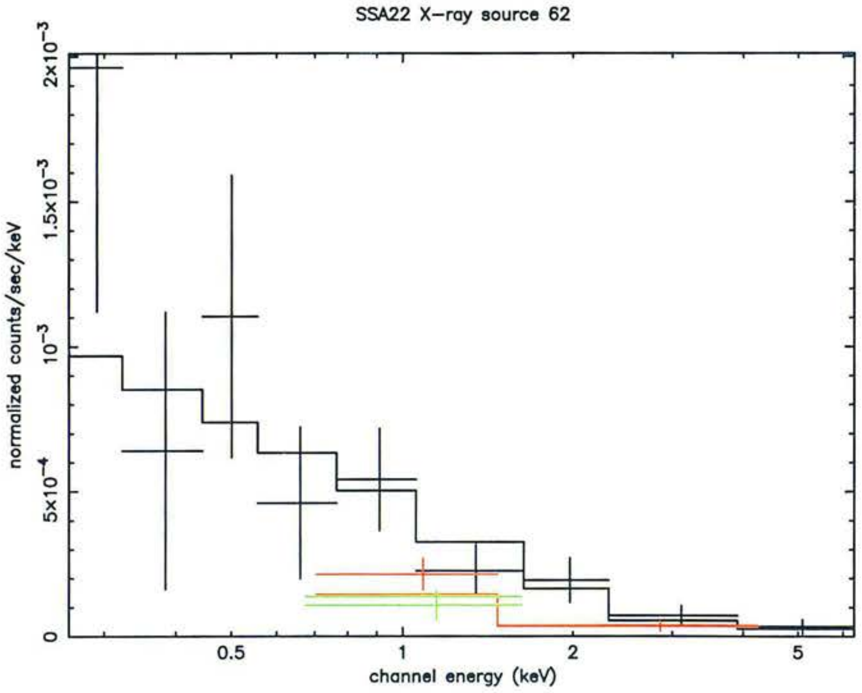

Figure 5.17: *Pulse height spectra of X-ray source 62. The data are from the pn (black), MOS1 (red), and MOS2 (green) cameras and the histograms are of a simultaneously fit obscured powerlaw model convolved with the instrument response for each camera. The best fit parameters, with a reduced χ^2 of 0.59, indicate an energy index $\alpha = 0.1 \pm 0.7$ and an obscuring column of $0.1 \pm 0.3 \times 10^{22}$ cm^{-2}.*

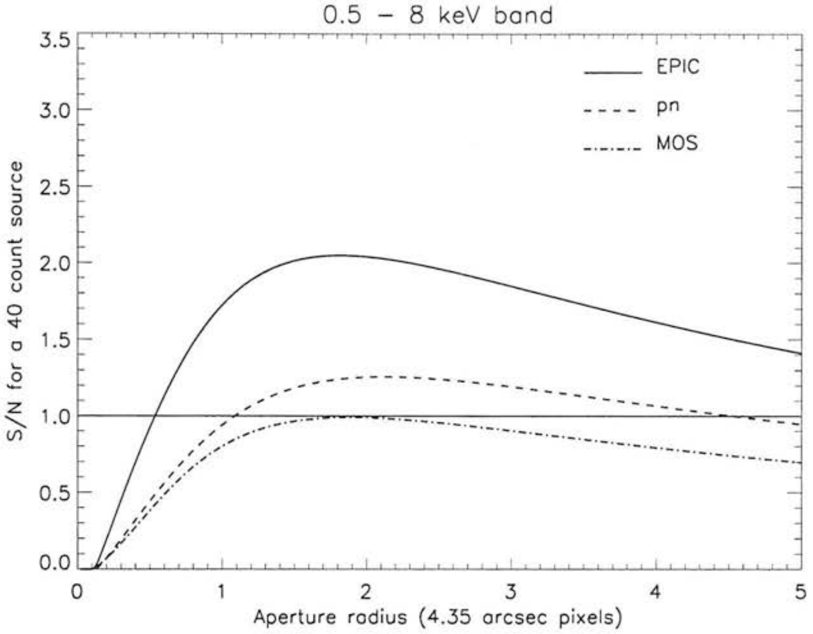

Figure 5.18: *Signal to noise within the aperture versus increasing aperture size for an XMM detection of a source with 40 counts in the 0.5 – 8 keV band. The encircled energy is taken from the XMM SAS Extended Accuracy PSF Model for MOS and pn, assuming 20 counts are detected with pn and 10 counts are detected with each of the MOS cameras. The assumed background per pixel is the average of randomly selected source-free apertures within the SSA22 exposure and is 0.069 for MOS and 0.146 for pn.*

with luminosity $> 10^{44}$ erg s^{-1} is expected in the Wang et al. (2004) sample.

5.5 Stacking analysis

While few protocluster objects are directly detected with XMM, a stacking analysis of the data can provide a more sensitive probe of the average X-ray properties of the high redshift populations comprising the $z = 3.09$ structure. The stacking technique — in which signal from objects of a well-defined class is combined to obtain a higher signal-to-noise measurement indicative of the average properties of that class — has long been applied to X-ray imaging data (Green et al. 1995, della Ceca et al. 1999). Recently, the stacking method has proven extremely successful in probing very faint emission from several classes of galaxies in the deepest Chandra surveys (Brandt et al. 2001b,c, Alexander et al. 2001, 2002, Hornschemeier et al. 2003b, Nandra et al. 2002) and has been used to constrain the X-ray flux of submillimetre sources in an XMM survey (Waskett et al. 2003). In this section I describe a stacking analysis in the SSA22 field carried out to constrain the X-ray emission from the Lyman-break, Lyα, and submillimetre-detected populations.

An XMM exposure is less sensitive to faint emission than a Chandra exposure of similar length as the higher background levels and larger PSF substantially decrease the signal to noise of aperture counts. This

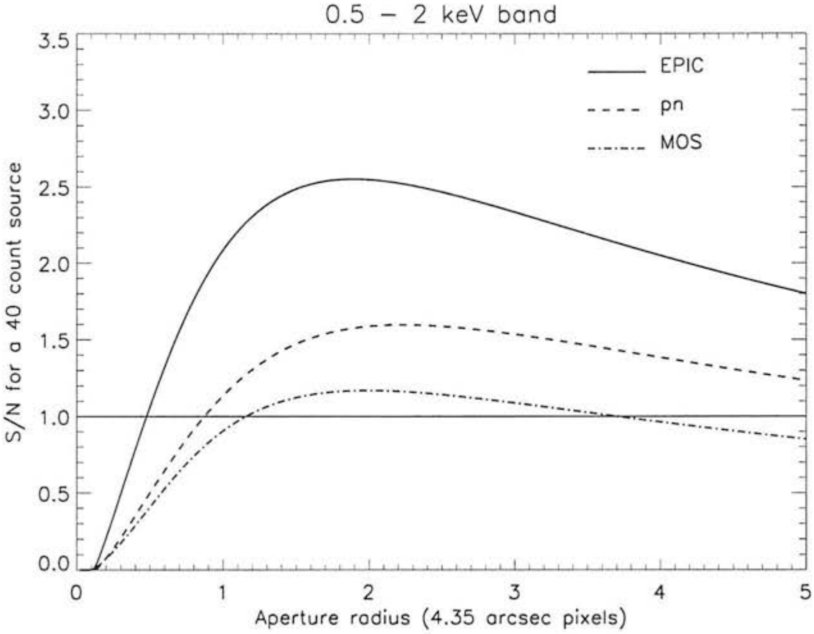

Figure 5.19: *As Figure 5.18, but for an XMM detection of a source with 40 counts in the 0.5 – 2 keV band. Assumed background per pixel is 0.044 for MOS and 0.082 for pn.*

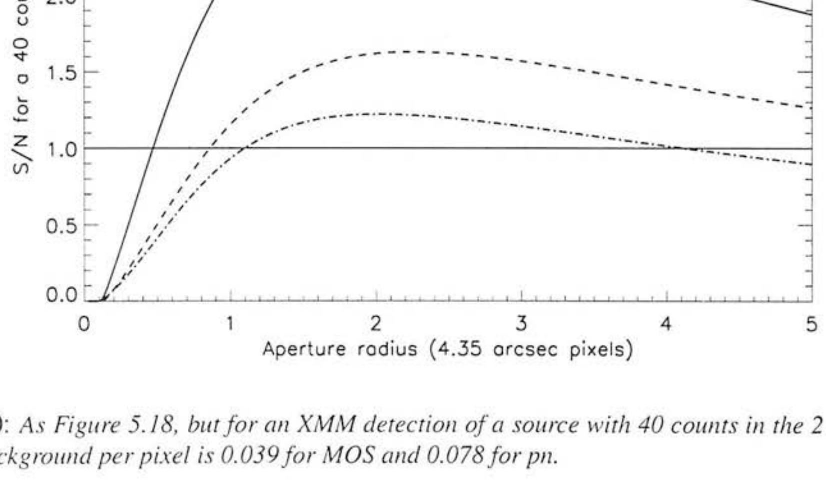

Figure 5.20: *As Figure 5.18, but for an XMM detection of a source with 40 counts in the 2 – 8 keV band. Assumed background per pixel is 0.039 for MOS and 0.078 for pn.*

difficulty is illustrated in Figures 5.18 – 5.20, which plot expected signal to noise versus increasing aperture size for a faint source detected with XMM in the full, soft, and hard bands.

Waskett et al. (2003) attempt to maximize the stacking signal by convolving the X-ray image with an estimate of the XMM PSF to obtain an optimal measure of the X-ray counts at each position. They then determine the significance of the measured counts relative to the background level through Monte Carlo simulations. The utility of this approach for studying the samples in the SSA22 field is questionable for two reasons. First, the best current calibration of the XMM PSF makes no attempt to model its two-dimensional shape and convolution of substantially off-angle sources with the radially symmetric model will lead to errors in the recovered flux. Second, because the measured background is a function of off-axis angle, accurate estimation of the background level for the sample through Monte Carlo methods requires selection of random positions with a similar distribution of off-axis angles. This requirement limits the number of independent samples which can be selected and, in practice, prohibits an accurate measurement of the variance in the background levels for large numbers of stacking positions. I therefore obtain counts and background levels through aperture photometry, and rely on the radially symmetric calibration of encircled energy to account for losses of flux outside the aperture.

Source counts and fluxes have been obtained at the stacking positions using an aperture photometry method very similar to that described in §5.3.3. For each instrument, raw counts are measured within apertures with 2 pixel (8.7″) radii centred at the stacking positions. As seen in Figures 5.18 – 5.20, the signal to noise within the aperture peaks for combined EPIC observations at roughly this radius. The smoothed WAVDETECT background maps used to obtain background counts in §5.3.3 were found to slightly misrepresent the background levels — likely due to differences between the radially averaged SAS PSF model and the two dimensional PSF shape — and were therefore not used in this analysis. Instead, the average background level was determined in roughly annular regions around each stacking position which excluded known X-ray sources and other stacking positions. Background subtracted counts were then aperture-corrected and converted to fluxes, and the measurements from the three EPIC cameras combined in weighted sums and averages as described above.

The net counts within the stacking apertures in the full, soft, and hard X-ray bands are plotted versus redshift or off-axis angle for the high redshift ($2 < z < 4$) Lyman-break, Lyα, and submillimetre detected samples in Figures 5.22, 5.23, and 5.24. Apertures which do not overlap the 3σ source cells of identified X-ray sources and are not within 3 pixels (13.05″) of any other stacking positions are marked in these figures with boxes. Only these isolated sources are included in the stacking to avoid contamination of the stacking apertures by nearby sources or duplication of pixel values contained in more than one stacking aperture. For apertures which have been excluded due to proximity to X-ray sources, estimates of the flux contributed to the aperture by the X-ray sources have been made and are indicated in Figures 5.22 – 5.24 by the thick black lines. These estimates rely upon the radially averaged PSF calibration model, however, and therefore cannot be used to accurately correct for the contamination. The mean count level for each sample is indicated by the dashed lines in Figures 5.22 – 5.24, and is a weighted average of all aperture counts for isolated apertures. The signal from each population is consistent with zero to within 3σ errors. Details of the number of sources stacked, the measured flux, and the inferred upper limits on the population

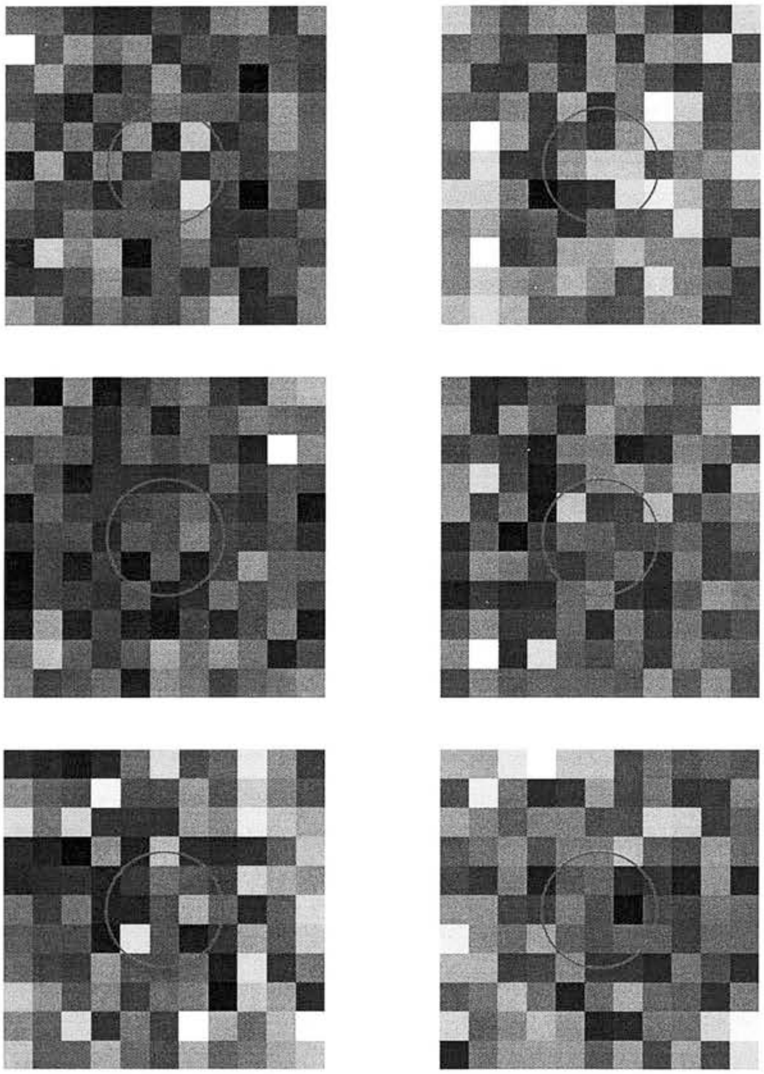

Figure 5.21: *Stacked images of high redshift populations in the SSA22 field. Stacking regions are accumulated from an image in which all detected X-ray sources have been masked, and mask regions assigned pixel values randomly selected from the Poisson distribution with the same mean as the local background. Images are 47.85″ on a side, and the green circles indicate the stacking apertures. Top row: 0.5 – 2 and 2 – 8 keV stacked images of 78* $2 < z < 4$ *LBGs. Middle row: 0.5 – 2 and 2 – 8 keV stacked images of 174 Ly*α *candidates. Bottom row: 0.5 – 2 and 2 – 8 keV stacked images of 18 submillimetre sources.*

Sample	No. stacked (Total no.)	Band (keV)	Flux (10^{-16}erg s^{-1} cm^{-2})	Luminosity (10^{43}erg s^{-1})
LBGs ($z > 2$)	34 (78)	0.5–8	-0.9 ± 1.8	< 2.6
		0.5–2	-0.3 ± 0.7	< 1.0
		2–8	2.4 ± 2.7	< 6.1
Lyα candidates	50 (174)	0.5–8	1.0 ± 1.4	< 3.2
		0.5–2	0.8 ± 0.4	< 1.3
		2–8	1.8 ± 2.0	< 4.9
Submm sources	7 (18)	0.5–8	4.8 ± 4.7	< 6.0
		0.5–2	2.9 ± 2.0	< 2.8
		2–8	-4.7 ± 6.3	< 4.5

Table 5.3: *Summary of stacking analysis performed on $2 < z < 4$ LBGs, Lyα candidates, and submillimetre detected sources in the SSA22 field. The first column lists the number of sufficiently isolated objects included in the stack and, in parenthesis, the total number of objects of the given class. Fluxes — derived assuming an $\alpha = 0.7$ powerlaw with a Galactic column of 3×10^{20} cm^{-2} — and 1σ errors are listed in 10^{-16} erg s^{-1} cm^{-2}. 3σ upper limits on the mean luminosity are given assuming $z = 3$ for the LBG sample, $z = 3.09$ for the Lyα sample, and and $z = 2.4$ for the SCUBA sample (Chapman et al. 2003a).*

luminosity are summarized in Tables 5.3, and discussed for each population in the sections below. Images of the stacked X-ray data for all of the objects each sample in the hard and soft bands are shown in Figure 5.21, and give no evidence that inclusion of the rejected apertures would lead to significant detections.

5.5.1 Lyman Break Galaxies

Less than half of the 78 spectroscopically confirmed high redshift LBGs at $z > 2$ were sufficiently isolated to provide a meaningful stacking estimate. The stacked signal of the 34 isolated sources is consistent with zero in the observed full, soft, and hard bands and, assuming a mean redshift of 3 and an $\alpha = 0.7$ powerlaw with Galactic column of 10^{20} cm^{-2}, corresponds to upper limits on the mean flux of 2.6, 1.0, and 6.1×10^{43} erg s^{-1}, respectively. These limits effectively rule out luminous AGN within the typical LBG in SSA22, but are not sensitive enough to exclude heavily obscured or lower-luminosity AGN.

Previous stacking analyses of samples of $2 < z < 4$ LBGs using the Chandra Deep Field North 1 Ms exposure were conducted by by Brandt et al. (2001c) and Nandra et al. (2002) and significantly detect individually undetected LBGs at flux rates consistent with a mean luminosity of 3.5×10^{41} erg s^{-1} in the hard X-ray band. These authors suggest the average X-ray flux from individually undetected LBGs is generated by stellar processes, which will be far too faint to observe even in stacked observations of SSA22.

5.5.2 Lyα candidates

The majority of the 178 Lyα detections in the field are also too near each other and / or other X-ray sources to be suitable for stacking. The remaining 50 sources produce a stacked signal in the full, soft, and hard bands which is consistent with zero, with 3σ upper limits on the luminosity of 3.2, 1.3, and 4.9×10^{43} erg

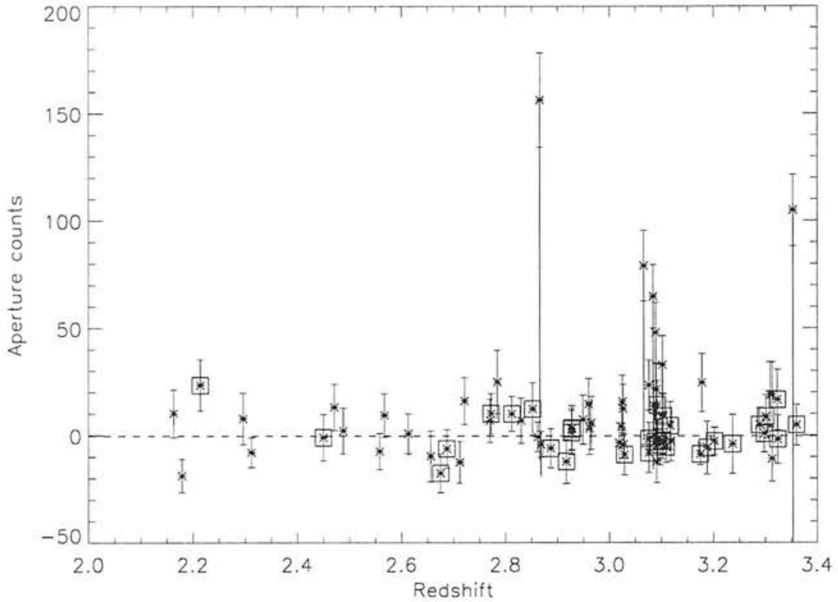

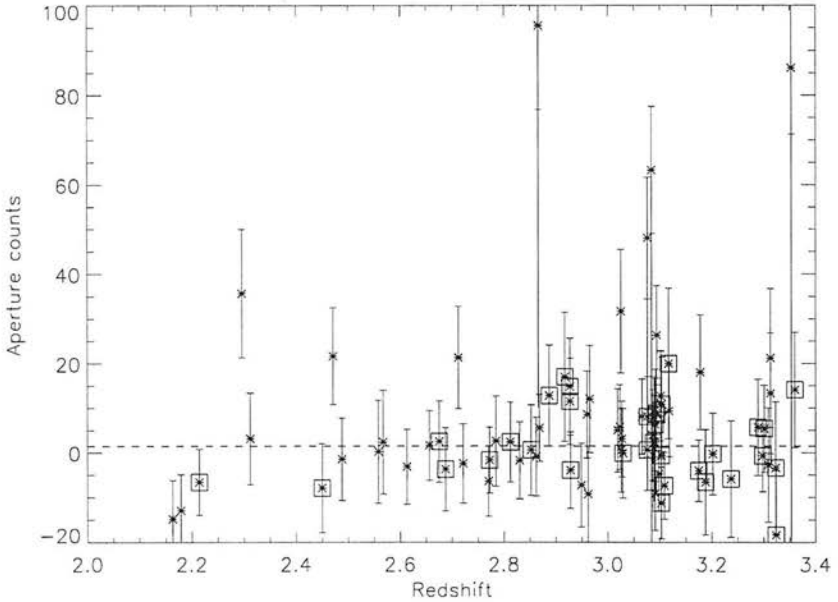

Figure 5.22: *Soft (top) and hard (bottom) band aperture fluxes at positions of confirmed high redshift Ly-break sources (Steidel et al. 2000). Boxed sources are sufficiently isolated to be included in the stacking analysis. Sources without boxes lie within the PSF of X-ray sources; vertical lines indicate the estimated contamination within the stacking aperture. The dashed line marks the error-weighted mean of the isolated sources. The ensemble flux is consistent with zero.*

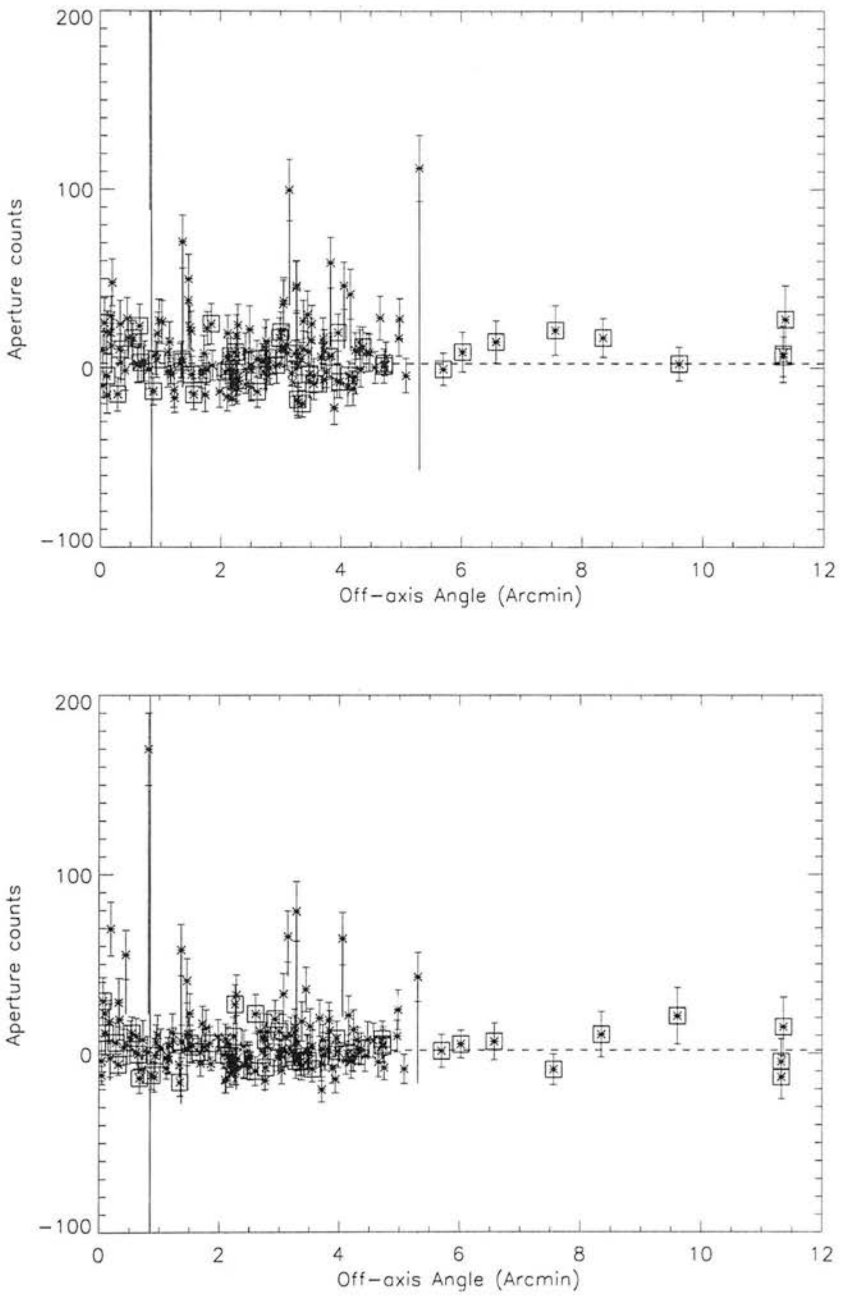

Figure 5.23: *Soft (top) and hard (bottom) band aperture fluxes at positions of Lyα candidates (Steidel et al. (2000) and §5.2). Symbols as in Figure 5.22.*

s^{-1} at $z = 3.09$, assuming an $\alpha = 0.7$ powerlaw with a Galactic column of 10^{20} cm^{-2}. Again, these limits exclude luminous AGN, but not obscured or low-luminosity AGN.

Previous stacked measurements of X-ray flux from high redshift Lyα emitting populations have been made by Malhotra et al. (2004) and Wang et al. (2004) for 70 $z \simeq 4.5$ Lyα sources in the Large Area Lyman Alpha survey, which were observed with Chandra for ~ 175 ks. They put a significantly tighter 3σ upper limit on the soft band luminosity of 2.8×10^{42}.

5.5.3 Submillimetre sources

Only 5 of the 18 submillimeter sources in the field are suitable for stacking, with 11 lying too close to bright X-ray sources and an additional 2 with overlapping stacking apertures. The resultant stacked flux limits (3σ) in the full, soft and hard bands are therefore quite high, at 1.9, 0.9, and 1.4×10^{-15}, respectively, again assuming an $\alpha = 0.7$ powerlaw with no intrinsic absorption. Though the error bars on the detected signal are consistent with 0, the values in the full and soft bands are a few $\times 10^{-16}$ erg s^{-1} cm^{-2}, within the range of values previously obtained in direct detections of SCUBA-detected galaxies in the Chandra Deep Field North by Alexander et al. (2003). Upper limits on the non-detections in the Alexander et al. (2003) sample are about an order of magnitude lower. The Waskett et al. (2003) stacking analysis of samples of 27 and 23 submillimeter sources in an XMM exposure of roughly 50 ks described above yielded somewhat tighter upper limits of 1.3 and 8.0×10^{-16} erg s^{-1} cm^{-2} in the soft band, and 6.6 and 13.0×10^{-16} erg s^{-1} cm^{-2} in the hard band, respectively.

5.6 Diffuse emission

The multiwavelength observations which identified a galaxy overdensity consistent with a massive protocluster in the SSA22 field also offer evidence of diffuse material in the environment. Steidel et al. (1998) note that metal-line absorption is observed at $z \simeq 3.09$ in the spectrum of a background quasar in the field, though none of the identified members of the structure lie near enough to the line of sight to be responsible. Similarly, Adelberger et al. (2003) find that Lyα forest transmission at $z = 3.1$ in the SSA22 field is very low. The narrow-band Lyα survey of Steidel et al. (2000) discovered two diffuse 'blobs' of Lyα flux, with equivalent widths indicating Lyα luminosities of 10^{44} erg s^{-1} and physical extents of ~ 100 kpc at $z = 3$. In a recent deeper narrow-band survey, Matsuda et al. (2004) identify 35 diffuse Lyα emitters in the field — of which the Steidel et al. (1998) blobs are the largest and most luminous — and note the strong clustering observed in these objects may indicate a dense environment which is relatively rich in neutral hydrogen.

The level of X-ray emission expected from diffuse material in the protocluster is highly uncertain. To date, the highest redshift, X-ray-luminous clusters found at $z \sim 1.3$ (Hashimoto et al. 2002, Rosati et al. 2004, Stanford et al. 2001, 2002) have temperatures of 2 – 6 keV and estimated bolometric luminosities of a few times 10^{44} erg s^{-1} (Ettori et al. 2004). Diffuse X-ray emission with luminosities of order 10^{45} erg s^{-1} over regions with radii of ~ 100 kpc has been observed around high redshift radio galaxies presumed to lie in protocluster regions at $z \sim 2$ (Fabian et al. 2001, 2003, Carilli et al. 2002, Scharf et al. 2003).

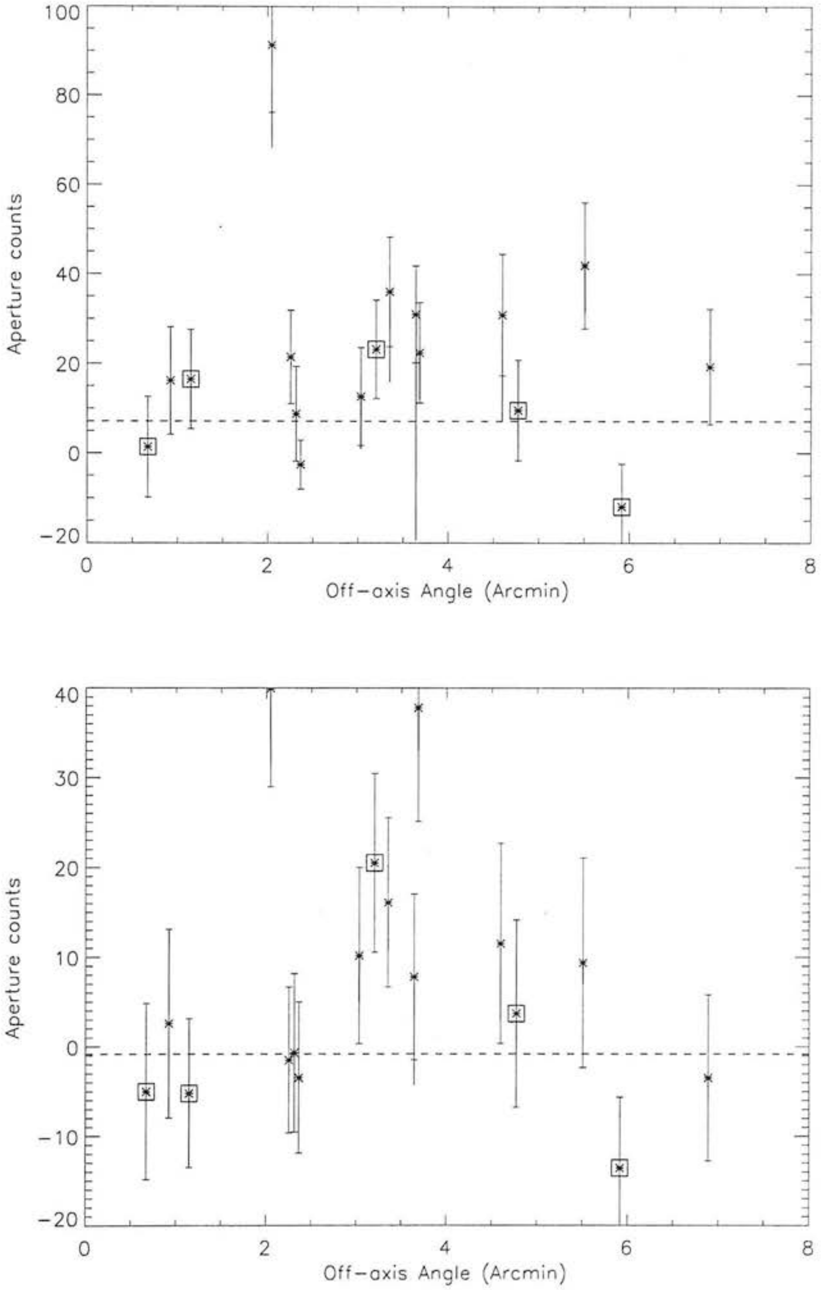

Figure 5.24: *Soft (top) and hard (bottom) band aperture fluxes at positions of radio-identified SCUBA sources in the SSA22 field (S. Chapman, private communication). Symbols as in Figure 5.22.*

However, in most cases this emission is likely non-thermal and is thought to result from Inverse-Compton scattering in a relativistic electron population associated with the central radio source, for which there is no counterpart in SSA22. In at least three $z > 1$ regions thought to be protocluster regions based on galaxy overdensities, no evidence of a hot ICM is found to luminosity limits of $\sim 10^{44}$ erg s^{-1} (Pentericci et al. 2002, Carilli et al. 2002, Neumann et al. 2003).

The expected X-ray characteristics of the Lyα nebulae depend upon their heating mechanism, which is still unknown despite several extensive multi-wavelength studies (Chapman et al. 2001, 2004, Ohyama et al. 2003, Bower et al. 2004). The Lyα emission could plausibly result from (i) photo-ionisation by a central starburst and/or AGN, (ii) cooling radiation of gravitationally collapsed material, or (iii) shock heating by a starburst-driven wind. As there is no evident ionising source for the blobs and the energy in the blobs is quite large, the photo-ionisation scenario requires a heavily obscured AGN at the core of each blob region. A more diffuse thermal X-ray component might be expected to accompany cooling radiation from gravitational collapse. However, in a theoretical study of forming galaxies, Fardal et al. (2001) find that most of the cooling radiation comes not from gas at the virial temperature of galaxies ($T \sim 10^6$ K) emitting in the X-ray, but from much cooler gas ($T < 2 \times 10^4$ K) emitting primarily in the Lyα line. Finally, soft X-ray emission may be expected from a massive starburst powerful enough to heat the Lyα nebulae through shock heating, but at flux levels far below the sensitivity of the XMM data.

5.6.1 Extended sources and background structure

In theory, the WAVDETECT algorithm used to detect the point sources in SSA22 should also successfully detect extended emission on scales of up to 16 pixels ($69.6''$). While the algorithm identified two sources in which the source cells were significantly ($> 4\sigma$) extended with respect to the nominal PSF size, both sources are at high off-axis angles ($> 13'$) where the radially averaged calibration model adopted by WAVDETECT significantly underestimates the PSF size. No significantly extended emission is detected throughout the region traced by the LBG and Lyα galaxy overdensities, and there is no X-ray detection at the locations of the diffuse Lyα blobs. To verify this result qualitatively, an image of diffuse emission was created by smoothing the coadded, exposure-corrected, EPIC image with a Gaussian of 5 pixels ($\sim 25''$) after masking the detected X-ray sources. Masking was done by blocking out an area equal to 3 times the WAVDETECT source cell and 'filling the holes' with values randomly selected from the Poisson distribution with the same mean as the surrounding background. In crowded areas this procedure left a surplus of flux in some source regions, and so the process was repeated. The resulting image is shown in Figure 5.25. Some artificial structure is observed near to the pn chip gaps and at the edges of the field of view, but there is no convincing indication of significant diffuse emission in the image.

Putting a quantitative limit on the lack of emission is complicated by large-scale non-uniformities in the background level. In order to avoid the sharp discontinuities of exposure over the pn chip gaps, limits on the diffuse emission were derived only from data from the two MOS cameras. As can be seen in Figure 5.25 for the full EPIC image, there is a significant radial structure to the exposure-corrected background levels such that higher background levels are observed toward the edges of the FOV. There is currently no explanation of this feature, which has been noted in other XMM datasets, but it likely results from errors

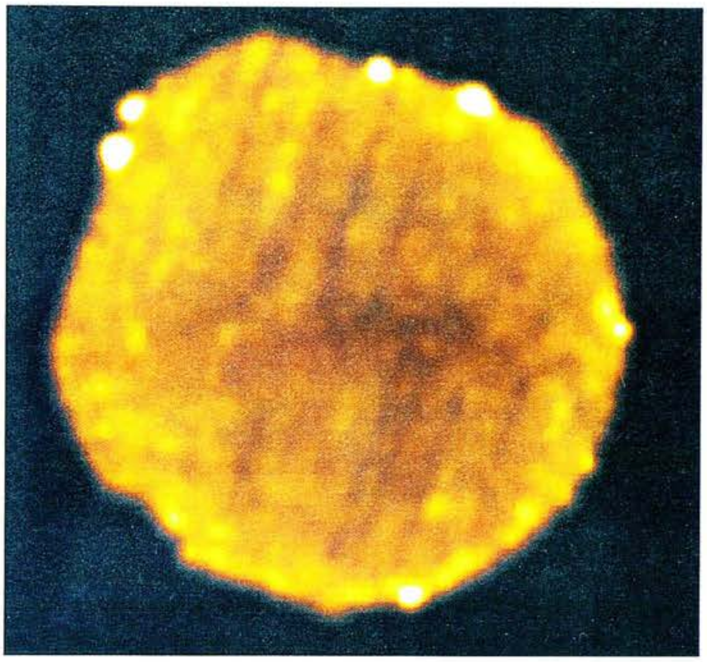

Figure 5.25: *0.5 – 2.0 keV image of diffuse emission in the SSA22 field. The image was made from the soft band EPIC data by masking the detected point sources with values derived from the local background, and smoothing the resulting image with a Gaussian with a FWHM of* $\sim 25''$. *The smoothing process has created artificial structure at chip gaps and at the edges of the FOV.*

in the SAS-generated exposure maps which seem to over-correct the vignetting of background flux in the raw data. The gradient is further illustrated in Figure 5.26, in which the thick black line indicate the mean MOS1+MOS2 count rate in annuli of $1'$ (excluding source regions) as a function of radius. Overplotted are the mean background values in arcs of $1'$ width extending from the aimpoint to the SE, SW, NE, and NW with 1σ Poissonian errors. The higher values in the Eastern quadrants are due to an offset between the centroid of the exposure map and the pointing position at the centre of the MOS chips.

5.6.2 Limits on a hot ICM

To put a limit on the level of diffuse thermal emission from the protocluster which could be detected by these observations, 15 circular regions with radii of 15 pixels ($\sim 65''$) were selected which i) avoided previously identified X-ray emission, ii) avoided the MOS chip gaps, and iii) were within $8'$ of the nominal telescope pointing. MOS 0.5 – 2 keV counts within the 15 background regions were then measured for aperture radii of 1 to 15 pixels (4.35 – 62.24$''$). Figure 5.27 shows the 3σ detection limit of diffuse emission on each scale as calculated from the standard deviation of the 15 apertures (solid line) as well as the square root of the mean count level per aperture (dotted line).

The deviation of these two lines toward larger apertures is further evidence of the non-uniformity of the

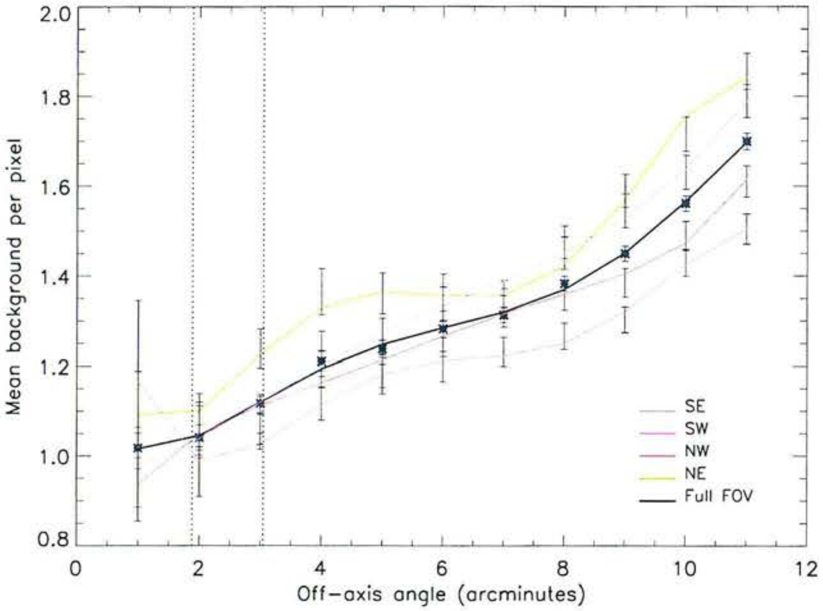

Figure 5.26: *Radial and azimuthal variation of the background levels of the MOS data. The thick black line indicates the mean MOS1+MOS2 background count rate in circular annuli with width of 1′ versus radius, while the coloured lines give average background levels in 1′ wide arcs in the four quadrants of the image.*

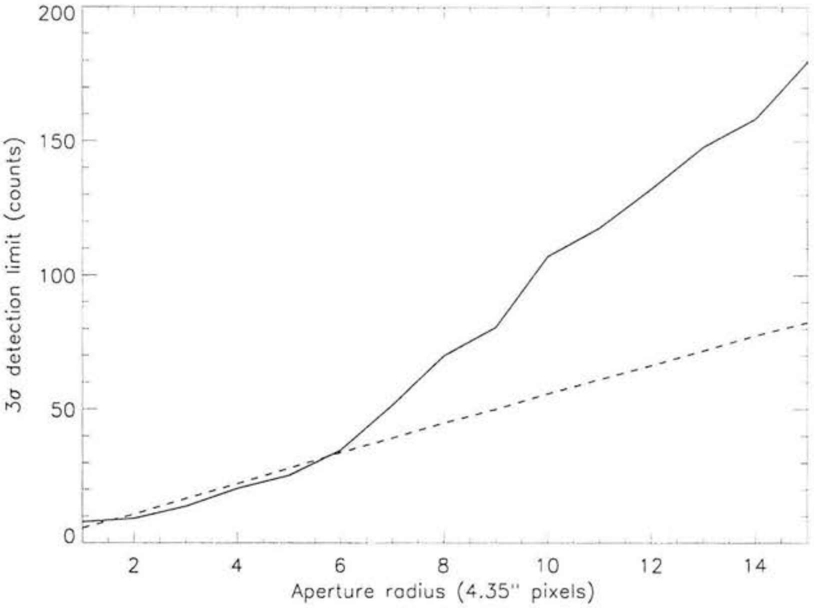

Figure 5.27: *Aperture radius versus 3σ detection limit for the $0.5-2$ keV MOS data. The limiting count levels are derived from the standard deviation of 15 background apertures (solid line). The square root of the mean background level is overplotted (dashed line).*

background on large scales. While a radial correction could be applied to the measured background levels to partially alleviate this effect, the non-radial variation illustrated in Figure 5.26 would introduce systematic errors which would be difficult to quantify. Instead, I choose to use the observed variance in background over the field to obtain a robust, conservative estimate of the diffuse detection limit over the protocluster region. It is worth noting that this estimate neglects the $\sqrt{N}$ errors from the detection aperture itself. For large apertures this additional error is negligible, as the error on the counts required for a 3σ detection is small compared to the error on the background. For small apertures with low numbers of counts, however, the addition of the $\sqrt{N}$ term will lead to an increase in the overall uncertainty of order 15%.

The largest radius shown on Figure 5.27 corresponds to a distance of just under 500 kpc at $z = 3.09$, which is roughly equivalent to the typical radius encompassing a density contrast of 500 (R_{500}) for a 4 keV cluster at $z \sim 1.3$ as given by Ettori et al. (2004). The upper limit on the $0.5-2$ keV count rate for an aperture of this radius is 1.15×10^{-3} ct s^{-1}, corresponding to an observed frame $0.5-2$ keV luminosity limit of $\sim 9 \times 10^{43}$ erg s^{-1} for thermal bremsstrahlung models with temperatures from $2-6$ keV. Here and throughout this section, I have used the XSPEC spectral fitting package to convert count rates to fluxes appropriate for the XMM MOS response and the assumed spectral model.

The XMM data therefore robustly exclude all but the faintest thermal emission seen in nearby clusters (see Edge 2004, Figure 1.1) on a scale of roughly 1 Mpc at the distance of the protocluster. This is likely a very conservative limit, as the R_{500} radius is surely an overestimate of the extent of any thermal emission at $z \sim 3$ and thermal emission on smaller scales is limited to substantially lower values as seen in Figure

5.27. In the $z > 1$ clusters currently known — RX J0910+5422 at $z = 1.1$ (Stanford et al. 2001), RX J1252-2927 at $z = 1.2$ (Rosati et al. 2004), RX J1053.7+5735 at $z = 1.26$ (Hashimoto et al. 2002) and RX J0849+4452 and RX J0848+4453 at $z = 1.3$ (Stanford et al. 2002) — the radius of the region of detectable X-ray flux is considerably smaller than R_{500} and typically $\leq$ 300 kpc. The 0.5 – 2 keV luminosities of three of these clusters have been measured within radii of $\sim$ 300 kpc, and range from $3.2 - 5.0 \times 10^{43}$ erg s^{-1}. The limiting soft band luminosity of the XMM observations of SSA22 for apertures of this size, derived as above, is 3.0×10^{43} erg s^{-1}, indicating cluster emission similar to that seen at $z \sim 1.3$ would be significantly, though marginally, detected if present in SSA22. Extended emission similar to that seen at higher redshifts around the radio galaxies 3C 294 (Fabian et al. 2001, 2003), 4C 41.17 (Scharf et al. 2003), and PKS 1138-262 (Carilli et al. 2002) is also strongly excluded, as the limiting luminosity on scales of $\sim$ 100 kpc is orders of magnitude below the diffuse X-ray luminosities observed in these objects.

5.6.3 Limits on X-ray emission associated with the Lyα blobs

To put a limit on diffuse X-ray emission associated with the two regions of bright, diffuse Lyα emission reported by Steidel et al. (2000), apertures with diameters of 34.8$''$ (8 pixels) were placed at the locations of the narrow-band sources. As the blob regions have angular sizes of 15$''$ and 17$''$, respectively, these apertures allow for the defocus due to the XMM PSF and enclose any associated flux. The background level was determined from 24 apertures of the same size, placed edge to edge over a 5 aperture by 5 aperture grid surrounding the Lyα positions. Background apertures which overlapped any part of detected X-ray source cells were discarded. The mean background aperture level was used as the background level, while the standard deviation of these apertures was adopted as the error on the background. Neither of the blobs was detected at greater than 3σ significance in any band. The limiting soft band count rates of the two blobs, given by 3 times the background error, is equivalent to within 1% for the two regions and equal to 1×10^{-4} ct s^{-1}. This limit is slightly tighter than would be implied from Figure 5.27, due to the use of a local background. The corresponding hard band limits are 8.6×10^{-5} ct s^{-1} and 1.1×10^{-4} cts s^{-1} for B1 and B2, respectively. These values imply limiting luminosities for thermal emission with temperatures of 2 – 6 keV at $z = 3.09$ of $\sim 8 \times 10^{42}$ erg s^{-1}and $\sim 2 \times 10^{43}$ erg s^{-1}in the observed frame 0.5 – 2 keV and 2 – 8 bands, respectively.

To limit the point source emission which might be associated with the Lyα haloes, the same procedure was repeated with an aperture size of 2 pixels for the soft and hard band MOS data. The measured count-rates were corrected for losses outside this aperture at the off-axis angles of the blobs, as described in §5.3.2. There was no significant detection in any band, and the resulting average count-rate limits are 8.8×10^{-5} ct s^{-1} and 8.3×10^{-5} ct s^{-1} for the hard and soft bands, respectively. Variation between the blobs in either band was $< 15\%$. Figure 5.28 plots the limiting rest-frame 0.5 – 8 keV luminosity for an absorbed powerlaw spectrum with energy index $\alpha = 0.9$ implied by the soft and hard band limits. The limits are plotted versus absorbing column, and corrected for intrinsic absorption. Point sources with absorbing columns of less than 10^{23} cm^{-2} are excluded to $L_{0.5-8} \simeq 5 \times 10^{43}$ erg s^{-1}, and all but Compton thick sources are excluded at $L_{0.5-8} < 10^{45}$ erg s^{-1}. Therefore, while heavily obscured AGN may still exist at the position of the Lyα blobs, there is no evidence for a source sufficiently luminous to power the diffuse emission.

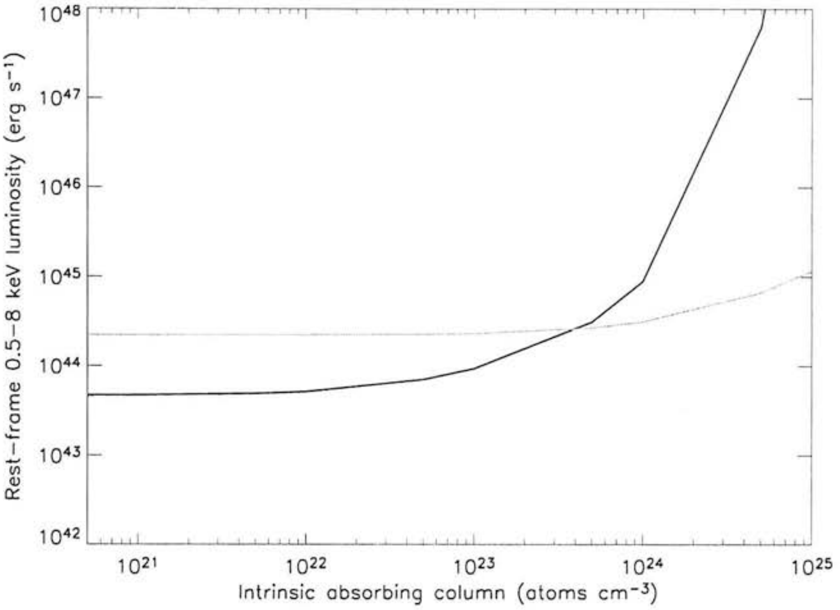

Figure 5.28: *3σ MOS upper limits of the 0.5 – 8 keV rest-frame luminosity of point-like sources at the location of the Lyα blobs versus model absorbing column. Values were derived from the limiting count rates in the soft (black) and hard (gray) bands assuming an $\alpha = 0.9$ obscured powerlaw model, and are corrected for intrinsic absorption.*

5.7 Conclusions

In this chapter I have presented two surveys of the SSA22 protocluster region. My wide-field narrow-band survey identified 30 new Lyα candidates, mostly in a northwest extension of the identified galaxy overdensity. The deep X-ray survey conducted with XMM identifies 190 point sources to a full band (0.5 – 8.0 keV) flux limit of $\sim 10^{-15}$ erg s^{-1} cm^{-2}.

Cross-correlation of the X-ray sources with the 176 known or candidate members of the SSA22 protocluster yields just 3 direct X-ray detections, all of which appear to be Type I quasars. One is a previously identified moderately-obscured quasar hosted by a LBG residing at a local peak in the density enhancement, while the other two are coincident with Lyα candidates. Of the latter, one is known to be a luminous quasar roughly 10 Mpc from the core of the protocluster, while the other is not spectroscopically identified. The identification of a single LBG within the sample is consistent with the measured AGN fraction of LBGs and galaxies overall, and indicates no surplus of activity within protocluster members. The identification of two quasars within the sample of 150 Lyα emitters in the field indicates a marginally higher level of AGN activity than in a similar sample at $z \sim 4.5$, but this increase cannot be considered significant. The XMM data effectively surveys the quasar population of the protocluster populations, but is not sensitive enough to identify any more heavily obscured or low-luminosity AGN populations which may be hosted by protocluster galaxies. A stacking analysis of the LBGs, Lyα emitters, and submillimetre-detected sources in the region puts somewhat tighter limits on the typical AGN population, but still is not sensitive enough to conclusively rule out populations of Seyferts and/or LLAGN.

No evidence for diffuse X-ray emission is found in the field. The XMM data robustly exclude all but the faintest thermal emission seen in nearby clusters on scales of ~ 1 Mpc, and just excludes the smaller-scale, lower-luminosity emission seen in the most distant clusters at $z \sim 1.3$. There is also no evidence for the sort of extended emission seen around high redshift ($z \sim 2$) radio-galaxies on scales of ~ 100 kpc, consistent with the interpretation that the diffuse emission in these sources arises in Inverse Compton scattering off relativistic electrons in the radio jets. Finally, no diffuse or point source X-ray emission is detected associated with the luminous Lyα blobs in the region. The sensitivity limits of the XMM data exclude heating of the Lyα blobs by moderately-obscured ($N_H < 10^{23}$ cm^{-2}) AGN with observed full-band luminosity $> 10^{44}$ erg s^{-1} and any AGN brighter than 10^{45} erg s^{-1}.

CHAPTER 6

Conclusions

This thesis presents three multiwavelength surveys of different environments based on deep X-ray observations, which together aim to develop our understanding of AGN and their role within the evolution of galaxies and their larger-scale environment. In this concluding chapter, I summarize the major results of my work (§6.1), discuss these results in the context of the growing understanding of AGN within the evolving Universe (§6.2), and suggest relevant future work (§6.3).

6.1 Review of major results

6.1.1 The ELAIS Deep X-ray Survey: the AGN field population

In Chapter 3, I presented work done in support of the ELAIS Deep X-ray Survey, which is based on 75 ks Chandra ACIS-I observations of the ELAIS N1 and N2 fields. The major goal of this 'blank-field' survey was to characterise the constituents of the XRB and their relation to populations selected at other wavelengths. My primary role within the EDXS consortium was leading the X-ray spectral analysis of the sample. The main results of this work were:

- Sources with harder X-ray spectra are found at fainter full-band X-ray flux. The sources responsible for this trend are identified in optical images as bright galaxies or optically faint objects. Sources with point-like optical counterparts, which dominate the source counts at bright fluxes, are far less common toward faint fluxes and show no significant X-ray spectral dependence on flux.
- Those sources with optically faint counterparts have similar X-ray spectral properties as those associated with galaxies, but extend to fainter optical magnitudes and redder optical colours, suggesting they may be a similar galaxy population at higher redshift.
- Sources with point-like counterparts have X-ray to optical ratios, $\frac{f_X}{f_{r'}}$, between 0 and 10, as is typical for quasars. There is a much larger spread in $\frac{f_X}{f_{r'}}$ for the sources associated with galaxies and optically faint objects, as would be expected for obscured AGN where the host galaxy, not the active nucleus, dominates the optical emission.
- Sources with point-like counterparts typically have X-ray hardness ratios clustering around -0.5 and optical colours of $1 \leq r' - H \leq 4$, values typical of quasars. The sources associated with galaxies and optically faint objects generally have harder X-ray spectra and redder optical colours which are consistent with dusty and/or evolved stellar populations. Several of the optically faint X-ray sources are EROs ($r' - H > 5$) which, as a class, are dominated by dusty starbursts and passively evolving old galaxies at $z \sim 1$.
- Hard X-ray selected sources which are faint and red in the optical are identified as AGN hosted by galaxies in a variety of evolutionary states. The three sources we study in Willott et al. (2003) are identified as a reddened quasar at $z \sim 2.6$, a radio galaxy at $z \sim 1.6$, and an ERO at $z \sim 1$.
- Disparities between the absorbing column inferred from optical reddening and that indicated by X-ray absorption are common, such that the definition of Type 1 and Type 2 objects must be considered wavelength dependent. This may be due to peculiarities of the absorbing material (unusually high or low gas-to-dust ratios), or to variations either in the light paths of the X-ray and optical emission or in the locations of the X-ray and optical absorbers.
- The reddened quasars in the Willott et al. (2004) sample have observed gas-to-dust ratios up to ten times higher than the Galactic value. As noted above, this may indicate that the X-ray and optical absorption are not co-spatial.

6.1.2 MS1054-0321: A massive cluster at z = *0.83*

In Chapter 4, I presented a survey of X-ray point sources in an archival 91 ks Chandra ACIS-S observation of the $z = 0.83$ cluster MS1054-0321. MS1054-03 is an Abell class 3 cluster which exhibits significant substructure both in the galaxy overdensity and in luminous ICM emission; weak lensing analysis indicates it is young, massive, and still relaxing. It has a low fraction of early-type galaxies in the core, a substantial fraction of merging galaxies, and hosts at least 6 radio-loud AGN. The goal of the X-ray study was to take a more complete census of AGN activity. The main results of this work were:

- 47 X-ray sources are detected within the $8.3' \times 8.3'$ field, of which two are immediately confirmed from pre-existing spectroscopy to be luminous AGN ($L_{0.5-8\ \mathrm{keV}} \sim 10^{43}$ erg s^{-1}) at the redshift of the cluster.
- At fluxes brighter than $S_{0.5-8\ \mathrm{keV}} = 5 \times 10^{-15}$ erg s^{-1} cm^{-2} there is a $\sim 2\sigma$ excess in source counts compared to predictions from field surveys, consistent with an excess of approximately 6 AGN. If these sources are associated with the cluster, they too are AGN with luminosities of order $L_{0.5-8\ \mathrm{keV}} \sim 10^{43}$ erg s^{-1}.
- Combined with the identification of 7 cluster AGN from deep radio observations (Best et al. 2002), these observations suggest significantly enhanced AGN activity in MS1054-03 compared to local galaxy clusters.
- Interestingly, the excess of X-ray detected AGN is found at radial distances of between 1 and 2 Mpc, suggesting they may be associated with infalling galaxies.
- The radio AGN are seen within the inner Mpc of the cluster and are largely undetected in the X-ray, suggesting they are either intrinsically less luminous and/or heavily obscured.

6.1.3 SSA22: A complex protocluster at z=*3.09*

In Chapter 5, I presented an 150 ks XMM exposure of the SSA22 protocluster field, as well as a narrow-band, wide-field, Lyα survey of the region. The protocluster was first identified in a Lyman break survey and subsequently probed with narrow-band Lyα and submillimetre observations; it is now thought to include ~ 150 galaxies and to trace out a mass overdensity of order $10^{15} M_{\odot}$. The goals of the X-ray survey were to (i) identify AGN associated with the protocluster, (ii) investigate the X-ray properties of the high redshift populations in the field, and (iii) search for diffuse emission associated either with the cooling protocluster or with the luminous, diffuse, Lyα emission it contains. The main results of this work are:

- 29 new Lyα candidates are identified in an area of $\sim 25' \times 25'$, the majority of which extend to the North and East from the confirmed protocluster region. Over roughly the same field, 190 point sources are detected in the XMM data to a full band flux limit of $S_{0.5-8\ \mathrm{keV}} \simeq 2 \times 10^{-15}$ erg s^{-1} cm^{-2}.
- Three protocluster members are detected directly in the X-ray image, all of which appear as point-like quasars in optical imaging and have estimated bolometric luminosities of order 10^{46} erg s^{-1}.

They are hosted by: (i) a LBG with a substantial X-ray column located at a peak in the galaxy overdensity; (ii) a broad-line QSO identified in deep narrow-band Lyα imaging and located ~ 10 Mpc in front of main galaxy overdensity; and (iii) a Lyα candidate with no spectroscopic ID. The observed AGN fractions of LBGs and Lyα candidates in SSA22 are $\sim 4\%$ and $\sim 1.3\%$, respectively, consistent with other studies (Brandt et al. 2001a, Nandra et al. 2002, Wang et al. 2004).

- Stacking analyses of the LBG, Lyα, and submillimetre samples in the field do not result in significant detections, and limit the average hard X-ray luminosity of each type of source to $\sim 5 \times 10^{43}$ erg s^{-1}. This is sufficient to rule out luminous quasars, but not obscured sources or LLAGN.
- There is no evidence of diffuse intracluster emission associated with the protocluster. Soft band X-ray flux on scales of ~ 1 Mpc is limited to $L_{0.5-2\ \mathrm{keV}} \lesssim 9 \times 10^{43}$ erg s^{-1}, robustly excluding all but the faintest thermal emission seen in local clusters. On smaller scales of ~ 0.6 Mpc which may be more typical of high redshift clusters, the limit is $L_{0.5-2\ \mathrm{keV}} \lesssim 3 \times 10^{43}$, which just excludes the level of emission seen in clusters at $z \sim 1.3$. The luminous extended emission seen around high redshift radio galaxies on scales of ~ 100 kpc, thought to be due to IC scattering of IR photons in the radio jets, is also strongly excluded.
- The limit on thermal X-ray emission associated with the Lyα 'blobs' is $L_{0.5-2\ \mathrm{keV}} \lesssim 1 \times 10^{42}$ erg s^{-1}. Point source limits exclude AGN with obscuring columns of $N_H \lesssim 10^{23}$ cm^{-2} to $L_{0.5-8\ \mathrm{keV}} \lesssim 5 \times 10^{43}$ erg s^{-1}, and all but Compton thick sources to $L_{0.5-8\ \mathrm{keV}} \lesssim 10^{45}$ erg s^{-1}.

6.2 AGN in the evolving Universe

6.2.1 The field population of AGN

One focus of this thesis was to explore the field population of AGN whose summed emission comprises the cosmic X-ray background. The X-ray and optical properties of the EDXS sample — and of contemporary X-ray surveys — confirm that the majority of the hard (< 10 keV) X-ray background emission arises in populations of variously obscured AGN. The X-ray luminosities, varied X-ray to optical flux ratios, extended optical morphologies and optical colours are all consistent with accretion onto nuclear black holes which is obscured at both X-ray and optical wavelengths, as predicted by XRB synthesis models. A small amount of the hard XRB may arise in an as yet unprobed, harder source population, which may be identified with even more heavily obscured AGN (Moretti et al. 2003). Furthermore, the contribution of the sources resolved below 10 keV to the total XRB flux is still model dependent. Constraining these models, and therefore the possible population of Compton thick sources which might contribute near the 30 keV peak of the background emission, will require a detailed knowledge of the newly-resolved obscured population.

While results from ROSAT and ASCA suggested a harder X-ray source population associated with galaxies, one surprising result emerging from the Chandra and XMM surveys was the large fraction of relatively low-redshift galaxies which contribute to the background flux. The heavily obscured, luminous AGN at high redshift which were predicted by many synthesis models to contribute much of the XRB are not found in large numbers. Instead, a majority of the flux is resolved into more moderately obscured objects at lower redshift. As discussed in Cowie et al. (2003), while the accretion activity in luminous and largely unobscured quasars peaks at $z \simeq 2$, near to the peak in the global star-formation rate, the number counts of less luminous and more often obscured AGN have been found to peak more recently, so that 54% of the total hard XRB is emitted at $z < 1$ (Barger et al. 2003). As seen within the EDXS sample, many of these lower redshift hosts are bright, early-type galaxies in which the red optical colours reflect evolved stellar populations.

Toward faint fluxes, an increasingly large fraction of the hard X-ray sources are associated with optically faint hosts. Many of these objects have X-ray spectral properties and optical colours which overlap and extend to the red of those of the bright galaxy population, suggesting they are similar objects at higher redshift. Characterisation of this large, optically faint population has been the major bottleneck in understanding the sources comprising the XRB. In the CDFN, the target of one of the most extensive follow-up programmes, Barger et al. (2003) find that some of these objects are evolved, bulge-dominated galaxies at high redshift ($1.5 < z < 2.5$) with uniformly old stellar populations. Within the EDXS, we have targeted subsamples of the most interesting and/or typical sources for further study — i.e., hard X-ray sources with red, faint optical counterparts in Willott et al. (2003) and reddened quasars in Willott et al. (2004) — and find high redshift hosts in a variety of evolutionary states.

Comparisons of the X-ray populations with submillimetre galaxies within field survey regions have begun to explore the links between galaxies and AGN in their epoch of formation. Within the EDXS, submillimetre-bright galaxies are not, in general, detected at X-ray wavelengths, but do appear to be significantly clustered with the X-ray population, suggesting they may populate the same large scale structures and form an evolutionary sequence (Almaini et al. 2003). Alexander et al. (2002) finds a larger fraction of SCUBA sources are detected within the 2 Ms observations of the CDFN, with luminosities more consistent with Seyfert galaxies ($\sim 10^{43-44}$ erg s^{-1}) and moderate absorbing columns. Page et al. (2004) explore the evolutionary link with submillimetre observations of samples of X-ray obscured and unabsorbed AGN, and find that strong submillimetre emission is exhibited only in the X-ray obscured sample, indicating the central active nuclei are hidden during the major growth phase of the galaxy spheroid. These authors find that the space density and luminosities of obscured AGN imply that they represent an evolutionary phase between Compton thick growth and unobscured quasar activity.

A significant challenge arising from the survey data is how to reconcile the full demographics of the obscured AGN population with the apparent link between black hole and galaxy growth and the AGN/host coevolution models which seek to explain it. How can the observation of evolved elliptical AGN host galaxies over a range of redshift for both X-ray obscured AGN (Barger et al. 2003) and unobscured quasars (e.g., Kukula et al. 2002) be understood within the paradigm of coeval growth? How does luminosity dependent evolution in AGN populations relate to the star formation history in galaxy hosts? Is there room within the still unresolved XRB for the significant population of very heavily obscured luminous AGN predicted by 'hidden quasar' models? Deep hard X-ray imaging is currently the most efficient way to take a census of all but Compton thick AGN, and it also provides a measure of the absorption by gas along the line of sight. Follow-up observations of populations of obscured AGN — especially targeted observations of the optically-faint, hard X-ray sources likely to have high redshift hosts — will help to address these issues.

The new survey data also have implications for unified models of AGN. The simplest forms of Type 1 / Type 2 orientation-dependent unification — well-proven for some Seyfert galaxies at low redshift — may not be applicable to all low-luminosity AGN, and seem certainly inapplicable at higher luminosities. The surveys with high levels of spectroscopic completeness offer good evidence of luminosity dependent obscuration (e.g., Ueda et al. 2003). Furthermore, as seen within subsets of the EDXS sample, significant fractions of AGN appear differently obscured at optical and X-ray wavelengths, leading to a more complicated picture than presented in the standard dusty/gaseous torus model. Page et al. (2004) give convincing evidence of fundamental differences in the isotropic submillimetre emission between obscured and unobscured quasars, indicating that obscuration in high luminosity sources cannot be due solely to orientation angle. That the orientation scheme works so well in many Seyferts suggests fundamental differences in the geometry of absorbing gas between low and high luminosity sources. Finally, as Matt et al. (2003) point out, the level of obscuration in some sources is seen to vary, indicating a more complex interaction between the apparent obscuration and the central engine. In the coming years, these new data will require revision of the unified model, and will also impact the interpretation of the XRB as a constraint of AGN demographics and evolution.

6.2.2 AGN within dense environments

A second and complementary focus of this thesis was to examine the AGN content of dense environments. As X-ray surveys of rich clusters had been hindered by poor resolution and many cluster AGN lack distinctive optical signatures (Martini et al. 2002, Best 2004), the populations of AGN within X-ray bright clusters such as MS1054-03 are only now beginning to be explored. The early results of these surveys have been quite encouraging. Populations of AGN have been discovered in nearly every cluster surveyed with Chandra. More luminous AGN populations are seen toward higher redshift, which could reflect evolution of the field population, the infall rate, and/or the efficiency of the cluster mechanism for damping out activity. Luminous AGN populations are not, however, found in every cluster; the prevalence of nuclear activity in cluster galaxies must also relate to parameters such as environment richness and dynamical state. Quantifying these dependencies in larger samples of cluster AGN may provide valuable insight into the evolution of AGN activity within individual galaxies and over cosmic time.

Study of the spatial distribution of the AGN populations seems particularly promising in terms of investigating the mechanisms by which activity in both AGN and their hosts are affected by environment. Many cluster AGN are hosted by galaxies already resident on the cluster red sequence (Martini et al. 2002), which may imply that different mechanisms regulate the AGN and star-forming activity within dense environments, as seems to be the case for the radio-loud AGN studied by Best (2004). Moreover, the dichotomy of the spatial distribution of radio-loud and radio-quiet sources in MS1054-03 echos the separation of emission-line and absorption-line AGN seen in the Best (2004) sample; luminous X-ray bright AGN may, like the emission-line sources, avoid the cluster cores and, instead, trace the outskirts of dense structures. In both MS1054-03 and in A2104 (Martini et al. 2002), there is tentative evidence that luminous AGN are hosted by newcomers to the dense environment, and therefore may be triggered by infall. The radio-loud, X-ray quiet AGN nearer the core of MS1054-03 may trace a population of fainter AGN in which nuclear activity has damped after longer residence in the cluster, and in which radio emission may be boosted by the hot ICM.

Clusters also offer an observationally efficient means of tracking the evolution of both star formation and accretion activity in massive galaxy populations which formed early and coevally in rare high density peaks in the Universe. High redshift protoclusters contain large samples of Lyman break, Lyα, and submillimetre selected sources which are thought to be the precursors of local massive ellipticals and which — by virtue of the black hole - bulge mass relation — must at some point host powerful AGN. The overall X-ray detection rate of these populations is rather low, with no SCUBA sources and roughly 1% of Lyα candidates and 3% of LBGs hosting AGN of quasar luminosities within the SSA22 field. As noted above, extremely sensitive observations of the SCUBA population in the hard X-ray reveal a higher detection rate ($\gtrsim 36\%$) at Seyfert luminosities. Lower luminosity X-ray emission is found in stacking analyses of the LBG population by Brandt et al. (2001a) and Nandra et al. (2002) which is consistent with star-formation activity, and no indication of X-ray emission is seen in stacking analyses of Lyα sources (Malhotra et al. 2004, Wang et al. 2004). It is an important question whether the black holes in these populations are undergoing luminous but heavily obscured accretion, growing at relatively low accretion rates, or not accreting at all.

Finally, there is some indication that the AGN which are identified in protocluster regions might trace higher density locations in these structures. The single AGN confirmed to be within the main galaxy overdensity in the SSA22 field is found at a peak in the local density field, which is several times more dense than the factor of 6 overdensity of the protocluster region as a whole. Similarly, Pentericci et al. (2002) find four of five X-ray sources likely to be associated with a protocluster containing MRC 1138-262 form a filament in the plane of the sky with the radio source. The numbers of identified protocluster AGN are far too small to make much of their spatial distribution, but observations of more dense environments, particularly at $1 < z < 2$, may help to define how increasing galaxy density and build-up of the hot ICM work to stamp out activity in cluster cores.

6.3 Future work

Extensions of the work presented in this thesis are planned which aim to i) explore the relationship between black hole and galaxy growth at high redshift and ii) further characterise the AGN populations of clusters and protoclusters. To conclude, I discuss each of these briefly, in turn.

6.3.1 Disentangling quasar and galaxy formation

Joint X-ray/submillimetre surveys offer the promise of probing accretion onto black holes within galaxies undergoing their major period of growth, thus constraining the coevolution process. Previous comparative hard X-ray/submillimetre surveys have been hindered by (i) incomplete redshift information, (ii) a small overlap in detected populations, and (iii) the inability to detect Compton-thick AGN. Here I outline two planned experiments which avoid these pitfalls and should thus provide unambiguous tests of current models of coeval galaxy and black hole growth.

XMM/SCUBA observations of radio galaxies

To investigate the evolution of dust mass in massive ellipticals with redshift, Archibald et al. (2001) conducted SCUBA observations of a sample of radio galaxies spanning the range $1 < z < 5$. Radio galaxies are the most massive galaxies known at these high redshifts and, by virtue of their high radio luminosity, are certain to host powerful AGN. Ruling out correlations with other galaxy properties, Archibald et al. (2001) find submillimetre detectability and luminosity increase significantly with redshift, with $\bar{L}_{\mathtt{submm}} \underset{\sim}{\propto} (1+z)^3$ to $z \simeq 4$. Here, SCUBA appears to be tracking the evolution of massive galaxies from dynamic, rapidly star-forming systems at high redshift to the relatively placid, passively-evolving ellipticals which host powerful AGN locally. Hard X-ray observations of these sources — by definition hosts of powerful AGN — will provide an ideal test of coeval galaxy spheroid/black hole growth scenarios which predict more highly obscured AGN in submillimetre bright hosts. Observations targeting a subset of the radio galaxy sample chosen to have similar radio power but a wide range in redshift ($1.78 < z < 4.25$) are scheduled for 2004.

Hard X-ray/SCUBA/SIRTF field surveys

Broader population studies will benefit from several large scale surveys at hard X-ray, submillimetre, and IR wavelengths which are already or will soon be available. The SHADES submillimetre survey will cover 0.5 square degrees to a 4 σ detection limit of 8 mJy at 850 μm. The survey will detect $\sim$ 200 submillimetre sources with redshift estimates for all to better than $\Delta z = 0.5$. Deep hard X-ray data is already available over the field, allowing a detailed census of AGN activity. SIRTF observations to be completed by 2005 will be able to isolate dust heated primarily by the AGN; AGN have warmer mid- to far-IR colours than starbursts and will be preferentially selected in the 8 and 24 μm SIRTF bands (Lonsdale et al. 2003). Finally, by mid-2006 the Ultradeep Survey of the UKIRT Infrared Deep Sky Survey will accumulate deep ($K = 23.0, J = 24.0$) wide-field (0.77 deg^2) WFCAM imaging within the survey region allowing measurement of the abundance of high redshift passive ellipticals to $z = 3$.

Following on from the radio galaxy study detailed above, these field samples will allow more generalised tests of galaxy evolution models. (Archibald et al. 2001) note that the redshift distribution of the SCUBA population as a whole is indistinguishable from that of their radio galaxy sample, and suggest that it may be representative of the massive elliptical population in general. Examination of the absorbing column vs. submillimetre luminosity relation for both radio-loud and radio-quiet sources within properly defined field samples will test this. Furthermore, the radio galaxy sample by design contains only the most massive galaxies. The field survey data will also probe coevolution of AGN and hosts comprising the large population of more moderate L* galaxies which produce the bulk of cosmic background emission.

6.3.2 Evolution of AGN activity in high redshift clusters

To date, most AGN associated with clusters and protoclusters have been serendipitously observed in X-ray data obtained to study the diffuse cluster gas. Because of this no unbiased sample exists with which to investigate how the prevalence and demographics of cluster and protocluster AGN relate to redshift, dynamical state, environment richness, and presence or absence of a luminous hot ICM. The study presented in Chapter 4 was the first X-ray study in an ongoing program to investigate the AGN content of clusters to a redshift of ~ 1. Extending this project to higher redshifts will probe the epoch of cluster formation. As seen in Chapter 4, AGN are fairly straightforwardly detected in high redshift clusters on the basis of X-ray point source excesses alone. Suitably deep X-ray data in confirmed cluster fields at $z > 1$ will allow (i) determination of the AGN fraction in dynamically young protoclusters, (ii) investigation of AGN demographics in clusters with and without a hot, dense intracluster medium, and (iii) study of cluster to field ratios through the peak of AGN and star-forming activity. Observations at optical, IR, and radio wavelengths will also be crucial for confirming environment richness, and fully examining the role of AGN and their hosts within forming clusters.

This project will entail amassing high quality X-ray data and complementary observations over a wide wavelength range for a sample of cluster and protocluster fields at high redshift. While the observational aspect of this work is ambitious, much of the necessary data is already or will soon be available. Several protoclusters have been discovered in Ly-α surveys around high redshift radio galaxies. Many of these fields already have excellent X-ray data publicly available in the archive. In other promising high redshift cluster fields HST imaging is already available (Best et al. 2003), and multi-object spectroscopy of the cluster candidates to confirm environment richness is ongoing. Finally, as radio galaxies are proving efficient beacons of high density peaks in the Universe, the radio galaxy sample to be observed with XMM described above may prove extremely valuable in this work as well, as cluster and protocluster regions over a wide range of redshifts may be serendipitously observed. Diffuse emission could plausibly be detected by XMM in these fields out to $z \sim 3$, and AGN overdensities may be identified from the X-ray data alone.

Bibliography

Abadi, M. G., Moore, B., and Bower, R. G.: 1999, *MNRAS* **308**, 947

Abell, G. O.: 1958, *ApJS* **3**, 211

Adelberger, K. L., Steidel, C. C., Shapley, A. E., and Pettini, M.: 2003, *ApJ* **584**, 45

Akiyama, M., Ohta, K., Yamada, T., Kashikawa, N., Yagi, M., Kawasaki, W., Sakano, M., Tsuru, T., Ueda, Y., Takahashi, T., Lehmann, I., Hasinger, G., and Voges, W.: 2000, *ApJ* **532**, 700

Alexander, D. M., Aussel, H., Bauer, F. E., Brandt, W. N., Hornschemeier, A. E., Vignali, C., Garmire, G. P., and Schneider, D. P.: 2002, *ApJ* **568**, L85

Alexander, D. M., Bauer, F. E., Brandt, W. N., Schneider, D. P., Hornschemeier, A. E., Vignali, C., Barger, A. J., Broos, P. S., Cowie, L. L., Garmire, G. P., Townsley, L. K., Bautz, M. W., Chartas, G., and Sargent, W. L. W.: 2003, *AJ* **126**, 539

Alexander, D. M., Brandt, W. N., Hornschemeier, A. E., Garmire, G. P., Schneider, D. P., Bauer, F. E., and Griffiths, R. E.: 2001, *AJ* **122**, 2156

Almaini, O.: 2004, in *ESO International Workshop: Physics of Active Galactic Nuclei*

Almaini, O., Scott, S. E., Dunlop, J. S., Manners, J. C., Willott, C. J., Lawrence, A., Ivison, R. J., Johnson, O., Blain, A. W., Peacock, J. A., Oliver, S. J., Fox, M. J., Mann, R. G., Pérez-Fournon, I., González-Solares, E., Rowan-Robinson, M., Serjeant, S., Cabrera-Guerra, F., and Hughes, D. H.: 2003, *MNRAS* **338**, 303

Almaini, O., Shanks, T., Boyle, B. J., Griffiths, R. E., Roche, N., Stewart, G. C., and Georgantopoulos, I.: 1996, *MNRAS* **282**, 295

Almaini, O., Shanks, T., Griffiths, R. E., Boyle, B. J., Roche, N., Georgantopoulos, I., and Stewart, G. C.: 1997, *MNRAS* **291**, 372

Antonucci, R.: 1993, *ARA&A* **31**, 473

Antonucci, R. R. J. and Miller, J. S.: 1985, *ApJ* **297**, 621

Archibald, E. N., Dunlop, J. S., Hughes, D. H., Rawlings, S., Eales, S. A., and Ivison, R. J.: 2001, *MNRAS* **323**, 417

Archibald, E. N., Dunlop, J. S., Jimenez, R., Friaça, A. C. S., McLure, R. J., and Hughes, D. H.: 2002, *MNRAS* **336**, 353

Bahcall, N. A.: 1999, in *Formation of Structure in the Universe*, p. 135

Balogh, M. L., Morris, S. L., Yee, H. K. C., Carlberg, R. G., and Ellingson, E.: 1999, *ApJ* **527**, 54

Barger, A. J., Cowie, L. L., Bautz, M. W., Brandt, W. N., Garmire, G. P., Hornschemeier, A. E., Ivison, R. J., and Owen, F. N.: 2001, *AJ* **122**, 2177

Barger, A. J., Cowie, L. L., Capak, P., Alexander, D. M., Bauer, F. E., Fernandez, E., Brandt, W. N., Garmire, G. P., and Hornschemeier, A. E.: 2003, *AJ* **126**, 632

Barger, A. J., Cowie, L. L., Sanders, D. B., Fulton, E., Taniguchi, Y., Sato, Y., Kawara, K., and Okuda, H.: 1998, *Nature* **394**, 248

Barthel, P. D. and Arnaud, K. A.: 1996, *MNRAS* **283**, L45

Bauer, F. E., Alexander, D. M., Brandt, W. N., Hornschemeier, A. E., Vignali, C., Garmire, G. P., and Schneider, D. P.: 2002, *AJ* **124**, 2351

Bertin, E. and Arnouts, S.: 1996, *A&AS* **117**, 393

Best, P. N.: 2004, *MNRAS* **351**, 70

Best, P. N., Lehnert, M. D., Miley, G. K., and Röttgering, H. J. A.: 2003, *MNRAS* **343**, 1

Best, P. N., van Dokkum, P. G., Franx, M., and Röttgering, H. J. A.: 2002, *MNRAS* **330**, 17

Birkinshaw, M.: 2004, in *Clusters of Galaxies: Probes of Cosmological Structure and Galaxy Evolution*, p. 162

Blandford, R. D. and Levinson, A.: 1995, *ApJ* **441**, 79

Blandford, R. D. and Narayan, R.: 1992, *ARA&A* **30**, 311

Bower, R. G., Lucey, J. R., and Ellis, R. S.: 1992, *MNRAS* **254**, 589

Bower, R. G., Morris, S. L., Bacon, R., Wilman, R. J., Sullivan, M., Chapman, S., Davies, R. L., de Zeeuw, P. T., and Emsellem, E.: 2004, *MNRAS* p. 21

Boyle, B. J., Georgantopoulos, I., Blair, A. J., Stewart, G. C., Griffiths, R. E., Shanks, T., Gunn, K. F., and Almaini, O.: 1998, *MNRAS* **296**, 1

Boyle, B. J., Griffiths, R. E., Shanks, T., Stewart, G. C., and Georgantopoulos, I.: 1993, *MNRAS* **260**, 49

Boyle, B. J., McMahon, R. G., Wilkes, B. J., and Elvis, M.: 1995, *MNRAS* **276**, 315

Brandt, W.: 2004, *astro-ph 0403646*

Brandt, W. N., Alexander, D. M., Hornschemeier, A. E., Garmire, G. P., Schneider, D. P., Barger, A. J., Bauer, F. E., Broos, P. S., Cowie, L. L., Townsley, L. K., Burrows, D. N., Chartas, G., Feigelson, E. D., Griffiths, R. E., Nousek, J. A., and Sargent, W. L. W.: 2001a, *AJ* **122**, 2810

Brandt, W. N., Hornschemeier, A. E., Schneider, D. P., Alexander, D. M., Bauer, F. E., Garmire, G. P., and Vignali, C.: 2001b, *ApJ* **558**, L5

Brandt, W. N., Hornschemeier, A. E., Schneider, D. P., Alexander, D. M., Bauer, F. E., Garmire, G. P., and Vignali, C.: 2001c, *ApJ* **558**, L5

Brinkmann, W., Laurent-Muehleisen, S. A., Voges, W., Siebert, J., Becker, R. H., Brotherton, M. S., White, R. L., and Gregg, M. D.: 2000, *A&A* **356**, 445

Burkert, A. and Silk, J.: 2001, *ApJ* **554**, L151

Butcher, H. and Oemler, A.: 1984, *ApJ* **285**, 426

Cappi, M., Mazzotta, P., Elvis, M., Burke, D. J., Comastri, A., Fiore, F., Forman, W., Fruscione, A., Green, P., Harris, D., Hooper, E. J., Jones, C., Kaastra, J. S., Kellogg, E., Murray, S., McNamara, B., Nicastro, F., Ponman, T. J., Schlegel, E. M., Siemiginowska, A., Tananbaum, H., Vikhlinin, A., Virani, S., and Wilkes, B.: 2001, *ApJ* **548**, 624

Carilli, C. L., Harris, D. E., Pentericci, L., Röttgering, H. J. A., Miley, G. K., Kurk, J. D., and van Breugel, W.: 2002, *ApJ* **567**, 781

Carter, B. J., Fabricant, D. G., Geller, M. J., Kurtz, M. J., and McLean, B.: 2001, *ApJ* **559**, 606

Chandra X-ray Center: 2002, *The CIAO Detect Manual (CIAO Software Release V2.2.1)*

Chapman, C. and Baugh, C.: 2004, *Carnegie Observatories Astrophysics Series, Vol. 3: Clusters of Galaxies: Probes of Cosmological Structure and Galaxy Evolution*

Chapman, S. C., Blain, A. W., Ivison, R. J., and Smail, I. R.: 2003a, *Nature* **422**, 695

Chapman, S. C., Lewis, G. F., Scott, D., Richards, E., Borys, C., Steidel, C. C., Adelberger, K. L., and Shapley, A. E.: 2001, *ApJ* **548**, L17

Chapman, S. C., Scott, D., Windhorst, R. A., Frayer, D. T., Borys, C., Lewis, G. F., and Ivison, R. J.: 2004, *ApJ* **606**, 85

Chapman, S. C., Windhorst, R., Odewahn, S., Yan, H., and Conselice, C.: 2003b, *ApJ* **599**, 92

Charlot, S. and Fall, S. M.: 1993, *ApJ* **415**, 580

Chokshi, A. and Turner, E. L.: 1992, *MNRAS* **259**, 421

Colless, M. et al.: 2001, *MNRAS* **328**, 1039

Comastri, A., Fiore, F., Vignali, C., Matt, G., Perola, G. C., and La Franca, F.: 2001, *MNRAS* **327**, 781

Comastri, A., Setti, G., Zamorani, G., and Hasinger, G.: 1995, *A&A* **296**, 1

Couch, W. J. and Sharples, R. M.: 1987, *MNRAS* **229**, 423

Cowie, L. L., Barger, A. J., Bautz, M. W., Brandt, W. N., and Garmire, G. P.: 2003, *ApJ* **584**, L57

Cowie, L. L. and Hu, E. M.: 1998, *AJ* **115**, 1319

Cowsik, R. and Kobetich, E. J.: 1972, *ApJ* **177**, 585

Cruddace, R. G., Hasinger, G. R., and Schmitt, J. H.: 1988, in *Astronomy from Large Databases*, pp 177–182

Daddi, E., Cimatti, A., Broadhurst, T., Renzini, A., Zamorani, G., Mignoli, M., Saracco, P., Fontana, A., Pozzetti, L., Poli, F., Cristiani, S., D'Odorico, S., Giallongo, E., Gilmozzi, R., and Menci, N.: 2002, *A&A* **384**, L1

Daddi, E., Cimatti, A., Pozzetti, L., Hoekstra, H., Röttgering, H. J. A., Renzini, A., Zamorani, G., and Mannucci, F.: 2000, *A&A* **361**, 535

David, L. P., Forman, W., and Jones, C.: 1991, *ApJ* **380**, 39

Della Ceca, R., Braito, V., Beckmann, V., Caccianiga, A., Cagnoni, I., Gioia, I. M., Maccacaro, T., Severgnini, P., and Wolter, A.: 2003, *A&A* **406**, 555

della Ceca, R., Castelli, G., Braito, V., Cagnoni, I., and Maccacaro, T.: 1999, *ApJ* **524**, 674

Dowsett, R., Johnson, O., Best, P. N., and Almaini, O.: 2004, *astro-ph 0403679*

Dressler, A. and Gunn, J. E.: 1983, *ApJ* **270**, 7

Dressler, A., Smail, I., Poggianti, B. M., Butcher, H., Couch, W. J., Ellis, R. S., and Oemler, A. J.: 1999, *ApJS* **122**, 51

Dressler, A., Thompson, I. B., and Shectman, S. A.: 1985, *ApJ* **288**, 481

Dunlop, J. S.: 2001, *New Astronomy Review* **45**, 609

Edge, A. C.: 1992, in *The Nature of Compact Objects in Active Galactic Nuclei*, pp 125–128

Edge, A. C.: 2004, in *Clusters of Galaxies: Probes of Cosmological Structure and Galaxy Evolution*, pp 58–+

Ehle, M., Breitfellner, M., Gonzales Riestra, R., Guainazzi, M., Rodriguez, P., Santos-Lleo, M., Schartel, N., Tomas, L., E., V., and Dahlem, M.: 2003, *XMM-Newton Users' Handbook: Version 2.1*

Ellingson, E.: 2003, *Ap&SS* **285**, 9

Elvis, M., Wilkes, B. J., McDowell, J. C., Green, R. F., Bechtold, J., Willner, S. P., Oey, M. S., Polomski, E., and Cutri, R.: 1994, *ApJS* **95**, 1

Ettori, S., Tozzi, P., Borgani, S., and Rosati, P.: 2004, *A&A* **417**, 13

Fabian, A. C.: 1999a, *MNRAS* **308**, L39

Fabian, A. C.: 1999b, *Theory of Black Hole Accretion Discs*

Fabian, A. C., Celotti, A., and Johnstone, R. M.: 2003, *MNRAS* **338**, L7

Fabian, A. C., Crawford, C. S., Ettori, S., and Sanders, J. S.: 2001, *MNRAS* **322**, L11

Fabian, A. C. and Iwasawa, K.: 1999, *MNRAS* **303**, L34

Fabian, A. C., Iwasawa, K., Reynolds, C. S., and Young, A. J.: 2000, *PASP* **112**, 1145

Fang, T., Marshall, H. L., Lee, J. C., Davis, D. S., and Canizares, C. R.: 2002, *ApJ* **572**, L127

Fardal, M. A., Katz, N., Gardner, J. P., Hernquist, L., Weinberg, D. H., and Davé, R.: 2001, *ApJ* **562**, 605

Ferrarese, L. and Merritt, D.: 2000, *ApJ* **539**, L9

Freeman, P. E., Kashyap, V., Rosner, R., and Lamb, D. Q.: 2002, *ApJS* **138**, 185

Fujita, Y.: 1998, *ApJ* **509**, 587

Fynbo, J. P. U., Ledoux, C., Möller, P., Thomsen, B., and Burud, I.: 2003, *A&A* **407**, 147

Gómez, P. L., Nichol, R. C., Miller, C. J., Balogh, M. L., Goto, T., Zabludoff, A. I., Romer, A. K., Bernardi, M., Sheth, R., Hopkins, A. M., Castander, F. J., Connolly, A. J., Schneider, D. P., Brinkmann, J., Lamb, D. Q., SubbaRao, M., and York, D. G.: 2003, *ApJ* **584**, 210

Gandhi, P., Crawford, C. S., Fabian, A. C., and Johnstone, R. M.: 2004, *MNRAS* **348**, 529

Gebhardt, K., Bender, R., Bower, G., Dressler, A., Faber, S. M., Filippenko, A. V., Green, R., Grillmair, C., Ho, L. C., Kormendy, J., Lauer, T. R., Magorrian, J., Pinkney, J., Richstone, D., and Tremaine, S.: 2000, *ApJ* **539**, L13

Gendreau, K. C., Mushotzky, R., Fabian, A. C., Holt, S. S., Kii, T., Serlemitsos, P. J., Ogasaka, Y., Tanaka, Y., Bautz, M. W., Fukazawa, Y., Ishisaki, Y., Kohmura, Y., Makishima, K., Tashiro, M., Tsusaka, Y., Kunieda, H., Ricker, G. R., and Vanderspek, R. K.: 1995, *PASJ* **47**, L5

Genzel, R., Pichon, C., Eckart, A., Gerhard, O. E., and Ott, T.: 2000, *MNRAS* **317**, 348

Georgantopoulos, I., Stewart, G. C., Blair, A. J., Shanks, T., Griffiths, R. E., Boyle, B. J., Almaini, O., and Roche, N.: 1997, *MNRAS* **291**, 203

Giacconi, R., Bechtold, J., Branduardi, G., Forman, W., Henry, J. P., Jones, C., Kellogg, E., van der Laan, H., Liller, W., Marshall, H., Murray, S. S., Pye, J., Schreier, E., Sargent, W. L. W., Seward, F., and Tananbaum, H.: 1979, *ApJ* **234**, L1

Giacconi, R., Gursky, H., Paolini, F. R., and Rossi, B. B.: 1962, *Physical Review Letters* **9**, 439

Giacconi, R., Rosati, P., Tozzi, P., Nonino, M., Hasinger, G., Norman, C., Bergeron, J., Borgani, S., Gilli, R., Gilmozzi, R., and Zheng, W.: 2001, *ApJ* **551**, 624

Giavalisco, M.: 1998, in *The Hubble Deep Field*, p. 121

Giavalisco, M. and Dickinson, M.: 2001, *ApJ* **550**, 177

Gilli, R., Salvati, M., and Hasinger, G.: 2001, *A&A* **366**, 407

Gioia, I. M., Henry, J. P., Maccacaro, T., Morris, S. L., Stocke, J. T., and Wolter, A.: 1990, *ApJ* **356**, L35

Gondhalekar, P. M., Kellett, B. J., Pounds, K. A., Matthews, L., and Quenby, J. J.: 1994, *MNRAS* **268**, 973

Gonzalez-Solares, E.: 2003, *Ph.D. thesis, Instituto de Astrofisica de Canarias*

Gonzalez-Solares, E., Perez-Fournon, I., Willott, C. J., Almaini, O., Manners, J. C., Johnson, O., McMahon, R. G., Sabbey, C., Oliver, S. J., and Rowan-Robinson, M.: 2004, *MNRAS, submitted*

Granato, G. L., De Zotti, G., Silva, L., Bressan, A., and Danese, L.: 2004, *ApJ* **600**, 580

Green, P. J. et al.: 2004, *ApJS* **150**, 43

Green, P. J., Schartel, N., Anderson, S. F., Hewett, P. C., Foltz, C. B., Brinkmann, W., Fink, H., Truemper, J., and Margon, B.: 1995, *ApJ* **450**, 51

Griffiths, R. E., Ptak, A., Boyle, B. J., Shanks, T., Stewart, G. C., Georgantopoulos, I., Gunn, K., Almaini, O., and Blair, A.: 2000, *Advances in Space Research* **25**, 853

Haardt, F. and Maraschi, L.: 1993, *ApJ* **413**, 507

Hashimoto, Y., Hasinger, G., Arnaud, M., Rosati, P., and Miyaji, T.: 2002, *A&A* **381**, 841

Hasinger, G., Burg, R., Giacconi, R., Schmidt, M., Trumper, J., and Zamorani, G.: 1998, *A&A* **329**, 482

Hasinger, G. et al.: 2001, *A&A* **365**, L45

Heckman, T. M.: 1980, *A&A* **87**, 152

Heckman, T. M., Smith, E. P., Baum, S. A., van Breugel, W. J. M., Miley, G. K., Illingworth, G. D., Bothun, G. D., and Balick, B.: 1986, *ApJ* **311**, 526

Henry, J. P. and Briel, U. G.: 1991, *A&A* **246**, L14

Ho, L. C., Filippenko, A. V., and Sargent, W. L. W.: 1994, in *IAU Symp. 159: Multi-Wavelength Continuum Emission of AGN*, pp 275–278

Hoekstra, H., Franx, M., and Kuijken, K.: 2000, *ApJ* **532**, 88

Holland, W. S., Robson, E. I., Gear, W. K., Cunningham, C. R., Lightfoot, J. F., Jenness, T., Ivison, R. J., Stevens, J. A., Ade, P. A. R., Griffin, M. J., Duncan, W. D., Murphy, J. A., and Naylor, D. A.: 1999, *MNRAS* **303**, 659

Hornschemeier, A. E., Bauer, F. E., Alexander, D. M., Brandt, W. N., Sargent, W. L. W., Bautz, M. W., Conselice, C., Garmire, G. P., Schneider, D. P., and Wilson, G.: 2003a, *AJ* **126**, 575

Hornschemeier, A. E., Bauer, F. E., Alexander, D. M., Brandt, W. N., Sargent, W. L. W., Bautz, M. W., Conselice, C., Garmire, G. P., Schneider, D. P., and Wilson, G.: 2003b, *AJ* **126**, 575

Hornschemeier, A. E., Brandt, W. N., Garmire, G. P., Schneider, D. P., Barger, A. J., Broos, P. S., Cowie, L. L., Townsley, L. K., Bautz, M. W., Burrows, D. N., Chartas, G., Feigelson, E. D., Griffiths, R. E., Lumb, D., Nousek, J. A., Ramsey, L. W., and Sargent, W. L. W.: 2001, *ApJ* **554**, 742

Hornschemeier, A. E., Brandt, W. N., Garmire, G. P., Schneider, D. P., Broos, P. S., Townsley, L. K., Bautz, M. W., Burrows, D. N., Chartas, G., Feigelson, E. D., Griffiths, R., Lumb, D., Nousek, J. A., and Sargent, W. L. W.: 2000, *ApJ* **541**, 49

Hu, E. and McMahon, R. G.: 1996, *Nature* **382**, 281

Hughes, D. H., Serjeant, S., Dunlop, J., Rowan-Robinson, M., Blain, A., Mann, R. G., Ivison, R., Peacock, J., Efstathiou, A., Gear, W., Oliver, S., Lawrence, A., Longair, M., Goldschmidt, P., and Jenness, T.: 1998, *Nature* **394**, 241

Jackson, N. and Eracleous, M.: 1995, *MNRAS* **276**, 1409

Jannuzi, B. T., Dey, A., Brown, M. J. I., Tiede, G. P., and NDWFS Team: 2002, *Bulletin of the American Astronomical Society* **34**, 1271

Jeltema, T. E., Canizares, C. R., Bautz, M. W., Malm, M. R., Donahue, M., and Garmire, G. P.: 2001, *ApJ* **562**, 124

Johnson, O., Best, P. N., and Almaini, O.: 2003, *MNRAS* **343**, 924

Kaspi, S., Smith, P. S., Netzer, H., Maoz, D., Jannuzi, B. T., and Giveon, U.: 2000, *ApJ* **533**, 631

Kauffmann, G. et al.: 2004, *astro-ph 0402030*

Kauffmann, G. and Haehnelt, M.: 2000, *MNRAS* **311**, 576

King, A.: 2003, *ApJ* **596**, L27

Kneissl, R., Jones, M. E., Saunders, R., Eke, V. R., Lasenby, A. N., Grainge, K., and Cotter, G.: 2001, *MNRAS* **328**, 783

Kukula, M. J., Dunlop, J. S., McLure, R. J., Baum, S. A., O'Dea, C. P., and Hughes, D. H.: 2002, *New Astronomy Review* **46**, 171

Kurk, J., Röttgering, H., Pentericci, L., Miley, G., and Overzier, R.: 2003, *New Astronomy Review* **47**, 339

Lawrence, A.: 1991, *MNRAS* **252**, 586

Lazzati, D., Campana, S., Rosati, P., Chincarini, G., and Giacconi, R.: 1998, *A&A* **331**, 41

Lewis, I. et al.: 2002, *MNRAS* **334**, 673

Lightman, A. P. and White, T. R.: 1988, *ApJ* **335**, 57

Lonsdale, C. J. et al.: 2003, *PASP* **115**, 897

Madau, P., Ghisellini, G., and Fabian, A. C.: 1994, *MNRAS* **270**, L17

Magorrian, J., Tremaine, S., Richstone, D., Bender, R., Bower, G., Dressler, A., Faber, S. M., Gebhardt, K., Green, R., Grillmair, C., Kormendy, J., and Lauer, T.: 1998, *AJ* **115**, 2285

Mainieri, V., Bergeron, J., Hasinger, G., Lehmann, I., Rosati, P., Schmidt, M., Szokoly, G., and Della Ceca, R.: 2002, *A&A* **393**, 425

Maiolino, R., Marconi, A., and Oliva, E.: 2001a, *A&A* **365**, 37

Maiolino, R., Marconi, A., Salvati, M., Risaliti, G., Severgnini, P., Oliva, E., La Franca, F., and Vanzi, L.: 2001b, *A&A* **365**, 28

Maiolino, R., Salvati, M., Bassani, L., Dadina, M., della Ceca, R., Matt, G., Risaliti, G., and Zamorani, G.: 1998, *A&A* **338**, 781

Malhotra, S., Wang, J. X., Rhoads, J. E., Heckman, T. M., and Norman, C. A.: 2004, *astro-ph* 0301622

Manners, J. C.: 2002, *Ph. D. thesis, The University of Edinburgh*

Manners, J. C., Johnson, O., Almaini, O., Willott, C. J., Gonzalez-Solares, E., Lawrence, A., Mann, R. G., Perez-Fournon, I., Dunlop, J. S., McMahon, R. G., Oliver, S. J., Rowan-Robinson, M., and Serjeant, S.: 2003, *MNRAS* **343**, 293

Manners, J. C., Serjeant, S., Bottinelli, S., Vaccari, M., Franceschini, A., Perez-Fournon, I., Gonzalez-Solares, E., Willott, C. J., Johnson, O., Almaini, O., Rowan-Robinson, M., and Oliver, S. J.: 2004, *MNRAS*

Margoniner, V. E., de Carvalho, R. R., Gal, R. R., and Djorgovski, S. G.: 2001, *ApJ* **548**, L143

Marshall, F. E., Boldt, E. A., Holt, S. S., Miller, R. B., Mushotzky, R. F., Rose, L. A., Rothschild, R. E., and Serlemitsos, P. J.: 1980, *ApJ* **235**, 4

Martin, C. L.: 1999, *ApJ* **513**, 156

Martini, P., Kelson, D. D., Mulchaey, J. S., and Trager, S. C.: 2002, *ApJ* **576**, L109

Mateus, A. and Sodré, L.: 2004, *MNRAS* **349**, 1251

Mather, J. C., Cheng, E. S., Eplee, R. E., Isaacman, R. B., Meyer, S. S., Shafer, R. A., Weiss, R., Wright, E. L., Bennett, C. L., Boggess, N. W., Dwek, E., Gulkis, S., Hauser, M. G., Janssen, M., Kelsall, T., Lubin, P. M., Moseley, S. H., Murdock, T. L., Silverberg, R. F., Smoot, G. F., and Wilkinson, D. T.: 1990, *ApJ* **354**, L37

Matsuda, J. X., Rhoads, J. E., Malhotra, S., Dawson, S., Stern, D., Dey, A., Heckman, T. M., Norman, C. A., and Spinrad, H.: 2004, *astro-ph* 0404611

Matsumoto, H., Tsuru, T. G., Koyama, K., Awaki, H., Canizares, C. R., Kawai, N., Matsushita, S., and Kawabe, R.: 2001, *ApJ* **547**, L25

Matt, G., Guainazzi, M., and Maiolino, R.: 2003, *MNRAS* **342**, 422

McCarthy, P. J., Carlberg, R. G., Chen, H.-W., Marzke, R. O., Firth, A. E., Ellis, R. S., Persson, S. E., McMahon, R. G., Lahav, O., Wilson, J., Martini, P., Abraham, R. G., Sabbey, C. N., Oemler, A., Murphy, D. C., Somerville, R. S., Beckett, M. G., Lewis, J. R., and MacKay, C. D.: 2001, *ApJ* **560**, L131

McHardy, I. M., Gunn, K. F., Newsam, A. M., Mason, K. O., Page, M. J., Takata, T., Sekiguchi, K., Sasseen, T., Cordova, F., Jones, L. R., and Loaring, N.: 2003, *MNRAS* **342**, 802

McHardy, I. M., Jones, L. R., Merrifield, M. R., Mason, K. O., Newsam, A. M., Abraham, R. G., Dalton, G. B., Carrera, F., Smith, P. J., Rowan-Robinson, M., Wegner, G. A., Ponman, T. J., Lehto, H. J., Branduardi-Raymont, G., Luppino, G. A., Efstathiou, G., Allan, D. J., and Quenby, J. J.: 1998, *MNRAS* **295**, 641

McNamara, B. R., Wise, M. W., Nulsen, P. E. J., David, L. P., Carilli, C. L., Sarazin, C. L., O'Dea, C. P., Houck, J., Donahue, M., Baum, S., Voit, M., O'Connell, R. W., and Koekemoer, A.: 2001, *ApJ* **562**, L149

Merritt, D. and Ferrarese, L.: 2001a, *MNRAS* **320**, L30

Merritt, D. and Ferrarese, L.: 2001b, in *ASP Conf. Ser. 249: The Central Kiloparsec of Starbursts and AGN: The La Palma Connection*, p. 335

Metevier, A. J., Romer, A. K., and Ulmer, M. P.: 2000, *AJ* **119**, 1090

Miller, N. A. and Owen, F. N.: 2003, *AJ* **125**, 2427

Miyaji, T., Hasinger, G., and Schmidt, M.: 2000, *A&A* **353**, 25

Miyoshi, M., Moran, J., Herrnstein, J., Greenhill, L., Nakai, N., Diamond, P., and Inoue, M.: 1995, *Nature* **373**, 127

Moller, P. and Warren, S. J.: 1998, *MNRAS* **299**, 661

Molnar, S. M., Hughes, J. P., Donahue, M., and Joy, M.: 2002, *ApJ* **573**, L91

Moore, B., Katz, N., Lake, G., Dressler, A., and Oemler, A.: 1996, *Nature* **379**, 613

Moretti, A., Campana, S., Lazzati, D., and Tagliaferri, G.: 2003, *ApJ* **588**, 696

Morrison, G. E. and Owen, F. N.: 2003, *AJ* **125**, 506

Mushotsky, R. F., Cowie, L. L., Barger, A. J., and Arnaud, K. A.: 2000, *Nature* **404**, 459

Mushotzky, R. F., Marshall, F. E., Boldt, E. A., Holt, S. S., and Serlemitsos, P. J.: 1980, *ApJ* **235**, 377

Nandra, K., Mushotzky, R. F., Arnaud, K., Steidel, C. C., Adelberger, K. L., Gardner, J. P., Teplitz, H. I., and Windhorst, R. A.: 2002, *ApJ* **576**, 625

Nandra, K. and Pounds, K. A.: 1994, *MNRAS* **268**, 405

Natarajan, P. and Almaini, O.: 2000, *MNRAS* **318**, L21

Neumann, D. M., Arnaud, M., Benoist, C., da Costa, L., Jørgensen, H. E., Olsen, L. F., Bardelli, S., Zucca, E., Arnouts, S., Biviano, A., and Ramella, M.: 2003, *A&A* **406**, 789

Norman, C., Hasinger, G., Giacconi, R., Gilli, R., Kewley, L., Nonino, M., Rosati, P., Szokoly, G., Tozzi, P., Wang, J., Zheng, W., Zirm, A., Bergeron, J., Gilmozzi, R., Grogin, N., Koekemoer, A., and Schreier, E.: 2002, *ApJ* **571**, 218

Ohyama, Y., Taniguchi, Y., Kawabata, K. S., Shioya, Y., Murayama, T., Nagao, T., Takata, T., Iye, M., and Yoshida, M.: 2003, *ApJ* **591**, L9

Oliver, S. et al.: 2000, *MNRAS* **316**, 749

Page, M. J., Stevens, J. A., Ivison, R. J., and Carrera, F. J.: 2004, *astro-ph 0407171*

Pascarelle, S. M., Windhorst, R. A., and Keel, W. C.: 1998, *AJ* **116**, 2659

Pentericci, L., Kurk, J. D., Carilli, C. L., Harris, D. E., Miley, G. K., and Röttgering, H. J. A.: 2002, *A&A* **396**, 109

Peterson, B. M. et al.: 2004, *astro-ph 0407299*

Phillips, L. A., Ostriker, J. P., and Cen, R.: 2001, *ApJ* **554**, L9

Pierre, M.: 2003, *The Cosmic Cauldron, 25th meeting of the IAU, Joint Discussion 10*

Poggianti, B.: 2002, *JENAM 2002 Workshop on "Galaxy Evolution in Groups and Clusters"* p. 121

Poggianti, B. M.: 2003, *Ap&SS* **285**, 121

Poggianti, B. M., Smail, I., Dressler, A., Couch, W. J., Barger, A. J., Butcher, H., Ellis, R. S., and Oemler, A. J.: 1999, *ApJ* **518**, 576

Reddy, N. A. and Yun, M. S.: 2004, *ApJ* **600**, 695

Refregier, A. and Loeb, A.: 1997, *ApJ* **478**, 476

Reichert, G. A., Mushotzky, R. F., Holt, S. S., and Petre, R.: 1985, *ApJ* **296**, 69

Risaliti, G., Marconi, A., Maiolino, R., Salvati, M., and Severgnini, P.: 2001, *A&A* **371**, 37

Roche, N., Shanks, T., Georgantopoulos, I., Stewart, G. C., Boyle, B. J., and Griffiths, R. E.: 1995, *MNRAS* **273**, L15

Roche, N. D., Almaini, O., Dunlop, J., Ivison, R. J., and Willott, C. J.: 2002, *MNRAS* **337**, 1282

Roche, N. D., Dunlop, J., and Almaini, O.: 2003, *MNRAS* **346**, 803

Romer, A. K., Viana, P. T. P., Liddle, A. R., and Mann, R. G.: 2001, *ApJ* **547**, 594

Rosati, P., della Ceca, R., Norman, C., and Giacconi, R.: 1998, *ApJ* **492**, L21

Rosati, P., Tozzi, P., Ettori, S., Mainieri, V., Demarco, R., Stanford, S. A., Lidman, C., Nonino, M., Borgani, S., Della Ceca, R., Eisenhardt, P., Holden, B. P., and Norman, C.: 2004, *AJ* **127**, 230

Rosati, P., Tozzi, P., Giacconi, R., Gilli, R., Hasinger, G., Kewley, L., Mainieri, V., Nonino, M., Norman, C., Szokoly, G., Wang, J. X., Zirm, A., Bergeron, J., Borgani, S., Gilmozzi, R., Grogin, N., Koekemoer, A., Schreier, E., and Zheng, W.: 2002, *ApJ* **566**, 667

Runyan, M. C., Ade, P. A. R., Bhatia, R. S., Bock, J. J., Daub, M. D., Goldstein, J. H., Haynes, C. V., Holzapfel, W. L., Kuo, C. L., Lange, A. E., Leong, J., Lueker, M., Newcomb, M., Peterson, J. B., Reichardt, C., Ruhl, J., Sirbi, G., Torbet, E., Tucker, C., Turner, A. D., and Woolsey, D.: 2003, *ApJS* **149**, 265

Salpeter, E. E.: 1964, *ApJ* **140**, 796

Sambruna, R. M., Eracleous, M., and Mushotzky, R. F.: 1999, *Bulletin of the American Astronomical Society* **31**, 872

Scharf, C., Smail, I., Ivison, R., Bower, R., van Breugel, W., and Reuland, M.: 2003, *ApJ* **596**, 105

Schmidt, M.: 1963, *Nature* **197**, 1040

Schmidt, M., Hasinger, G., Gunn, J., Schneider, D., Burg, R., Giacconi, R., Lehmann, I., MacKenty, J., Trumper, J., and Zamorani, G.: 1998, *A&A* **329**, 495

Seyfert, C. K.: 1943, *ApJ* **97**, 28

Shanks, T., Georgantopoulos, I., Stewart, G. C., Pounds, K. A., Boyle, B. J., and Griffiths, R. E.: 1991, *Nature* **353**, 315

Shapley, A. E., Steidel, C. C., Adelberger, K. L., Dickinson, M., Giavalisco, M., and Pettini, M.: 2001, *ApJ* **562**, 95

Shlosman, I., Frank, J., and Begelman, M. C.: 1989, *Nature* **338**, 45

Silk, J. and Rees, M. J.: 1998, *A&A* **331**, L1

Simpson, C.: 1998, *ApJ* **509**, 653

Smail, I., Edge, A. C., Ellis, R. S., and Blandford, R. D.: 1998, *MNRAS* **293**, 124

Smail, I., Ivison, R. J., and Blain, A. W.: 1997, *ApJ* **490**, L5

Smail, I., Morrison, G., Gray, M. E., Owen, F. N., Ivison, R. J., Kneib, J.-P., and Ellis, R. S.: 1999, *ApJ* **525**, 609

Sramek, R. A. and Weedman, D. W.: 1980, *ApJ* **238**, 435

Stanford, S. A., Holden, B., Rosati, P., Eisenhardt, P. R., Stern, D., Squires, G., and Spinrad, H.: 2002, *AJ* **123**, 619

Stanford, S. A., Holden, B., Rosati, P., Tozzi, P., Borgani, S., Eisenhardt, P. R., and Spinrad, H.: 2001, *ApJ* **552**, 504

Steffen, A. T., Barger, A. J., Cowie, L. L., Mushotzky, R. F., and Yang, Y.: 2003, *ApJ* **596**, L23

Steidel, C. C., Adelberger, K. L., Dickinson, M., Giavalisco, M., Pettini, M., and Kellogg, M.: 1998, *ApJ* **492**, 428

Steidel, C. C., Adelberger, K. L., Shapley, A. E., Pettini, M., Dickinson, M., and Giavalisco, M.: 2000, *ApJ* **532**, 170

Steidel, C. C., Adelberger, K. L., Shapley, A. E., Pettini, M., Dickinson, M., and Giavalisco, M.: 2003, *ApJ* **592**, 728

Steidel, C. C., Hunt, M. P., Shapley, A. E., Adelberger, K. L., Pettini, M., Dickinson, M., and Giavalisco, M.: 2002, *ApJ* **576**, 653

Stern, D., Moran, E. C., Coil, A. L., Connolly, A., Davis, M., Dawson, S., Dey, A., Eisenhardt, P., Elston, R., Graham, J. R., Harrison, F., Helfand, D. J., Holden, B., Mao, P., Rosati, P., Spinrad, H., Stanford, S. A., Tozzi, P., and Wu, K. L.: 2002, *ApJ* **568**, 71

Stoughton, C. et al.: 2002, *AJ* **123**, 485

Sun, M. and Murray, S. S.: 2002, *ApJ* **577**, 139

Tanaka, Y., Nandra, K., Fabian, A. C., Inoue, H., Otani, C., Dotani, T., Hayashida, K., Iwasawa, K., Kii, T., Kunieda, H., Makino, F., and Matsuoka, M.: 1995, *Nature* **375**, 659

Taniguchi, Y., Shioya, Y., and Kakazu, Y.: 2001, *ApJ* **562**, L15

Terashima, Y. and Wilson, A. S.: 2003, *ApJ* **583**, 145

Tozzi, P., Rosati, P., Nonino, M., Bergeron, J., Borgani, S., Gilli, R., Gilmozzi, R., Hasinger, G., Grogin, N., Kewley, L., Koekemoer, A., Norman, C., Schreier, E., Szokoly, G., Wang, J. X., Zheng, W., Zirm, A., and Giacconi, R.: 2001, *ApJ* **562**, 42

Tran, K. H., Kelson, D. D., van Dokkum, P., Franx, M., Illingworth, G. D., and Magee, D.: 1999, *ApJ* **522**, 39

Turner, T. J., Weaver, K. A., Mushotzky, R. F., Holt, S. S., and Madejski, G. M.: 1991, *ApJ* **381**, 85

Ueda, Y., Akiyama, M., Ohta, K., and Miyaji, T.: 2003, *ApJ* **598**, 886

Ueda, Y., Takahashi, T., Inoue, H., Tsuru, T., Sakano, M., Ishisaki, Y., Ogasaka, Y., Makishima, K., Yamada, T., Akiyama, M., and Ohta, K.: 1999, *ApJ* **518**, 656

Valtchanov, I., Pierre, M., and Gastaud, R.: 2001, *A&A* **370**, 689

van Dokkum, P. G., Franx, M., Fabricant, D., Illingworth, G. D., and Kelson, D. D.: 2000, *ApJ* **541**, 95

van Dokkum, P. G. and Stanford, S. A.: 2003, *ApJ* **585**, 78

Vecchi, A., Molendi, S., Guainazzi, M., Fiore, F., and Parmar, A. N.: 1999, *A&A* **349**, L73

Venemans, B. P., Kurk, J. D., Miley, G. K., and Röttgering, H. J. A.: 2003, *New Astronomy Review* **47**, 353

Venemans, B. P., Kurk, J. D., Miley, G. K., Röttgering, H. J. A., van Breugel, W., Carilli, C. L., De Breuck, C., Ford, H., Heckman, T., McCarthy, P., and Pentericci, L.: 2002, *ApJ* **569**, L11

Wandel, A., Peterson, B. M., and Malkan, M. A.: 1999, *ApJ* **526**, 579

Wang, J. X., Rhoads, J. E., Malhotra, S., Dawson, S., Stern, D., Dey, A., Heckman, T. M., Norman, C. A., and Spinrad, H.: 2004, *astro-ph* 0404611

Warwick, R. S., Pye, J. P., and Fabian, A. C.: 1980, *MNRAS* **190**, 243

Waskett, T. J., Eales, S. A., Gear, W. K., Puchnarewicz, E. M., Lilly, S., Flores, H., Webb, T., Clements, D., Stevens, J. A., and Thuan, T. X.: 2003, *MNRAS* **341**, 1217

Watson, M. G., Pye, J. P., Denby, M., Osborne, J. P., Barret, D., Boller, T., Brunner, H., Ceballos, M. T., Della Ceca, R., Fyfe, D. J., Lamer, G., Maccacaro, T., Michel, L., Motch, C., Pietsch, W., Saxton, R. D., Schröder, A. C., Stewart, I. M., Tedds, J. A., and Webb, N.: 2003, *Astronomische Nachrichten* **324**, 89

Willott, C. J., Simpson, C., Almaini, O., Johnson, O., Lawrence, A., Dunlop, J. S., Roche, N. D., Mann, R. G., Manners, J. C., González-Solares, E., Pérez-Fournon, I., Ivison, R. J., Serjeant, S., Oliver, S. J., McMahon, R. G., and Rowan-Robinson, M.: 2004, *ApJ* **610**, 140

Willott, C. J., Simpson, C., Almaini, O., Manners, J. C., Johnson, O., Lawrence, A., Dunlop, J. S., Ivison, R. J., Rawlings, S., González-Solares, E., Pérez-Fournon, I., Serjeant, S., Oliver, S. J., Roche, N. D., Mann, R. G., and Rowan-Robinson, M.: 2003, *MNRAS* **339**, 397

Wilman, R. J., Fabian, A. C., and Nulsen, P. E. J.: 2000, *MNRAS* **319**, 583

Wilson, A. S. and Colbert, E. J. M.: 1995, *Bulletin of the American Astronomical Society* **27**, 830

APPENDIX A

Point source catalog for MS1054-03

The following table lists X-ray point sources detected in the MS1054-03 field. The quoted error is the average of the positional error in RA and DEC added in quadrature to the mean astrometric error. The source significance is the output value from WAVDETECT, defined in §4.3, and equal to the source counts divided by the Gehrels error on the background counts. The flux values and associated Poisson errors were calculated assuming $\alpha = 0.7$ powerlaw spectra.

ID	Name (CXOU)	RA (J2000)	Dec (J2000)	Err (arcsec)	Net Counts	Source Significance	0.5 - 8 keV Flux (10^{-14} erg cm^{-2} s^{-1})	Hardness Ratio
1	105658.8-033850	10:56:58.82	-03:38:50.7	0.50	442.9	111.7	3.58±0.17	-0.36±0.04
2	105710.4-034013	10:57:10.49	-03:40:13.9	0.50	302.8	88.3	2.46±0.14	-0.57±0.05
3	105655.6-034029	10:56:55.65	-03:40:29.4	0.50	273.1	86.7	2.18±0.13	-0.59±0.05
4	105646.3-034023	10:56:46.31	-03:40:23.3	0.50	251.4	71.7	2.14±0.13	-0.30±0.06
5	105646.5-033905	10:56:46.56	-03:39:05.7	0.50	199.4	64.9	1.64±0.11	-0.50±0.06
6	105650.6-033509	10:56:50.66	-03:35:09.1	0.51	163.0	45.5	1.31±0.10	-0.77±0.05
7	105710.6-033500	10:57:10.65	-03:35:00.9	0.53	176.8	34.6	1.45±0.11	-0.79±0.05
8	105705.1-033541	10:57:05.11	-03:35:41.9	0.52	125.2	33.5	1.00±0.09	-0.57±0.07
9	105708.4-033611	10:57:08.48	-03:36:11.5	0.52	115.5	31.3	0.92±0.08	-0.52±0.08
10	105646.9-033510	10:56:46.95	-03:35:10.6	0.52	112.7	30.9	0.91±0.08	-0.93±0.03
11	105714.1-033348	10:57:14.14	-03:33:48.5	0.56	185.7	30.4	1.64±0.12	-0.53±0.06
12	105705.5-033550	10:57:05.52	-03:35:50.5	0.52	84.9	23.5	0.67±0.07	-0.58±0.09
13	105700.0-033446	10:57:00.05	-03:34:46.4	0.54	69.9	19.3	0.58±0.07	-0.50±0.10
14	105641.4-033853	10:56:41.40	-03:38:53.7	0.53	59.0	18.7	0.49±0.06	-0.35±0.12
15	105650.0-033343	10:56:50.03	-03:33:43.8	0.57	85.2	18.2	0.72±0.08	-0.56±0.09
16	105707.6-034147	10:57:07.61	-03:41:47.1	0.53	48.7	17.8	0.78±0.11	-0.50±0.12
17	105708.1-033940	10:57:08.14	-03:39:40.0	0.52	48.4	17.1	0.40±0.06	-0.49±0.13
18	105648.8-033726	10:56:48.90	-03:37:26.0	0.52	48.6	16.1	0.39±0.05	-0.64±0.11
19	105702.7-033943	10:57:02.73	-03:39:43.4	0.51	36.5	13.1	0.28±0.04	0.08±0.17
20	105652.6-033819	10:56:52.67	-03:38:19.8	0.51	36.4	12.8	0.29±0.05	-0.44±0.15
21	105643.8-033829	10:56:43.81	-03:38:29.8	0.54	32.5	10.7	0.27±0.04	0.10±0.17
22	105705.4-033433	10:57:05.48	-03:34:33.6	0.57	33.9	10.6	0.28±0.05	-0.48±0.14
23	105650.8-033504	10:56:50.90	-03:35:04.8	0.57	22.5	7.4	0.18±0.04	-0.46±0.20
24	105713.0-033528	10:57:13.04	-03:35:28.3	0.74	27.9	7.3	0.23±0.04	-0.47±0.18
25	105715.6-033502[a]	10:57:15.65	-03:35:02.2	0.60	22.3	7.2	0.18±0.04	-0.55±0.16

---

[a] CXOU105715.7-033502 and CXOU105715.7-033506 are resolved by WAVDETECT as two separate detections in the full band, but are detected as a single source in the soft band.

ID	Name (CXOU)	RA (J2000)	Dec (J2000)	Err (arcsec)	Net Counts	Source Significance	0.5 - 8 keV Flux (10^{-14} erg cm^{-2} s^{-1})	Hardness Ratio
26	105715.7-033506[a]	10:57:15.72	-03:35:06.5	0.63	20.7	6.4	0.17±0.04	-0.47±0.17
27	105644.4-033807	10:56:44.40	-03:38:07.3	0.54	15.8	5.8	0.13±0.03	0.32±0.24
28	105651.4-033800	10:56:51.46	-03:38:00.5	0.53	15.1	5.7	0.12±0.03	-0.77±0.16
29	105704.9-033820	10:57:04.92	-03:38:20.7	0.57	17.5	5.7	0.14±0.03	0.67±0.18
30	105656.3-033636	10:56:56.33	-03:36:36.5	0.54	16.4	5.3	0.13±0.03	-0.25±0.23
31	105704.8-034053	10:57:04.86	-03:40:53.8	0.56	13.7	5.0	0.11±0.03	0.11±0.26
32	105702.4-033337	10:57:02.42	-03:33:37.8	0.63	14.7	4.9	0.12±0.03	0.05±0.25
33	105643.7-033733	10:56:43.77	-03:37:33.1	0.58	13.5	4.8	0.11±0.03	-0.14±0.27
34	105647.9-033401	10:56:47.96	-03:34:01.9	0.66	17.2	4.8	0.14±0.04	0.42±0.23
35	105649.0-033833	10:56:49.00	-03:38:33.5	0.54	10.6	4.3	0.08±0.02	-0.55±0.25
36	105647.7-034002	10:56:47.73	-03:40:02.6	0.61	12.3	4.3	0.10±0.03	-0.17±0.29
37	105710.5-033611	10:57:10.58	-03:36:11.6	0.58	10.4	4.1	0.08±0.02	-0.20±0.31
38	105648.5-033324	10:56:48.56	-03:33:24.8	0.64	12.3	3.9	0.10±0.03	1.00±0.00
39	105651.9-033623	10:56:51.96	-03:36:23.4	0.60	10.7	3.9	0.08±0.02	-0.44±0.27
40	105649.6-033452	10:56:49.64	-03:34:52.7	0.59	10.6	3.8	0.08±0.02	-0.21±0.31
41	105645.2-033609	10:56:45.21	-03:36:09.9	0.62	10.0	3.8	0.08±0.03	0.17±0.30
42	105700.3-033649	10:57:00.32	-03:36:49.6	0.55	12.9	3.7	0.10±0.03	0.52±0.25
43	105702.2-034059	10:57:02.26	-03:40:59.5	0.53	8.8	3.6	0.07±0.02	-0.41±0.30
44	105652.9-033336	10:56:52.97	-03:33:36.3	0.68	10.2	3.3	0.08±0.03	-0.33±0.30
45	105705.5-033850	10:57:05.56	-03:38:50.0	0.60	8.3	3.2	0.06±0.02	0.64±0.26
46	105706.2-034016	10:57:06.24	-03:40:16.0	0.59	7.6	3.1	0.06±0.02	0.85±0.18
47	105656.3-033929	10:56:56.30	-03:39:29.1	0.54	7.5	3.0	0.06±0.02	0.17±0.35

APPENDIX B

Lyα candidates in the SSA22 field

The following table lists candidate $z \simeq 3.09$ Ly-α emitters from narrow-band mosaic imaging described in §5.2. The listed NB and g' magnitudes are total magnitudes from ellipsoidal apertures, while the $NB - g'$ colours are from smaller matched isophotal apertures.

ID	R.A. (J2000)	Dec. (J2000)	NB	g'	$g' - NB$
LFC_NB1	22:17:43.726	+00:03:39.29	21.96	> 26.5	1.68
LFC_NB2	22:17:22.537	+00:03:41.42	22.73	> 26.5	1.77
LFC_NB3	22:17:32.900	+00:03:41.47	23.46	> 26.5	1.91
LFC_NB4	22:17:13.586	+00:06:40.10	22.97	24.57	1.65
LFC_NB5	22:17:50.229	+00:07:27.45	23.74	25.03	1.72
LFC_NB6	22:18:05.955	+00:10:03.26	21.82	> 26.5	2.12
LFC_NB7	22:16:53.328	+00:10:17.52	21.30	23.90	1.75
LFC_NB8	22:16:51.841	+00:10:17.51	22.35	26.24	1.56
LFC_NB9	22:18:16.875	+00:10:26.93	19.95	23.55	2.60
LFC_NB10	22:18:08.350	+00:10:22.05	22.73	24.13	1.42
LFC_NB11	22:18:20.691	+00:11:47.09	23.86	25.46	1.20
LFC_NB12	22:18:12.524	+00:14:33.12	24.28	25.52	1.35
LFC_NB13	22:17:07.317	+00:15:02.60	23.26	24.28	2.33
LFC_NB14	22:18:20.208	+00:16:23.31	24.08	24.84	0.97
LFC_NB15	22:17:38.613	+00:16:47.59	24.97	25.36	0.97
LFC_NB16	22:17:00.747	+00:17:18.59	21.21	23.21	3.54
LFC_NB17	22:17:06.724	+00:17:44.71	20.90	22.33	2.22
LFC_NB18	22:17:24.771	+00:17:17.24	24.12	24.88	1.04
LFC_NB19	22:17:16.245	+00:17:44.73	23.74	24.94	1.22
LFC_NB20	22:17:09.646	+00:18:01.00	22.93	24.78	1.93
LFC_NB21	22:17:03.267	+00:18:29.82	21.60	22.86	1.97
LFC_NB22	22:17:18.867	+00:18:16.28	24.43	25.18	0.94
LFC_NB23	22:16:51.431	+00:18:31.88	22.40	23.30	0.93
LFC_NB24	22:18:20.354	+00:19:19.48	23.11	26.39	0.94
LFC_NB25	22:17:38.328	+00:19:20.66	24.46	24.88	0.97
LFC_NB26	22:17:28.967	+00:19:59.57	23.98	24.83	1.05
LFC_NB27	22:17:45.286	+00:20:05.77	24.78	27.33	2.12
LFC_NB28	22:17:20.229	+00:20:19.33	22.36	23.76	1.37
LFC_NB29	22:18:11.375	+00:20:42.97	24.19	24.84	0.90
LFC_NB30	22:17:42.100	+00:21:02.22	24.76	26.26	1.87
LFC_NB31	22:17:30.601	+00:21:35.50	22.89	23.84	0.93
LFC_NB32	22:17:20.281	+00:24:37.44	24.54	25.47	1.07

APPENDIX C

X-ray detections in the SSA22 field

The following table lists the sources identified in the XMM exposure of the SSA22 field, as described in §5.3. The positions, positional errors, and source significance values are taken directly from the WAVDETECT source list obtained from the full-band EPIC image. The net counts are the sum of background-subtracted, exposure corrected total counts detected by the individual EPIC cameras. The fluxes are error-weighted sums of the fluxes found by each instrument in each band. The hardness ratios are defined as $\frac{H-S}{H+S}$, which H and S are the 0.5–2 keV and 2–8 keV band error-weighted average count rates given by each instrument, incorporating background subtraction and exposure correction. In cases where sources fell partially outside of the FOV or on chip gaps for a given instrument, information from this instrument was excluded from the sum or average.

ID	RA	Dec	Err	Net Counts	Significance	$S_{0.5-8\ \mathrm{keV}}$	$S_{0.5-2\ \mathrm{keV}}$	$S_{2-8\ \mathrm{keV}}$	HR
1	22:16:40.127	+00:16:20.07	1.58	243.6	21.5	42.6 ± 4.1	16.6 ± 1.8	22.3 ± 4.7	-0.50 ± 0.09
2	22:16:43.871	+00:13:50.79	1.75	97.5	7.0	7.8 ± 1.5	2.5 ± 0.6	6.6 ± 2.2	-0.20 ± 0.20
3	22:16:45.745	+00:19:57.84	1.57	272.7	14.6	10.4 ± 1.2	5.0 ± 0.5	1.0 ± 1.3	-0.90 ± 0.12
4	22:16:49.136	+00:20:47.46	1.66	144.2	7.7	5.2 ± 1.0	2.0 ± 0.4	2.2 ± 1.4	-0.57 ± 0.22
5	22:16:49.522	+00:15:07.85	1.53	1058.5	35.8	31.3 ± 1.6	16.0 ± 0.8	0.7 ± 1.3	-0.98 ± 0.04
6	22:16:51.806	+00:18:48.11	1.60	152.2	9.5	5.0 ± 0.8	1.4 ± 0.3	4.9 ± 1.3	-0.07 ± 0.17
7	22:16:51.819	+00:11:00.37	1.61	69.9	6.6	2.3 ± 0.7	0.5 ± 0.2	2.7 ± 1.1	0.13 ± 0.30
8	22:16:52.401	+00:09:41.78	1.55	2.4	5.1	$- \pm -$	0.1 ± 0.3	$- \pm -$	1.93 ± 6.66
9	22:16:52.890	+00:12:14.67	1.68	128.3	8.6	5.2 ± 0.9	1.0 ± 0.3	7.2 ± 1.6	0.30 ± 0.18
10	22:16:53.225	+00:19:31.59	1.54	483.0	23.5	15.9 ± 1.2	4.9 ± 0.5	13.2 ± 1.7	-0.20 ± 0.08
11	22:16:54.079	+00:11:47.78	1.62	100.1	6.1	2.6 ± 0.7	0.9 ± 0.3	1.8 ± 1.0	-0.35 ± 0.28
12	22:16:54.145	+00:24:14.79	1.64	377.5	21.1	20.6 ± 1.8	9.6 ± 0.8	2.8 ± 1.8	-0.87 ± 0.08
13	22:16:54.961	+00:21:51.93	1.69	92.0	5.1	5.4 ± 1.1	1.6 ± 0.4	4.7 ± 1.6	-0.17 ± 0.21
14	22:16:55.332	+00:07:52.87	1.66	51.0	7.4	3.9 ± 1.2	1.4 ± 0.5	2.4 ± 1.7	-0.40 ± 0.32
15	22:16:56.448	+00:16:59.69	1.55	398.8	16.8	11.0 ± 1.0	4.5 ± 0.4	4.9 ± 1.2	-0.57 ± 0.09
16	22:16:56.452	+00:14:06.41	1.60	130.2	8.2	3.6 ± 0.7	1.4 ± 0.3	1.7 ± 1.0	-0.53 ± 0.22
17	22:16:57.218	+00:24:08.81	1.53	1202.7	57.8	62.2 ± 2.7	23.7 ± 1.2	33.1 ± 3.2	-0.48 ± 0.04
18	22:16:57.620	+00:09:15.90	1.61	178.2	10.4	5.3 ± 0.8	2.0 ± 0.3	3.2 ± 1.1	-0.43 ± 0.16
19	22:16:58.150	+00:21:59.42	1.54	461.1	20.7	15.2 ± 1.2	4.5 ± 0.5	14.0 ± 1.8	-0.13 ± 0.08
20	22:16:59.089	+00:15:12.51	1.57	299.2	11.8	7.3 ± 0.8	3.0 ± 0.3	3.4 ± 1.1	-0.55 ± 0.12
21	22:17:00.211	+00:19:58.31	1.58	96.4	5.7	2.5 ± 0.7	0.4 ± 0.2	3.6 ± 1.1	0.36 ± 0.28
22	22:17:00.499	+00:21:22.14	1.59	309.7	12.6	9.5 ± 1.0	3.6 ± 0.4	5.6 ± 1.4	-0.44 ± 0.11
23	22:17:00.585	+00:04:23.27	1.88	100.5	11.5	17.8 ± 3.0	2.9 ± 0.9	26.5 ± 5.1	0.40 ± 0.16
24	22:17:01.014	+00:25:06.70	1.60	96.8	6.3	4.2 ± 0.9	1.5 ± 0.4	2.6 ± 1.4	-0.41 ± 0.25
25	22:17:02.434	+00:25:50.17	1.55	340.9	19.5	14.5 ± 1.4	5.2 ± 0.5	9.3 ± 1.9	-0.38 ± 0.10
26	22:17:03.364	+00:24:06.84	1.60	112.2	4.8	3.5 ± 0.9	0.2 ± 0.3	6.8 ± 1.6	0.79 ± 0.25
27	22:17:03.628	+00:22:39.99	1.62	99.0	6.2	3.3 ± 0.8	1.1 ± 0.3	2.2 ± 1.2	-0.35 ± 0.26
28	22:17:04.494	+00:07:23.20	1.59	53.7	5.5	1.8 ± 0.6	0.5 ± 0.2	1.9 ± 1.0	0.00 ± 0.37
29	22:17:04.867	+00:09:40.89	1.57	240.6	9.9	6.4 ± 0.8	1.8 ± 0.3	6.3 ± 1.2	-0.06 ± 0.13
30	22:17:05.380	+00:15:12.71	1.53	663.7	24.8	14.4 ± 0.9	5.4 ± 0.4	8.8 ± 1.2	-0.42 ± 0.06

ID	RA	Dec	Err	Net Counts	Significance	$S_{0.5-8\ \mathrm{keV}}$	$S_{0.5-2\ \mathrm{keV}}$	$S_{2-8\ \mathrm{keV}}$	HR
31	22:17:05.390	+00:26:29.79	1.60	121.7	11.8	5.0 ± 1.0	2.0 ± 0.4	1.9 ± 1.5	-0.61 ± 0.24
32	22:17:05.686	+00:22:21.38	1.61	71.4	5.7	2.0 ± 0.7	0.8 ± 0.3	1.0 ± 1.1	-0.53 ± 0.42
33	22:17:05.720	+00:19:49.81	1.60	66.9	5.2	1.7 ± 0.6	0.1 ± 0.2	3.5 ± 1.1	0.89 ± 0.40
34	22:17:05.969	+00:26:47.18	1.57	99.3	10.0	5.1 ± 1.1	2.2 ± 0.5	1.3 ± 1.5	-0.74 ± 0.27
35	22:17:07.376	+00:17:22.20	1.61	54.5	4.3	1.3 ± 0.5	0.6 ± 0.2	$- \pm -$	-1.01 ± 0.55
36	22:17:07.719	+00:03:01.73	1.72	64.0	8.0	5.8 ± 1.5	1.8 ± 0.6	5.0 ± 2.1	-0.18 ± 0.25
37	22:17:08.896	+00:27:15.51	1.53	882.7	51.4	69.6 ± 3.5	27.1 ± 1.5	34.9 ± 4.0	-0.51 ± 0.05
38	22:17:10.006	+00:04:56.16	1.59	168.6	9.5	5.2 ± 0.9	2.1 ± 0.3	2.4 ± 1.1	-0.56 ± 0.18
39	22:17:10.110	+00:11:57.43	1.57	285.0	12.9	5.6 ± 0.7	2.0 ± 0.3	3.7 ± 0.9	-0.36 ± 0.12
40	22:17:10.381	+00:06:04.79	1.54	885.3	36.0	26.0 ± 1.4	9.4 ± 0.6	16.6 ± 1.8	-0.39 ± 0.05
41	22:17:10.431	+00:11:04.89	1.61	58.6	4.2	0.9 ± 0.6	0.3 ± 0.2	0.5 ± 0.8	-0.45 ± 0.71
42	22:17:10.589	+00:02:53.44	1.57	400.7	29.3	35.9 ± 2.7	13.2 ± 1.2	21.4 ± 3.3	-0.42 ± 0.07
43	22:17:11.141	+00:19:50.42	1.58	95.2	5.7	1.9 ± 0.6	0.8 ± 0.2	0.6 ± 0.8	-0.68 ± 0.36
44	22:17:12.022	+00:12:43.97	1.54	410.3	19.0	8.0 ± 0.7	0.7 ± 0.2	14.7 ± 1.3	0.68 ± 0.08
45	22:17:12.558	+00:21:47.30	1.60	114.6	7.7	3.0 ± 0.7	1.2 ± 0.3	1.2 ± 0.9	-0.60 ± 0.25
46	22:17:12.901	+00:24:44.50	1.55	525.0	21.9	17.6 ± 1.3	6.0 ± 0.5	12.5 ± 1.8	-0.32 ± 0.07
47	22:17:13.531	+00:11:56.68	1.58	185.0	8.7	3.7 ± 0.6	1.4 ± 0.2	1.8 ± 0.8	-0.53 ± 0.17
48	22:17:15.039	+00:12:01.07	1.58	231.4	11.6	4.6 ± 0.7	1.7 ± 0.3	2.7 ± 0.9	-0.42 ± 0.15
49	22:17:15.056	+00:01:37.11	1.77	103.8	8.8	10.8 ± 2.1	2.6 ± 0.7	12.3 ± 3.3	0.09 ± 0.19
50	22:17:15.189	+00:26:14.92	1.51	2705.3	91.5	104.3 ± 2.9	39.4 ± 1.3	58.4 ± 3.5	-0.46 ± 0.03
51	22:17:15.346	+00:18:48.02	1.54	709.0	24.0	14.5 ± 1.0	5.9 ± 0.4	6.9 ± 1.1	-0.55 ± 0.06
52	22:17:15.542	+00:05:43.68	1.59	216.8	13.1	6.5 ± 0.8	2.0 ± 0.3	5.4 ± 1.2	-0.19 ± 0.13
53	22:17:15.795	+00:27:48.31	1.62	65.2	5.9	5.1 ± 1.4	1.5 ± 0.5	4.3 ± 2.1	-0.18 ± 0.29
54	22:17:16.148	+00:07:27.93	1.62	59.8	5.9	1.9 ± 0.7	0.5 ± 0.2	1.8 ± 1.1	-0.08 ± 0.38
55	22:17:16.231	+00:27:14.88	1.71	83.5	5.0	3.8 ± 1.0	1.2 ± 0.4	3.1 ± 1.5	-0.20 ± 0.28
56	22:17:16.711	+00:17:13.39	1.59	54.1	4.7	0.8 ± 0.4	$- \pm -$	1.9 ± 0.7	1.18 ± 0.75
57	22:17:16.935	+00:22:09.59	1.54	266.9	13.8	6.8 ± 0.8	3.5 ± 0.4	0.0 ± 0.8	-1.00 ± 0.11
58	22:17:17.834	+00:21:57.03	1.55	255.8	13.3	5.7 ± 0.8	1.9 ± 0.3	4.3 ± 1.1	-0.28 ± 0.14
59	22:17:19.058	+00:18:11.66	1.65	53.7	4.7	2.3 ± 0.8	1.0 ± 0.3	1.0 ± 1.0	-0.61 ± 0.32
60	22:17:19.072	+00:09:52.22	1.62	94.2	4.9	1.9 ± 0.5	0.5 ± 0.2	2.1 ± 0.8	0.05 ± 0.29

ID	RA	Dec	Err	Net Counts	Significance	$S_{0.5-8\ \mathrm{keV}}$	$S_{0.5-2\ \mathrm{keV}}$	$S_{2-8\ \mathrm{keV}}$	HR
61	22:17:19.296	+00:14:27.57	1.59	292.0	14.5	8.3 ± 0.9	4.1 ± 0.4	1.1 ± 0.8	−0.87 ± 0.09
62	22:17:20.185	+00:20:17.65	1.58	213.6	9.6	4.2 ± 0.6	1.6 ± 0.3	2.4 ± 0.9	−0.46 ± 0.16
63	22:17:20.738	+00:18:58.19	1.58	163.9	8.3	3.1 ± 0.5	1.1 ± 0.2	2.1 ± 0.8	−0.35 ± 0.18
64	22:17:20.768	+00:18:31.70	1.58	101.8	6.2	1.9 ± 0.5	0.3 ± 0.2	3.1 ± 0.8	0.46 ± 0.26
65	22:17:20.781	+00:10:35.27	1.60	116.7	6.1	2.2 ± 0.5	0.6 ± 0.2	2.2 ± 0.8	−0.07 ± 0.23
66	22:17:21.869	+00:01:05.54	1.70	96.7	13.8	19.1 ± 3.2	7.0 ± 1.3	11.7 ± 4.0	−0.41 ± 0.16
67	22:17:22.275	+00:18:33.05	1.58	99.2	5.7	1.9 ± 0.5	0.8 ± 0.2	0.7 ± 0.7	−0.65 ± 0.30
68	22:17:22.307	+00:16:40.13	1.57	245.3	9.9	3.8 ± 0.6	1.2 ± 0.2	3.4 ± 0.8	−0.16 ± 0.15
69	22:17:22.561	+00:21:07.67	1.66	141.9	6.1	3.2 ± 0.6	1.1 ± 0.2	2.6 ± 0.9	−0.23 ± 0.20
70	22:17:23.346	+00:19:51.26	1.59	149.1	8.8	2.8 ± 0.6	1.1 ± 0.2	1.3 ± 0.8	−0.56 ± 0.22
71	22:17:23.641	+00:16:52.34	1.55	420.4	16.6	6.9 ± 0.6	0.9 ± 0.2	11.3 ± 1.1	0.52 ± 0.09
72	22:17:25.419	+00:10:51.49	1.58	199.5	8.8	3.5 ± 0.5	0.7 ± 0.2	4.7 ± 0.9	0.23 ± 0.15
73	22:17:25.666	+00:01:40.58	1.75	38.8	5.6	7.2 ± 2.2	3.3 ± 1.0	1.4 ± 2.5	−0.81 ± 0.31
74	22:17:25.941	+00:28:05.58	1.59	302.0	14.4	13.6 ± 1.2	5.7 ± 0.5	4.7 ± 1.5	−0.66 ± 0.09
75	22:17:26.300	+00:03:46.81	1.61	97.6	9.1	2.6 ± 0.8	0.7 ± 0.3	2.7 ± 1.2	−0.02 ± 0.30
76	22:17:27.456	+00:06:04.92	1.59	106.4	6.0	3.0 ± 0.6	1.1 ± 0.2	1.8 ± 0.9	−0.41 ± 0.23
77	22:17:27.462	+00:02:16.17	1.61	153.9	9.8	7.5 ± 1.2	3.0 ± 0.5	3.2 ± 1.5	−0.58 ± 0.17
78	22:17:27.745	+00:24:27.19	1.56	489.8	23.8	14.0 ± 1.1	6.9 ± 0.5	1.2 ± 1.1	−0.92 ± 0.07
79	22:17:28.306	+00:18:19.78	1.59	94.3	4.6	1.7 ± 0.4	− ± −	3.8 ± 0.8	1.05 ± 0.30
80	22:17:28.860	+00:16:01.26	1.56	127.3	5.6	2.0 ± 0.4	0.4 ± 0.2	2.8 ± 0.7	0.32 ± 0.22
81	22:17:28.932	+00:07:53.97	1.60	65.4	4.5	1.5 ± 0.5	0.1 ± 0.2	2.7 ± 0.9	0.66 ± 0.38
82	22:17:29.509	+00:27:00.99	1.62	123.0	8.2	4.4 ± 0.9	1.6 ± 0.3	2.8 ± 1.3	−0.38 ± 0.22
83	22:17:29.771	+00:08:46.55	1.57	108.8	6.2	2.1 ± 0.6	0.1 ± 0.2	4.4 ± 1.0	0.90 ± 0.28
84	22:17:30.284	+00:13:45.80	1.58	81.8	4.7	1.2 ± 0.4	0.1 ± 0.1	2.2 ± 0.7	0.66 ± 0.38
85	22:17:30.293	+00:26:12.37	1.60	85.2	5.4	3.1 ± 0.8	1.4 ± 0.3	0.5 ± 1.1	−0.84 ± 0.32
86	22:17:30.347	+00:28:41.34	1.60	91.4	7.1	3.0 ± 1.0	1.7 ± 0.4	1.9 ± 1.4	−0.56 ± 0.28
87	22:17:30.544	+00:14:47.05	1.66	132.0	6.3	2.1 ± 0.4	0.4 ± 0.1	2.9 ± 0.7	0.30 ± 0.20
88	22:17:30.872	+00:09:11.34	1.59	91.7	4.8	1.9 ± 0.6	0.6 ± 0.3	3.9 ± 1.0	0.25 ± 0.29
89	22:17:31.231	+00:20:00.20	1.53	948.4	34.8	17.8 ± 0.9	6.5 ± 0.4	11.8 ± 1.2	−0.38 ± 0.05
90	22:17:31.757	+00:17:14.75	1.59	97.7	4.3	1.4 ± 0.4	0.2 ± 0.2	2.0 ± 0.7	0.39 ± 0.32

ID	RA	Dec	Err	Net Counts	Significance	$S_{0.5-8\ \mathrm{keV}}$	$S_{0.5-2\ \mathrm{keV}}$	$S_{2-8\ \mathrm{keV}}$	HR
91	22:17:32.073	+00:01:23.38	1.68	86.5	8.8	8.2 ± 1.7	3.3 ± 0.7	3.7 ± 2.1	-0.57 ± 0.20
92	22:17:32.347	+00:10:59.97	1.54	631.4	23.4	11.2 ± 0.8	4.3 ± 0.3	6.5 ± 1.0	-0.46 ± 0.07
93	22:17:33.211	+00:14:25.42	1.59	81.4	4.1	1.2 ± 0.4	0.5 ± 0.2	0.5 ± 0.6	-0.64 ± 0.37
94	22:17:33.462	+00:20:51.96	1.60	52.1	5.4	1.3 ± 0.5	0.4 ± 0.2	1.4 ± 0.8	-0.02 ± 0.40
95	22:17:33.512	+00:25:33.82	1.62	120.1	6.5	3.9 ± 0.8	1.6 ± 0.3	1.5 ± 1.1	-0.64 ± 0.23
96	22:17:33.782	+00:19:59.85	1.58	111.3	6.7	2.1 ± 0.5	0.3 ± 0.2	3.2 ± 0.8	0.43 ± 0.25
97	22:17:33.793	+00:13:02.92	1.58	82.5	4.4	1.4 ± 0.4	0.4 ± 0.2	1.4 ± 0.6	-0.08 ± 0.31
98	22:17:34.966	+00:05:09.57	1.62	49.4	4.9	1.5 ± 0.6	0.5 ± 0.2	1.2 ± 1.0	-0.21 ± 0.43
99	22:17:35.249	+00:09:29.29	1.55	301.3	12.6	5.9 ± 0.6	2.2 ± 0.3	3.8 ± 0.9	-0.39 ± 0.11
100	22:17:35.535	+00:11:27.87	1.58	170.7	8.3	2.7 ± 0.5	0.4 ± 0.2	4.3 ± 0.8	0.47 ± 0.19
101	22:17:36.639	+00:10:05.39	1.53	1219.3	39.3	22.8 ± 1.0	9.0 ± 0.5	12.4 ± 1.2	-0.49 ± 0.04
102	22:17:36.658	+00:16:22.36	1.57	147.8	7.3	2.2 ± 0.5	0.6 ± 0.2	2.4 ± 0.7	0.03 ± 0.21
103	22:17:37.306	+00:27:45.11	1.60	65.3	4.8	3.0 ± 0.9	0.7 ± 0.3	3.2 ± 1.4	0.04 ± 0.30
104	22:17:38.462	+00:12:05.75	1.55	1567.2	41.6	25.5 ± 1.0	10.9 ± 0.5	10.6 ± 1.1	-0.61 ± 0.03
105	22:17:38.698	+00:09:38.96	1.55	341.2	13.7	6.7 ± 0.7	2.8 ± 0.3	2.9 ± 0.8	-0.58 ± 0.10
106	22:17:39.218	+00:29:02.04	1.64	129.9	8.9	10.2 ± 1.7	4.0 ± 0.7	4.8 ± 2.4	-0.54 ± 0.19
107	22:17:39.588	+00:15:26.43	1.59	90.9	5.0	1.3 ± 0.4	0.5 ± 0.2	0.7 ± 0.6	-0.45 ± 0.36
108	22:17:39.657	+00:08:16.91	1.61	133.3	6.6	2.6 ± 0.6	1.0 ± 0.2	1.5 ± 0.8	-0.45 ± 0.24
109	22:17:39.659	+00:06:53.52	1.54	756.0	28.8	18.3 ± 1.1	6.6 ± 0.5	11.9 ± 1.4	-0.38 ± 0.06
110	22:17:39.910	+00:12:59.22	1.59	88.0	4.1	1.4 ± 0.4	0.6 ± 0.2	0.4 ± 0.6	-0.72 ± 0.35
111	22:17:41.314	+00:05:50.17	1.62	214.4	10.3	5.9 ± 0.8	2.4 ± 0.3	2.6 ± 1.1	-0.58 ± 0.15
112	22:17:41.627	+00:09:08.66	1.59	98.3	6.2	1.9 ± 0.5	0.8 ± 0.2	0.5 ± 0.7	-0.73 ± 0.33
113	22:17:41.872	+00:18:54.97	1.59	126.9	7.6	2.4 ± 0.5	0.9 ± 0.2	1.4 ± 0.7	-0.42 ± 0.22
114	22:17:43.929	+00:20:07.57	1.61	200.9	8.6	4.0 ± 0.6	1.6 ± 0.2	2.0 ± 0.8	-0.51 ± 0.16
115	22:17:43.962	+00:17:19.93	1.55	497.9	27.7	8.3 ± 0.7	3.4 ± 0.3	3.8 ± 0.8	-0.56 ± 0.08
116	22:17:45.072	+00:29:59.56	1.67	90.3	8.3	7.9 ± 1.6	3.1 ± 0.6	3.5 ± 2.5	-0.56 ± 0.25
117	22:17:45.126	+00:14:46.66	1.53	1107.6	32.8	18.9 ± 0.9	5.2 ± 0.3	19.7 ± 1.4	-0.03 ± 0.05
118	22:17:45.139	+00:24:47.30	1.57	237.3	15.6	8.2 ± 1.0	2.9 ± 0.4	5.6 ± 1.4	-0.35 ± 0.12
119	22:17:45.322	+00:18:55.96	1.53	1135.1	38.1	22.1 ± 1.1	7.2 ± 0.4	18.5 ± 1.5	-0.21 ± 0.05
120	22:17:45.988	+00:19:33.76	1.55	463.9	20.2	9.2 ± 0.8	2.8 ± 0.3	8.3 ± 1.1	-0.15 ± 0.08

ID	RA	Dec	Err	Net Counts	Significance	$S_{0.5-8\ \mathrm{keV}}$	$S_{0.5-2\ \mathrm{keV}}$	$S_{2-8\ \mathrm{keV}}$	HR
121	22:17:46.239	+00:07:28.92	1.57	367.9	17.2	9.3 ± 0.8	3.2 ± 0.3	6.9 ± 1.2	-0.29 ± 0.09
122	22:17:47.092	+00:17:59.99	1.65	97.6	6.1	1.6 ± 0.5	0.5 ± 0.2	1.3 ± 0.8	-0.23 ± 0.33
123	22:17:47.181	+00:16:47.03	1.53	1076.5	37.7	26.3 ± 1.3	12.8 ± 0.6	4.4 ± 1.1	-0.84 ± 0.04
124	22:17:47.252	+00:26:31.60	1.57	256.7	12.1	10.6 ± 1.2	3.8 ± 0.5	6.5 ± 1.7	-0.41 ± 0.12
125	22:17:47.650	+00:13:32.91	1.55	569.3	20.6	10.0 ± 0.7	2.8 ± 0.3	10.4 ± 1.1	-0.03 ± 0.07
126	22:17:48.000	+00:12:24.30	1.51	1640.4	60.3	29.7 ± 1.1	11.1 ± 0.5	18.9 ± 1.4	-0.40 ± 0.04
127	22:17:48.081	+00:15:51.90	1.52	970.8	31.4	16.7 ± 0.9	6.0 ± 0.4	11.4 ± 1.2	-0.36 ± 0.05
128	22:17:48.579	+00:12:41.69	1.50	574.8	20.4	10.5 ± 0.7	4.0 ± 0.3	6.3 ± 0.9	-0.43 ± 0.07
129	22:17:48.626	+00:01:28.79	1.65	120.2	10.4	12.4 ± 2.0	5.2 ± 0.9	4.9 ± 2.3	-0.61 ± 0.16
130	22:17:49.190	+00:11:29.18	1.53	1132.6	37.0	21.6 ± 1.0	7.7 ± 0.4	15.2 ± 1.4	-0.34 ± 0.05
131	22:17:49.748	+00:06:48.64	1.58	211.3	9.4	5.7 ± 0.8	2.1 ± 0.3	3.4 ± 1.1	-0.43 ± 0.15
132	22:17:49.777	+00:24:33.99	1.62	92.1	6.2	3.5 ± 0.8	1.1 ± 0.3	2.8 ± 1.2	-0.22 ± 0.24
133	22:17:49.896	+00:23:01.92	1.63	51.7	4.3	2.4 ± 1.0	0.7 ± 0.4	2.6 ± 1.5	-0.01 ± 0.40
134	22:17:51.248	+00:11:46.19	1.51	1720.3	57.6	33.0 ± 1.3	13.2 ± 0.6	16.8 ± 1.4	-0.52 ± 0.03
135	22:17:51.262	+00:20:38.65	1.57	257.0	10.0	6.3 ± 0.8	2.4 ± 0.3	3.4 ± 1.1	-0.48 ± 0.13
136	22:17:52.399	+00:16:53.28	1.61	173.5	7.9	3.0 ± 0.6	1.0 ± 0.2	2.3 ± 0.8	-0.28 ± 0.19
137	22:17:52.402	+00:14:47.77	1.61	102.9	5.2	1.9 ± 0.5	0.3 ± 0.2	2.9 ± 0.8	0.43 ± 0.28
138	22:17:52.411	+00:09:26.38	1.55	601.6	22.2	13.9 ± 0.9	5.4 ± 0.4	7.7 ± 1.2	-0.48 ± 0.07
139	22:17:52.413	+00:08:12.55	1.65	45.3	4.2	1.4 ± 0.6	0.2 ± 0.2	1.8 ± 1.0	0.44 ± 0.55
140	22:17:52.922	+00:16:14.64	1.61	96.2	4.9	1.6 ± 0.5	0.7 ± 0.2	0.8 ± 0.7	-0.54 ± 0.34
141	22:17:53.084	+00:05:40.57	1.69	74.9	4.9	2.4 ± 0.7	1.1 ± 0.3	1.8 ± 1.3	-0.39 ± 0.32
142	22:17:53.492	+00:22:10.36	1.61	54.8	5.0	1.5 ± 0.6	0.5 ± 0.2	1.1 ± 1.0	-0.34 ± 0.45
143	22:17:53.584	+00:19:19.68	1.62	220.9	10.0	5.1 ± 0.7	1.1 ± 0.2	6.6 ± 1.2	0.19 ± 0.14
144	22:17:54.658	+00:17:55.02	1.59	91.0	4.9	2.0 ± 0.5	0.6 ± 0.2	2.0 ± 0.8	-0.09 ± 0.26
145	22:17:54.689	+00:16:39.46	1.54	221.6	9.3	5.1 ± 0.7	1.7 ± 0.3	3.9 ± 1.0	-0.28 ± 0.14
146	22:17:54.940	+00:05:14.57	1.60	79.3	5.5	2.7 ± 0.8	0.9 ± 0.3	2.1 ± 1.2	-0.23 ± 0.30
147	22:17:55.214	+00:15:12.61	1.53	1066.9	30.9	20.7 ± 1.0	8.0 ± 0.4	11.9 ± 1.3	-0.46 ± 0.05
148	22:17:55.278	+00:29:08.21	1.60	105.8	8.9	9.2 ± 1.7	3.1 ± 0.6	6.7 ± 2.7	-0.29 ± 0.21
149	22:17:59.546	+00:25:33.81	1.55	438.9	21.0	18.3 ± 1.4	6.6 ± 0.6	11.3 ± 2.0	-0.40 ± 0.08
150	22:17:59.597	+00:11:28.66	1.60	132.5	7.3	3.1 ± 0.6	1.3 ± 0.3	1.3 ± 0.9	-0.60 ± 0.23

ID	RA	Dec	Err	Net Counts	Significance	$S_{0.5-8\ \mathrm{keV}}$	$S_{0.5-2\ \mathrm{keV}}$	$S_{2-8\ \mathrm{keV}}$	HR
151	22:18:01.090	+00:02:39.46	1.73	59.0	9.9	6.6 ± 1.8	2.0 ± 0.7	5.8 ± 2.6	-0.15 ± 0.28
152	22:18:01.308	+00:11:28.71	1.58	10.6	8.6	0.3 ± 0.6	0.1 ± 0.2	0.3 ± 1.0	-0.17 ± 2.15
153	22:18:01.737	+00:15:01.10	1.68	95.3	6.0	3.2 ± 0.8	0.5 ± 0.3	4.7 ± 1.3	0.39 ± 0.23
154	22:18:01.923	+00:07:37.68	1.63	76.2	6.7	2.5 ± 0.7	0.8 ± 0.2	1.8 ± 1.1	-0.26 ± 0.32
155	22:18:01.933	+00:18:54.33	1.54	928.7	35.1	24.3 ± 1.2	8.2 ± 0.5	18.7 ± 1.7	-0.27 ± 0.05
156	22:18:03.435	+00:04:48.79	1.56	280.4	15.0	11.3 ± 1.2	3.6 ± 0.4	9.3 ± 1.8	-0.21 ± 0.11
157	22:18:04.585	+00:10:19.33	1.58	227.3	10.8	7.1 ± 0.9	2.7 ± 0.4	4.2 ± 1.2	-0.44 ± 0.13
158	22:18:04.857	+00:21:31.21	1.60	135.8	7.7	4.4 ± 0.8	1.1 ± 0.3	4.4 ± 1.3	0.00 ± 0.20
159	22:18:05.509	+00:12:50.93	1.61	133.3	6.6	3.1 ± 0.7	1.0 ± 0.3	2.3 ± 1.0	-0.28 ± 0.24
160	22:18:05.747	+00:09:13.36	1.56	278.4	15.2	9.5 ± 1.0	3.9 ± 0.4	4.0 ± 1.3	-0.59 ± 0.11
161	22:18:05.940	+00:15:05.58	1.60	66.5	5.0	1.7 ± 0.6	0.4 ± 0.2	2.2 ± 0.9	0.22 ± 0.34
162	22:18:06.558	+00:09:26.85	1.50	98.2	5.2	3.1 ± 0.8	1.7 ± 0.4	2.5 ± 1.2	-0.46 ± 0.22
163	22:18:06.593	+00:05:35.80	1.55	369.1	19.4	14.3 ± 1.3	5.7 ± 0.5	6.5 ± 1.6	-0.56 ± 0.09
164	22:18:07.992	+00:18:52.35	1.60	99.6	6.8	3.6 ± 0.8	1.3 ± 0.3	2.0 ± 1.2	-0.46 ± 0.25
165	22:18:08.848	+00:27:37.02	1.65	50.9	5.9	4.5 ± 1.5	2.0 ± 0.6	0.5 ± 2.2	-0.88 ± 0.49
166	22:18:09.128	+00:15:53.46	1.59	57.1	4.1	1.7 ± 0.6	0.5 ± 0.2	1.4 ± 1.0	-0.18 ± 0.40
167	22:18:10.282	+00:19:33.25	1.63	189.1	10.8	6.4 ± 0.9	2.2 ± 0.4	4.6 ± 1.4	-0.31 ± 0.15
168	22:18:11.452	+00:13:03.72	1.62	99.2	6.5	3.0 ± 0.7	0.9 ± 0.2	2.7 ± 1.1	-0.11 ± 0.25
169	22:18:12.318	+00:14:56.67	1.61	59.4	5.5	2.0 ± 0.7	0.3 ± 0.2	3.5 ± 1.2	0.55 ± 0.32
170	22:18:12.653	+00:05:02.55	1.89	33.5	4.9	7.9 ± 2.7	2.8 ± 1.1	5.0 ± 3.6	-0.39 ± 0.35
171	22:18:13.247	+00:14:26.30	1.59	99.2	4.8	2.6 ± 0.7	1.0 ± 0.3	1.5 ± 1.1	-0.44 ± 0.32
172	22:18:13.460	+00:26:22.90	1.63	126.8	10.2	10.8 ± 1.8	3.8 ± 0.7	7.1 ± 2.8	-0.36 ± 0.19
173	22:18:13.852	+00:16:24.45	1.55	609.5	24.4	19.8 ± 1.2	0.4 ± 0.2	42.8 ± 2.6	0.93 ± 0.04
174	22:18:14.164	+00:20:49.38	1.56	296.5	14.2	11.7 ± 1.2	5.0 ± 0.5	3.7 ± 1.5	-0.69 ± 0.11
175	22:18:15.863	+00:10:14.49	1.63	94.0	5.3	3.2 ± 0.8	1.5 ± 0.3	0.5 ± 1.2	-0.83 ± 0.34
176	22:18:16.095	+00:09:39.75	1.57	270.7	14.8	10.2 ± 1.1	3.3 ± 0.4	8.2 ± 1.6	-0.23 ± 0.11
177	22:18:19.291	+00:23:34.59	1.67	150.3	11.7	9.6 ± 1.4	3.3 ± 0.5	6.5 ± 2.2	-0.34 ± 0.17
178	22:18:19.341	+00:10:32.41	1.59	71.0	5.5	3.2 ± 0.8	1.0 ± 0.3	2.7 ± 1.4	-0.19 ± 0.28
179	22:18:20.470	+00:18:54.93	1.62	115.9	7.2	4.7 ± 1.0	1.9 ± 0.4	1.8 ± 1.4	-0.62 ± 0.24
180	22:18:20.488	+00:13:04.45	1.63	83.1	6.3	3.4 ± 0.9	1.2 ± 0.3	2.1 ± 1.4	-0.38 ± 0.30

ID	RA	Dec	Err	Net Counts	Significance	$S_{0.5-8\ \mathrm{keV}}$	$S_{0.5-2\ \mathrm{keV}}$	$S_{2-8\ \mathrm{keV}}$	HR
181	22:18:21.928	+00:08:00.05	1.50	0.0	33.8	$- \pm -$	$- \pm -$	$- \pm -$	-0.61 ± 1.89
182	22:18:22.155	+00:14:47.87	1.65	184.8	11.1	7.6 ± 1.0	2.2 ± 0.4	7.2 ± 1.6	-0.11 ± 0.14
183	22:18:22.185	+00:27:07.05	1.50	0.0	5.6	$- \pm -$	$- \pm -$	$- \pm -$	-0.00 ± 0.71
184	22:18:22.471	+00:09:09.56	1.63	89.6	7.6	4.1 ± 1.0	0.8 ± 0.3	5.5 ± 1.7	0.26 ± 0.23
185	22:18:23.115	+00:16:05.21	1.66	103.5	6.6	4.2 ± 1.0	2.0 ± 0.4	0.5 ± 1.4	-0.88 ± 0.31
186	22:18:25.094	+00:24:26.02	1.52	1334.4	88.6	120.1 ± 4.8	32.4 ± 1.7	130.0 ± 7.9	0.00 ± 0.04
187	22:18:28.324	+00:14:48.51	1.62	107.2	6.5	5.2 ± 1.1	1.9 ± 0.4	2.7 ± 1.6	-0.49 ± 0.24
188	22:18:29.149	+00:09:52.77	1.68	37.2	4.9	2.9 ± 1.3	0.6 ± 0.4	4.7 ± 2.4	0.34 ± 0.39
189	22:18:30.082	+00:12:21.33	1.61	126.8	10.4	7.7 ± 1.3	2.7 ± 0.5	5.3 ± 2.0	-0.34 ± 0.19
190	22:18:35.553	+00:11:51.11	1.65	40.6	5.2	3.5 ± 1.4	0.6 ± 0.4	5.4 ± 2.6	0.39 ± 0.36